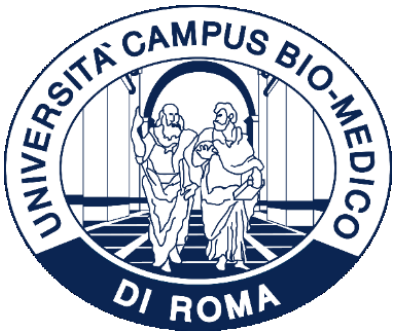

UNIVERSITA' CAMPUS BIO-MEDICO DI ROMA

PhD in SCIENCE AND ENGINEERING FOR HUMANS AND THE ENVIRONMENT

XXXVII cycle A.Y. 2021-2022

ADVANCED BATCH AND IN-FLOW SYNTHESES OF POLYMERIC MICRO AND NANO PARTICLES FOR DRUG DELIVERY AND CELL-ENCAPSULATION

PhD candidate

Emanuele Limiti

Supervisor

Chiar.ma Prof.ssa Marcella Trombetta

Table of Contents

ABSTRACT

The present work introduces innovative strategies in the synthesis and application of nanomaterials and microfluidic technologies for drug delivery and single-cell encapsulation. The main goal is to address the critical limitations of conventional methodologies, including poor reproducibility, limited scalability, and restricted material design.

In recent years, nanogels (NGs) are emerging as a promising class of nanomaterial thanks to their unique properties, such as swelling, high drug loading, and good biocompatibility. To overcome the constrains of traditional NGs syntheses, a novel Mixed Emulsion/Evaporation Technique (MEET) and advanced microfluidic platforms, equipped with pneumatic actuation, were employed for the synthesis of hyaluronic acid – linear polyethyleneimine (HA-LPEI) NGs.

MEET method overcomes the requirements of hydrophilic/hydrophobic polymer system in traditional emulsification/evaporation processes. The resulting NGs exhibited remarkable stability and controlled drug release. Moreover, folate surface functionalization was also introduced to further enhance targeting specificity towards tumor cells overexpressing folate receptors.

In parallel, droplet-based microfluidic chip equipped with pneumatic micro-actuation allows the fine manipulation NG properties, such as size, monodispersity, and drug release kinetics. Microfluidically synthesized NGs showed unparalleled cell internalization and therapeutic efficacy, especially when compared with their bulk counterpart. To further explore the potentiality of these systems, a process optimization using Response Surface Methodology (RSM) was conducted and the developed empirical model allowed the prediction and control of NG physicochemical and biological properties as a function of synthesis parameters, including flow rate ratio and molar ratio.

Additionally, a comparative analysis of two microfluidic geometries—flow-focusing junction (FFJ) and T-junction (TJ)—for alginate beads generation revealed the superior performance of the FFJ system. The FFJ device achieved higher production frequencies, reduced polydispersity, and enhanced bead circularity. Altogether, these performances strengthened the FFJ application as an ideal platform for single-cell encapsulation. The good viability of SKOV3 cells after the encapsulation process validates the applicability and stability of the alginate microbead system for up to seven days.

Overall, this work proposes novel strategies in the design and functionalization of nanomaterials for drug delivery and reveals the promising application of microfluidic platforms for cell encapsulation purposes. These findings fulfill existing gaps in material synthesis and biomedical engineering, highlighting the promising application of microfluidics for future clinical translation in nanomedicine and personalized medicine.

PART I
INTRODUCTION

1. Introduction

1.1 Nanoparticles Classification, Properties and Biomedical Applications

According to International Organization for Standardization (ISO), nanoparticles (NPs) are defined as nanostructured materials with all external dimensions in the nanoscale, where the lengths of the longest and the shortest axes do not differ significantly.[1] The small sizes provide NPs with peculiar characteristics that led the growing interest in such materials in the past decades. In particular, the distinctive surface effects that characterize nanomaterials, compared to their larger counterpart, can be attributed to three main factors[2]: I) very high surface area and high number of particles for mass unit; II) the increased fraction of atom at the nanomaterials surface; III) the surface atoms have fewer direct neighbors, therefore limiting their mutual influence. Altogether, these factors provide NPs with augmented and unparalleled reactivity. Due to their peculiar characteristics, NPs are employed in a wide range of applications, such as drug delivery, water treatment, agriculture, catalysis, electronics, etc.

Generally, NPs can be classified on the basis of their physical and chemical characteristics. As first classification, it is possible to broadly distinguish between inorganic, and organic NPs.[3] Moreover, each of these classes can be further divided into a few other subgroups.

1.1.1 Inorganic nanoparticles.

Inorganic NPs can be categorized based on the nature of the inorganic material used for their synthesis (*Figure 1.1*). In particular, they can be made of semiconductor, ceramic, or magnetic metal atoms bound together with covalent or metallic bonds.[3–5] These NPs are characterized by high stability and good mechanical properties, mainly due to the high ordered three-dimensional lattice structure formed by the crystallization of inorganic precursors.

Generally, inorganic NPs consist of a core-shell structure where the inorganic core is crowned by other organic compounds, such as polymers or bio-macromolecules. The core-shell arrangement provides these nanoparticles with suitable surface for further functionalization with bio-active molecules, or to avoid unwanted interaction with the biological environment.[6]

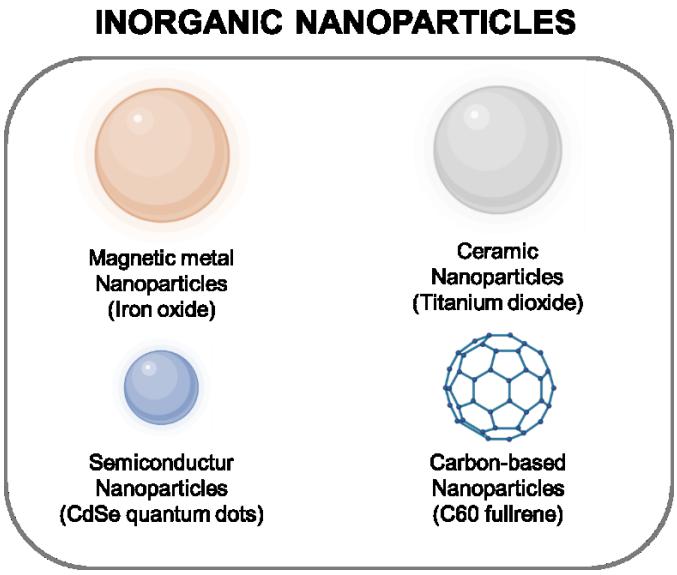

Figure 1.1 General classification of inorganic nanoparticles. image generated by Biorender.

Different classes of inorganic NPs can be recognized, such as magnetic metal NPs, ceramic NPs, semiconductor NPs, and carbon-based NPs. Overall, these nanomaterials share some common characteristics. In particular they have optimal mechanical properties, small dimensions, good uniformity, and easy production procedures.[3,7–14]

1.1.2 Organic nanoparticles.

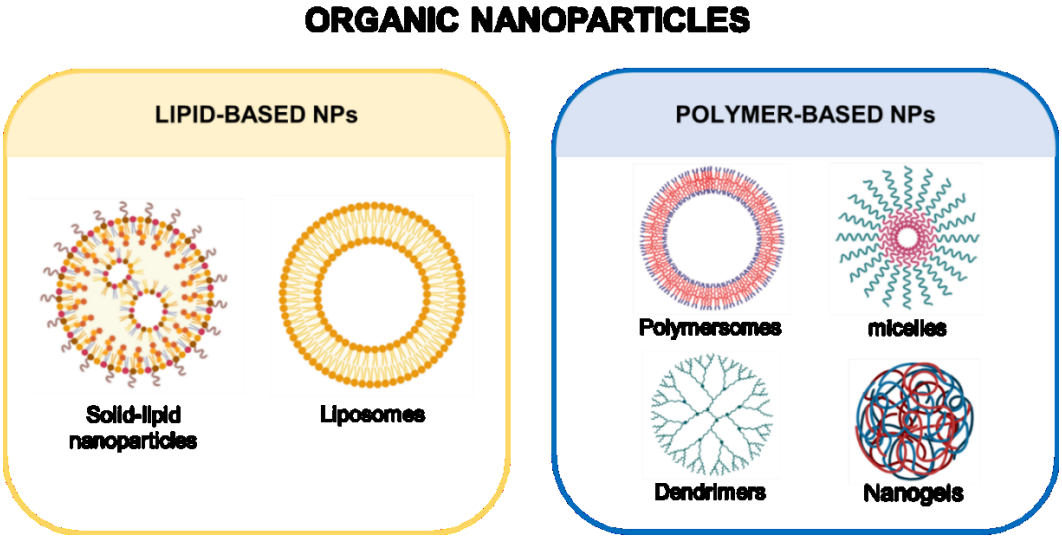

Figure 1.2 General classification of organic nanoparticles. image generated by Biorender.

Organic NPs are principally based on lipid or polymeric nanosystems (*Figure 1.2*). However, protein NPs and pro-drug NPs are recently gaining increasing attention as suitable alternatives.[15,16] Generally, their physicochemical properties can be easily modulated, and

their high biocompatibility, biodegradability, colloidal stability, and relatively large size allow incorporating and carrying a wide combination of different drugs.[17] Indeed, these nanostructured materials found their main application in drug and gene delivery as non-viral alternative to the traditional viral delivery systems. Depending on the route of preparation, it is possible to distinguish between self-assembly NPs, which have an amphiphilic nature, and NPs obtained by specific synthesis processes.

Lipid-based nanoparticles.

Several classes of lipid-based NPs have been developed in the past decades.[16] Typically, they comprise at least one lipid bilayer surrounding one internal aqueous core. Liposomes and solid-lipid NPs (SLNPs) represent the most widely explored lipid nanosystems in basic research and in clinics for drug delivery purposes. Their success is mainly due to their formulation simplicity, self-assembly properties, biocompatibility, high bioavailability, high drug loading, and easy modulation of their physicochemical properties.

Liposomes are formed by natural or synthetic phospholipids (or other lipid molecules, such as cholesterol) that mimic the properties of the biological membranes by self-assembling into lipid bilayer vesicles.[18] Thanks to this structural composition, liposomes are able to carry both hydrophilic and hydrophobic active compounds by loading the first ones into the polar core and the seconds into the bilayer (in the acyl chain region), improving, therefore, the solubilization of lyophilic drugs in aqueous solvents. Additionally, the hosting of drugs in the liposome membrane reduces drug degradation.[19] According to their physico-chemical properties, liposomes are suitable candidates for surface functionalization strategies. These are designed to graft specific moieties, such as ligands (e.g., proteins, antibodies, small molecules) and polymers (e.g., PEG), with the final aim of enhancing the circulation time, and implementing the selective targeting and stimulus-responsive behavior.[20]

By contrast, SLNPs have a solid lipid core matrix usually composed of lecithin, triacylglycerol and waxes.[18,21] The solid core is usually stabilized by surfactants or polymers in a spherical shape of dimensions ranging between 50 to 100 nm. They can load and carry both hydrophilic and lipophilic drugs but suffer of a low drug loading, limited by the solubility of drug in the lipid.[3,9]

Polymer-based nanoparticles.

Three main classes of polymeric NPs can be recognized (*Figure 1.3*): dendrimers, nano-capsules (such as polymersomes and micelles), and nano-spheres.[15,22]

Dendrimers are highly branched polymeric structure consisting of three main domains: a focal core, being the atom or molecule from which the three-dimensional structure branches out; the dendrons, which are the monomers forming new layers and enlarging the dendritic matrix; and the final functional groups, which are responsible for the interaction with the molecular environment.[23] External functional groups are of fundamental importance to define many dendrimer properties, such as their biocompatibility, cellular internalization, drug loading and release performances. Therefore, dendrimers are extensively applied in biomedical research especially in the drug delivery field. The ability to engineer each of the three compartments of a dendritic matrix make them suitable for the encapsulation and delivery of specific active principles.[23,24]

Nano-capsules are characterized by a reservoir form in which the liquid or semi-solid core is surrounded by a solid polymer layer.[22,25] Their vesicular architecture makes them among the most studied polymeric NPs for the delivery of many active principles.[26] The central cavity acts as a reservoir where the molecules of interest can be stored until reaching the desired site of delivery, while the polymeric shell protects the core from the external environment and provides an easily functional surface. Nano-capsules can show self-assembly feature or can be synthesized depending on the selected formulation protocol.[15] Polymersomes and micelles are amphiphilic nanoparticles that can be easily prepared through self-assembling. The polymeric double layer, characterized by hydrophilic inner and outer surfaces and hydrophobic inner membrane, make polymersomes the polymeric counterpart of liposomes. Their vesicles-like shape enables the delivery of both water-soluble and hydrophobic active molecules: the first ones are loaded in the central core, whereas the lyophilic molecules are entrapped in the surrounded membrane.[27] They demonstrate enhanced chemical and physical stability and resilience, primarily due to the incorporation of high-molecular-weight polymers that entangle with one another, thereby enhancing their structural properties.[28,29] Polymeric micelles are self-assembled structures of amphiphilic copolymers. Their self-assembly features occur when the polymer concentration is higher than the critical micelle concentration (CMC). The structure is composed of an outer hydrophilic layer and a hydrophobic core, which enables the loading and delivery of lyophilic drugs. Additionally, hydrophilic active compounds can be delivered by surface conjugation.[30,31]

By contrast, nano-spheres are homogenous matrix systems wherein a dispersed or dissolved therapeutic compound is adsorbed on the surface or entrapped within the polymeric matrix

structure by physical entrapment or chemical bonding.[15] Among the many types of polymeric nano-spheres, nanogels (NGs) represent one of the most promising alternatives. NGs are chemically or physically cross-linked polymeric matrix capable of absorbing great amount of water. They are characterized by high colloidal stability, prolonged cargo retention, high biocompatibility, and the swelling feature that enhances dispersion stability.[32–34] Swelling is a unique property of NGs systems which allow them to highly encapsulate several types of cargos, both hydrophilic and hydrophobic, within the polymeric matrix. Moreover, the swelling/deswelling behavior can be modulated by biological relevant signals enabling a stimuli-responsive release of the encapsulated active principle.[35,36] Furthermore, the high number of functional groups present in their surface allow the grafting of bioactive moieties. Therefore, NGs chemico-physical characteristics can be easily adapted to the specific area of application through surface functionalization strategies.[32,34] Indeed, NGs are gaining increasing attention mainly due to their versatility, easy of fabrication, and outstanding biocompatibility compared to other nanosized systems.

1.2 Traditional Nanoparticles Preparation methodologies

Over time, various methods have been developed to synthesize polymeric NPs, with the ultimate goal of engineering nanocarriers that exhibit tailored physical, chemical, or mechanical properties. These properties are crucial to ensuring controlled drug release and optimizing suitability for specific biomedical applications. A key aspect in NP design is protecting the therapeutic cargo while preserving its pharmacological activity.[37]

Polymeric NPs can be obtained either through polymerization processes, starting from individual monomers, or by utilizing preformed polymers. The use of preformed polymers avoids the formation of toxic byproduct or residues, such as monomers or initiators, and simplifying the purification process of the obtained NPs.[37] The production of polymeric NPs starting from preformed polymers is generally categorized into: (i) Two-step procedures, and (ii) One-step procedures.

Two-step methods are based on: emulsification as the first step, followed by NP formation by solvent removal, which can be performed using different strategies. Several techniques can be considered to perform the emulsification step, including mechanical agitation (high or low energy stirring) and spontaneous emulsification driven by the ouzo effect - a phenomenon in which an organic solvent containing a hydrophobic oil diffuses rapidly into water upon dilution, spontaneously forming an oil-in-water emulsion.[38]

The second phase of NP synthesis involves removing the organic solvent, leading to polymer precipitation. The specific technique used depends on the method of solvent elimination:[37,38]

- **Solvent evaporation**:[39] The polymer is dissolved in a volatile organic solvent (e.g., dichloromethane, chloroform, or ethyl acetate), then emulsified in water with a surfactant. The solvent is evaporated via mechanical stirring or reduced pressure, causing NP formation.
- **Solvent diffusion**: Here, the polymer solvent is partially water-miscible. The system is first stabilized through mutual saturation of both phases, then destabilized by water dilution, triggering solvent diffusion and NP precipitation.
- **Reverse salting-out method**: A water-miscible polymer solvent is mixed with an aqueous gel containing a salting-out agent (e.g., electrolytes). These agents retain water molecules, modifying solvent miscibility and inducing spontaneous emulsification. Adding excess water reduces salt concentration, facilitating NP formation.

On the other hand, one-step procedures are known to be fast, simple and easy scalable techniques. The two major example of one-step processes are nanoprecipitation and dialysis methods. Nanoprecipitation (also called solvent displacement), is one of the simplest, fastest, and most cost-effective techniques for NP synthesis. It requires only three components: the polymer, a solvent (e.g., acetone), and a non-solvent. The polymeric solution is added dropwise to the non-solvent, leading to rapid solvent diffusion and NP precipitation. This process is driven by the Marangoni effect, where interfacial tension differences enhance droplet formation and NP size control.[40] Similarly, in dialysis method, a polymer solution is dialyzed against a non-solvent through membranes with a defined molecular weight cut-off (MWCO). As the non-solvent displaces the polymer solvent within the membrane, solubility decreases, leading to progressive NP precipitation.

1.3 Microfluidics

Over the past decades, microfluidics has emerged as a promising field of technological and scientific research[41], with the objective of developing innovative strategies for controlling and understanding the fluid dynamics of nano/pico liter fluid volumes inside microchannel devices. Its versatility in both theoretical and practical applications makes it a subject of interest to a number of scientific disciplines, including engineering, physics, chemistry, mathematics, biology, and others.[42]

To date, microfluidics has been successfully implemented as a groundbreaking technology in the biotechnology and bioengineering fields. It demonstrated unparalleled advantages in many applications such as diagnosis, organ-on-a-chip, flow chemistry, and nanomaterial synthesis.[43–45]

The peculiarity of these systems arises from the different physical principles that apply to them. In this context, the significant role of surface tension and capillary forces, rather than that of gravity, gives rise to a series of phenomena that may appear counterintuitive when compared to the large-scale phenomena that are part of our daily experience.[46] A few representative examples are laminar flow, diffusive rather than convective mass transfer, and capillary force, which are well established at the micrometer scale.

1.3.1 Dimensionless numbers

The complex fluid dynamics involved in microfluidic applications arise from the balancing of several competing forces influencing the fluid motion. Dimensionless numbers determine the relative importance of particular phenomena over their competing counterpart. For example, Reynold number (Re) expresses the ratio between inertial forces to viscous forces; the Péclet number (Pe) highlights the relationship between convection and diffusion; and Capillary number (Ca) relates viscous forces to surface tension.[47–49] Before moving further into the analysis of these dimensionless numbers a brief review of the basic fluid properties and their governing equation is given.[46,50]

Traditional mechanics uses discrete quantities, such as forces, to describe the motion of objects with defined volume or mass. This concept can be extended to the fluid dynamics under the assumption that fluids are continuum materials, therefore instead of mass and forces continuous fields like density ρ and force density f defined per unit volume are used to describe their motion.

Following this path, the Navier-Stokes equation describing the velocity field for a Newtonian fluid is the continuum counterpart of the more famous second law of dynamics $\boldsymbol{F} = m\boldsymbol{a}$:

$$\rho\left(\frac{\partial \boldsymbol{u}}{\partial t} + \boldsymbol{u}\cdot\nabla\boldsymbol{u}\right) = -\nabla \mathrm{p} + \eta\nabla^2\boldsymbol{u} + \boldsymbol{f}, \tag{1}$$

Where $\boldsymbol{u}$ is the velocity vector of the fluid, ∇ is the del operator, t is time, ρ is the fluid density, p the pressure, η the dynamic shear viscosity, and $\boldsymbol{f}$ the body force vector per unit of volume.

In this equation, the left side represents the inertial acceleration, and the right side represents the force densities. In particular, the inertial acceleration term is composed of a time-dependent acceleration $\rho\frac{\partial \boldsymbol{u}}{\partial t}$ and a convective acceleration $\rho\boldsymbol{u}\cdot\nabla\boldsymbol{u}$. Moreover, the diffusion term $\eta\nabla^2\boldsymbol{u}$ represent the divergence of the viscous stresses $\boldsymbol{\sigma}$, which are defined as follows:

$$\boldsymbol{\sigma} = \eta[\nabla\boldsymbol{u} + (\nabla\boldsymbol{u})^T]. \tag{2}$$

Another important governing equation is that expressing the mass conservation principle:

$$\frac{\partial\rho}{\partial t} + \nabla\cdot(\rho\boldsymbol{u}) = 0, \tag{3}$$

Here, under the assumption of slowly flowing fluids with constant density it is possible to reduce this equation to its incompressible continuity equation form:

$$\nabla\cdot\boldsymbol{u} = 0. \tag{4}$$

In the hypothesis of two-phase flow several boundary conditions must be considered to properly describe the liquid-liquid interface motions. In particular, the continuity of normal velocity and tangential viscous stress at the immiscible interface plays crucial role:

$$\boldsymbol{u_d}\cdot\boldsymbol{n} = \boldsymbol{u_c}\cdot\boldsymbol{n}, \tag{5}$$

$$\boldsymbol{\sigma_d}\cdot\boldsymbol{t} = \boldsymbol{\sigma_c}\cdot\boldsymbol{t}, \tag{6}$$

where the subscripts stand for dispersed (*d*) or continuous (*c*) phase fluid, $\boldsymbol{n}$ is the unit normal vector outward the interface, and $\boldsymbol{t}$ the tangential vector at the interface. Moreover, the normal stress difference that arises at the interface between dispersed and continuous phase is balanced by capillary pressure:

$$\boldsymbol{T_d}\cdot\boldsymbol{n} - \boldsymbol{T_c}\cdot\boldsymbol{n} = -\gamma\kappa, \tag{7}$$

where $\boldsymbol{T_x}$ is the stress tensor defined as $\boldsymbol{T_x} = -\mathrm{p_x}\boldsymbol{I} + \boldsymbol{\sigma_x}$ (with $\mathrm{p_x}$ being the pressure, and $\boldsymbol{I}$ the identity matrix), γ is the interfacial tension, and $\kappa = R_1^{-1} + R_2^{-1}$ is twice the mean curvature of the interface, with R_1 and R_2 being the principal radii of the curvature.

The simple theoretical analysis reported above highlights the presence of four main forces playing a role in the context of microfluidics. These forces are inertial force, viscous force, capillary force, and external body force. In the simplest case, the latter is represented only by gravity. Considering a volume of fluid flowing in a microfluidic device of characteristic

length L at a velocity u, it is possible to derive simple scaling law for each of the four forces involved. To allow comparison, it is better to normalize them per unit of area and express their influence as stress.

For instance, consider a fluid flowing in a channel contracting over a length L. Applying the law of conservation of mass its velocity increases with the position z in the channel as $u(z) = U_0\left(1+\frac{z}{L}\right)$, where U_0 is the velocity at $z = 0$. The inertial force f_i scales with the inertial acceleration terms expressed as in the Navier-Stokes equation:

$$f_i \sim \rho \frac{du}{dt}. \tag{8}$$

When a fluid is flowing through a channel, its acceleration can be described not only as the time variation of the fluid velocity but also as its variation with respect to its position z following the well-known relation:

$$\frac{du}{dt} = \frac{du}{dz} \cdot \frac{dz}{dt}. \tag{9}$$

Using equation (9) in equation (8), and recalling the variation of $u(z)$ with the z coordinate it is possible to derive the scaling law for inertial force:

$$f_i \sim \rho \frac{du}{dt} \approx \rho U_0 \frac{du}{dz} \sim \frac{\rho U_0^2}{L}\ . \tag{10}$$

Finally, we can derive the inertial stress by multiplying f_i , which is a force per unit volume, by the characteristic length of the device to get a force per unit of area:

$$\tau_i \sim f_i \cdot L \sim \rho U_0^2\ . \tag{11}$$

Furthermore, viscous stress and the stresses associated to the capillary pressure and gravity are defined as:

$$\tau_v \sim \eta \frac{U_0}{L}, \tag{12}$$

$$\tau_c \sim \gamma\kappa = \frac{\gamma}{L}, \tag{13}$$

$$\tau_g = \rho g L\,. \tag{14}$$

With equation (13) true under the assumption $\kappa \approx \frac{1}{L}$.

In principle, any ratio between two of the stresses mentioned above define a dimensionless number.

Reynolds number: Laminar flow.

Reynolds number (Re) is defined as the ratio between inertia and viscous stresses:

$$Re = \frac{\tau_i}{\tau_v} = \frac{\rho U_0 L}{\eta}. \tag{15}$$

It expresses the relative importance of inertia to viscous force. In microfluidics, Re usually ranges between 10^{-6} and 10 indicating that inertial forces are overwhelmed by viscous stresses and making the non-linear convective acceleration of equation (1) negligible. As a result, the fluid motion can be described using the simplified stokes equation:

$$\rho \frac{\partial \boldsymbol{u}}{\partial t} = -\nabla \mathrm{p} + \eta \nabla^2 \boldsymbol{u} + \boldsymbol{f}. \tag{16}$$

The main effect is the establishment of linear predictable fluid trajectories known as laminar flow.

Capillary number.

Capillary number (Ca) is one of the most commonly used dimensionless number to describe the fluid dynamics of microfluidic devices, especially when used for droplet generation. It is defined as the ratio of viscous stress to capillary pressure:

$$Ca = \frac{\tau_v}{\tau_c} = \frac{\eta U_0}{\gamma}. \tag{17}$$

Ca is a useful tool to express the competition between interfacial stresses and viscous stresses in a two-phase fluid system. Indeed, these two stresses affect the liquid-liquid interface in two opposite manners: surface tension γ tends to reduce the interfacial area, while viscous stresses drag the interface along with the fluid flow direction causing the interface to elongate. In droplet microfluidics the balancing of these two forces causes the generation of droplets.

Weber number.

Weber number (We) is obtained from the ratio between inertial stresses and capillary pressure derived stresses:

$$We = \frac{\tau_i}{\tau_c} = \frac{\rho U_0^2 L}{\gamma}, \tag{18}$$

It compares the effect of inertia to that one of surface tension. Even if inertia effects are usually negligible in microfluidics application, the strong dependence on the velocity can yield high value of We when high flow ratios are considered in the microfluidic channels, meaning that at high velocities inertia can play an important role in defining fluid motion.

Bond number.

Bond number (Bo) is considered only in two-phase flow in which the density difference between the two phases is large enough to increase the effect of gravity compared to that of surface tension. Indeed, Bo is defined as follows:

$$Bo = \frac{\tau_g}{\tau_c} = \frac{\Delta\rho g L^2}{\gamma}, \tag{19}$$

where $\Delta\rho$ is the density difference between the two phases. Typically, both $\Delta\rho$ and L are small for liquid-liquid flow, hence $Bo \ll 1$.

Peclet number: The problem of mixing.

The absence of turbulences in typical low-Re microfluidic flows causes diffusion to be the only driving force for mass transfer and mixing.[46,47] Even if in some applications, such as sorting, a low fluid mixing is desirable, the in-flow chemical reactions still require fast and homogeneous mixing to provide suitable and reproducible outcome. To ensure proper mixing, scientists developed several solutions. Passive mixers are usually based on chaotic advection, where fluids are randomly stretched and folded due to irregular changes in pressure and velocity within the microfluidic channels. Chaotic advection is highly effective at low Re number, and it is generated essentially by modifying the channel shape to stir the flow.[47,50] Among the many, the staggered herringbone micromixers (SHM) and tesla mixers represent the golden standard in passive mixers due to their design simplicity and mixer efficiency.

Peclet number (Pe) is a useful tool to evaluate the relative importance of mass transport due to convection to that due to diffusion in a straight microfluidic channel, and it is expressed as:

$$Pe = \frac{U_0 w}{D}. \quad (20)$$

Where w is the characteristic dimension of the channel and D is the diffusion coefficient. Moreover, applications such as droplet-microfluidics or digital microfluidics arise as good alternatives to improve mixing and lower reagent consumption.

1.4 Droplet microfluidics

In the early 1990s, the introduction of continuous microfluidic systems, which offered greater predictability and easier control of fluid flows, led to a significant breakthrough in numerous research fields.[51] Separation technology, flow cytometry, lab-on-chip, and organ-on-a-chip applications are just a few examples of research areas that benefited from the advent of microfluidics. However, the advantages of continuous systems are strongly limited by a number of factors, including low mixing efficiency, low throughput, Taylor dispersion, interaction between channel walls and reagents, high fluid volume and extended channel needed to perform chemical reactions.[47,52] For these reasons, droplet-microfluidics, which aims at the generation and manipulation of emulsified systems (such as water-in-oil W/O or oil-in-water O/W emulsion), emerged as a suitable alternative to overcome the abovementioned issues.[53] Its advantages are principally due to the small droplet dimensions. Indeed, scale dependencies for mass and heat transport are reduced, resulting in a more efficient mixing, the confined volume together with the high production rate with exquisite control over the size (droplets are formed up to kilohertz frequencies) allows for high throughput and fast reaction kinetics.[54,55] Moreover, these systems have the ability to perform a large number of reactions without increasing device size or complexity. Altogether, the peculiar performances of droplet-microfluidics encouraged its application in the fields of chemistry, biology, and material science with particular attention for single-cell analysis, nanomaterial synthesis, and multiplexed genomics.[56]

1.4.1 Device geometries

Droplets can be generated using several active or passive methods. Passive methods have proved to be robust in generating thousands of sub-nanoliter droplets per second with very high monodispersity. In these devices, droplet manipulation is typically carried out by varying the flow rate of dispersed and continuous phases, and droplets are stabilized by the use of surfactant. The most commonly adopted designs for passive droplet generation are cross-flow, co-flow, and flow focusing. [50,55]

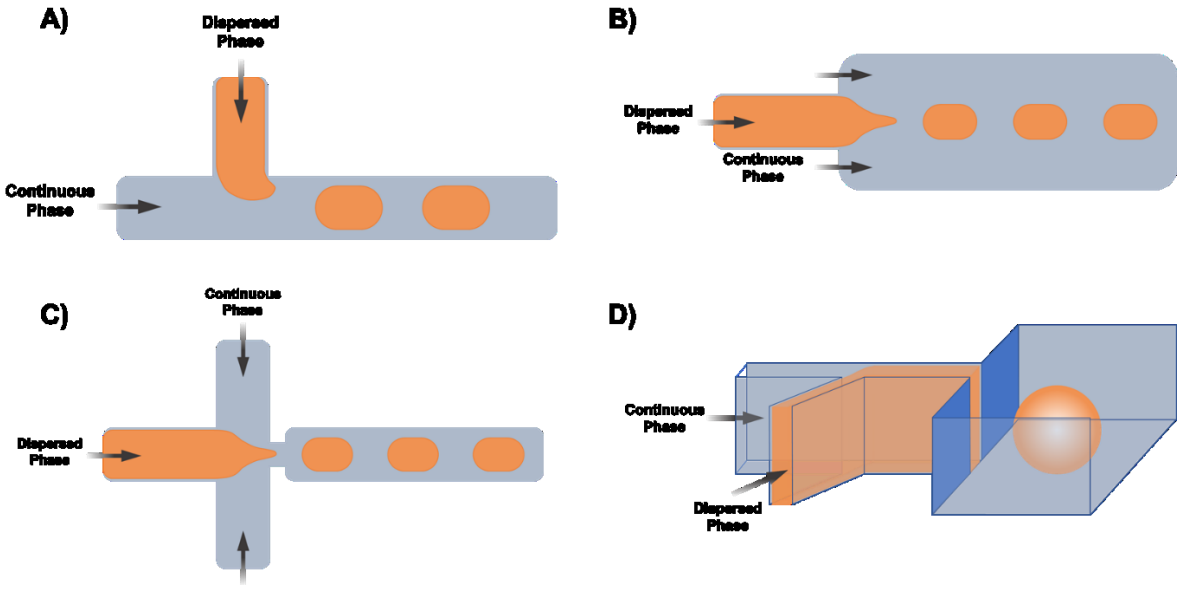

Figure 1.3 Schematic representations of the most commonly implemented geometries for passive droplet generation: A) T-junction; B) co-flow; C) flow focusing; D) step-emulsification. Adapted from: Passive and active droplet generation with microfluidics: a review [50].

Cross-flow.

In cross-flow configuration[57] (*Figure 1.3A*) the dispersed and continuous phase meet at the junction with an arbitrary angle. Based on this angle, cross-flow designs are classified into two different groups: T-junction and Y-junction geometries. In the former, the contact angle between the inlets is equal to 90 °, while, in the latter, the angle ranges between 0 ° and 180 °. As fluid flow continues, the shear stress applied by the continuous phase force causes the head of the dispersed phase to elongate in the main channel and eventually break up into droplets of uniform size. Indeed, the relative flow rates of the input flows, the viscosity of the fluid involved in the process, channel dimensions, and the surface tension are the main properties that control the droplet size and frequency of production in these devices.

Cross-flow devices owe their popularity to their simplicity and relative small dimensions, which ensure their easy integration in more complex microfluidic platforms.

Co-flow.

In co-flow devices[58] (*Figure 1.3B*), the dispersed and continuous phases meet each other in parallel streams. Here, droplet generation happens when the streamwise forces exceed interfacial tension, and most of the time their formation is due to the Rayleigh-Plateau

instability. Droplet size results to be function of the dispersed channel width as well as fluid viscosity, and flow rates, with production rate reaching tens of kilohertz.

Flow focusing.

Due to the superior versatility exhibited by the flow-focusing configuration (*Figure 1.3C*) in controlling both droplet size and frequency, this particular design emerges as the most employed compared to those mentioned so far.[59] In this configuration, the two continuous phase side channels and the central dispersed phase are forced through a striction. The symmetric shear forces of the continuous phases on the dispersed phase are even increased by the striction, resulting in an unparallel droplet formation in terms of stability, robustness, and monodispersity. As for the co-flow case, droplet size and frequency can be finely controlled through flow rates variation. Moreover, the striction width and length have remarkable impact on the droplet generation process by adjusting the shear stress imposed on the dispersed phase.

Step emulsification devices.

The aforementioned microfluidic devices rely on the use of shear forces applied on the dispersed phase to produce droplets. Although these methods are widely employed, their dependance from flow rates make them less suitable. Indeed, flow rate or pressure fluctuations can result in process instabilities and can affect the final outcome of the experiments. For these reasons, new technologies in which the droplet formation is governed by other forces have been developed. Among them, step emulsification is characterized by the generation of uniform droplets through a sudden variation in channel confinement, which in turn causes a sharp change in capillary pressure.[60] This phenomenon drives the formation of droplets through the application of interfacial tension stresses.[50]

A generic configuration for the step emulsification geometry (*Figure 1.3D*) provides the stabilized co-flow of the dispersed and continuous phases within the high-aspect-ratio inlet channel. Upon reaching an abrupt geometric step, the aforementioned co-flow transitions into discrete droplets, subsequently released into a less confined channel. This configuration has several advantages, such as droplet generation less sensitive to flow or pressure fluctuations, and the possibility to increase the production yield by increasing the flow rate without affecting the droplet size and uniformity.

1.2.2 Droplet generation

Depending on the selected device, several breakup modes can be observed in microfluidic droplet-generators. In particular, the most common shear-based droplet generators (cross-flow, co-flow, and flow-focusing) have 5 working modalities (*Figure 1.5A*): squeezing, dripping, jetting, tip-streaming, and tip-multi-breaking. While three breakup modes have been identified for step emulsification: shear-induced, step-regime, and jetting-regime. For reason of concision, here we focused only on the break-up modalities of the shear-based droplet generators.[61]

By adjusting the capillary number of both dispersed (Ca_d) and continuous (Ca_c) phases it becomes possible to navigate through the phase diagram of breakup modes, allowing for the selection of the preferred droplet fragmentation mechanism. *Figure 1.5B* illustrates the phase diagram highlighting phase transitions and pair of capillary numbers corresponding to each generating mode.

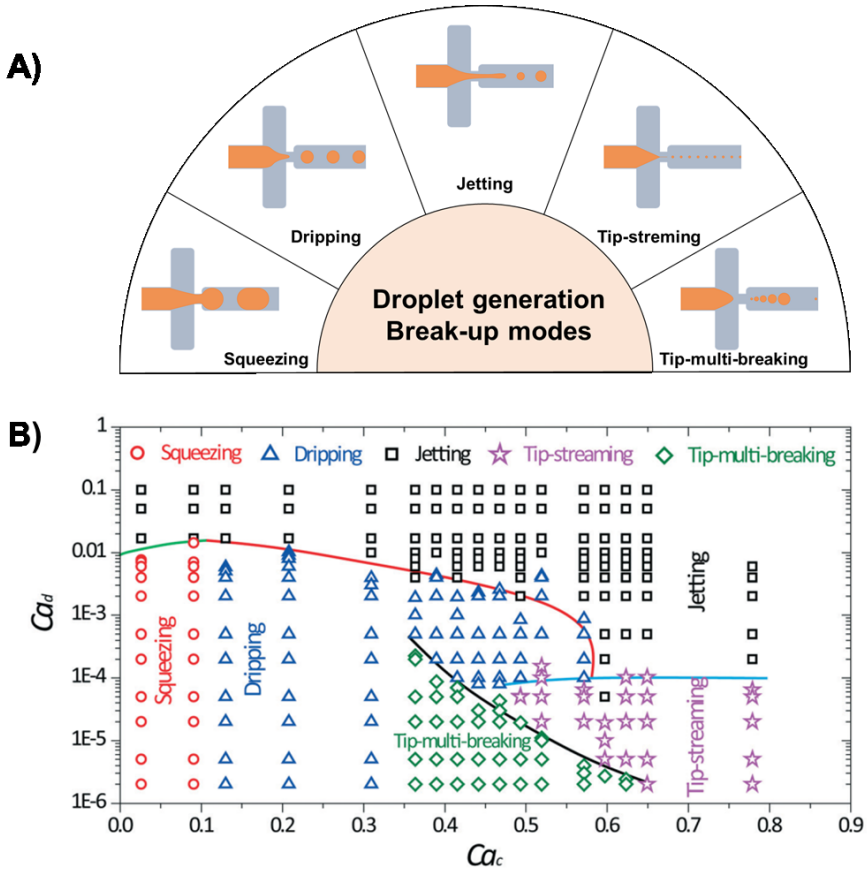

Figure 1.5 A) Representation of the five droplet generation break-up modes established in shear-based microfluidic devices; B) Phase diagram in (Cac, Cad) plane for various modes observed in microcapillary flow-focusing devices, adapted from Passive and active droplet generation with microfluidics: a review[50].

Squeezing.

The squeezing mode occurs for low Ca_d and Ca_c.[62] In this modality, viscous stresses are too weak to drag and breakup the dispersed stream into droplets. Therefore, the head of the dispersed phase continue to grow until complete obstruction of the junction region. Consequently, the pressure gradient at the interface starts to increase. When the pressure exerted by the continuous phase overcomes the pressure inside the growing droplet, the interface undergoes a process of squeezing and subsequent collapse, resulting in the formation of a droplet. Therefore, droplets are characterized by dimensions greater than that of the collecting channel. This leads to the generation of a plug-like shape, which is a direct consequence of the geometric confinement.

Dripping.

Increasing the Ca_c the transition from squeezing to dripping happens due to the raise in the viscous forces, which now dominate over interfacial tension. In dripping,[63] the shear forces are strong enough to break up the dispersed fluid before it obstructs the collecting channel, generating droplets with dimensions smaller than the microchannel. Indeed, the rupture into droplet occur as a consequence of the capillary instability at the junction between the dispersed and continuous channel. Moreover, thanks to the constant viscous stress, droplets are generated with extremely high uniformity in size.

Jetting.

The jetting mode[50,63] becomes predominant in the upper part of the phase diagram. Therefore, it can be observed that an increase in both Ca_d and Ca_c is responsible for the establishment of this breaking up mode. It is possible to achieve this by increasing the flow rate of the two phases, while maintaining the other system characteristics unchanged. In jetting mode droplets are generated at the end of a jet extended from the dispersed channel towards the main collecting channel as a consequence of the Rayleigh-Plateau instability. Due to its distinctive properties, jetting is susceptible to capillary instabilities, which lead to the formation of polydisperse droplets. Generally, jetting occurs when the sum of the viscous forces exerted by the continuous phase and the inertia stresses of the dispersed phase exceed the interfacial tension forces. Based on what is the predominant force, it is possible to distinguish between two different jetting modalities: narrowing jetting arises when the viscous forces of the continuous phase dominate; and widening jetting, which in contrast arises when the process is dominated by dispersed fluid inertia.

Tip-streaming.

Tip-streaming[64] is a phenomenon that occurs under conditions of extreme imbalance between the capillary numbers of the two phases (Ca_c and Ca_d). As illustrated in the phase diagram, this mode of droplet generation is observed for exceedingly high Ca_c values and low Ca_d values. In these conditions, the tip of dispersed phase at the junction is deformed into a cone-jet structure which resembles that of the Taylor cone in charged liquid. From this jet, droplets of a size ranging from the micrometer to the sub-micrometer scale are produced with exceptional uniformity and rapidity.

Tip-multi-breaking.

Tip-multi-breaking occurs for intermediate Ca_c values compared to tip-streaming. In this case, the formation of the cone-jet structure is unstable and results in the intermittent production of droplets with size changing periodically.[65] In particular, droplets are generated from the jet apex due to the Rayleigh-Plateau effect, but the intrinsic instability of this break-up mode causes the oscillation of the conic meniscus which disrupt the continuous droplet generation leading to the formation of trains of droplet with non-uniform size distribution.

1.5 Microfluidics for polymeric nanoparticles synthesis

Polymeric NPs can be synthesized starting from precursor monomer by polymerization reaction or by the chemical or physical crosslinking of preformed polymers.[26] Focusing on the latter, two main types of polymer can be employed according to their source of origin: natural or synthetic polymers.[15,66] To date, both classes have their own advantages and disadvantages, and neither has emerged as the preferred group for biomedical applications.[67] Natural polymers, such as alginate, chitosan, gelatin, and other polysaccharides show great biocompatibility and biodegradability, they are often ubiquitous and inexpensive, moreover most of them posses bio-active properties which ensure the smart engineering of the nanosystem.[3,66] As example, hyaluronic acid is a well-known polysaccharide showing affinity to the CD44 receptor which is highly overexpressed in many tumor types.[10] Therefore, including this polymer in the NPs formulation can enhance the target ability of the synthesized nanocarrier. On the other hand, natural polymers present high polydispersity, which may affect the batch-to-batch reproducibility of the synthesis, and can exhibit poor mechanical performance. By contrast, synthetic polymers are highly tunable and easy controllable materials. Their mechanical and biological properties can be finely designed starting from the choice of the synthetic building blocks (monomeric units).[68] However,

under certain condition, synthetic polymers can result in poorly bio-compatible materials compared to the natural ones. Synthetic polymers cover an extremely broad library of materials including polylactic acid (PLA), poly(lactic-co-glycolic) acid (PLGA), polycaprolactone (PCL), polyethylene glycol (PEG), and many others.[66]

The most common traditional approaches for polymeric NPs synthesis can be summarized in emulsification (solvent evaporation or diffusion), nanoprecipitation, and ionic gelation.[67,69] While these methods are straightforward, well-established, and readily scalable, significant challenges can arise in their implementation. In particular, the use of large volumes of valuable chemicals and drugs, the generation of highly polydisperse nanocarriers, and the difficulties in designing carriers loaded with multiple therapeutic agents represent sources of expensive costs and inefficient procedures. Furthermore, the increasing demand for nanoparticles in ad-hoc nanomedicine applications strongly requires suitable platforms for the industrial scale-up of NPs production, avoiding limitations related to batch-to-batch reproducibility.[70,71] The high batch-to-batch variation typical of batch syntheses is due to the insufficient control of the mixing within the reaction volume. In conditions of limited mixing and mass transfer, the nucleation, growth, and agglomeration of NPs occur simultaneously in an uncontrolled manner, leading to the formation of NPs with varying chemical and physical properties. This issue becomes even more pronounced in scaled-up batch reactors, where mixing efficiency is inherently lower.[72]

In recent times, microfluidics has emerged as a crucial instrument in the synthesis of NPs.[71–73] Its capacity to overcome the limitations of conventional bulk techniques has prompted a growing commitment from the scientific community to investigate and advance novel technological solutions founded upon its utilization. First of all, the fine manipulation of small fluid volume exerted by microfluidic technology enable accurate dosing of NPs precursor rather than drug molecules resulting in the unparalleled control over final NPs size, morphology, and composition.[74,75] Furthermore, the rapid heat and mass transfer, along with the high mixing efficiency that can be achieved in microfluidic processes, ensure the optimal reproducibility of the established procedure for nanoparticle formation. Additionally, the extensive reaction interfaces established within the microchannels, in conjunction with the diminutive device dimensions, facilitate accelerated reaction kinetics, thereby creating optimal conditions for the facile and suitable scale-up to an industrial level.[72,73,76]

A microfluidic system can be classified according to the number of phases involved in the reaction. In particular, two main categories can be distinguished: continuous single-phase microfluidic systems and segmented multi-phase microfluidic systems.[72–74]

1.5.1 Single-phase microfluidic synthesis

NPs synthesis in single-phase systems is typically implemented trough *in-flow* nanoprecipitation.[75] The formation of NPs in such a system is a multistage process involving three main steps: nucleation, growth, and precipitation (or separation).[72,75] These steps are typically occurring at the same time in traditional batch syntheses causing loss of performances. The superiority of microfluidics resides in its capability to ensure sequential occurrence of these step as a function of the distance from the initial mixing point (*Figure 1.6*).[74]

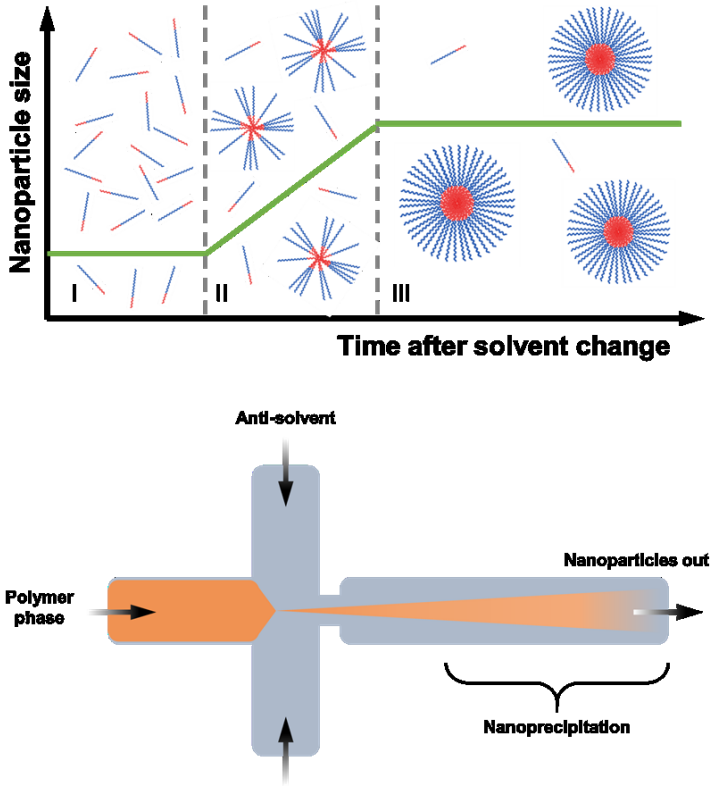

Figure 1.6 schematic representation of the nanoprecipitation process. In the upper part the self-assembly of polymeric nanoparticles is described as a function of time after solvent change. At the bottom the process of mixing within a microfluidic flow-focusing device.[74]

Nucleation describes the formation of atomic or molecular clusters. This process can be induced by a change in solute solubility, which can be achieved by mixing a solvent and an antisolvent. This results in the creation of a supersaturated system that possesses high Gibbs free energy. As a consequence, the high free energy is reduced by clusters formation. It is

important to note that high nucleation rate contributes to the uniform growth and formation of NPs: the faster and more uniform the nucleation, the smaller and more homogeneous the particles formed.

After the nuclei are formed, they start to growth with the two steps well isolated only in the case of high rate of nucleation. The growth of the particles can be attributed to the following diffusion and absorption of the reacting molecules onto the nuclei surfaces. This process can be either controlled by the diffusion of the reactants from the bulk solution towards the nuclei surfaces or by the reaction establishing at the nuclei surface. In the event that the rate of molecular diffusion is relatively low, the diffusion process becomes the rate-limiting step, thereby resulting in a diffusion-controlled growth phenomenon. In all other instances, the growth will be surface-controlled. The final stage of the process is phase separation, which results in the precipitation of the NPs once the equilibrium state is reached in the growth process.

This method was successfully implemented by Heshmatnezhad F. *et al.*[77] for the synthesis of polycaprolactone NPs (PCL NPs) in a flow focusing device. In this work, the authors investigated the effect of different parameters on the physical and chemical properties of the PCL NPs. In particular, the effect of flow rate ratio (FRR), total flow rate (TFR), organic solvents (tetrahydrofuran THF or dimethylformamide DMF), surfactants (polyvinyl alcohol PVA and Tween 80), and polymer molecular weight were evaluated. Results showed that smaller NPs whit narrow size distribution can be obtained by increasing both FRR and TFR due to a higher diffusive mixing and lower residence time. Furthermore, the process was found to be optimal when a higher molecular weight polymer was used in conjunction with DMF as an organic solvent and a surfactant mixture comprising a lower amount of PVA and a higher Tween 80 content.

Another great example of *in-flow* nanoprecipitation was provided by Fabozzi A. and colleagues[78] who employed a double-step microfluidic process to produce both irinotecan (IRI)-loaded HA/PLGA/PP NPs and IRI-loaded PLGA/PP NPs. The synthesis of these NPs was achieved without the use of any chemical modification, with the formation occurring as a result of electrostatic interactions driven by the lipophilicity gradient between the polymers. The as synthesized NPs were also compared to their bulk synthesized counterpart, revealing the augmented performances of the microfluidic synthesis that allows the production of smaller particles with narrower size distribution and higher drug encapsulation

efficiency. In addition, the introduction of a bio-active compound such as HA in the NPs formulation resulted in a higher NPs internalization in both HS578T and L929 tested cell lines. This can be attributed to the affinity between HA and the CD44 receptor which established a receptor mediated endocytosis.

Bovone G. *et al.*[79] designed a 3D coaxial jet mixer (CJM) for the continuous nanoprecipitation of poly (ethylene glycol)-block-polylactide (PEG-b-PL) NPs with various co-solvents. Here, researchers aimed to overcome some of the most common issues involved in 2D microfluidic nanoprecipitation, such as channel clogging which limit the scale-up of this procedure. At low production rate the NPs synthesis was found to be suitable and to produce NPs with narrow size distribution and hydrodynamic diameters ranging between 50 and 100 nm by varying the polymer concentration, solvent, and flow conditions in the CJM. More interestingly, the authors claim that CJM can reach productivities up to 30-folds compared to traditional batch syntheses paving the way for future scale-up.

In addition, Baby T. *et al.*[80] designed the synthesis of curcumin-loaded shellac nanoparticles (CUR-Shellac NPs) through the 3D microfluidic nanoprecipitation process. They found that a combinatory approach using a mixture of three solvents (ethanol, DMF, and DMSO) was the optimal solution to tailor the performances of the synthesized CUR-Shellac NPs in terms of drug loading and drug release. In particular, the multiple-solvent approach offers a novel strategy for the synthesis of polymer nanoparticles with adjustable drug loading, ranging from low (1–5%) to exceptionally high (50%) levels. In addition, CUR-Shellac NPs showed an inherent pH-responsive behavior enabling the drug release at acidic pH.

1.5.2 Multi-phase microfluidic synthesis

To Date, multi-phase microfluidic systems (droplet or plug-based) are widely studied for the synthesis of inorganic NPs. This field of research experienced a tremendous growth in the past decades, leading the development of innovative microfluidic reactors with many advantages compared to the single-phase counterpart. In segmented flow, the reduction in volume where reactions occur results in enhanced mixing efficiency, thereby improving the predictability and reproducibility of the synthesis of NPs in both in-batch and batch-to-batch scenarios.[81] Among the many, this technology has been applied to formulate several types of inorganic nanoparticles, such as gold,[82] silica,[83] silver[84], titanium oxide,[85] cadmium,[81] and many others.

With respect to polymeric systems, its application remains less investigated. Few years ago, Rezvantalab S. and Moraveji M. K. conducted a critical review on the microfluidic assisted synthesis of PLGA drug delivery systems.[86] They pointed out that there is a substantial division between continuous flow systems and segmented flow systems in the synthesis of PLGA-based carriers. The first are mainly utilized for the synthesis of NPs exploiting the nanoprecipitation protocol. While, segmented flow systems are typically devoted to the formation of microparticles (*Figure 1.7*).

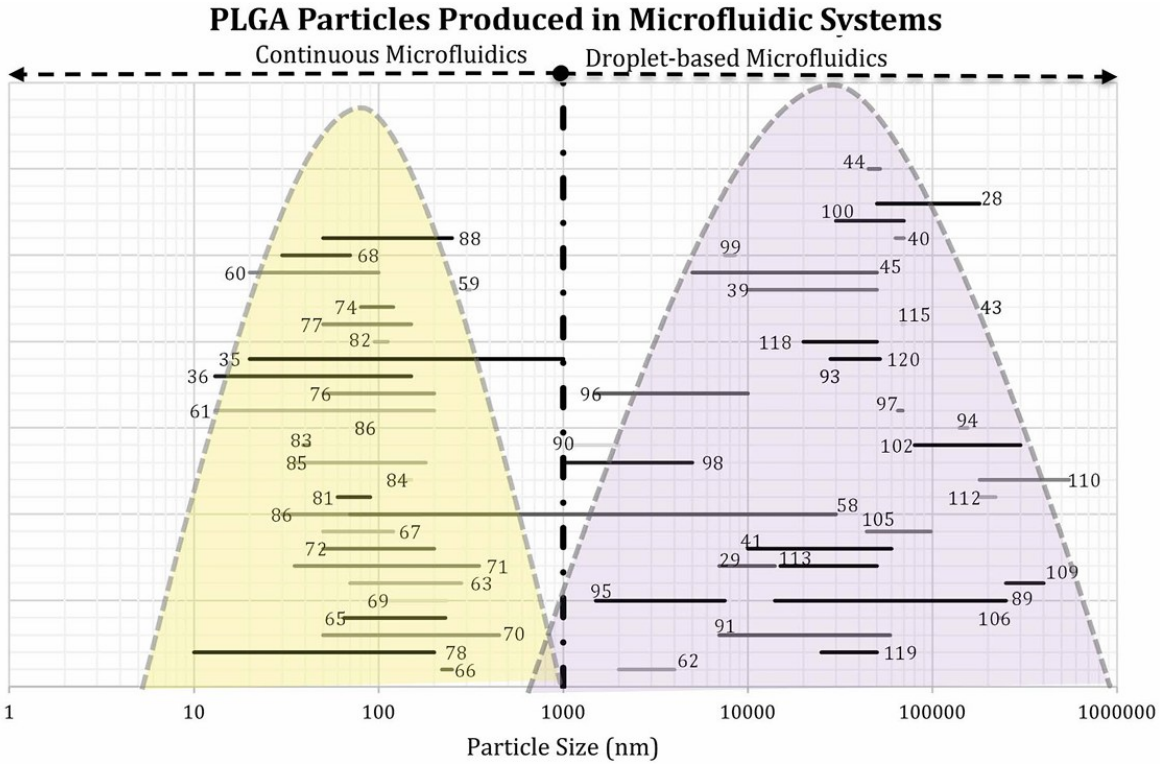

Figure 1.7 The relationship between microfluidics type and the final size of PLGA-based drug delivery systems. Each line represents the size range of drug delivery system (DDS) reported in the related reference that is produced in droplet-based or continuous microfluidics.[86]

In essence, this fundamental concept can be readily expanded to encompass all varieties of polymeric particles. Consequently, considerable effort must be devoted to the investigation of innovative solutions for the droplet-based synthesis of polymeric NPs, in order to fulfill the expectations that the theory promises. However, few reports on the segmented flow microfluidics for polymeric NPs production are already reported in literature. Hung L. *et al.*[87] reported the successful implementation of a droplet-based solvent extraction device for the synthesis of PLGA NPs. After dissolving the PLGA prepolymer in a DMSO phase, droplets of PLGA-DMSO and water were generated in sequence in a silicon oil continuous phase through the use of two following T-junctions. The merging between two following

water and PLGA-DMSO droplet in the collecting channel leads to sudden precipitation of PLGA NPs due to supersaturation of PLGA. Each droplet function as a micro-reactor in which numerous nanospheres are produced. By varying the PLGA concentration, the authors were able to finely tune the NPs dimensions between 70 – 500 nm range, keeping an overall good polydispersity index (PDI).

Another good example is provided by Effatti E. and coworkers.[88] In this work they demonstrate the suitable synthesis of polypyrrole (PPy) NPs using a simple W/O droplet generator. Here the oxidating agent ammonium persulfate (APS) was dissolved in water and emulsified in a capillary microfluidic device using hexadecane and span 80 as continuous phase. After the emulsification, a second inlet introduce the pyrrole monomer dissolved in hexadecane. The diffusion of the monomer within the water droplet, where the oxidating agent is confined, leads the instauration of the redox reaction with the following formation of the PPy NPs. NPs were generated in the 60-180 nm range and showed better electrical performances compared to those synthesized by regular bulk synthesis.

An insightful work in understanding the principle of polymer NPs synthesis in segmented flow systems was conducted by Moffit M. G. and his group. In a first publication[89] they proposed the microfluidic synthesis of poly(caprolactone)-*block*-poly(ethylene oxide) (PCL-*b*-PEO) NPs in a plug-based liquid-gas system. Three different streams were combined at the junction with an Air stream to create the liquid plugs. The three streams consisted of 1) PCL-*b*-PEO in DMF, 2) a DMF separating stream, and 3) a water stream functioning as antisolvent phase. The role of the intermediate stream was to avoid polymer precipitation prior of plug formation. Indeed, the working principle is based on the same principle as for the continuous *in-flow* nanoprecipitation. However, the reduced dimension of the plug and the convective mixing induced by the plug motion within the channel allow the production of monodisperse particle of about 70 nm in the optimum flow condition. The loading and release of a model dye were also evaluated to validate the promising application of these platforms for the synthesis of drug delivery systems. Furthermore, they continued with a successive work to compare the performances of the developed plug-based device with a common single-phase staggered herringbone (SHB) mixer, and a traditional batch approach,[90] concluding that: 1) NPs morphology between bulk synthesized NPs and microfluidically synthesized ones was different; 2) crystallinities from the bulk and single-phase SHB mixer preparations were similar; 3) NPs morphologies, dimensions, and internal crystallinities changed with increasing flow rate in the two-phase mixer but not in the single-

phase SHB mixer. Indeed, results demonstrate that the increasing PCL crystallization is linked to the increasing shear stress, which were experienced only in the two-phase system for increasing FRR. This result suggests that while the mixing rate strongly affects the NP morphologies and dimensions, mixing rate has a much weaker effect on core crystallinities, which are mainly influenced by shear effects.

1.6 Microfluidics for cell encapsulation

The investigation of cell status relies on technologies based on massive samples. State-of-the-art methods, such as qPCR, RNA-seq, and western blotting, provide valuable information, which, however, only represent an average cell of the starting population.[91] Indeed, cell-to-cell interactions, the actual state of each cell in the population, and cell heterogeneity remain unrevealed from these analyses.[92]

Alternatively, flow cytometric methodologies are efficient platforms for single-cell analysis.[92] However, investigating cell-to-cell interactions can be challenging due to the requirement of maintaining cells in suspension.[91] Therefore, much effort has recently been dedicated to developing new approaches for single-cell analysis.[93] In particular, encapsulating cells within polymer micro-capsules, which resemble the structure of the extracellular matrix, is gaining increasing attention as a valuable alternative to overcome the aforementioned issues. Common natural polymers employed in cellular encapsulation are: alginate, gelatin, agarose, and collagen.[94]

Recently, droplet-based microfluidic systems have emerged as a promising alternative for cellular encapsulation. These platforms enable the generation of microcapsules with uniform sizes, offering precise control over their dimensions while enhancing the delivery of oxygen and nutrients to the encapsulated cells. Additionally, microfluidic technology facilitates the customization of microcapsule properties, such as shape, mechanical strength, and permeability, to meet specific application requirements.[95]

Beyond these functional advantages, microfluidic approaches for cellular encapsulation present notable economic benefits. The miniaturized processes typically require smaller quantities of reagents and are easily automatable, enabling cost-efficient production at scale. This not only reduces manufacturing costs but also increases accessibility for both therapeutic applications and research purposes. Furthermore, microscale systems can be effortlessly integrated with analytical devices or placed within cell incubators, providing

enhanced observation and real-time monitoring of cells during encapsulation and subsequent culture phases.[95]

Yu *et al*.[96] successfully developed a T-junction microfluidic system for the generation of alginate microspheres encapsulating breast cancer cells. Upon gelation, triggered by the cross-linking reaction between alginate and calcium ions in the medium, the resulting beads were trapped within micro-sieve structures, enabling cell culture under continuous perfusion conditions. This alginate-based microenvironment supported cell proliferation and facilitated the formation of multicellular tumor spheroids. Subsequently, the response of these spheroids to doxorubicin, an antitumor drug, was assessed. The study revealed that spheroids exhibited multicellular drug resistance, a behavior markedly distinct from that of tumor cells cultured in monolayers.

In the context of transfusion medicine, hemoglobin (Hb) encapsulation within polysaccharide hydrogels has emerged as a potential substitute for red blood cells (RBCs). Martinez *et al*.[97] described a microfluidic approach for encapsulating living cells within alginate hydrogel microparticles derived from monodisperse double emulsion templates. The authors utilized a microcapillary device to produce double emulsions, consisting of an inner alginate droplet surrounded by a layer of mineral oil. Gelation occurred when the alginate droplet detached from the mineral oil phase and interacted with calcium ions (Ca^{2+}) in the continuous phase, resulting in alginate hydrogel microparticles with diameters ranging from 60 to 230 μm. After one week of culture, 65% of the encapsulated cells remained viable within the alginate microparticles. This method demonstrated significant potential as a tool for the encapsulation of living cells within uniformly sized hydrogel particles.

More recently, Ahmed *et al*.[98] proposed a microfluidics-assisted double emulsion technique for the synthesis of alginate-poly-l-lysine-g-polyethylene glycol (PLL-g-PEG) microspheres loaded with Hb. This method relied on an on-chip process involving sequential injections of alginate-Hb solutions into emulsified droplets of aqueous calcium chloride ($CaCl_2$), followed by a secondary injection of PLL-g-PEG. The fabrication process was performed using a PDMS-based microfluidic device equipped with a flow-focusing point and two picoinjection sites. At the first picoinjection site, the alginate-Hb solution was combined with $CaCl_2$ as the droplet moved through the channel, inducing gelation. At the second site, PLL-g-PEG was introduced to reinforce the microgel structure and minimize protein loss, ensuring stability of the Hb-loaded microspheres.

PART II
TRADITIONAL BATCH SYNTHESIS

2. MEET: Mixed Emulsion-Evaporation Technique

2.1 MEET implementation for the synthesis of hyaluronic acid-polyethyleneimine nanogel for drug delivery in ovarian cancer

An especially attractive class of NGs is represented by hydrophilic networks synthesized *via* the so-called emulsification/solvent evaporation technique. This strategy relies on the formation of an emulsion[99]—either water-in-oil or oil-in-water—, with the following constraints: *i*) at least one of the two starting polymers has to be soluble and dissolved in a volatile organic solvent, that is immiscible with water, *ii*) the other hydrophilic polymer needs to be dispersed in the aqueous phase. The polymer crosslinking takes place at the water-oil interface, avoiding bulk reactions, and forms a highly structured 3D nanonetwork thanks to the interfacial reactions among the different reactive moieties. Finally, the resulting nanoscaffolds are collected following the evaporation of the organic solvent. As an example, the emulsion/evaporation method has led to the formulation of polyethylene glycol (PEG) and polyethyleneimine (PEI) nanogels, where PEG is activated with imidazole groups and dissolved in dichloromethane (the organic phase), whereas PEI is dissolved in water (the aqueous phase), and the formation of NGs occurs through chemical crosslinking between PEG imidazole and PEI amine groups. Such NGs have been validated in different cancers[100] and neurodegenerative disorders.[101] A similar strategy has been developed using poloxamers (*i.e.*, block copolymers of poly(ethylene oxide) and poly(propylene oxide)) functionalized imidazole and PEI[102]. Additionally, nanoscaffolds have been also prepared using stearic acid and oleic acid at different ratios in an aqueous poloxamer solution to design an *in situ* mucoadhesive gel.[103]

The emulsion/evaporation method is suitable to modulate size, shape, composition and surface properties of the NGs, by simply tuning the concentration of the polymers and the droplet size of the dispersed phase. However, the need to have one of the NG building-blocks soluble in an organic solvent, immiscible with water, limits the range of eligible polymers and, as a consequence, the applicability of the technique. Indeed, the synthesis of these nanocarriers using hydrophilic polymers only cannot be carried out. An alternative strategy to address this limitation is represented by the micellar approach, which requires one component to form polymeric micelles in aqueous phase, exposing as external layer its reactive moieties for the crosslinking with a second polymer.[102,104] However, the micellar behavior is restrictive to design NGs, in terms of polymer choice and sustained drug release

in specific tumor microenvironment. To solve this challenge, in this work we propose a novel approach based on a herein defined mixed emulsion, where each of the two polymers constituting the NGs is separately dissolved in water and dispersed as phase droplet, without the addition of surfactants, in a continuous phase composed of an organic volatile solvent, easily removable by evaporation at room temperature. For these reasons, we named the protocol as Mixed Emulsion/Evaporation Technique (MEET).

In detail, we have applied this strategy to design NGs composed of hyaluronic acid (HA) and linear polyethyleneimine (LPEI), two polymers that are not soluble in water-immiscible organic solvents. HA is an anionic, non-sulfated glycosaminoglycan commonly used in the fabrication of biomaterials for tissue engineering, drug delivery and imaging purposes, due to its highly biodegradable, biocompatible, viscoelastic, non-toxic, and non-immunogenic nature.[105,106] Among the biological applications, HA has been widely investigated for target therapy in cancer, thanks to its well-demonstrated affinity to CD44 (hyaluronan receptor), overexpressed on the surface of many tumor cells[107]. For this reason, the polymer may act as an active targeting moiety for the intracellular delivery of anticancer drugs and represents a suitable component for the synthesis of nanocarriers[108,109]. On the other side, LPEI is a cationic polymer widely used in the synthesis of nanocarriers for drug and gene delivery due to its unique proton-sponge effect.[110,111] The presence of amine groups in the polymer backbone enables the modification *via* covalent coupling with specific functionalities/biomolecules and the formation of 3D nanomatrices with a huge internal space and a soft skeleton structure for further encapsulation of drug molecules relying on electrostatic interactions with the LPEI positive charge density.[112] Moreover, the potential cytotoxicity of neat LPEI is overcome by its conjugation with other polymers, thereby justifying its use in the design of nanoscaffolds.[112,113]

The production of HA-PEI nanocarriers through MEET simplifies the synthetic routes commonly used and widely discussed in published works to design HA-based or PEI-based nanoscaffolds. Indeed, our strategy requires few synthetic and purification steps to activate the polymers and form NGs, defining a straightforward and rapid method. In the literature, HA-PEI nanoscaffolds are generally obtained through: *i)* activation of HA with aldehyde/disulfide moieties[114–116] and subsequent reaction with primary amines of branched PEI, *ii)* surface decoration of PEI-PEG, PEI-PLGA or PEI-PBAE pre-formed particles with HA chains[117–119], or *iii)* formation of nanocomplexes *via* electrostatic interactions.[120–124] Overall, these procedures involve multiple orthogonal activation routes, longer reaction

times and the use of larger volumes of water and organic solvents. Furthermore, these nanocarriers preferentially result in a core-shell configuration, characterized by a sectorial and inhomogeneous distribution of the different chains in the whole nanonetwork, which could affect the performance in drug delivery and cell uptake. Our MEET approach, exploiting the emulsion/evaporation principles, allows us to obtain homogeneous HA-LPEI NGs, otherwise feasible with longer and more complex chemical pathways, where significant additional benefit results by the combination within a single nanoscaffold of both physical (by HA) and electrostatic (by LPEI) interactions with the payload, coupled to HA-mediated affinity toward cancer cells and PEI-mediated endosomal escape.[125]

The synthesized NGs were characterized in terms of size, morphology and surface charge, and loaded with doxorubicin (a known antiblastic drug) to validate their potential application as a therapeutic delivery system in ovarian cancer, using the cell line OVCA433 as representative of tumor cells overexpressing CD44. Through a competitive assay, we could demonstrate an involvement of CD44 in the NG internalization process. We have also documented that NG-mediated delivery of doxorubicin (DOX) significantly affected the cell metabolic activity, outperforming the conventional DOX administration route as a non-encapsulated drug.

Hence, this study demonstrates a convenient route for NG synthesis, which is less stringent than conventional emulsification/solvent evaporation methods in terms of polarity and solubility figures, therefore expanding the range of applicability to a larger class of biopolymers and validating their use as CD44-mediated drug delivery nanocarriers for cancer treatment.

2.1.1 Materials & Method

Materials. HA sodium salt (HA, ultralow Mw = 8−15 kDa) was purchased from Biosynth Carbosynth (Compton, UK), and LPEI (Mw = 2.5 kDa) was purchased from Polysciences Inc. (Warrington, USA). Doxorubicin was purchased form Teva Italia S.r.l. (Milan, Italy). All other chemicals were purchased from Merck KGaA (Darmstadt, Germany) and used as received, without any further purification. The solvents were of analytical grade. Cy5-derivatives were stored at −20 °C.

LPEI Functionalization with Cy5 (LPEI-Cy5). LPEI and Cy5 were crosslinked according to a two-step procedure discussed in a previous work.[126] The first stage concerned the modification of LPEI with alkyne groups: the polymer (250 mg, 0.1 mmol) was dissolved in

methanol (7 mL), and 80 wt % propargyl bromide solution in toluene (108 μL, 1 mmol) was added dropwise at 0 °C. The resulting solution was kept under stirring for 24 h at room temperature (RT) in the dark. Methanol was evaporated under reduced pressure, and the resulting viscous intermediate was redissolved in deionized water (DIW). The solution was purified by membrane dialysis against DIW (dialysis membrane MWCO = 100−500 Da) for 2 days, with daily water exchange, and the alkyne-modified LPEI was collected as a solid after freeze drying. In the second stage, copper(I)-catalyzed alkyne− azide cycloaddition (CuAAC) occurred: functionalized LPEI (220 mg, 0.088 mmol) was dissolved in DIW (10 mL) and Cy5-azide (200 μL, 2 mg/mL in DMSO) was added dropwise to the system. The copper catalyst ($CuSO_4$,13μg, 0.08 μmol) and sodium ascorbate (16 μg, 0.08 μmol) were added to the mixture, which was left under stirring for 36 h at 50 °C, in the dark. The product was dialyzed (membrane MWCO = 100−500 Da) against DIW for 2 days with daily water exchange to remove unreacted species. The final LPEI Cy5 was collected after freeze drying.

NG Synthesis. The NG synthesis involved the use of aqueous solutions of HA and LPEI. HA (10 mg) was dissolved in DIW (2 mL), and the coupling agents N-(3-dimethylaminopropyl)-N′-ethyl carbodiimide hydrochloride (EDC, 22.66 mg, 0.12 mmol) and N-hydroxy succinimide (NHS, 5.56 mg, 0.048 mmol) were added to the polymer solution at a molar ratio of HA carboxyl groups/EDC/NHS of 1:5:2. The reaction system was kept under stirring for 3 h at RT. Pristine LPEI and LPEI-Cy5 (1 mg, 1:1 by weight) were dissolved in 1 mL of dilute HCl (pH = 4.5). The polymer crosslinking reaction occurred as follows: dichloromethane (DCM, 3 mL) was added dropwise to the activated HA solution and sonicated for 30 min, generating the first W/O emulsion. Then, the LPEI solution (i.e., pristine LPEI and LPEI-Cy5) was added dropwise to the system and the final mixture was further sonicated for 15 min, generating a mixed emulsion of two disperse aqueous phases and a continuous organic one. This emulsified system was left under vigorous stirring overnight, at RT, allowing the organic solvent to evaporate. Finally, it was dialyzed against DIW (membrane MWCO = 6−8 kDa) for 2 days with daily water exchange, freeze-dried, and collected as a sponge-like solid. The HA/LPEI ratio of the present formulation was chosen following a preliminary evaluation of the NG size and cytotoxicity, as described in the Appendix I.

NMR and IR Analysis. The starting materials, intermediates, and final nanoscaffolds were analyzed by nuclear magnetic resonance (^{1}H NMR) carried out with a Bruker AC (400 MHz, Bruker Corp., Billerica, MA) spectrometer using deuterium oxide (D2O) as the deuterated

solvent, and the chemical shifts were reported as δ values (ppm) relative to the tetramethyl silane internal reference compound. Further characterizations were performed by attenuated total reflectance Fourier transform infrared spectroscopy (FT-IR) using a Thermo Nexus 6700 spectrometer coupled to a Thermo Nicolet Continuum infrared microscope equipped with a 15× Reflachromat Cassegrain objective (Thermo Fisher Scientific, Waltham, MA) in the wavenumber range of 4000−800 cm^{-1}, with 32 accumulated scans and at a resolution of 4 cm^{-1} for each specimen.

Dynamic Light Scattering Analysis. The final size, the polydispersity index (PDI), and the ζ-potential of the NGs were determined by dynamic light scattering (DLS) analysis (Zetasizer Nano ZS, Malvern Panalytical, Malvern, UK) in phosphate-buffered saline (PBS), acid (pH = 4.5), and basic (pH = 8.5) solutions. The specimens were prepared at a concentration of 1 mg/mL and sonicated to ensure the complete dispersion in the medium, minimizing potential aggregates. Additionally, NG enzymatic degradation was evaluated using a solution of hyaluronidase from bovine testes (HAase, 400−1000 U/mg solid) at two different specific activities of 10 and 150 U/mL: according to the literature, the NGs were dispersed (1 mg/mL) in 0.1 M sodium acetate buffer plus 0.15 NaCl containing BSA (1 mg/mL) and HAase at 37 °C. At defined time points, the effective hydrodynamic diameter and light scattering intensity of the NG suspensions were monitored in situ. Readings were performed in triplicate.

Atomic Force Microscopy Analysis. Atomic force microscopy (AFM) measurements were carried out using a Dimension 3100 AFM system with a Nanoscope III controller (Veeco Instruments Inc., Cambridge, UK) fitted with gold cantilevers (NanoWorld Pointp robe) in contact mode with a spring constant of 0.08 N m^{-1}. The specimen was resuspended in distilled water at a concentration of 0.5 mg/mL, sonicated for 10 min at 20 °C, and added dropwise (2 μL) on Thermo polysine slides (Thermo Fisher Scientific) until reaching the evaporation of the solvent on the substrate at RT. AFM images on 30 × 30 μm areas were recorded for the preliminary morphologic evaluation, followed by the analysis of 4 × 4 μm ROIs.

Scanning Electron Microscopy. The NG specimen was prepared as described in the previous section on mica sheets and sputter-coated with platinum. A field-emission scanning electron microscopy (SEM) (FEI XL 30 ESEM-FEG, Thermo Fisher Scientific) analysis was performed at an accelerating voltage of 10 kV in the secondary electron detection mode.

Transmission Electron Microscopy. The morphology of NGs, both as-synthesized and following enzymatic degradation, was evaluated by transmission electron microscopy (TEM) (FEI Tecnai G2 Microscope, Thermo Fisher Scientific). The NG suspensions were diluted to a final concentration of 250 μg/mL in DIW, and 3 μL was added dropwise on a lacey carbon-coated 300 mesh copper grid (Agar Scientific Stansted, Essex, UK), followed by dehydration at 50 °C until complete solvent evaporation. TEM micrographs were recorded at an accelerating voltage of 120 kV.

Drug Loading. Doxorubicin (DOX) was chosen as a representative drug to evaluate the performance of the synthesized nanocarrier in terms of encapsulation and controlled release of therapeutics. DOX loading was performed in PBS (pH = 7.4) as follows: 30 μL of a 100 μM DOX solution was added to the lyophilized specimens (3 mg), and the samples were centrifuged for 15 s at 6000 rpm. Then, the system was left at RT for 15 min to complete the uptake of DOX. Finally, the resulting loaded nanocarriers were dialyzed (membrane MWCO = 3.5 kDa) against PBS for 30 min in order to remove the nonabsorbed drug. The encapsulation efficiency (EE %) was estimated according to the following equation (equation 21)

$$EE\% = \frac{DOX_{NG}}{DOX_{tot}} \cdot 100\% = \frac{DOX_{tot} - DOX_{sol}}{DOX_{tot}} \cdot 100\% \quad (21)$$

where DOX_{NG} represents the encapsulated fraction and DOX_{sol} is the residual unabsorbed fraction of the total drug payload (DOX_{tot}). DOX_{sol} was determined by fluorescence spectroscopy (λex = 488 nm; λem = 590 nm) of withdrawn aliquots (3 × 100 μL) at defined time points based on a DOX standard calibration curve (Appendix I).

Drug Release Profile. The DOX-loaded nanosystems were diluted to a final concentration of 10 mg/mL, and 100 μL of the NG suspension was allowed to exchange against PBS (0.6 mL) at 37 °C. At defined time points, 100 μL aliquots were withdrawn and spotted into 96-well plates for fluorescence spectrophotometric analysis. At each withdrawal, the elution buffer was replenished with fresh PBS to avoid mass transfer equilibrium between the nanosystem and the surrounding solution. The cumulative percentage of released DOX was estimated by fluorescence spectroscopy at λex = 488 nm and λem = 590 nm according to the drug calibration curve. Additionally, drug release studies were performed in acidic (pH = 4.5, representative of the pH levels in the stomach), alkaline (pH = 8.5, as a threshold value which can be reached in a diseased intestine), and HAase-containing solutions. Experimental

data were collected from three independent replicates and reported as mean ± standard deviation (SD).

Cell Cultures. The human epithelial ovarian cancer cell line OVCA433 was obtained from the American Type Culture Collection (ATCC) (LGC Standards, Teddington, UK). Cells were cultured in Dulbecco's modified Eagle's medium (Cat# 21885-025, GIBCO Thermo Fisher Scientific), supplemented with 10% fetal bovine serum, 50 U/mL penicillin, and 50 µg/mL streptomycin. Cells were incubated at 37 °C in a humidified atmosphere with 5% CO_2.

Cell Viability and NG Biocompatibility. Cell viability in the presence of the NGs was assessed using a Vybrant cytotoxicity assay kit (Thermo Fisher Scientific) according to the manufacturer's protocol. The NGs were suspended in the culture medium (20 µg/ mL) and administered to OVCA433, 24 h after their seeding at a density of 1.5×10^4 cells/cm^2. 50 µL of the supernatant was transferred into a 96-well plate, and after 10 min of incubation with 50 µL of a resazurin/reaction mixture at 37 °C in 5%CO_2, the fluorescent metabolite of resazurin (resorufin) was detected (λex = 530 nm; λem = 590 nm) using an Infinite M200-Pro multiplate reader (Tecan, Mannerdorf, Switzerland). The release of the cytosolic enzyme glucose 6-phosphate dehydrogenase (G6PD) from damaged cells into the surrounding medium was quantified after 2, 6, and 24 h. The measured fluorescence is proportional to the amount of G6PD released into the medium, which is correlated with dead cells in each specimen. Each experiment was performed in triplicate for each time point, and the viability levels were normalized to the control (i.e., fully lysed cells).

Flow Cytometric Analysis. The selectivity of the NGs for CD44 and the involvement of the hyaluronan receptor in the internalization process were studied. OVCA433 were seeded at a density of 1.5×10^4 cells/cm^2 into 12-well plates for 24 h, and CD44 was blocked with an anti-CD44 blocking/neutralizing antibody (clone IM7, PE-Cy7 labeled; Thermo Fisher Scientific). In brief, the cells were washed in PBS and incubated for 45 min at RT with the antibody (1.25 ng/ µL in PBS). Then, the cells were washed in PBS (three times) and the NGs were administered at a final concentration of 20 µg/mL. The control group was represented by cells without CD44 blocking treatment. At 2, 6, and 24 h time points, the cells were analyzed by f low cytometry (CytoFLEX flow cytometer, Beckman Coulter, Brea, CA) with CytExpert software (Beckman Coulter). The living cells were gated on a forward versus side-scatter (FSC/SSC) dot plot; the NG signal was recorded in the allophycocyanin (APC-

A700) channel and quantified as the median fluorescence intensity (MFI) fold change at each time point. Fluorescence compensation was applied to correct the fluorescence spillover of Cy5 (NGs) and Cy7 (antibody) dyes.

Fluorescence Staining and Confocal Microscopy Analysis. The cellular internalization of the NGs was also visualized using confocal microscopy. OVCA433 cells were seeded at a concentration of 1.5×10^4 cells/cm^2 into an 8-well chamber slide (Ibidi GmbH, Grafelfing, Germany) for 24 h, while CD44 blocking and NG uptake were performed as described in the previous section. After 24 h, the cells were fixed in paraformaldehyde (4% in PBS) for 15 min at RT and then incubated for 5 min in Triton X-100 (0.1% in PBS) to permeabilize the cell membranes. Subsequently, they were washed three times in PBS, incubated with ActinGreen 488 stain (GeneCopoeia, Rockville, MD; 1:80 dilution in PBS for 40 min, in the dark), washed in PBS (3 times), and counterstained with DAPI (Thermo Fisher Scientific; 1:1000 dilution in PBS for 10 min, in the dark). Micrographs were collected using a Nikon A1R+ laser scanning confocal microscope (Nikon Instruments, Tokyo, Japan) with a 20× NA1.0 air objective.

Cell Assay of NG-Mediated DOX Delivery. Cell metabolic activity was evaluated following the administration of the DOX loaded NGs to validate their potential therapeutic effect. OVCA433 were seeded at a density of 1.5×10^4 cells/cm^2 in the growth medium and incubated for 24 h. Then, DOX-loaded NGs (DOX-NG, 5.8 ng of DOXper mg of NG) were added to the cells at a concentration of 20 μg/mL. The cells incubated with pristine (i.e., nonencapsulated) DOX represented the control group. All conditions were set to achieve the same final concentration of 0.2 μM drug in the culture medium. The MTT assay was used according to the manufacturer. The experiments were performed in triplicate at different time points (24 h, 48 h, 72 h, and 1 week).

Statistical Analysis. The experimental data were analyzed using Prism ver. 9.3.0 (GraphPad Software, San Diego, CA) and reported as mean ± SD if not otherwise specified. One-way analysis of variance (ANOVA) followed by Tukey's multiple comparison test was used to assess the statistical significance, which was set at the 0.05 level.

2.1.2 Results & Discussion

Chemical characterization of nanogels. HA-LPEI nanogels were synthesized in a surfactant-free emulsion medium, consisting of two polymeric solutions of HA and PEI as aqueous dispersed phases, and a continuous organic one. This multiphase system represents

a challenging approach compared to the standard emulsion-based strategies, where at least one of the starting polymers is soluble in an organic solvent, immiscible with water, and the hydrophilic counterpart is present in the aqueous phase. Our procedure was designed to exhibit all the classical behaviors of the metastable colloids, detectable in the conventional single (W/O or O/W) and multiple (W/O/W or O/W/O) emulsions,[127,128] combined with enhanced phenomena of droplet interactions between the two aqueous phases, driven by the interfacial cohesion forces. This resulted in initiating the chemical crosslinking between HA and LPEI at the droplet-droplet interface and in completing the formation of the 3D nanoscaffold upon the droplet coalescence, exploiting the Brownian and Van der Waals mutual interactions of the polymeric disperse phases.[129]

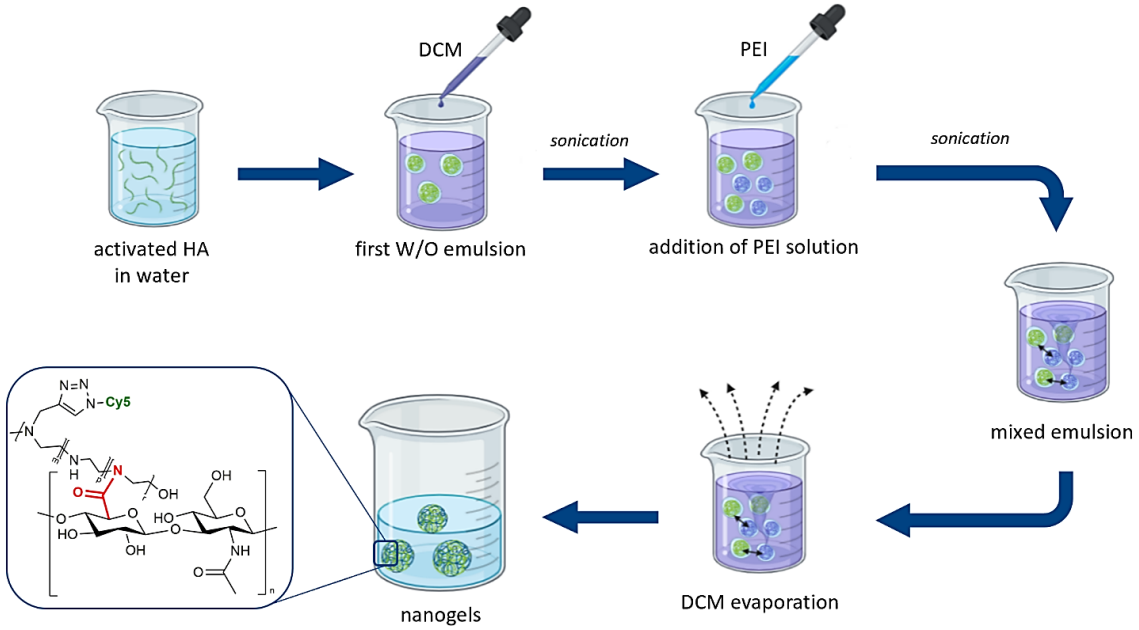

Figure 2.1 Scheme of NGs synthesis through MEET (Mixed Emulsion/Evaporation Technique). On the left: putative representation of the forming NG structure where the amide bond is highlighted (in red).

In detail, the proposed MEET protocol (*Figure 2.1*) involved the preparation of a first W/O emulsion of HA in DCM by sonication, followed by the addition of the LPEI aqueous phase, again under sonication. The resulting emulsion could be classified as a mixed one and was characterized by the absence of surfactants, in order to avoid potential side-reactions in the formation of the NG scaffolds. The chemical reaction occurred between HA NHS-ester intermediate and LPEI amine groups and the final nanosystems were collected in a single aqueous phase, after the evaporation of the organic solvent.

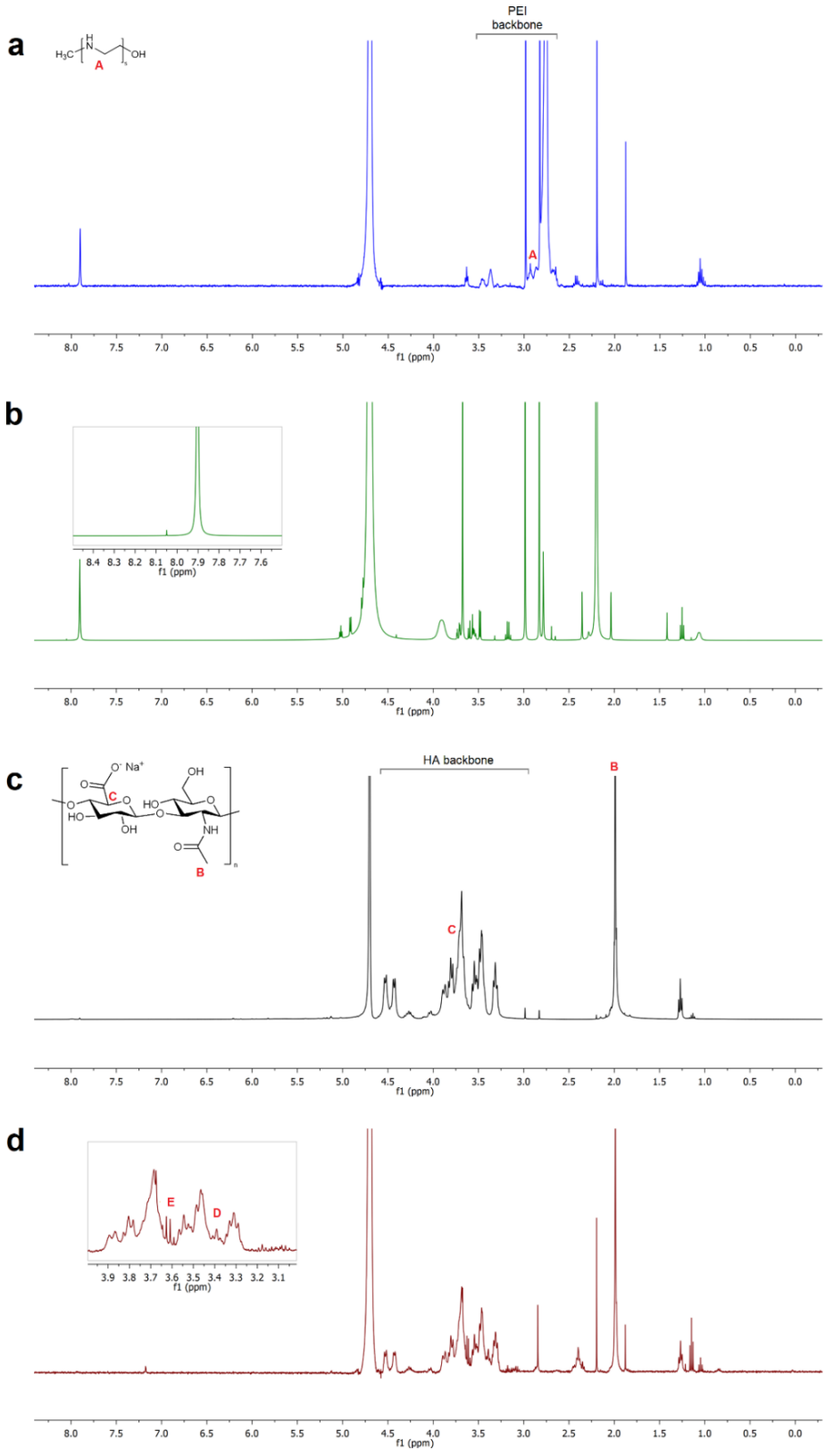

Figure 2.2 [1]H-NMR spectra of LPEI (a, blue; due to the different protonation degree of amino groups in the polymer backbone, A is indicative of the methylene protons subsequently involved in the crosslinking reaction), LPEI functionalized Cy5 (b, green), HA (c, black) and NGs (d, red). The signals of HA-LPEI crosslinking are highlighted.

Results of ^{1}H-NMR analysis confirmed the Cy5 conjugation on PEI chains (characteristic triazole peak at 8.05 ppm[130,131]) and the formation of NGs. In particular, in *Figure 2.2*, the chemical crosslinking through amide bond was confirmed by the shift of the signals ascribable to the methylene protons (N-*CH*$_2$-CH$_2$, *D*) of PEI monomer and the methine group (*CH*-COOH, *E*) of the HA ring moiety, involved in the reaction: the former was detectable at 3.38 ppm (signal at 2.93 ppm in the spectrum of neat LPEI) and the latter at 3.62 ppm (shoulder signal at 3.80–3.70 ppm in the HA spectrum). Moreover, the characteristic peak of HA methyl groups and of PEI backbone were clearly detectable, at 2.00 ppm and 2.85 ppm, respectively.[132,133] An estimation of the HA:PEI molar ratio in the nanoscaffold was conducted considering the integral values of their characteristic peaks and it resulted in HA:PEI 6:1, approximately.

The synthetic route leading to NG formulation was also monitored through FT-IR analysis, as shown in *Figure 2.3*. In detail, HA spectrum (*Figure 2.3c*) presented the characteristic peaks of –OH stretching at 3259 cm^{-1} and aliphatic C–H stretching at 2880 cm^{-1}. The signal at 1739 cm^{-1} could be ascribed to the carbonyl stretching of the carboxylic group. The peak at 1608 cm^{-1} was representative of the amide II (C=O stretching), whereas the signals at 1407 cm^{-1} and 1376 cm^{-1} could be assigned to the C–H bending. The stretching of the C–CH$_3$ amide could be observed at 1315 cm^{-1}, and the bands related to the stretching C–O–C bridge and the skeletal vibration involving the C–O stretching at 1148 cm^{-1} and 1035 cm^{-1}, respectively[134,135]. LPEI spectrum (*Figure 2.3a*) showed the signal of –OH stretching at 3366 cm^{-1} and the asymmetric and symmetric stretching vibration of the CH$_2$ at 2907 cm^{-1} and 2819 cm^{-1}, respectively. Moreover, N–H bending could be observed at 1622 cm^{-1} and C–H bending and C–N stretching vibrations could be ascribed to the signals in the wavenumbers range 1450÷900 cm^{-1}. The conjugation of Cy5 on the PEI backbone (*Figure 2.3b*) was confirmed by the triazole linkage, ascribable to the signals at 1437 cm^{-1}(*) and 1458 cm^{-1}(**), and by the cyanine peaks around 2880 cm^{-1} and in the wavenumbers range 1500 ÷ 800 cm^{-1}, partially overlapped to PEI signals. Finally, the NG spectrum (*Figure 2.3d*) showed the characteristic signal of C=O stretching of the amide bond at 1703 cm^{-1} (†), representative of the successful HA-LPEI covalent crosslinking and the consequent nanoscaffold formation, besides showing all the characteristic peaks of the starting polymers.

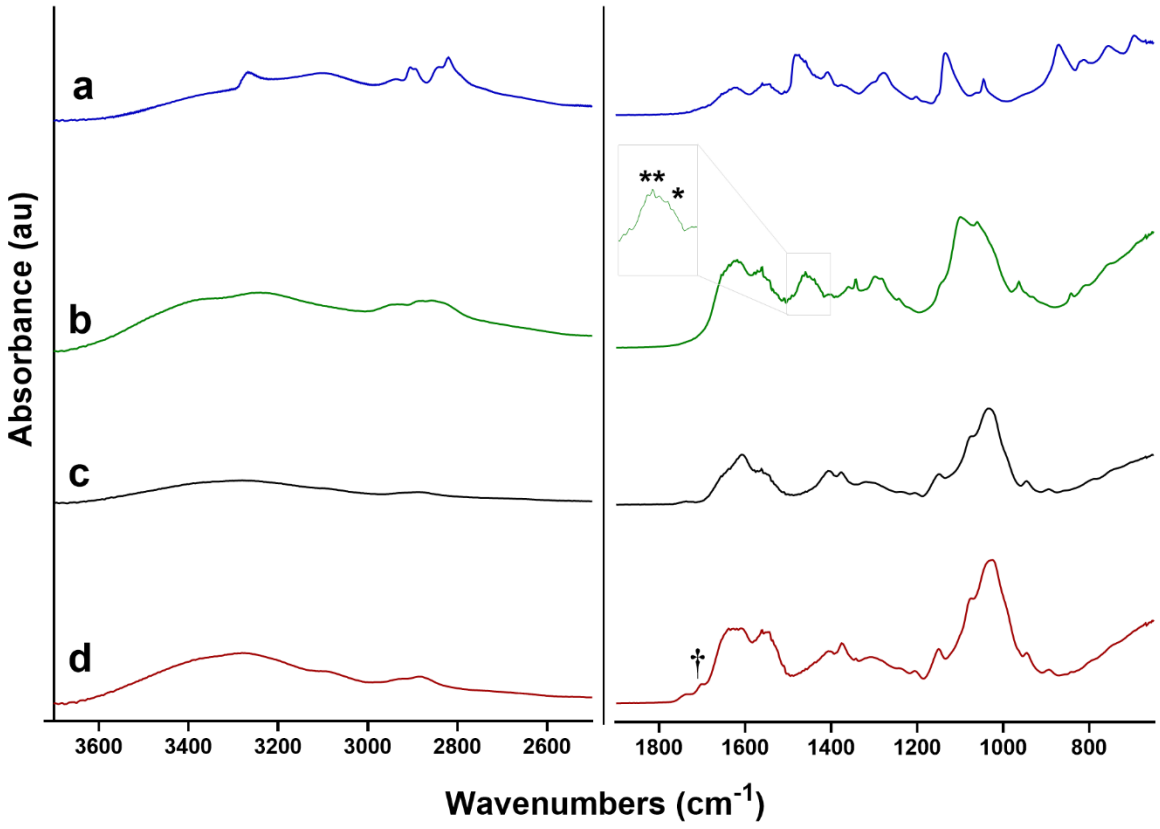

Figure 2.3 FT-IR spectra of LPEI (a, blue), LPEI functionalized Cy5 (b, green), HA (c, black) and NGs (d, red).

Physical characterization of nanogels: size and stability. The evaluation of NG size was conducted through DLS, AFM, SEM and TEM analyses (*Figures 2.4* and *2.5c*). DLS measurements of the hydrated NG specimens were carried out in different conditions (PBS, acidic and basic solutions) to investigate potential variations in NG size and their stability over time. In PBS medium, we recorded a mean hydrodynamic diameter of *ca*. 220 nm (polydispersity index PDI = 0.204) and a ζ-potential value of *ca*. – 8.7 mV. Additionally, NG stability was characterized by an initial phase of swelling due to the on-going hydration of the lyophilized specimen, followed by an equilibrium state with the surrounding environment (which resulted in an almost constant NG diameter from the 24 h time point). This initial swelling (maximum hydrodynamic diameter of 292.6 nm) was paralleled by a corresponding peak in the NG negative surface charge (-9.6 mV), suggesting a correlation between the two entities. Considering the HA:LPEI 6:1 molar ratio in NGs, the higher amount of negatively charged HA dictated the physicochemical behavior of the nanosystem. Indeed, as well documented in the literature, HA is characterized by solvation and diffusion of molecules/ions toward the polymer backbone at a faster rate than the chain relaxation:[136]

this resulted in an increased hydration effect and in an expanded polymer conformation with larger end-to-end distance (overshoot value); when this elongation is counterbalanced by the polymer chain reactive force, some of the absorbed molecules are forced out of the HA network, and an equilibrium state is achieved.[137,138] In parallel, this behavior supported the maximization of the overall electrostatic and polar interactions between the HA functional groups and the ionic species, providing a slight increase in the value of the negative electrical double layer associated to the nanostructure, until the equilibrium condition. After drug encapsulation, a slight variation in NGs size was recorded (Appendix I), attributable to the steric hindrance of the entrapped drug and its physico-chemical interaction with the polymer chains: however, this difference can be considered not relevant in terms of cellular uptake.[131]

Furthermore, NG stability was also tested in acidic (pH 4.5) and basic (pH 8.5) solutions: a moderate increase in plateau diameter was observed in both conditions, underlying no aggregation and a good stability. The pH-dependent variations in hydrodynamic diameters could be ascribed to the different ionic nature of the polymers: PEI exhibits the highest protonation degree at pH 4.5, whereas it is substantially deprotonated in alkaline condition;[139,140] on the other hand, HA is characterized by a lower net negative charge in acidic *vs.* basic medium and a decreasing radius of gyration at alkaline pH values.[141] As a result, at pH 4.5, the prevailing PEI positive charge density gave rise to repulsion forces between the protonated residual amino groups, favoring the increase in NG size (*ca.* 80 nm increase in hydrodynamic diameter); in alkaline conditions, the HA ionic strength and the electrostatic repulsion between its carboxyl and hydroxyl groups favors an elongated configuration of the polymer chains, which resulted in slightly larger NGs (*ca*. 50 nm increase) compared to the specimens in PBS buffer. These observations were confirmed by the ζ-potential values: indeed, NGs showed an almost neutral charge at pH 4.5 and were negatively charged at pH 8.5.[142,143]

AFM analysis (*Figure 2.4c*) was conducted in air on partially hydrated NGs and gave a diameter value of *ca.* 195 nm; the discrepancy between DLS and AFM measurements was attributable to the different measurement conditions: DLS analysis was performed on fully solvated NGs and the measured values corresponded to the NG hydrodynamic diameter, whereas for AFM measurements, a certain degree of dehydration was attributable to the experimental settings. Moreover, AFM conditions enhanced the typical Marangoni effect occurring in colloids: the crosslinked polymeric chains tended to spread according to the mass transfer driven by the surface tension gradient, induced by the variation in the

evaporation flow across the surface of the laid droplet.[144,145] Due to this phenomenon, sample deposition procedure could result in colloidal agglomeration of NGs. In addition, SEM images (*Figure 2.4d*) showed a spherical morphology with a smooth surface and an approximate size around 114 nm. In this case, the smaller NG dimensions were related to the high-vacuum conditions, which led to a shrinking of the NG meshes due to the progressive transition from a swollen to a fully dehydrated state.

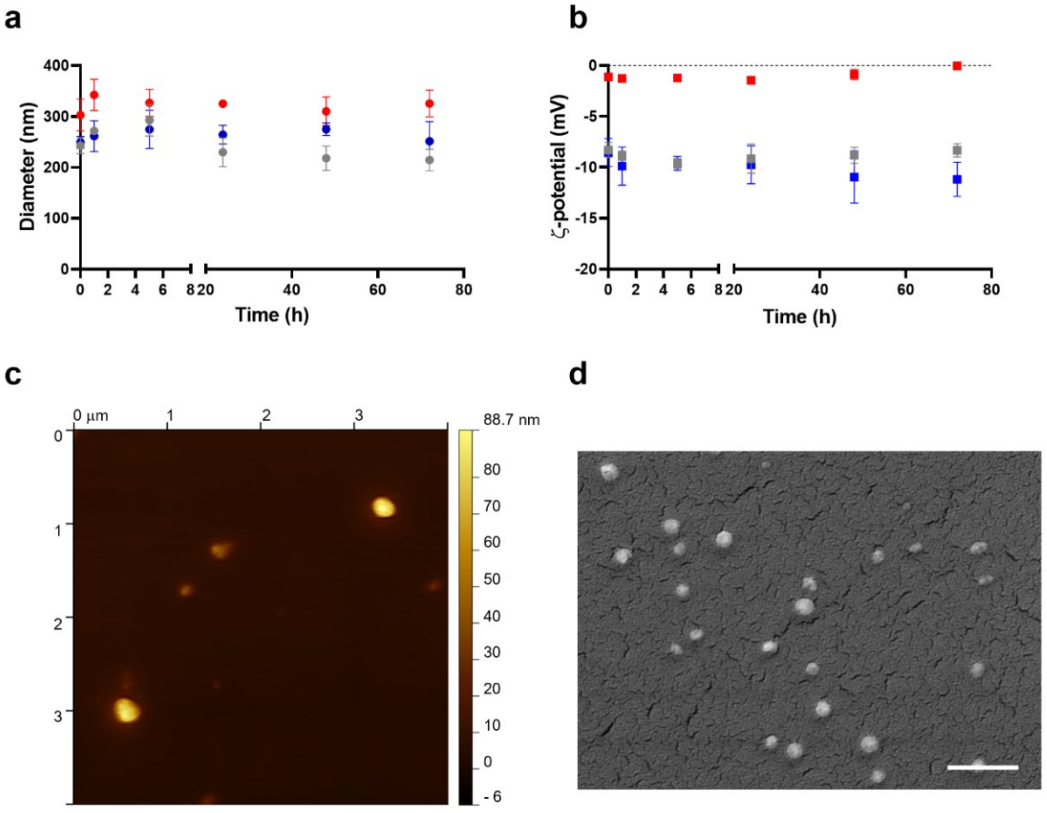

Figure 2.4 (a,b) Evaluation of NGs size and ζ-potential through DLS analysis in PBS (grey), acidic (red, pH 4.5) and alkaline (blue, pH 8.5) solutions. (c) AFM image of NGs. (d) SEM image of NGs. Scale bar = 500 nm.

Additionally, the enzymatic degradation of the nanocarrier was explored. HAase was chosen as an enzyme, at two different concentrations (10 and 150 U/mL) commonly used in *in vitro* experiments,[146–148] and the variation in NG size and morphology were evaluated through DLS and TEM analyses.

Results revealed a HAase dose-dependent degradation behavior of the NGs. *Figure 2.5* shows the progressive decreases of the hydrodynamic diameter (up to 70% at 48 h) and the relative count rate for the specimen treated with HAase at the higher concentration (150 U/mL), highlighting the gradual degradation of the nanomaterial: in particular, the reduction

in count rate is representative of the lower density of NGs in suspension, correlated to the decreased number of existing nanostructures.[149,150]

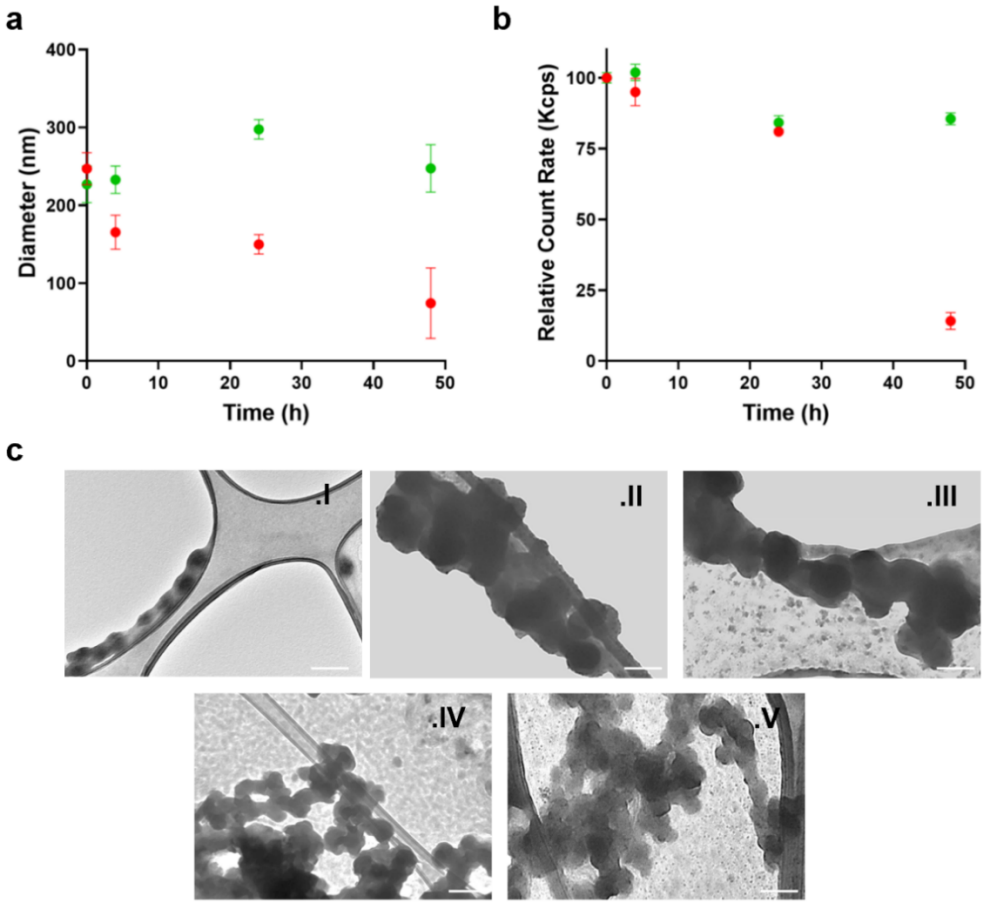

Figure 2.5 (a,b) DLS evaluation of NGs enzymatic degradation (size and relative count rate, respectively) in hyaluronidase solution 10 U/mL (green) and 150 U/mL (red). (c) Representative TEM images of NGs morphology in PBS solution (I, as-synthesized NGs) and following the treatments with HAase solution at 37 °C (II: 10 U/mL, 24 h; III: 10 U/mL, 48 h; IV: 150 U/mL, 24 h; V: 150 U/mL, 48 h). Scale bar = 250 nm.

Conversely, at 10 U/mL (a concentration giving an *in vitro* degradation rate similar to the *in vivo* conditions[151]) the count rate decreased to an almost constant value. The reported increase in the NG size at 24 h may be attributed to an augmented swelling capacity due to the complete or partial cleavage of HA chains, which can generate local defects and nano-voids.[149,152] However, in this case, NGs did not show a substantial degradation up to 48 h, suggesting a better stability of the nanocarrier for controlled drug delivery purposes (Appendix I). Furthermore, TEM images confirmed DLS analysis (discrepancies in NG dimension can be attributed to the dry state of the specimens for TEM analysis), and showed the progressive alteration of NG morphology at 150 U/mL HAase solution, whereas the size of the NG treated with the enzymatic solution at 10 U/mL showed no significant reduction.

Drug release. The performance of NGs as a controlled drug delivery system was investigated using DOX as a candidate drug. DOX is a cytotoxic anthracycline antibiotic commonly used against several tumor microenvironments, such as lung,[153] breast,[154] melanoma,[155] bladder,[156] and ovarian[157] cancer. The DOX encapsulation efficiency was about 83.4%, as detected by UV-vis spectroscopy, and its release profiles in PBS, acidic and basic conditions are reported in *Figure 2.6a*. NGs ensured a high encapsulation efficiency and a sustained drug delivery over time, showing a cumulative release of *ca*. 85% in PBS and almost completed at acid and alkaline pH (*ca*. 93% and 97%, respectively), after 15 days. The trend in PBS could be ascribed to a diffusion mechanism mainly controlled by the aliphatic-aromatic stacking interactions between HA and DOX, as documented in systems where the high local density of atoms in aliphatic and aromatic rings, to some orientations and distances, results in increased electrostatic and dispersive interactions, producing a stabilization effect.[158–160] Here, this phenomenon could take place between the aliphatic rings of the HA and the aromatic moieties of the drug, generating non-covalent interactions which provided a stacked arrangement of the drug molecules within the NGs architecture, reducing the release rate of DOX from the nanomatrix.

In acidic medium, NGs exhibited a drug release profile similar to that observed in PBS buffer up to 10 days, with an increase of the cumulative DOX release in the following days. Despite the larger NG size at pH 4.5 than in PBS, the obtained result could be explained by considering the higher protonation degree of LPEI which gave rise to additional noncovalent interactions, defined as cation-π interactions,[161] between the protonated amine moieties of the polymer and the aromatic rings of the drug. The physical nature of this interaction could contribute, together with the aliphatic-aromatic stacking, to tune the progressive release of DOX in the first days. At pH 8.5, drug release was faster compared to the other conditions: here, the increased negative charge on HA backbone induced a repulsion between the carboxylate and hydroxide groups of HA and DOX, partially counteracting the interaction between the disaccharide units and the aromatic moiety of the drug, and, as a result, increasing the drug release from the nanomeshes.

Figures 2.6b, 2.6c and *2.6d* show the cumulative release against time to the power of 0.43 (i.e., $t^{1/2.3}$). In this representation, linearity of data is representative of a Fickian diffusion regime and the y-axis intercept value is an indication of the burst release, which is assumed equal to zero for an ideal controlled release system.[131,162] Collected data showed good linearity, confirming that DOX release was mediated by Fickian regime, and no initial burst

release was noted, emphasizing the potential lifetime of this nanocarrier as drug delivery system.[163] In particular, a double diffusion regime with different slopes could be detected in all investigated conditions. The transition and duration of the two regimes could be ascribed to the nature of the predominant interactions drug-NGs over time. The first diffusion trend (*i*), which occurred in the first 6 h, could be associated to the adsorbed DOX at the interface NGs/water, which could be released at a faster rate according to the diverse pH values; whereas the second regime (*ii*) could correspond to the interactions in the nanoscaffold core: the aliphatic-aromatic stacking which delayed and sustained the drug release in PBS, the aliphatic-aromatic and the cation-π interactions which prolonged the drug release in acidic buffer, and the electrostatic repulsions which counterbalanced the aliphatic-aromatic stacking for a faster DOX release in alkaline condition.

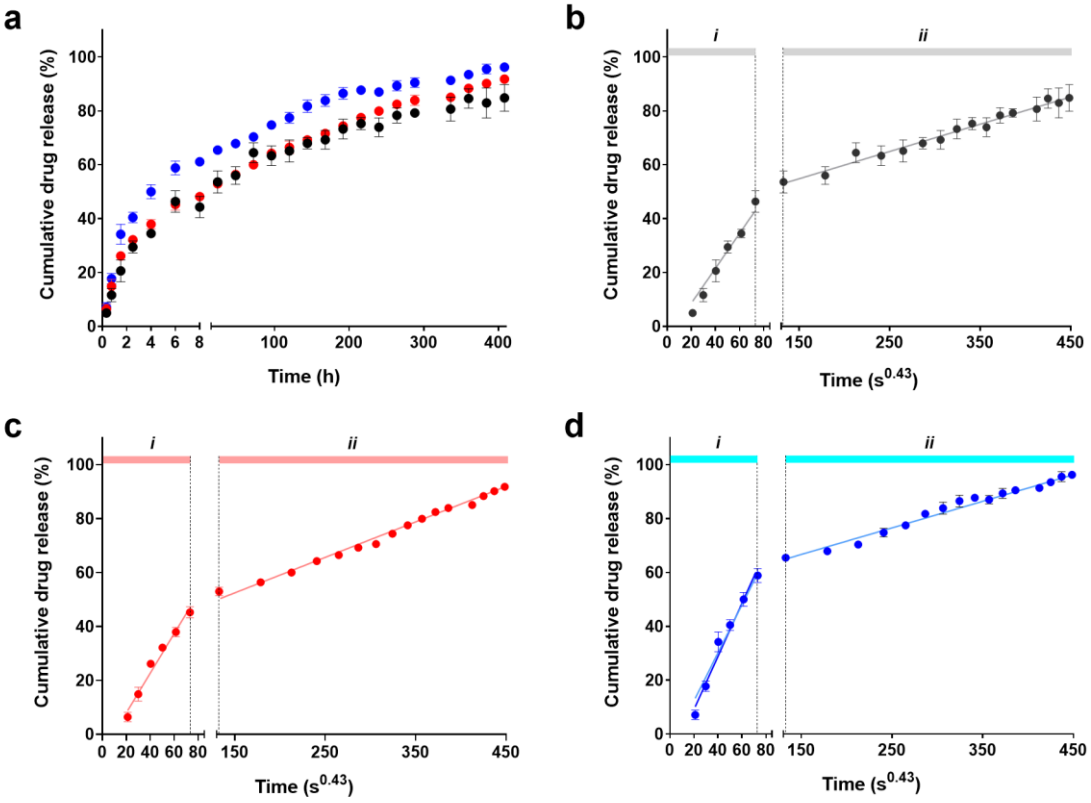

Figure 2.6 (a) Release profile of DOX delivered by NGs in PBS (black), acidic (pH = 4.5, red) and alkaline (pH = 8.5, blue) solutions. (b,c,d) The slope of the drug release against time expressed as $t^{1/2.3}$ is representative of the Fickian diffusion coefficient of drugs in NGs, at the different investigated conditions. Cumulative drug release is represented as a percentage of the total drug payload (mean value ± SD is plotted).

NG biocompatibility. OVCA433 cells were chosen as a representative cell line expressing good affinity toward HA thanks to its high levels of CD44 expression (Appendix I). Indeed, HA is considered the major ligand for CD44 and its isoforms in different cancer

scenarios.[164,165] Proving the biocompatibility and the internalization of our NGs would highlight their potential use as therapeutic nanocarriers in ovarian cancer. G6PD assay demonstrated that HA-LPEI NGs did not generate cytotoxic effects on cells: *Figure 2.7a* reports high normalized viability levels (above 98%) with no significant difference *vs*. control (*i.e.*, cells without NGs).

NG internalization. To evaluate the involvement of CD44 on NG internalization process, flow cytometric analysis of CD44-naïve and CD44-blocked OVCA433 following NG administration was conducted.

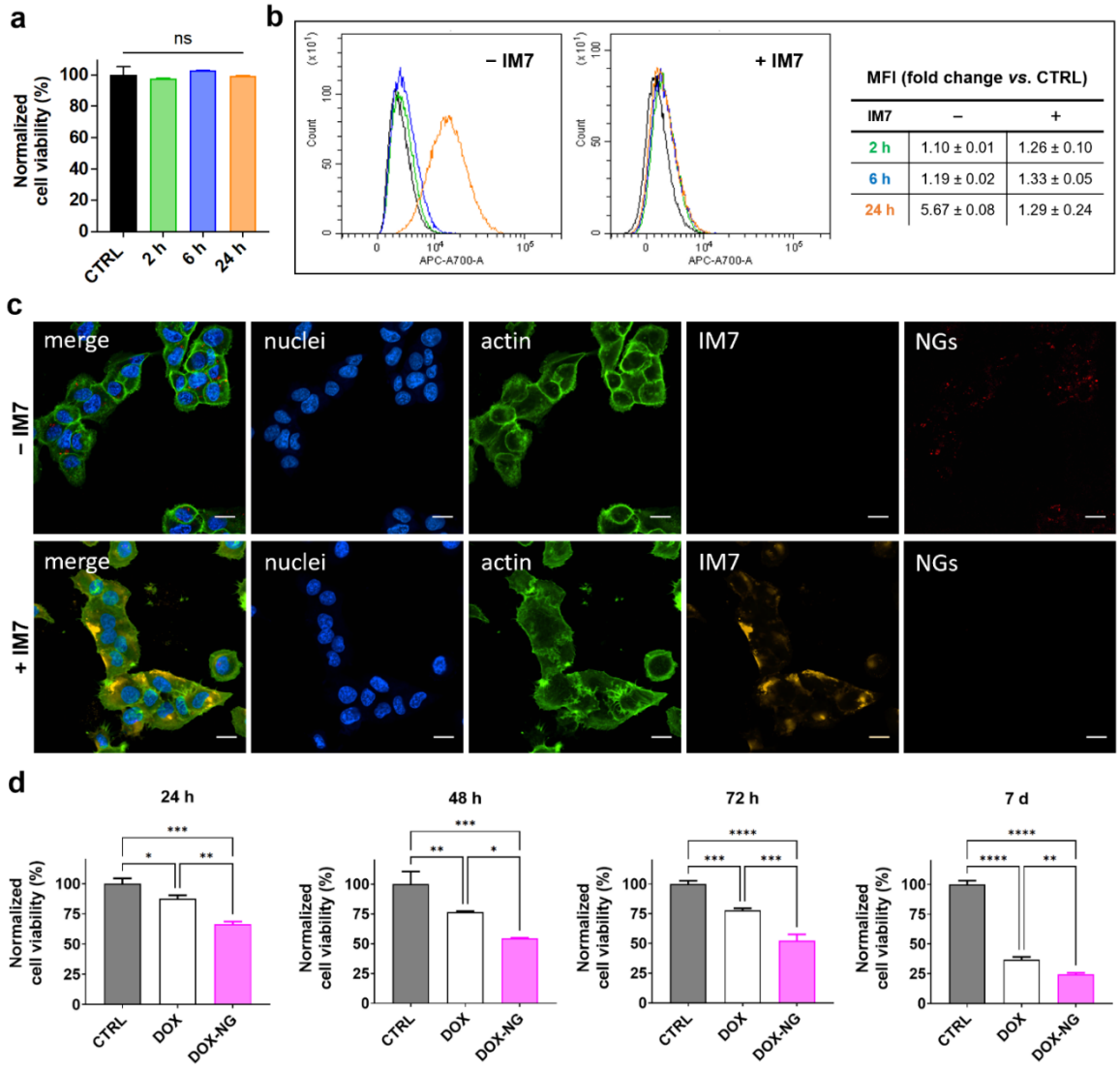

Figure 2.7 (a) Cell viability by G6PD assay of OVCA433 cells following incubation with NGs for 24 h. Results are normalized to CTRL group and expressed as mean ± SD. (b) Flow cytometric analysis of naïve OVCA433 (–IM7) vs. OVCA433 treated with CD44 neutralizing/blocking antibody (+IM7), after NGs uptake at 2 h (green), 6 h (blue) and 24 h (orange): plot reports the shift of the allophycocyanin (APC-A700-A) signal for each time point in the target gate (CTRL in black). The fold changes in MFI, calculated vs. internal control cells, are specified in the table. (c) Representative

*confocal micrographs of NGs (in red) internalization in OVCA433 cells after 24 h of incubation. NG internalization was not detectable in +IM7 group. Actin cytoskeleton was stained with FITC-labeled phalloidin and nuclei were counterstained with DAPI. Scale bar = 20 μm. (d) DOX-induced cytotoxicity in OVCA433 at 24 h, 48 h, 72 h and 7 days, after the administration of free-drug (DOX) and drug-loaded NGs (DOX-NG). The therapeutic effect is expressed in terms of cell viability levels normalized against internal controls, measured through the MTT assay. Results are the mean ± SD of three independent experiments. Statistical analysis was performed using one-way ANOVA. * $p < 0.05$, ** $p < 0.01$, **** $p < 0.001$, **** $p < 0.0001$, ns = not significant.*

Figure 2.7b shows the distribution of cell fluorescence at the investigated time points (2 h, 6 h and 24 h), where an increase of the MFI over time is representative of the progressive NG uptake by cells. A significantly different trend could be observed in the two conditions: in control cells expressing CD44 surface receptors (–IM7), the uptake of the nanocarriers occurred over time and it resulted clearly detectable at 24 h, with a 5.7-fold change in MFI; on the other hand, in cells treated with CD44 neutralizing/blocking antibody (+IM7), no relevant increase in MFI was observed and fluorescence histograms were comparable at all time points. These results demonstrated that CD44 was directly involved in the mechanism of NG internalization, suggesting their potential use as a CD44-targeting drug delivery system. However, as recently discussed in the literature,[166,167] this outcome should not be interpreted as a cell surface event of selective binding, because a rational approach to CD44 selective targeting through hyaluronan-based nanosystems is challenging: an unclear correlation between CD44 expression, HA binding and its internalization process does not allow CD44 to be assigned an exclusive role as a selective binder and internalizer in the uptake of HA-based nanomaterials.

A further validation of the internalization process was provided by fluorescence microscopy, as shown by the confocal images in *Figure 2.7c*, representative of the NG uptake at 24 h. Blocking CD44 receptors (+IM7) resulted in substantial inhibition of NG uptake, while in CD44-naïve cells (–IM7), the nanocarriers were clearly detectable, with a progressive intracytoplasmic localization (a 3D volume rendering of confocal z-stack is provided as Appendix I).

Effect of NGs-mediated release of DOX on cells. To validate our NG formulation, we performed an *in vitro* evaluation of the therapeutic effects of NG-mediated DOX release, comparing the nanoencapsulation approach to the conventional administration route of the pristine drug. We selected an ideal sublethal drug concentration of 0.2 μM, corresponding to a 14% cell viability reduction, as estimated through the dose-response curve at 24 h on OVCA433 cultured in adhesion, using the MTT assay (Appendix I). Moreover, this drug

concentration falls in the range of values commonly investigated for ovarian cancer treatments.[168–170] The cell metabolic activity was estimated through MTT assay, up to 7 days, as reported in *Figure 2.7d*. The administration of DOX-loaded NGs (DOX-NG) boosted the therapeutic effect of the drug, as clearly detectable after 24 h ($p<0.0001$ *vs.* CTRL), outperforming the non-encapsulated DOX ($p<0.01$ *vs.* DOX). Moreover, the sustained drug release ensured prolonged effects on cell metabolism over time, with a constant improved performance than the conventional drug administration route, leaving a low residual cell viability at 1 week ($p<0.0001$ *vs.* CTRL and $p<0.01$ *vs.* DOX).

Overall, these results offered a new perspective on the synthesis of NGs *via* MEET, overcoming the limitations in the design of nanoscaffolds related to the use of organic-insoluble adducts, and resulting in a biocompatible nanomaterial system with enhanced drug delivery performances for pharmacological therapies.

2.2 Folic acid surface functionalization to improve selective targeting ability toward cancer cells

The use of cancer cell receptors as targets for drug delivery systems represents one of the most specific and sensitive strategies for tumor treatment, offering enhanced precision compared to conventional therapies such as chemotherapy and radiotherapy.[171,172] By exploiting the biochemical differences between normal and cancer cells, modified nanohydrogels have recently been proposed to selectively target overexpressed tumor-specific membrane receptors.[173] Notably, in solid tumor environments, cancer cells exhibit elevated levels of the alpha isoform of the Folate Receptor (αFR). The expression of αFR is correlated with disease progression and serves as a negative prognostic marker in cancers such as breast, colon, endometrium, and ovarian malignancies.[174–176] Consequently, αFR is regarded as an efficient therapeutic target, enabling the development of folic acid-functionalized nanostructures for the targeted delivery of anticancer agents to αFR-overexpressing cancer cells.[175]

This study aims to synthesize and functionalize Hyaluronic Acid–Linear Polyethyleneimine nanohydrogels for selective targeting of αFR-expressing cancer cells. Nanohydrogels were initially formulated using the mixed emulsion-evaporation technique (MEET) and subsequently conjugated with folic acid through an EDC/NHS coupling reaction. The resulting samples were subjected to physical and chemical characterization using Nuclear Magnetic Resonance (NMR), Dynamic Light Scattering (DLS), and Transmission Electron Microscopy (TEM) to analyze their composition, size, and polydispersity index (PDI).

To establish the relationship between folate-conjugated nanohydrogels and their internalization in αFR-overexpressing cancer cells, both qualitative and quantitative analyses were conducted. Cellular uptake of pristine and folate-conjugated nanohydrogels was evaluated using Confocal Laser Scanning Microscopy and Flow Cytometry on Human Dermal Fibroblasts (HDF), serving as a non-tumoral control, and on the Human Epithelial Cervical Carcinoma (HeLa) cell line, representing the cancer model with αFR overexpression. Additionally, an MTT assay was performed to assess the biocompatibility of both pristine and folate-conjugated nanohydrogels on HDF and HeLa cells.

2.2.1 Materials & Method

Materials. Ultralow molecular weight (MW) 8-15kDa Hyaluronic Acid Sodium Salt (HA) was purchased from BioSynth Carbosynth. Linear polyethyleneimine (MW: 2.5kDa, LPEI),

folic acid (FA), N-Hydroxy-succinimide 98% (NHS), N-(3-Dimethylaminopropyl)-N'-ethilcarbodiimide hydrochloride ≥ 98.0% (EDC), propargyl bromide ($B_R\equiv$), cyanine 5 azide 95% (Cy5-azide), copper (II) sulfate ($CuSO_4$), sodium ascorbate (Na_{ASC}) and all solvents were purchased from Sigma Aldrich® Chemical. Spectrum™ Spectra/Por™ dialysis membrane with molecular weight cut-off (MWCO) 100-500 Da/6-8 kDa/15 kDa were purchased from Thermo Fisher Scientific. Dulbecco's Modified Eagle's Medium – high glucose (Cat# D5671, DMEM), TrypLe™ Express (Cat# 12605-10), phosphate buffered saline (PBS) were purchased from GIBCO Thermo Fischer Scientific. HeLa cell line (cervical cancer cell line), and Human Dermal Fibroblast (HDF) were stored at -80°C or in liquid nitrogen. All chemicals were of analytical grade from commercial used without any further purification.

LPEI functionalization through click chemistry. LPEI functionalization with the Cy5 chromophore was performed as described in the materials and methods section of chapter 2.1.

Mixed Emulsion/Evaporation Technique. NGs synthesis was performed as described in the materials and methods section of chapter 2.1.

Nanohydrogel surface functionalization. Folic acid conjugation to the nanogel surface was performed following the protocol reported below (*Figure 2.8*). Briefly, pristine FA (1.67 mg, 0.0037 mmol) was dissolved in a mixture of deionized water (5 mL) and DMSO (1mL). For activating FA carboxylic groups, EDC (18.12 mg, 0.094 mmol) and NHS (10.88 mg, 0.094 mmol) were added to the system, which was left under stirring for 3 hours at room temperature. Afterwards, NGs specimen (8 mg, 0.019 mmol) was added to the solution. The reaction was left under magnetic stirring for 24-36 hours at room temperature in the dark. Then, dialysis was performed for 3 days in deionized water using a membrane with MWCO: 15kDa and with daily exchange of water. Finally, the specimen was lyophilized and stored at -20°C. This functionalization was obtained using a molar ratio between FA and HA monomer (HA_m) of FA : HA_m = 0.2 : 1, therefore we refer to this sample as NGs-$FA_{0.2}$. The same reaction has been performed by varying the used amount of FA (4.17 mg, 0.0094 mmol) reaching a molar ratio of FA : HA_m = 0.5 : 1, the as prepared specimen is named NGs-$FA_{0.5}$.

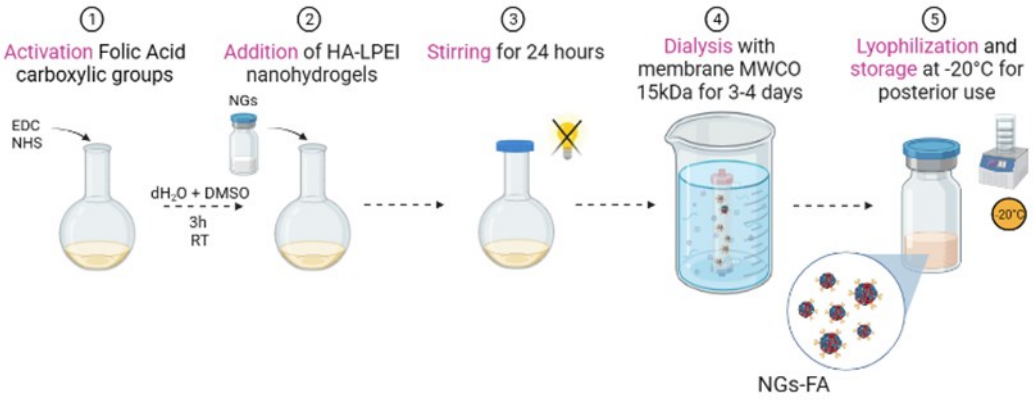

Figure 2.8 Schematic representation of folate-conjugated NGs preparation. image generated by Biorender.

Physiochemical characterization. The physico-chemical characteristics of the synthesized nanohydrogels were evaluated through several techniques.

Nuclear Magnetic Resonance (^{1}H-NMR). The proton nuclear magnetic resonance was executed on a Bruker AC spectrometer (400MHz). Tests have been performed on samples diluted in deuterium oxide (D_2O) acquiring 128 scans for each analysis. Tetramethylsilane (TMS) has been considered as reference compound for defining chemical shifts.

Dynamic Light Scattering (DLS). DLS analyses were carried out using a Zetasizer Nano ZS instrument determining the hydrated diameter, the polydispersity index (PDI) and the ζ-potential of the analyzed samples. For what concerns the specimen preparation, NGs were suspended in PBS at a concentration 1 mg/mL and sonicated for 10 min to reach the complete dispersion in the medium before analysis.

Cell cultures. Human Dermal Fibroblasts (HDF) and Human Epithelial Cervical Carcinoma (HeLa) were cultured in Dulbecco's modified Eagle's medium-high glucose (DMEM), supplemented with 10% fetal bovine serum (FBS), 1% penicillin-streptomycin and 1% L-glutamine. Both cell lines were maintained in humified incubator at 5% CO_2 and 37°C.

Cellular uptake – Laser Scanning Confocal Microscopy analysis. Cellular internalization of NGs, NGs-$FA_{0.2}$ and NGs-$FA_{0.5}$ was observed using confocal laser scannering microscopy (CLSM). HDF and HeLa cells were seeded into an 8-well chamber slide at a density of $1.5x10^4$ cells/well. Incubation of NGs, NGs-$FA_{0.2}$ and NGs-$FA_{0.5}$ in both cell lines at 100µg/mL concentration was performed for 24 hours. After 24 hours, cell culture medium was removed, and cells were washed twice in 200µL PBS. Then, cells were fixed in 200µL of paraformaldehyde (4% in PBS) for 10 minutes at RT in the dark. The paraformaldehyde solution was removed, and cells were washed for 3 times with PBS (200µL) and then

incubated for 5 min in Triton X-100 (0.1% in PBS) to permeabilize the cell membranes. Subsequently, they were washed three times in PBS, incubated with ActinGreen 488 stain (GeneCopoeia, Rockville, MD; 1:80 dilution in PBS for 40 min, in the dark), washed in PBS (3 times), and counterstained with DAPI (Thermo Fisher Scientific; 1:1000 dilution in PBS for 10 min, in the dark).. Cells were incubated with 200µL of the *cellular tracker* (1:1000 in PBS) for 10 minutes at RT in the dark, to stain cell membranes. After washing with PBS two times, nuclei were counterstained with 200µL DAPI (1:1000 in PBS). Images were collected using a Nikon A1R+ laser scanning confocal microscope (Nikon Instruments) with a 20x NA1.0 air objective and 60x in oil.

Cellular uptake – Flow cytometry analysis. Fluorescently labelled Cy5 NGs and folate-conjugated nanohydrogels internalization was investigated through flow cytometry analysis. Both cell lines were seeded into a 12-well plate at a density of $3.5x10^4$ cells/well in folate free complete culture medium for 24 hours. After 24 hours, HDF cells were incubated with 50µg/mL of NGs, NGs-$FA_{0.2}$ and NGs-$FA_{0.5}$. HeLa cells were incubated with three different concentrations of each formulation: 50µg/mL, 100µg/mL and 300µg/mL. Samples were prepared in folate free complete culture medium. Then, the solutions were vortexed and placed in an ultrasonic bath for 5 minutes at 59kHz to disperse them. After incubating for 24 hours, HDF and HeLa cells were washed twice with PBS and 200µL of trypLE was added for 5 minutes at 5% CO_2 and 37°C, in order to detach cells. Afterwards, trypLE was stopped by adding with 1mL of PBS and centrifugated for 5 minutes at 1200 rpm. After centrifugation, the supernatant was discarded, and the pellet was resuspended in 100 µL of PBS. NGs internalization was analyzed by flow cytometry (CytoFLEX flow cytometer, Beckman Coulter) with CytExpert software (Beckman Coulter). NGs, NGs-$FA_{0.2}$ and NGs-$FA_{0.5}$ signals were recorded in the allophycocyanin (APC-A700) channel. The living cells were gated on a forward *versus* side-scatter (FSC/SSC) dot plot and quantified as the median fluorescence intensity (MFI) fold change.

Cell Viability – MTT assay. HDF and HeLa cell viability in the presence of NGs and folate-conjugated nanohydrogels was assessed using MTT assay. HDF and HeLa cells were plated at a density of $5.0x10^3$ cells/well, respectively, in 96-well plates and cultured in folate free complete culture medium 24 h prior the incubation with NGs. 50 µg/mL, 100 µg/mL, and 300 µg/mL of NGs, NGs-$FA_{0.2}$ and NGs-$FA_{0.5}$ were prepared in folate free DMEM-high glucose and administrated to HDF and HeLa cells for 24 hours. At the end of the incubation time, the media was replaced by 100µL of MTT solution (0.5 mg/mL) in each well, incubated

for 4 hours under 5% CO_2 and 37°C conditions. Then, formazan crystals were solubilized with the addition of DMSO (100µL in each well). Supernatant was transferred into a new 96-well plate and the metabolic activity of both cell lines at the different concentrations was detected at 570 nm using an Infinite M200 multiple reader (Tecan). For each concentration, tests were carried out in triplicate. NGs and folate-conjugated nanohydrogels biocompatibility on HDF and HeLa cell line has been calculated as percentage with respect to the negative control.

2.2.2 Results & Discussions

The synthesis of HA-LPEI nanogels was conducted using a mixed emulsion/evaporation technique. The initial step involved the activation of the carboxylic acid groups present in HA. This was followed by the generation of the first water-in-oil (W/O) emulsion through the gradual addition of the HA solution into DCM. Subsequently, a mixture comprising pristine LPEI and LPEI-Cy5 was introduced into the system, resulting in the formation of a secondary W/O emulsion and the establishment of a mixed emulsion system. The resulting emulsion was subjected to vigorous stirring overnight to facilitate the evaporation of the volatile solvent DCM, which was necessary for the formation of the nanogels. Upon the evaporation of the dichloromethane, the droplets from the two polymeric phases underwent progressive coalescence, thereby enabling the crosslinking reaction between the activated HA ester groups and the amino functionalities along the LPEI backbone. This process resulted in the establishment of the three-dimensional crosslinked polymeric nano-network, then recovered in a single aqueous phase. Successively, the conjugation of folic acid (FA) onto the NGs surface was achieved through the prior activation of the carboxylic groups of FA followed by the NGs introduction into the reaction mixture to promote the conjugation process overnight. FA conjugation was conducted specifically on the hyaluronic acid monomer (HAm), with the FA-to-HAm molar ratios set at 1:0.2 and 1:0.5 to investigate the influence of FA concentration. The reaction was conducted in a solution of deionized water and DMSO.

Physicochemical characterization. The successful syntheses of HA-LPEI NGs, NGs-$FA_{0.2}$, and NGs-$FA_{0.5}$ were confirmed by ^{1}H-NMR (*Figure 2.9*).

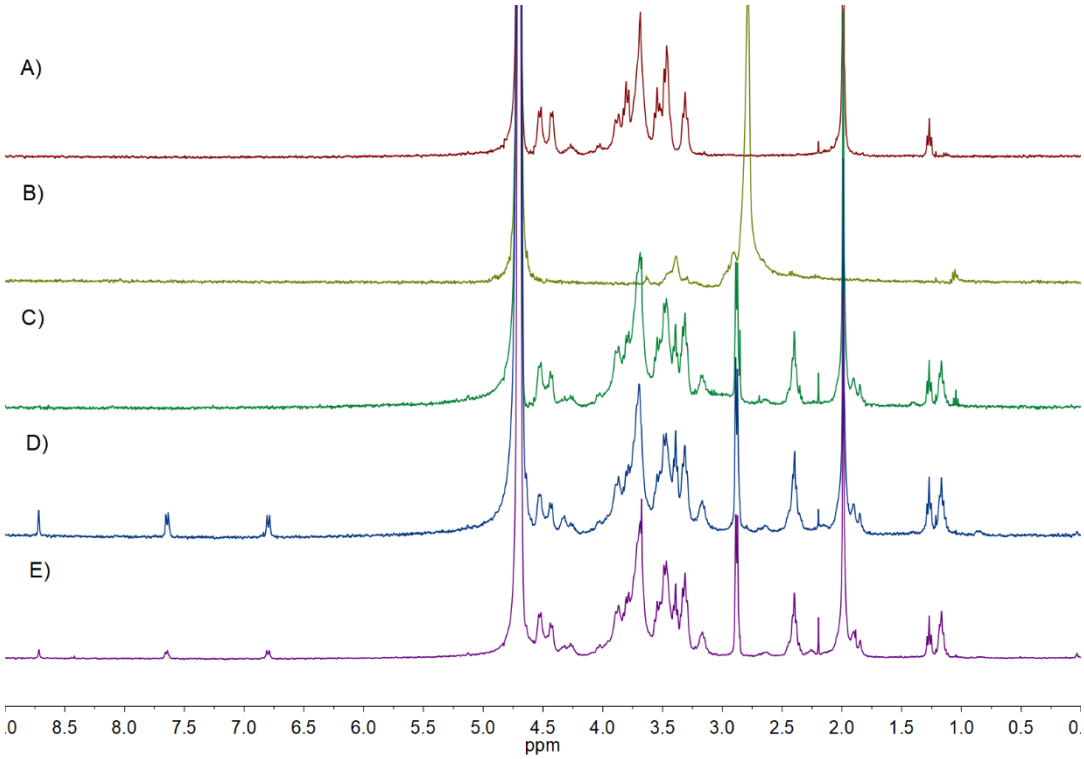

Figure 2.9 ^{1}H-NMR spectra: A) HA, B) LPEI, C) (HA-LPEI) NGs, D) NGs-FA$_{0.5}$, E) NGs-FA$_{0.2}$. Signals were collected by using Bruker AC spectrometer (400 MHz)

In particular, *Figure 2.9A* and *B* show the spectra of the pristine HA and LPEI. Moreover, the correct crosslinking between HA and LPEI can be observed in the spectrum of the NGs in *Figure 2.9C*. The characteristic peak at 3.62 ppm can be ascribed to the methine group of the HA carboxyl groups in the polysaccharide ring, which is involved in the amide crosslinking reaction between HA-ester and LPEI. Furthermore, signals attributable to both polymers can be detected in the NGs spectrum confirming the crosslinking of the polymeric network.

To evaluate the effective FA conjugation, the ^{1}H-NMR spectra of the folate-conjugated nanogels, NGs-FA$_{0.5}$ and NGs-FA$_{0.2}$ (*Figure 2.9D* and *E*), were compared with the spectrum of unmodified NGs. The spectra of both FA-functionalized nanohydrogels exhibited aromatic proton peaks associated with FA at 6.6, 7.7, and 8.6 ppm, thereby confirming the successful incorporation of folic acid onto the nanogels via the EDC/NHS coupling reaction. Moreover, the relative intensities of these aromatic peaks varied between NGs-FA$_{0.5}$ and NGs-FA$_{0.2}$, with higher intensities observed in NGs-FA$_{0.5}$. This reflected the increased FA content used in this formulation, confirming that NGs-FA$_{0.5}$ exhibited a higher degree of folate functionalization compared to NGs-FA$_{0.2}$.

Successively, the size, polydispersity (PDI) of the NGs and folate-conjugated nanohydrogels were investigated by DLS. *Figure 2.10* reports the collected data.

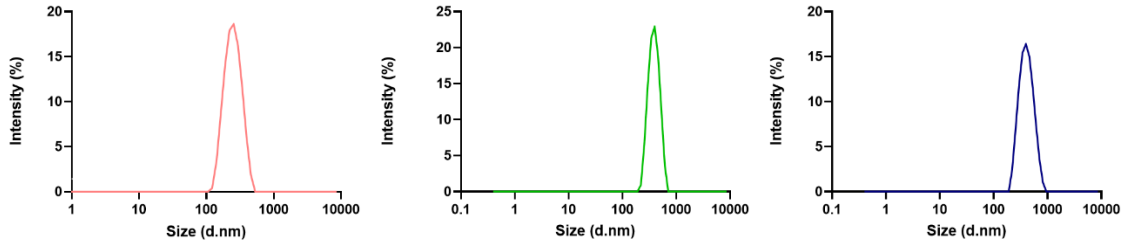

Figure 2.10 A) DLS measurements: (red) NGs, (green) NGs – $FA_{0.2}$, (blue) NGs-$FA_{0.5}$; DLS analyses were carried out using a Zetasizer Nano ZS instrument.

The PDI for each NGs and NGs-FA formulation were determined using DLS analysis to evaluate the size heterogeneity of the nanoparticles. As summarized in *Table 2.1*, tested samples exhibited PDI value raging between 0.26 to 0.41, with NGs measurement in agreement with previously discussed data (see result and discussion of chapter 2.1). NGs-$FA_{0.2}$ showed a slightly increased PDI value compared with the other formulations. However, no statistically significant differences were detected, therefore the surface functionalization did not seem to affect the homogeneity of the NGs (one-way ANOVA: NGs vs. NG-$FA_{0.2}$, p-value = 0.267; NGs vs. NG-$FA_{0.5}$, p-value = 0.809; NG-$FA_{0.2}$ vs. NG-$FA_{0.5}$, p-value = 0.120).

Table 2.1 DLS analysis, Polydispersity Index (PDI) and Particle Size (nm)

	PDI (-)	**Size (nm)**	**ζ-potential (mv)**
NGs	0.30 ± 0.10	273.7 ± 3.4	- 6.4 ± 1.5
NG-$FA_{0.2}$	0.41 ± 0.08	395.2 ± 29.3	-11.9 ± 1.2
NG-$FA_{0.5}$	0.26 ± 0.04	462.2 ± 14.0	-17.3 ± 0.7

In contrast, DLS measurements revealed an effect of the surface functionalization on the particle sizes. In particular, increasing the amount of the folate conjugation results in bigger particles, with only slight variations observed between NGs-$FA_{0.2}$ and NGs-$FA_{0.5}$. The significant size difference between NGs and folate-conjugated nanohydrogels can be attributed to the presence of folic acid molecules on the NGs surface, likely inducing a steric effect. In contrast, the minimal difference between NGs-$FA_{0.2}$ and NGs-$FA_{0.5}$ is consistent with the differing amounts of FA incorporated during their synthesis. Moreover, the effect of the surface functionalization on NGs size was also statistically confirmed by one-way

ANOVA test. In particular, results confirmed the above discussed findings, also highlighting the major effect between unmodified and folate-conjugated NGs (NGs vs. NG-$FA_{0.2}$, p-value = 0.0005; NGs vs. NG-$FA_{0.5}$, p-value < 0.0001; NG-$FA_{0.2}$ vs. NG-$FA_{0.5}$, p-value = 0.0114).

TEM was employed to examine the morphology of both non-conjugated and folate-conjugated nanohydrogels (*Figure 2.10B*). TEM images confirmed that the nanohydrogels displayed a nearly spherical shape. Moreover, a comparison of DLS and TEM data revealed differences in the particle sizes of NGs and folate-conjugated NGs among different techniques. Specifically, TEM measurements were consistently smaller than those obtained by DLS. This discrepancy is likely due to the nature of the measurements: DLS captures the hydrodynamic size distribution of nanohydrogels in solution, accounting for the swelling behavior over time, whereas TEM provides a direct visualization of the dry-state nanohydrogel structure. The observed swelling behavior, indicative of the nanohydrogel's soft and dynamic nature, was corroborated by these complementary techniques.

The swelling-deswelling mechanism observed in nanohydrogels enables structural adaptation to environmental changes, a feature that can be harnessed for stimuli-responsive applications. This behavior offers several advantages, including: (1) enhanced drug absorption, (2) gradual and controlled drug release, and (3) a protective barrier shielding the drug from environmental factors such as oxidation, hydrolysis, or interaction with other molecules.[177]

In general, nanohydrogels range in size from a few nanometers to several hundred nanometers. The size parameter is crucial as it influences their properties and functionality. Smaller nanohydrogels, with diameters in the lower nanometer range, are often favored in drug delivery systems due to their higher efficiency in cellular internalization. Importantly, nanohydrogel size can be precisely tuned during the synthesis process to meet specific application requirements.

Subsequently, the surface charge of the synthesized NGs was evaluated through the measurement of their zeta potential. It is noteworthy that the ζ-values exhibited a reduction from -6.4 mV to -17.3 mV in accordance with the folate content, thereby providing further confirmation of the successful functionalization of the synthesized nanogels. The surface properties of nanoparticles are of fundamental importance in defining their interaction with the biological environment. Accordingly, the statistical significance of these findings (one-way ANOVA: NGs vs. NG-$FA_{0.2}$, p-value = 0.0030; NGs vs. NG-$FA_{0.5}$, p-value < 0.0001;

NG-$FA_{0.2}$ vs. NG-$FA_{0.5}$, p-value = 0.0031) allows for an in-depth examination of the biological behavior of these NGs.

Cellular uptake. The cellular uptake of the synthesized NGs was investigated in both HDF and HeLa cell lines to verify the selective-targeting ability of the engineered NGs. In particular, HDF were used as healthy cells model, with low level of αFR expression. By contrast, HeLa cells is a well-known and highly utilized cervical cancer model with high overexpression of the target receptor.

Table 2.2 Flow cytometry data obtained from NGs and NGs-FA internalization in HeLa cells at 50μg/mL, 100μg/mL and 300μg/mL.

	NGs-$FA_{0.2}$		**NGs-$FA_{0.5}$**	
	Median APC-A700-A	**MFI Fold increase vs. CTRL**	**Median APC-A700-A**	**MFI Fold increase vs. CTRL**
50 μg/mL	1207.90 ± 28.09	1.68 ± 0.07	1033.10 ± 51.47	1.44 ± 0.07
100 μg/mL	5900.53 ± 681.46	6.58 ± 0.76	1190.50 ± 37.75	1.33 ± 0.04
300 μg/mL	7570.43 ± 164.44	12.03 ± 0.26	1914.87 ± 19.12	3.04 ± 0.03

Figure 2.11A illustrates the cytofluorimetric analyses of the internalization after 24h of incubation performed on both cell lines with NGs, NGs-$FA_{0.2}$, and NGs-$FA_{0.5}$ at a concentration of 50 μg/mL. The APC-A700-A channel was selected to analyze the fluorescent signal ascribable to the Cy5 linked to the NGs formulations. Median Fluorescence Intensity (MFI) data were reported as fold increase with respect to the MFI of the control cells. Unmodified NGs showed a statistically significant MFI 2-fold change in HDF model underlying that they were internalized in the healthy model. Interestingly, the fold change increased to 6-fold compared to the control when analysing the internalization in the HeLa cells. Hence, pristine NGs showed only a preferential internalization toward target cells rather than an actual selective targeting characteristic. On the other hand, folate conjugated-NGs showed a general lower level of internalization in the HeLa cells (1.5- and 1.7-fold change for NGs-$FA_{0.5}$ and NGs-$FA_{0.2}$, respectively) and, more interestingly, no evidence of fold change of MFI was detected in the HDF model. Indeed, no statistically significant difference was observed between the MFI of both folate-conjugated NGs and HDF negative control group. The data substantiate the hypothesis that the NGs surface modification with folate moieties confers selective targeting abilities towards αFR receptors. This enables the development of novel nanocarriers for precision medicine.

To better explore the uptake performances of folate NGs in HeLa cells, analyses with increasing concentrations (50, 100, and 300 µg/mL) were performed post 24h incubation (*Figure 2.11B*).

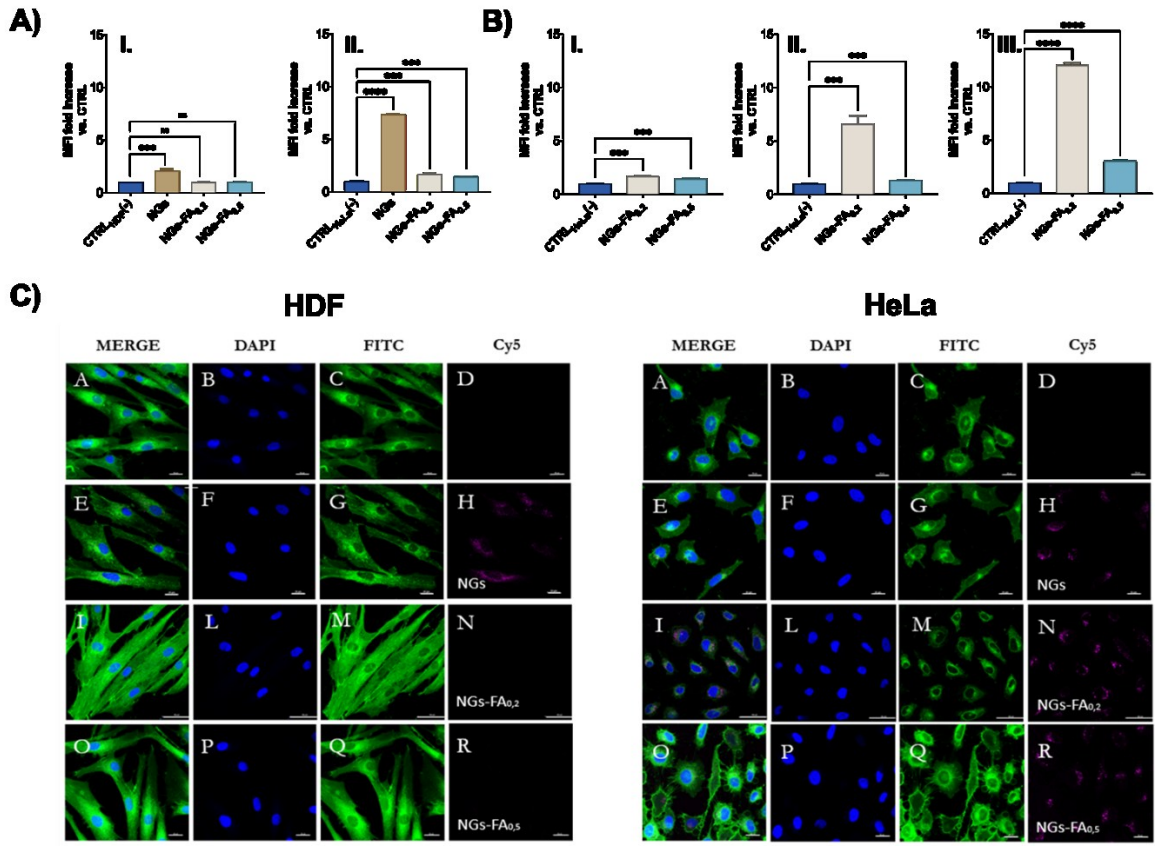

Figure 2.11 A) MFI fold increase evaluated through cytofluorimeter after 24h of incubation with NGs, NG-FA$_{0.2}$, and NG-FA$_{0.5}$ at 50 µg/mL: I. HDF cell line; II: HeLa cell line. B) Effect of nanoparticles concentration on the internalization of folate-modified NGs in HeLa Cells: I. 50 µg/mL; II. 100 µg/mL; III. 300 µg/mL. Statistical analysis performed: t-test vs. control group. C) Confocal micrographs obtained after 24h of incubation of NGs and folate-modified NGs at 300 µg/mL in both cell lines.

Table 2.2 reported the raw data and the calculated MFI fold changes. Both formulations had increasing internalization with increasing concentration. Interestingly, NG-FA$_{0.2}$ reached high level of internalization at 100 and 300 µg/mL with fold increase of 6.58 and 12.03 respectively, outperforming NG-FA$_{0.5}$. This can be attributed to the major steric hindrance in NGs-FA$_{0.5}$ due to the higher functionalization level, which can limit the folate-αFR interaction, coupled with its lower ζ-potential value which can lead to a major electrostatic repulsion between highly negative NGs and the negatively charged cell membrane, causing a reduction in the total nanogels internalization. However, the FA-NGs uptake appeared to have a dose-dependent behaviour, leading to high cellular internalization only at

concentration above a certain value, especially for NG-FA$_{0.2}$. The underlying mechanism driving this behavior has not been fully investigated, thus further investigations are needed.

Successively, qualitative confocal analysis was also performed. HDF and HeLa cells were incubated for 24h with NGs, NGs-FA$_{0.2}$, and NGs-FA$_{0.5}$ at a concentration of 300 µg/mL. *Figure 2.11C* showed the panel for both cell lines consisting of the merge, DAPI (nuclei), phalloidin-FITC (cytoskeleton), and Cy5 (NGs) images. The confocal data essentially confirmed the results of the cytofluorimetric analysis, confirming the selective targeting ability of the folate conjugate NGs at the higher concentration tested. Indeed, the Cy5 signals of unmodified NGs can be detected both in HDF and HeLa cells while signals ascribable to NGs-FA$_{0.2}$ and NGs-FA$_{0.5}$ are observed only in the HeLa group.

Nanogel biocompatibility. The biocompatibility of both unmodified NGs and folate-conjugated nanohydrogels (NGs-FA$_{0.2}$ and NGs-FA$_{0.5}$) was evaluated on HDF and HeLa cells by assessing their metabolic activity through the MTT assay.

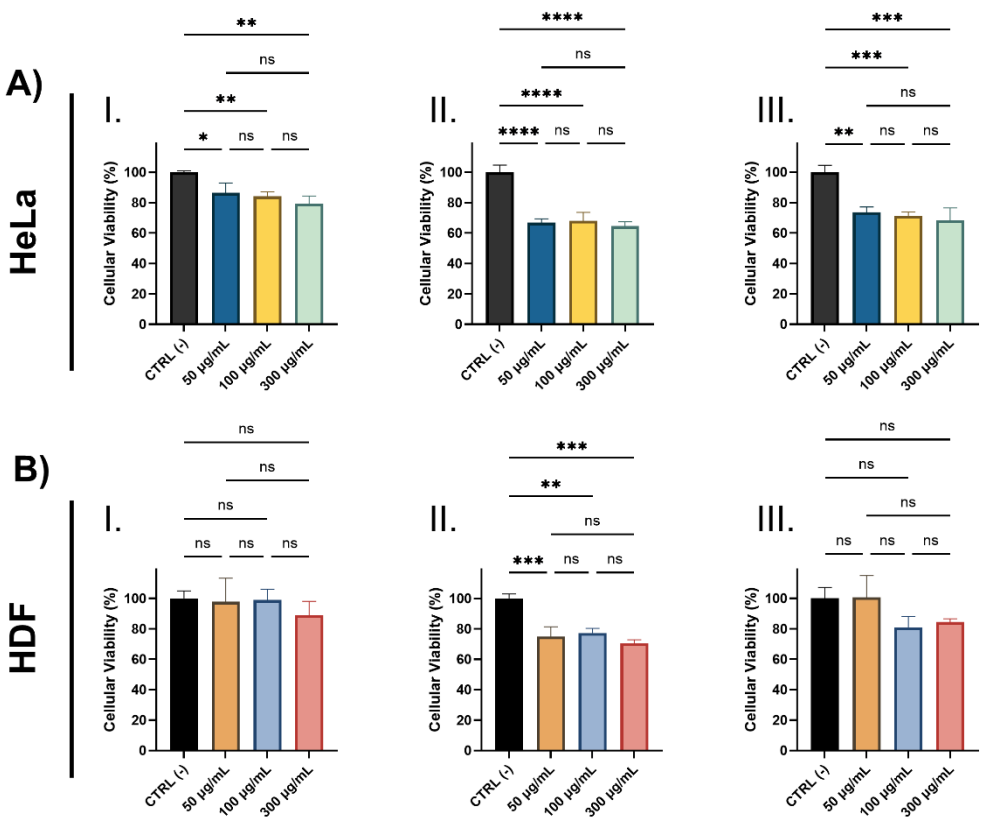

Figure 2.12 Cell viability in HeLa (A) and HDF (B) cell line of: I.) NGs, II.) NGs-FA$_{0.2}$, and III.) NGs-FA$_{0.5}$, at 50 µg/mL, 100 µg/mL and 300 µg/mL. Statistical analysis was performed using one-way ANOVA. ns = not significant.

Both cell lines were incubated for 24 hours with NGs and folate-conjugated nanohydrogels at three different concentrations (50 μg/mL, 100 μg/mL, and 300 μg/mL), and the results are summarized in *Figure 2.12*. As shown, no statistically significant differences in cell viability were observed between the three concentrations for either NGs-$FA_{0.2}$ or NGs-$FA_{0.5}$ in both cell lines (*Figure 2.12A-B II. & III.*). Furthermore, the biocompatibility of unmodified NGs in both cell models (*Figure 2.12 A I. & B I.*) aligns with the outcomes reported in the previous section. According to ISO 1993-5,[178] a formulation is considered biocompatible when the treated cells exhibit a viability of at least 70%. In spite of the statistically significant differences that have been reported in comparison with the negative control, both pristine nanohydrogels and folate-functionalized NGs exhibited biocompatibility at all of the tested concentrations, as cell viability exceeded the 70% threshold.

In conclusion, the easy surface functionalization and the proved selective targeting ability and biocompatibility of the synthesized NGs-FA highlight their potential as innovative materials for drug delivery application in cervical ovarian cancer scenarios.

2.3 Conclusions

In this part, a novel method (MEET) to synthesize hydrophilic NGs has been proposed. In particular, NGs were formulated in the HA-LPEI system, which is not suitable for conventional emulsion syntheses due to the hydrophilic nature of the two polymers. The design of a mixed emulsion strategy allows the hydrophilic polymers to constitute different dispersed aqueous phases, capable of interacting at their interface to activate the NG crosslinking reaction. This obviates the need for a hydrophobic polymeric counterpart, as required in the conventional W/O emulsification/evaporation method. The resulting NGs were validated for the controlled release of doxorubicin, a common anticancer drug, demonstrating a high drug loading capability and a sustained release over time. Choosing ovarian cancer as a model, we demonstrated that the hyaluronan receptor CD44 was involved in the NG internalization process, in such a way that the selective CD44 blockade resulted in the significant inhibition of NG uptake, thereby underlining the CD44-targeting nature of the developed nanosystem. Additionally, DOX-loaded NGs exhibited an enhanced therapeutic effect outperforming the conventional non-encapsulated drug administration route, even at sublethal dosages.

Successively, the implementation of folate modification on the surface of the HA-LPEI NGs allows for the selective targeting of αFR-overexpressing cancer cells. NGs-FA uptake was tested in HeLa cells, used as a model of αFR-positive cancer cells, and in HDF, used as a non-tumoral model (αFR-negative). Results confirmed the selective targeting feature of the folate-modified NGs showing no internalization in HDF healthy cells, while a dose-dependent behavior was highlighted in the HeLa tumor model. Interestingly, the rate of functionalization appeared to play a role in the internalization process with lower functionalized NGs (NGs-$FA_{0.2}$) outperforming the higher modified ones (NGs-$FA_{0.5}$). Moreover, a comparative analysis was performed with uncoated NGs showing high level of cellular internalization in both HDF and HeLa cells.

Collectively, our results suggest that HA-LPEI NGs may represent a promising targeted drug delivery system in cervical and ovarian cancers. Additionally, the enhanced targeting ability of the folate-conjugated NGs justify the need for the facile functionalization and strengthening the promising application of these materials as drug delivery systems. Moreover, the proposed MEET approach, overcoming the major limitations of the standard emulsion/evaporation technique, has the potential to offer a new perspective in the design of smart NGs for cancer therapy.

PART III
ADVANCED MICROFLUIDIC SYNTHESIS

3. Droplet-based microfluidic synthesis of nanogels for controlled drug delivery

3.1 Tailoring nanomaterial properties via pneumatically actuated flow focusing junction

When synthesizing NPs with droplet microfluidics, each droplet works as a micro-reactor, ensuring rapid heat and mass transfer within the confined microvolume, which enable faster reaction kinetics. Moreover, this technique gives precise control over process parameters such as size and composition of the droplets, that are produced in series as multiple identical micro-reactor units.[54,61] To date, microdroplet-based approaches have been used to produce NPs *via* highly controlled precipitation induced by diffusion-mediated mixing of solvent and anti-solvent,[52,179] ionic gelation, physical crosslinking, or chemical crosslinking. Referring to the latter, the chemical reactions are generally based on reduction or oxidation processes and aimed to produce inorganic NPs.[180,181] Moreover, the synthesis of organic-inorganic hybrid nanomaterials has been proposed combining photopolymerization techniques and the traditional hydrolysis or condensation reactions. However, the droplet-based microfluidics enabling the synthesis of polymeric nanocarriers through covalent crosslinking of polymer chains has not been fully investigated yet. Literature proposes several works where different design of droplet-based microfluidics are discussed for the synthesis of polymeric scaffolds at the microscale (according to the microdroplet dimensions), but not at the nanoscale.[54,182,183]

Therefore, further investigations are needed to define a synthetic route that combines the advantages of droplet microfluidics with the organic chemistry reactions and leads to an advanced strategy to synthesize NPs with improved properties for nanomedicine.

We propose the synthesis of polymeric nanocarriers *via* droplet-based microfluidics using a chip endowed with a pneumatic micro-actuator, enabling the active tuning of the hydrodynamic flow-focusing (HFF) geometry, thereby modulating the diameter of the microdroplets.[184,185] The rationale underlying this chip configuration is two-fold: first, to achieve the covalent crosslinking of polymer chains in each droplet to produce highly monodispersed NPs; and second, to actively control NP dimension by acting on the tunable HFF junction. In detail, in this work, hyaluronic acid (HA) and linear polyethyleneimine (LPEI) have been chosen as starting polymers to synthesize NGs potentially aimed to cancer therapy: the combination of the well-known features of HA in cancer therapy

scenarios[107,166,167,186] and the unique proton-sponge effect of PEI can improve the drug delivery performance of the synthetized nanocarriers.[110,111] The proposed pressure-actuated microfluidic system produces tunable water-in-oil (W/O) microemulsions, where the polymers are dissolved in the aqueous dispersed phase to form NGs. The validation of the synthetized nanoscaffolds was performed *in vitro* demonstrating the benefits of the NG-mediated drug delivery in a representative cancer scenario still demanding for innovative therapeutic strategies: the ovarian cancer.

3.1.1 Materials & Method

Materials. Hyaluronic acid sodium salt (HA, ultra-low molecular weight, Mw = 8–15 kDa, Biosynth Carbosynth, Compton, UK) and linear polyethyleneimine (LPEI, Mw = 2.5 kDa, Polysciences, Warrington, PA) were used as reagents for nanogel formulation. SU-8 photoresist (MicroChem, Newton, MA) and polydimethylsiloxane (PDMS, Sylgard 184, Dow Corning, Midland, MI) were used for chip fabrication. Doxorubicin (DOX) was purchased from Teva Italia S.r.l. (Milan, Italy). All other chemicals were purchased from Merck KGaA (Darmstadt, Germany) and used as received, without any further purification. Solvents were of analytical-grade purity. The Cy5-conjugated products were stored at −20 °C.

Chip microfabrication. The microfluidic device, featuring a HFF junction flanked by dead-end pressurizable channels to act as a pneumatic microactuator modulating the junction width, was designed using a CAD suite (Layout Editor, juspertor GmbH, Unterhaching, Germany) and fabricated by soft-lithography starting from a photolithographically obtained silicon master. Master mold was fabricated in SU-8 2050 negative photoresist on a 3″ silicon wafer following a standard photolithographic process. The master was silanized overnight in a chamber saturated with trimethylchlorosilane (TMCS) vapors to facilitate demolding. Replicas were obtained by casting PDMS (10:1 w/w prepolymer to curing agent ratio) onto the silicon master, followed by thermal curing (2 h at 70 °C). Once cured, replicas were carefully peeled off and fluidic ports were created using a biopsy puncher prior to oxygen plasma bonding to 1″ ×3″ microscope glass slides (Femto Plasma Etcher, Diener electronic, Ebhausen, Germany). Finally, the microfluidic channels were silanized by flushing with a stream of nitrogen saturated with TMCS for 15 min followed by thermal treatment at 140 °C for 10 min.

Polymer functionalization. HA carboxyl groups were activated through carbodiimide/hydroxy succinimide coupling, and LPEI was functionalized with the far-red dye Cy5 (*Figure 3.1*). In detail, HA (6.8 mg, 0.016 mmol of monomer) was dissolved in deionized water (DIW, 1.5 mL) and N-(3-dimethylaminopropyl)-N′-ethyl carbodiimide hydrochloride (EDC, 15.3 mg, 0.08 mmol) and N-hydroxy succinimide (NHS, 3.76 mg, 0.032 mmol) were added to the polymer solution, resulting in a 1:5:2 molar ratio for HA carboxyl groups, EDC and NHS, respectively. The reaction system was stirred for 3 h at room temperature (RT), and directly used in the microfluidic NG synthesis. On the other side, the Cy5 conjugation of LPEI was performed as described in previous sections: briefly, LPEI was first functionalized with alkyne moieties through nucleophilic substitution with propargyl bromide (LPEI:C_3H_3Br molar ratio = 1:10) in methanol, and then used in a copper-catalyzed alkyne–azide cycloaddition (CuAAC) with a 2 mg mL^{-1} solution of Cy5-N3 in DMSO (LPEI : Cy5-N3 molar ratio = 1:0.01) with CuSO4 as the catalyst and sodium ascorbate as the reducing agent. The click reaction was performed in water, at 50 °C for 36 h, in the dark and under stirring. The final product was collected as a freeze-dried polymer after dialysis (membrane MWCO = 100–500 Da) against DIW.

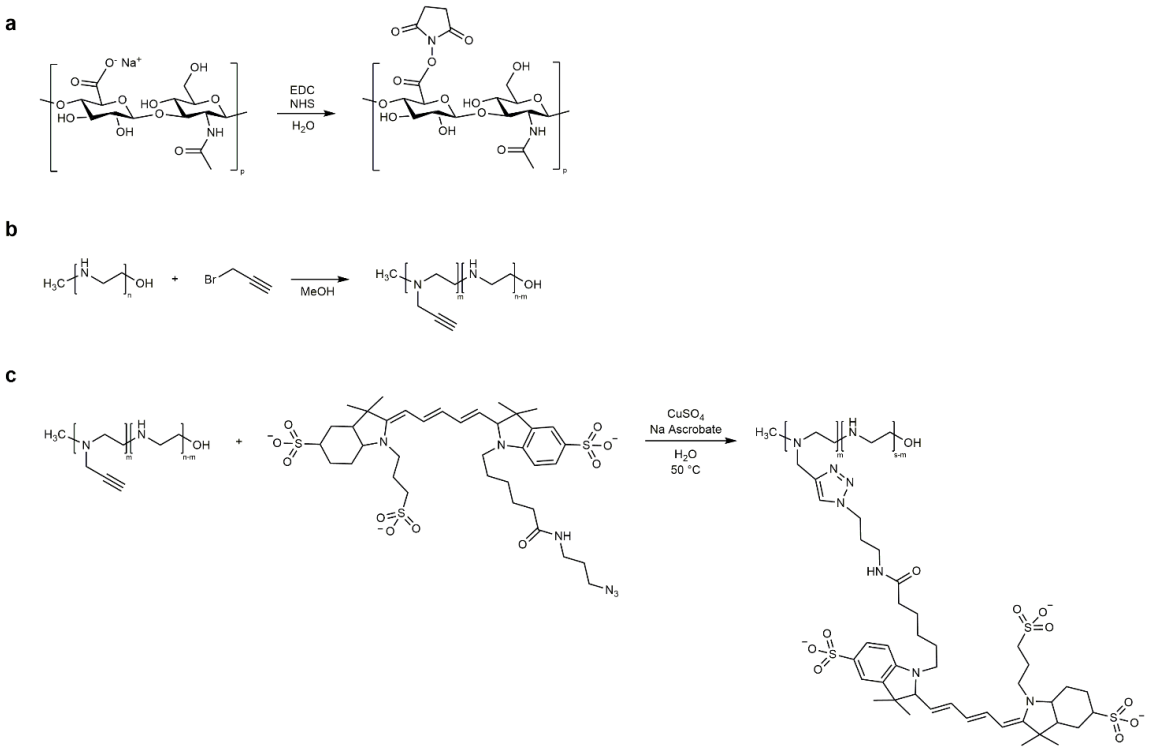

Figure 3.1 Reaction scheme of HA and LPEI functionalization: a) HA activation; b) LPEI modification with alkyne groups; c) CuAAC reaction between LPEI and Cy5-azide.

Nanogel synthesis through droplet-based microfluidics. The nanogel synthesis required the preparation of an aqueous and an organic solution as the dispersed and continuous phase, respectively. The aqueous phase was obtained as follows: LPEI–Cy5 (6.8 mg, 2.7 μmol) was dissolved in DIW (1.5 mL), then the same amount of pristine LPEI was added, and the pH of the solution was adjusted to 4.5 with 1 M HCl, to enhance the solubility of the pristine polymer in the aqueous medium. The resulting mixture was added dropwise to the solution of activated HA and vortexed for 1 min; finally, the obtained blend was loaded into a 2.5 mL gas-tight glass syringe (Hamilton Company, Reno, NV) connected to the chip inlet for the dispersed phase. The organic solution consisted of 3% w/v Span 80 in mineral oil (5 mL) and was loaded into a 5 mL gas-tight glass syringe (Hamilton) connected to the chip inlet for the continuous phase. The two liquid phases were injected into the chip channels through a programmable syringe pump (Nemesys, CETONI GmbH, Korbussen, Germany): the flow rates were set to 2 μL min−1 for the polymer solution and to 10 μL min−1 for the organic phase. To avoid the precipitation of pristine LPEI during the experiments, the whole set-up was kept at 37 °C. The on-chip micro actuator was pneumatically driven using a programmable pressure controller (OB-1 MK3, Elveflow, Paris, France) fed by compressed air. Pressurization caused the deflection of the thin PDMS walls separating the pressurized channels from the flow-focusing junction. Droplet generation occurred at the junction, forming a W/O microemulsion which was collected at the end of the output channel. A preliminary evaluation of the droplet size as a function of orifice deformation was conducted in the pressure range compatible with chip operation, and the two process conditions stably generating the largest (i.e., 0 bar) and smallest (i.e., 2 bar) droplets, without transient jetting phenomena, were chosen for further investigation. Consistently, the resulting NGs were labeled NG_0 and NG_2, respectively. Microdroplet formation was monitored under a motorized inverted optical microscope (Eclipse Ti-E, Nikon Instruments, Tokyo, Japan) equipped with a high-sensitivity camera (Neo 5.5, Andor Technology, Belfast, UK) and a dedicated control software (NIS Elements AR, Nikon). Full frame micrographs were acquired at 10 μs exposure time, while videos of 128 × 128 pixel ROIs were grabbed at 1600 fps. The collected microemulsions were broken by adding diethyl ether (10 mL), and the separated aqueous phase containing the NGs was further extracted with diethyl ether (2 × 5 mL) and purified via dialysis (MWCO = 6–8 kDa) against DIW, with daily changes for 2 days. The NG_0 and NG_2 specimens were finally obtained as solid powders after freeze drying.

Nanogel characterization techniques.

NMR analysis. Reaction intermediates and final products were analyzed by Nuclear Magnetic Resonance (^{1}H NMR) performed on a Bruker AC spectrometer (400 MHz, Bruker Corp., Billerica, MA) using deuterium oxide (D_2O) as a solvent, and the chemical shifts were reported as δ values (ppm) with respect to tetramethylsilane (TMS) as the internal standard reference.

ATR/FTIR analysis. Attenuated Total Reflectance Fourier Transform InfraRed spectroscopy (ATR/FTIR) was performed using a Thermo Nexus 6700 spectrometer coupled to a Thermo Nicolet Continuum Infrared microscope equipped with a 15× Reflachromat Cassegrain objective (Thermo Fisher Scientific, Waltham, MA). Spectra were acquired at RT in air, with 32 accumulated scans in the wavenumber range 4000–800 cm^{-1} at a resolution of 4 cm^{-1}.

DLS analysis. The size, polydispersity index (PDI) and ζ-potential of nanogels were determined by Dynamic Light Scattering (DLS) in PBS solution, using a Zetasizer Nano ZS (Malvern Panalytical, Malvern, UK). NG_0 and NG_2 specimens were analyzed at a concentration of 1 mg/mL, after sonication to minimize potential aggregation effects. Readings were performed in triplicate.

AFM analysis. Atomic Force Microscopy (AFM) measurements were performed in contact mode using a Dimension 3100 AFM with a Nanoscope III controller (Veeco Instruments Inc., Cambridge, UK) fitted with gold cantilevers (NanoWorld Pointprobe) with a spring constant of 0.08 $N \cdot m^{-1}$. The specimen was dissolved in distilled water at a concentration of 0.5 mg/mL, sonicated 10 min at 20 °C, and dipped (2 mL) on Thermo polysine slides (Thermo Fisher Scientific, Waltham, MA), until reaching the evaporation of the solvent on the substrate at RT. AFM micrographs were recorded on 30 × 30 μm areas for the preliminary morphologic evaluation and the analysis was conducted on 4 × 4 mm ROIs.

SEM. Scanning Electron Microscopy (SEM) was performed on dehydrated NGs with a field-emission SEM (FEI XL 30 ESEM-FEG, Thermo Fisher Scientific). Specimens were prepared at a concentration of 3 mg/mL in DIW and dropped (2 mL) on mica, where they were left to dry up at RT. Finally, NGs were coated with sputtered platinum before SEM analysis, which was performed at an acceleration voltage of 10 kV and with SE (secondary electrons) detection mode.

TEM. Transmission Electron Microscopy (TEM) analysis was conducted using a FEI Tecnai G2 Microscope (Thermo Fisher Scientific). A suspension of NGs (3 mL, at a concentration of 100 mg/mL) were dropped on a lacey carbon coated 300 mesh copper grid (Agar Scientific, Stansted, UK). Samples were dried at 50 °C and TEM images were collected at an acceleration voltage of 120 kV.

Drug loading & drug release. Drug loading and drug release experiments were performed in PBS following the protocol described in the materials & methods of section 2.1.

Cell culture. Human epithelial ovarian cancer cell line OVCA433 was obtained from the American Type Culture Collection (ATCC, Manassas, VA). OVCA433 cells were cultured in Dulbecco's modified Eagle medium (DMEM low glucose, GIBCO, Thermo Fisher Scientific), supplemented with 10% fetal calf serum, 100 units/mL penicillin and 100 μg/mL streptomycin. Cells were incubated at 37 °C in a humidified atmosphere with 5% CO_2.

Nanogel cytocompatibility: G6PD assay. Cytotoxicity associated to the administration of NGs to OVCA433 was assessed using Vybrant Cytotoxicity Assay (Thermo Fisher Scientific) as reported in a previous work[51]. Cells were seeded at the density of 1.5 $\times 10^4$ cells/cm^2 into 96-well plate for 24 h and then supplemented with NGs at a concentration of 20 mg/mL. The release of the cytosolic enzyme glucose 6-phosphate dehydrogenase (G6PD) from damaged cells into the surrounding medium was quantified after 24 h of incubation with NGs. 50 mL of supernatant were transferred into a 96-well plate and, after 10 min of incubation with 50 mL of resazurin/reaction mixture at 37°C in 5% CO_2, the fluorescent metabolite of resazurin (resorufin) was detected (λ_{ex} = 530 nm, λ_{em} = 590 nm; TECAN Infinite M200-Pro). Cytotoxicity was calculated as the ratio between the fluorescence values for the NG-treated cells and fully-lysed control cells (positive control), previously background corrected by subtracting from each reading the value of healthy untreated cells (negative control). Experiments were performed in triplicate.

Flow cytometric analysis for nanogel internalization. OVCA433 cells were seeded at a density of 1.5×10^4 cells/cm^2 into 12-well plates for 24 h. Then, a NG suspension at a concentration of 20 μg/mL was added. At selected timepoints (0.5, 1 and 2 h), cells were analyzed by flow cytometry (CytoFLEX flow cytometer, Beckman Coulter, Brea, CA) with CytExpert software (Beckman Coulter). Live cells were gated based on their forward and side scatter parameters; NG signal was recorded in the allophycocyanin (APC-A700) channel and quantified as the median intensity value at each time point.

Confocal microscopy. The cellular internalization of NG_0 and NG_2 specimens was also visualized through fluorescence microscopy. Cells (1.5×10^4 cells/cm^2) were seeded into 8-well glass bottom µ-Slide chambers (Ibidi GmbH, Gräfelfing, Germany). After 24 h, cells were incubated with NGs at a concentration of 20 µg/mL for 30 min. Cells were then fixed with 4% buffered paraformaldehyde (PFA) for 15 min at RT and incubated for 5 min in Triton X-100 (0.1% in PBS) to permeabilize cell membranes. After washing in PBS (3 times), cells were incubated with 1% bovine serum albumin in PBS (blocking buffer) for 30 min, stained with FITC-labeled phalloidin (Acti-stain 488, Cytoskeleton Inc., Denver, CO; 1:200 dilution in blocking buffer for 40 min) and counterstained with DAPI (Thermo Fisher Scientific; 1:1000 dilution in PBS for 10 min). Representative micrographs were collected using a Nikon A1R+ laser scanning confocal microscope (Nikon Instruments, Tokyo, Japan) with a 20× NA1.0 air objective.

Biological activity of NG-mediated DOX delivery. NGs were validated with a cell-based assay, measuring cell metabolic activity following DOX administration. OVCA433 were seeded at a density of 1.5×10^4 cells/cm^2 in growth medium and incubated for 24 h. Then, DOX was encapsulated in NG_0 and NG_2 specimens (23 ng DOX per mg NG) and the resulting systems (labeled as DOX/NG_0 and DOX/NG_2, respectively) were separately added to cells at a concentration of 20 mg/mL and incubated for 30 min, followed by medium exchange. A reference group was represented by OVCA433 cells supplemented with pristine (*i.e.*, non-encapsulated) DOX at the same final concentration of 0.8 mM in culture medium. MTT assay was used according to the manufacturer's instructions. Briefly, activity of mitochondrial dehydrogenases in living cells was measured in terms of absorbance at 570 nm (TECAN Infinite M200-Pro) after 3 h exposure to a 0.5 mg/mL MTT solution in PBS, at 37 °C and 5% CO_2. Absorbance values obtained in the absence of cells were used for background subtraction. Untreated cells were used as a control for normalization. Experiments were performed in triplicate at different time points (24 h, 48 h, 72 h and 1 week).

Statistical analysis. Data were analyzed using Prism ver. 9.2.0 (GraphPad Software, San Diego, CA) and reported as mean ± SD unless otherwise specified. One-way analysis of variance (ANOVA) followed by Tukey's multiple comparisons test was used to assess statistical significance, which was set at the 0.05 level.

3.1.2 Results & Discussions

Nanogel formation and physico-chemical characterization. NG synthesis was carried out through a droplet-based microfluidic approach, using a chip endowed with micro-actuation features. Two immiscible fluids were supplied to the device to generate a W/O microemulsion: the polymer solution constituted the aqueous dispersed phase, and mineral oil with a nonionic surfactant represented the organic continuous phase (*Figure 3.2b*). The formation of the microemulsion was obtained *via* hydrodynamic flow focusing, exploiting the flow rates, the shear force and the interfacial tension between the two phases, and the geometry of the microfluidic channels.[187]

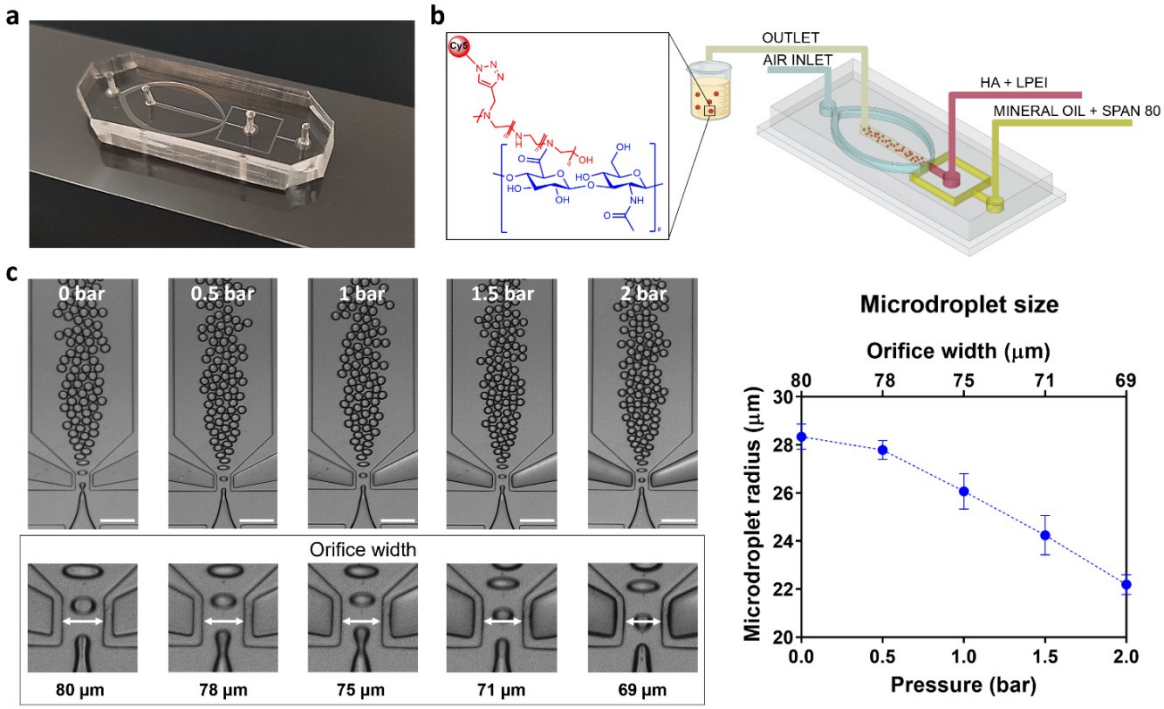

Figure 3.2 PDMS microfluidic device (a) and schematic representation of the droplet-based microfluidic approach for NGs production (b). Representative micrographs of the pressure-active control over microdroplet size distribution are collected at the optical microscope and the values of microdroplet radii vs pressure and orifice width are plotted in the graph (c). Measurements of the orifice width were performed on three different microfluidic devices, each of them set at the investigated pressure levels, in the range 0-2 bar.Scale bar: 200 µm

In particular, a flow ratio of 0.2 was set between the flow rates of the aqueous and the organic phases, in order to avoid jetting mode during the droplet generation. The resulting microdroplets were monodisperse and stable in the continuous phase, without coalescence phenomena. The design of a pneumatic actuator to pressurize the flow-focusing junction enabled the active tuning of the flow-focusing geometry (representative 3D volume reconstructions in *Figure S2*, Appendix II), thereby modulating the diameter of the formed

microdroplets (*Figure 3.2c*), which ranges from 57±0.4 μm at 0 bar to 44±0.3 μm at 2 bar, indicating a volume reduction of ca. 54% between the two conditions. The pivotal role of the valve actuation lays in the dynamic control of the orifice geometry, resulting in on-demand variation of the droplet size without changing the input flow rates of the two immiscible phases. Slow-motion videos of the droplet generation process were recorded to determine the stability, the accessible range of droplet diameters and the process reproducibility. Each microdroplet was conceived as a self-contained reaction chamber, where the crosslinking reaction between the HA-NHS ester derivatives and the LPEI amine groups occurred, forming the 3D nanoscaffold (see also *Figure S3*, Appendix II). The covalent bonding between the polymers is proportional to the volume concentration of the polymeric chains: considering a homogeneous distribution of the reagents in the disperse phase, a minor concentration of reactive polymers, which should be ascribed to the smaller microdroplets, will lead to the formation of smaller NGs. This can be linked to the limited reactive sites available in the droplet volume that will generate smaller nanoarchitectures, as discussed below. Furthermore, the use of a single microfluidic platform capable of tuning NG size minimizes the demand of devices to produce nanoscaffolds with different dimensions, and as a result, the consumption of reagents in chip fabrication is restricted.

Active droplet generation in microfluidics represents a milestone of different approaches reported in the literature:[184,188] for example, a valve-based flow-focusing junction was used to generate foams as templates for graded porous structures and 3D-printed constructs as bone models,[189] and cross-junctions and T-junctions were designed to generate droplets containing the precursors species by shear force or electro-pneumatic regulators to synthesize inorganic nanoparticles.[181,190,191] However, the use of pressure-actuated microfluidic platforms to produce polymer-based nanoscaffolds *via* microdroplet generation has not been comprehensively investigated yet;[192,193] indeed, these nanoparticles are usually fabricated by microfluidic nanoprecipitation and the procedure does not involve a chemical crosslinking reaction between different polymers in each individual droplet.[194–197] Furthermore, in this field, the design of nanogels is still unexplored. These considerations highlight the relevance of the present work, which may represent a significant breakthrough.

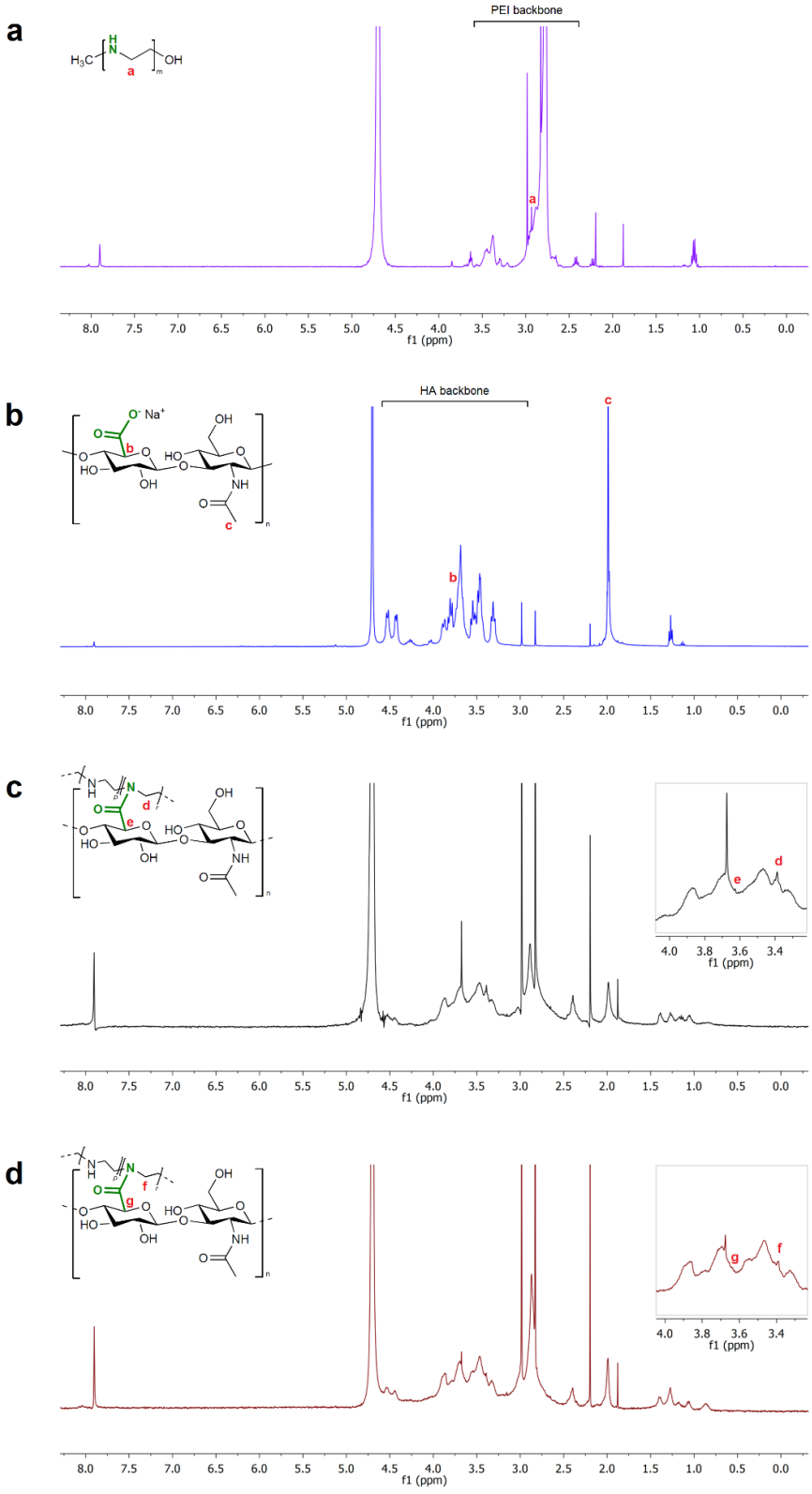

Figure 3.3 [1]H-NMR spectra of starting polymers and NG specimens: LPEI (a, violet; due to the different protonation degrees of amino groups in the polymer backbone, a is indicative of the methylene protons subsequently involved in the crosslinking reaction), HA (b, blue), NG_0 (c, black) and NG_2 (d, red). The characteristic signals of LPEI and HA and the relative shifts (e and d in NG_0; g and f in NG_2) after crosslinking reaction are highlighted.

The formation of NGs was confirmed by NMR and FT-IR analyses. ^{1}H-NMR spectra of both NG_0 and NG_2 showed the chemical shifts of polymer moieties related to the amide bonding between HA and LPEI. In detail, the signal ascribable to the methylene protons (N-*CH*$_2$-CH$_2$, *d* and *f* in *Figure 3.3*) of LPEI monomer shifted to 3.39 ppm (at 2.93 ppm in the spectrum of neat LPEI), whereas the methine group (*CH*-COOH, *e* and *g* in *Figure 3.3*) of the HA ring moiety involved in the reaction was recognizable at 3.62 ppm (shifting from 3.72 ppm in the spectrum of pristine HA). Moreover, in both specimens, the characteristic peak of HA backbone and methyl groups (range 4.60÷3.25 ppm and 2.00 ppm, respectively) and of LPEI backbone (range 3.06÷2.70 ppm) were clearly detectable.[132,133] An estimation of NG composition, in terms of molar ratio between the two polymers, could be carried out considering the integration of the peaks attributable to each polymer: as a result, NG_0 specimen was approximately characterized by a LPEI:HA 2.3:1 molar ratio, whereas NG_2 presented a LPEI:HA ratio of 1.8:1.

FT-IR spectra of both NG specimens (*Figure 3.4*) showed the characteristic signal of C=O stretching at 1724 cm^{-1}, indicative of the crosslinking between HA and LPEI *via* amide bond. Furthermore, both spectra presented the peculiar peaks ascribable to the starting polymers. In detail, HA signals were recognizable at 3281 cm^{-1} (–OH stretching), 1736 cm^{-1} (carbonyl stretching of the carboxylic group), 1606 cm^{-1} (Amide II, C=O stretching), 1400 cm^{-1} and 1367 cm^{-1} (C–H bending), 1295 cm^{-1} (stretching of the C–CH$_3$ amide), and 1040 cm^{-1} (skeletal vibration of the C–O stretching).[134,135] LPEI showed its signals at 3367 cm^{-1} (–OH stretching), 2879 cm^{-1} (stretching vibration of the aliphatic C–H), 1610 cm^{-1} (N–H bending) and in the wavenumbers range 1450÷900 cm^{-1} (C–H bending and C–N stretching vibrations).

NG specimens were also evaluated in terms of size and morphology through DLS, AFM, SEM and TEM analyses, in order to define a correlation between the active tuning of the flow focusing geometry and the physical features of the resulting nanoscaffolds. DLS measurements showed mean hydrodynamic diameters of 188.3 nm for NG_0 and 92.4 nm for NG_2, indicating a volume reduction of ca. 88% between the two specimens, and a monodispersity level (PDI_{NG_0} = 0.023; PDI_{NG_2} = 0.015) far higher than that of HA-LPEI NGs produced *via* conventional W/O emulsion-based batch synthesis (*Figure S4* and *Table S1*, Appendix II). Additionally, both specimens were characterized by a slightly negative z-potential value (NG_0: -2.2 mV; NG_2: -2.13 mV) and showed good dimensional stability in aqueous environment (*Figure S5,* Appendix II).

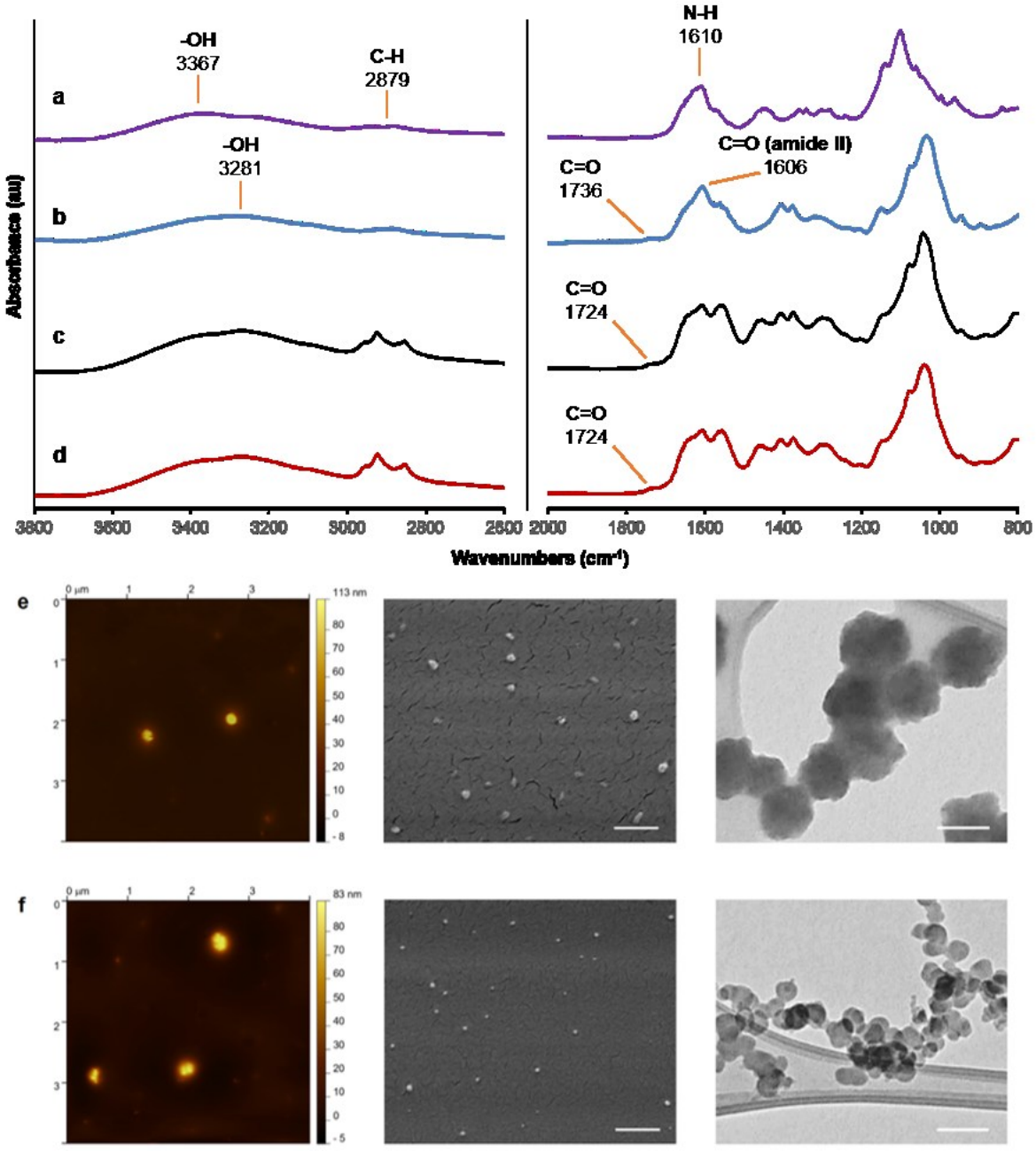

Figure 3.4 a-d) FT-IR spectra of LPEI (a, violet), HA (b, blue), NG_0 (c, black) and NG_2 (d, red). e-f) AFM, SEM (scale bar = 500 nm) and TEM (scale bar = 100 nm) micrographs of NG_0 (e) NG_2 (f).

AFM analysis, conducted in air on hydrated NGs, gave NG diameter values of ca. 130 nm and 73 nm for NG_0 and NG_2, respectively. The discrepancy between DLS and AFM measurements was attributable to the different sample processing: DLS analysis was performed on fully solvated NGs and the recorded dimensions corresponded to the NG hydrodynamic diameters, whereas the AFM samples did not consider the thickness of the water-adsorption layer.[198] Moreover, in the AFM conditions, the Marangoni effect could lead to the formation of colloidal nano-agglomerates due to the variation of the surface tension

gradient during the evaporation flow across the surface of the laid droplet.[144,145,199] In particular, the NG configuration as colloidal cluster was more noticeable in the AFM image of NG_2. Additionally, SEM analysis, performed on dehydrated specimens, gave diameters of *ca.* 92 nm for NG_0 and 57 nm for NG_2, indicating a dynamic behavior of the nanoscaffold during the forced transition from hydrated to dry state, under SEM vacuum. This confirmed the capability of the synthesized nanosystems to absorb and retain water, when dissolved in aqueous medium, which is typical of hydrogel matrices.[200,201] TEM analysis showed that NGs were rough surfaced with a quasi-spherical morphology, with nanoparticle size values comparable to those observed by SEM. Collectively, results from the physico-chemical characterization emphasize that the proposed microfluidic chip design allowed us to tune the morphological features of the resulting NGs via active modulation of the FFJ during microdroplet generation.

Drug release. DOX was chosen as a candidate drug to test the use of NGs as controlled drug delivery systems. DOX is an anthracycline and an effective anticancer drug, widely used in the chemotherapeutic treatment of various cancers, ranging from lung[153] and breast[154] to melanoma[155] and ovary.[157]

As measured by fluorescence spectroscopy, the two NG classes showed similar drug encapsulation efficiency levels (77.7% for NG_0 and 77.5% for NG_2). Conversely, they were characterized by different drug release profiles. As reported in *Figure 3.5*, in NG_0 specimens, the DOX release was almost completed after 2 days (*ca.* 98% of released drug), whereas NG_2 presented a more sustained release, up to 10 days. In particular, NG_2 exhibited a slightly higher initial DOX release than NG_0, whereas after 8 h the trends were switched. This variation pointed out that NG size and composition could affect the drug distribution between the inner core and the surface of the polymeric nanonetwork and, consequently, the drug diffusion regime, mainly driven by the DOX-polymer interactions.

An estimation of the drug diffusion regime could be performed by plotting the cumulative drug release against time to the power of 0.43 (i.e., $t^{1/2.3}$, exponent typically used to approximate the spherical geometry of the nanocarriers), where a linear relationship is indicative of a Fickian diffusion. No initial burst release was observed for both samples. Moreover, in NG_2, the good linearity of the data defined a double diffusion regime with different slopes, whereas in NG_0 a single linear trend was visible, confirming in both specimens that the drug release was mediated by Fickian regime. The main interactions

tuning the drug release are reliably attributable to the drug adsorption at the NG surface and the aliphatic-aromatic stacking occurring between DOX and HA.[158,159,202] The smaller dimensions of NG_2 reliably led to a higher amount of DOX adsorbed at the NG outer layer, which was firstly released (steeper slope of regime *i*, corresponding to DOX adsorption at the interface NGs/water), whereas the residual amount, entrapped in the nanomeshes, diffused out more slowly (regime *iii*): this could be ascribed to the aliphatic-aromatic stacking which provided a stacked arrangement of the DOX molecules within the NG architecture, characterized by a higher amount of HA compared to NG_0, and delayed the drug release.[203] On the other hand, NG_0 showed a single diffusion regime (*ii*) due to the larger size, which did not give a net transition between the two diffusion mechanisms: in this case, a higher DOX fraction was reliably encapsulated within NG meshes, and a lower amount of drug adsorbed at the NG surface was subjected to a quick diffusion process. Both specimens outperformed the controlled drug release by HA-LPEI NGs synthetized *via* conventional W/O batch emulsion (*Figure S6*, Appendix II).

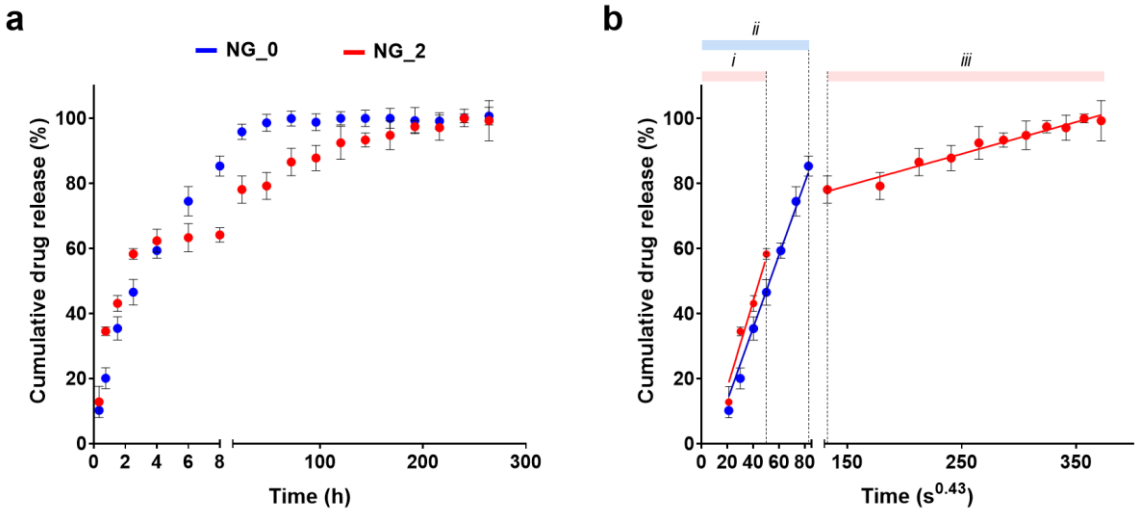

Figure 3.5 (a) Release profile of DOX delivered by NG_0 (blue) and NG_2 (red). (b) Drug release against time expressed as $t^{1/2.3}$. Good linearity of data is indicative of a Fickian diffusion process, with the slope representing the empirical kinetic constant for the DOX/NG system. Cumulative drug release is represented as a percentage of the total drug payload (mean value ± SD is plotted).

Cell viability and NG internalization. The cytocompatibility analysis and the cell uptake of NG_0 and NG_2 were performed using OVCA433, chosen as a representative cancer cell line. In this way, we tested our HA-LPEI NGs as candidate nanomaterials for the definition of a therapeutic approach for ovarian cancer, with the aim to demonstrate an improved effect than the conventional anticancer therapies. A suspension of pristine NGs (without drug

payload) was directly added to the cell medium and the cell viability, measured by G6PD assay on culture supernatants, was close to 97.5% after 24 h for both NGs, indicating good biocompatibility of the nanomaterials. In detail, *Figure 3.6a* reports the high normalized viability levels of NG-treated cells showing no significant differences between the conditions. Once proven that NGs were permissive for cell survival, the internalization process of NG_0 and NG_2 was assessed by flow cytometric analysis of OVCA433 at different time points (30 min, 1 h, 2 h), after the administration of the nanomaterial at the concentration of 20 μg/mL. The increase of the median fluorescence intensity (MFI) level over time confirmed the progressive NG uptake by cells. In particular, as reported in *Figure 3.6b*, after just 30 min exposure to NGs, the distribution of cell fluorescence shifted to higher values (3.7-fold change in MFI for NG_0 and 3.5-fold change for NG_2) as a consequence of nanocarrier uptake.[204] At 1 h and 2 h, further increases in MFI measurements were observed, up to *ca.* 13- and 17-fold change for NG_0 and NG_2 specimens after 2h, respectively.

A further validation of the internalization process was provided by fluorescence microscopy, where the collected representative images (*Figure 3.6d* and *3.6e*) showed the NG distribution in the cytosol, with a progressive perinuclear localization. Overall, these results demonstrated the efficient NG uptake and indicated the potential of these nanocarriers as controlled drug delivery systems in the treatment of ovarian carcinoma. For these reasons, we evaluated the *in vitro* therapeutic effects of DOX delivered by both formulated NGs: in order to select an ideal sublethal drug concentration, we first estimated a preliminary dose-response curve at 24 h on OVCA433 cultured in adhesion using the MTT assay (*Figure 3.6c*) and the value of 0.8 μM was identified as the IC_{25} level (*i.e.*, the concentration at which the drug produces a 25% viability reduction). This level was chosen to set the drug payload for DOX/NG_0 and DOX/NG_2, and the NG-associated treatments were compared to the administration of the same DOX concentration in a non-encapsulated form. *Figure 3.6f* shows the evaluation of the OVCA433 metabolic activity through MTT assay, up to 7 days: it was clearly detectable that the NG-mediated delivery of DOX enhanced the therapeutic effect of the drug. In detail, after 24 h, both DOX/NG_0 and DOX/NG_2 effectively reduced cell viability ($p<0.001$ and $p<0.0001$ *vs.* CTRL for DOX/NG_0 and DOX/NG_2, respectively), outperforming the non-encapsulated drug ($p<0.001$ *vs.* DOX).

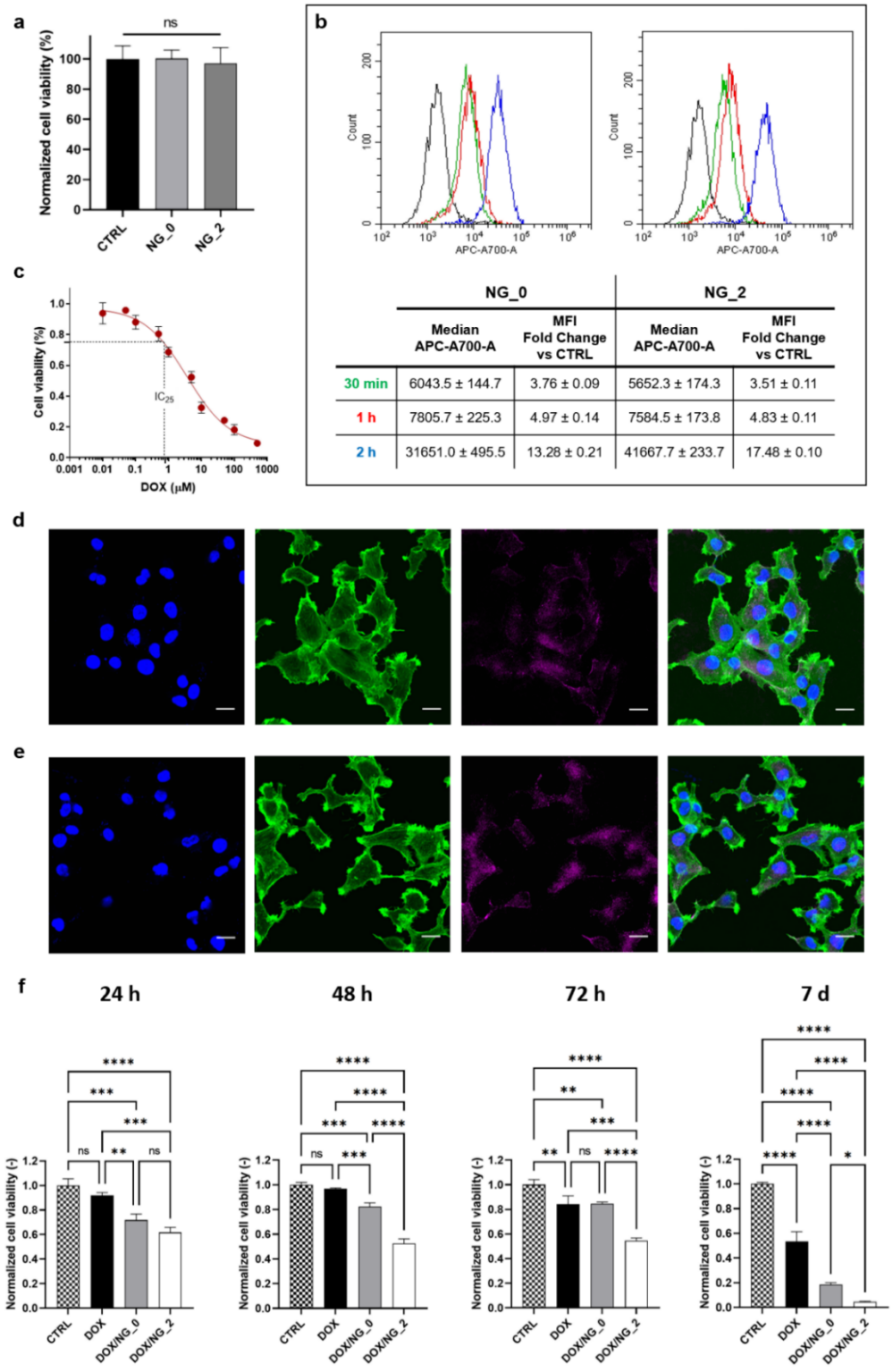

	NG_0		NG_2	
	Median APC-A700-A	MFI Fold Change vs CTRL	Median APC-A700-A	MFI Fold Change vs CTRL
30 min	6043.5 ± 144.7	3.76 ± 0.09	5652.3 ± 174.3	3.51 ± 0.11
1 h	7805.7 ± 225.3	4.97 ± 0.14	7584.5 ± 173.8	4.83 ± 0.11
2 h	31651.0 ± 495.5	13.28 ± 0.21	41667.7 ± 233.7	17.48 ± 0.10

Figure 3.6 (a) Cytocompatibility of pristine NG_0 and NG_2 by G6PD assay. Viability levels have been normalized to CTRL group and expressed as mean ± SD. (b) Flow cytometric analysis of NG internalization by OVCA433 cells after 30 min (green), 1 h (red) and 2 h (blue); plot reports the shift of the allophycocyanin (APC-A700-A) signal for each time point in the target gate (median fluorescence intensity values are specified in the table, and fold change is calculated vs. control cells). (c) Dose–response curve of DOX using the MTT assay. The solid line represents the fitted curve according to four-parameter logistic curve, defining an IC_{25} of 0.8 μM. (d, e) Representative confocal micrographs of NG_0 (d, in purple,

*false color) and NG_2 (e, in purple, false color) internalization in OVCA433 after 30 min. Actin cytoskeleton was stained with FITC-labeled phalloidin (in green) and nuclei were counterstained with DAPI (in blue). Scale bar = 20 μm. (f) DOX-induced cytotoxicity in OVCA433 at 24 h, 48 h, 72 h and 7 days, after the administration of free-drug (DOX) and drug-loaded NGs (DOX/NG_0 and DOX/NG_2). All groups refer to a 30 min incubation with the indicated treatment. The therapeutic effect is expressed in terms of cell viability levels normalized against their internal controls, measured through the MTT assay. Results are the mean ± SD of three independent experiments. Statistical analysis was performed using one-way ANOVA. * $p < 0.05$, ** $p < 0.01$, *** $p < 0.001$, **** $p < 0.0001$, ns = not significant.*

Moreover, the DOX release mediated by NG_2 ensured a sustained and prolonged effect on cell metabolism over time, with 5% residual viability at 1 week ($p<0.0001$ *vs.* CTRL). A promising trend could also be observed in the case of DOX/NG_0, where cell viability reduced to 18% after 1 week ($p<0.0001$ *vs.* CTRL). Both nanoformulations confirmed a significant cytotoxic effect *vs*. the free drug administration at the same time point ($p<0.0001$ *vs.* DOX for both DOX/NG_0 and DOX/NG_2). The different results in NG treatments could be ascribed to the diverse drug release profiles in NG_0 and NG_2: indeed, considering that both specimens presented a similar percentage of cell internalization, NG_2 bar were characterized by a prolonged DOX release mediated by the aliphatic-aromatic stacking, which led to a more sustained intracellular drug delivery over time, improving the DOX cytotoxic effects.

Overall, the obtained results confirmed that the effect of NG-conveyed DOX was significantly higher than that of non-encapsulated drug in terms of lowering and mitigating the metabolic activity, thus demonstrating a clear advantage of NGs as carriers of the chemotherapeutic agent. Moreover, these *in vitro* therapeutic effects outperform the results achievable with the administration of drug-loaded NGs by batch synthesis (*Figure S7*, Appendix II). The active tuning of the flow focusing geometry in our microfluidic platform ensured the modulation and control of the NG synthesis beyond the morphological and physical features, also affecting the drug release performances according to the defined microfluidic set-up.

3.2 Optimization of the Droplet-based Microfluidic Synthesis of Nanogels for Drug Delivery through a Design of Experiment approach

Since microfluidics offers tight control over a variety of parameters (both compositional and fluid-dynamic) that can influence the synthesis outcome, it is desirable to conduct a multi-parametric optimization to identify the most suitable process conditions. In this framework, Design of Experiment (DoE) approach is a straightforward method for streamlining nanomaterials design procedures revealing the influence that independent input variables (or predictors) can exert on dependent output variables (or responses) [205]. In particular, Response Surface Method (RSM) is used to develop appropriate functional relationships between variables, which are usually approximated with low-degree polynomial model. Furthermore, RSM can also highlight higher order effects, which are usually neglected in simple linear approximation [206]. Literature reports some early optimization approaches applied to the microfluidic synthesis of nanomaterials. Terada *et al.* [207] applied a DoE approach to the synthesis of lipid nanoparticles containing cationic lipid for the delivery of siRNA, evaluating the influence of process parameters on their physicochemical properties and loading capacity. Similarly, Whiteley *et al.* [208] investigated the synthesis and drug loading of chitosan-based NGs produced in a single-phase flow system through DoE and RSM. However, none of these studies addressed the use of droplet-based microfluidics to synthesize nanocarriers. In addition, the focus was limited to the synthesis process, while the bioperformance aspects were not investigated.

In this work, we used a DoE approach integrated with RSM to investigate the production of NGs in the hyaluronic acid – linear polyethyleneimine (HA-LPEI) system through a droplet-based microfluidic device. In particular, we set a two-factor three-level design to investigate the influence of FRR and LPEI/HA molar ratio (MR) on several physicochemical (size, PDI, composition, and drug release) and biological (cytocompatibility, cellular uptake, and performance as a DDS) properties, with the final aim to develop an empirical model for process optimization purposes.

3.2.1 Materials & Methods

Materials. Hyaluronic acid sodium salt (HA, ultra-low molecular weight, MW = 8–15 kDa, Biosynth Carbosynth, Compton, UK) and linear polyethyleneimine (LPEI, MW = 2.5 kDa, Polysciences, Warrington, PA) were used as the starting polymers for NG formulation. SU-8 photoresist (MicroChem, Newton, MA) and polydimethylsiloxane (PDMS, Sylgard 184,

Dow Corning, Midland, MI) were used for chip microfabrication. All other chemicals were purchased from Merck KGaA (Darmstadt, Germany) and used as received, without any further purification. Solvents were of analytical-grade purity.

Chip design and microfabrication. The microfluidic device was fabricated using standard photo- and soft-lithography techniques. SU-8 2075 photoresist was spin-coated with a thickness of 60 μm on a 3" silicon wafer and patterned by UV exposure through a chrome-on-glass photomask. The obtained master was silanized overnight in a chamber saturated with trimethylchlorosilane (TMCS) vapor to ease demolding.

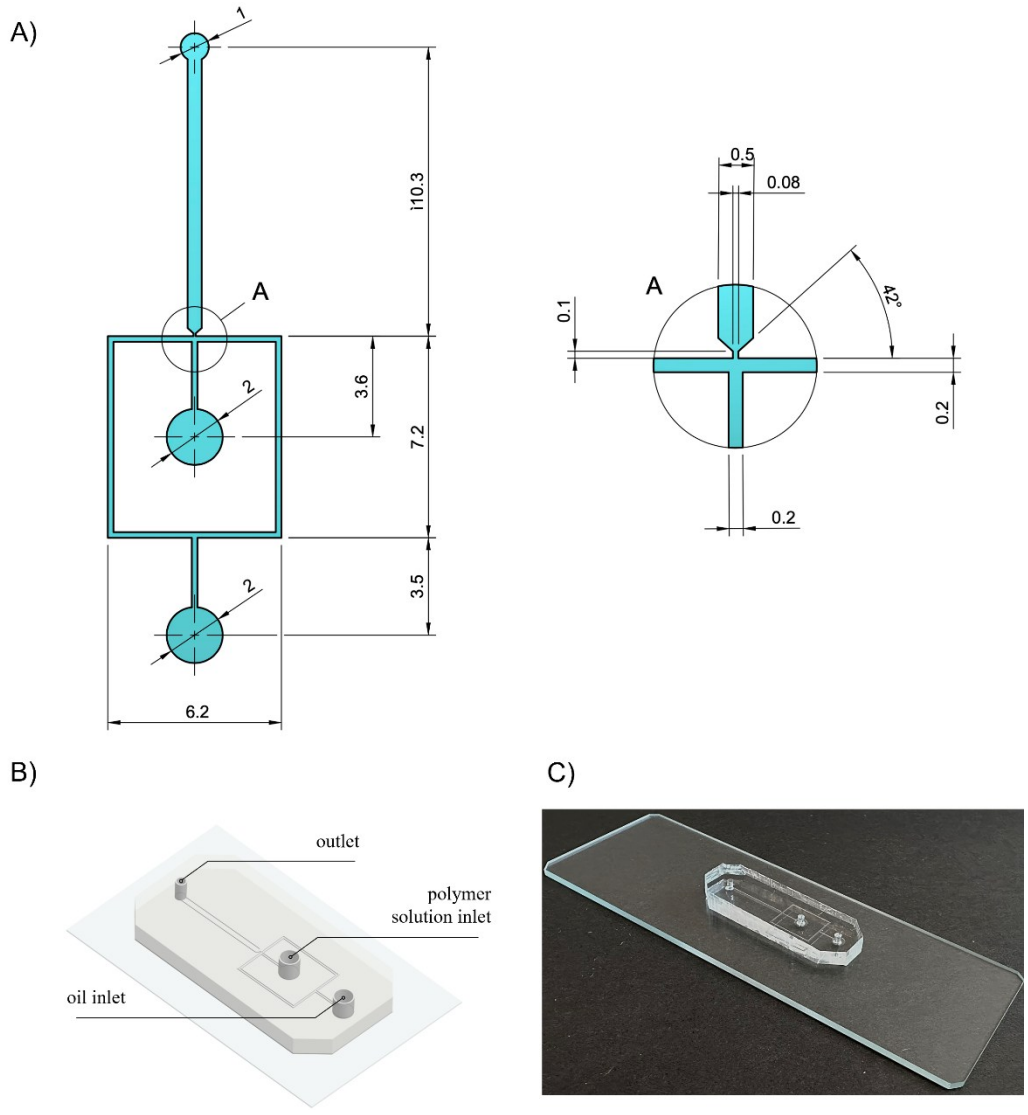

Figure 3.7 (A) Sketch of the fluidic unit of the device, with a high magnification inset of the flow focusing junction (quotes are in mm); (B-C) Rendered image (B) and optical macrograph (C) of the microfluidic device.

PDMS solution (10:1 w/w prepolymer to curing agent ratio) was poured onto the silicon master, cured in an oven at 70 °C for 2h, peeled off and used to assemble the device.

Microfluidic inlets and outlets were created using a biopsy puncher. Afterward, the chip was assembled by coupling the PDMS replica to a glass microscope slide via oxygen plasma bonding (Femto Plasma Etcher, Diener electronic, Ebhausen, Germany).

Finally, hydrophobic modification of the channels surface was achieved by flowing a stream of TMCS-saturated nitrogen for 15 min followed by thermal treatment at 140 °C for 10 min.

The chip design consists of a standard Hydrodynamic Flow Focusing (HFF) configuration used as droplet-generator, as reported in *Figure 3.7*. The inlet and outlet channels were 200 and 500 μm wide, respectively, while the junction orifice had a width of 80 μm and a length of 100 μm.

Polymer functionalization

LPEI functionalization with RhB (LPEI-RhB). The LPEI functionalization with the chromophore RhB was performed using a two-step procedure, as reported in our previous works [209,210]. Initially, the polymer was modified by adding alkyne moieties: LPEI (250 mg, 0.1 mmol) was dissolved in 7 mL of methanol and propargyl bromide 80% w/w in toluene (108 μL, 1 mmol) was added dropwise at 0 °C. The resulting solution was stirred for 24 h at RT in the dark. The solvent was evaporated under vacuum, and the product was re-dissolved in DIW. The final mixture was dialyzed against DIW for 2 days (membrane MWCO: 100–500 Da) with daily exchange of water. The sample was then freeze-dried and collected as a solid.

In the second step, the alkyne-modified LPEI was reacted with Rhodamine B azide (RhB-N_3) through Copper(I)-catalyzed Azide-Alkyne Cycloaddition (CuAAC). Derivatization of RhB-N_3 is detailed in Supplementary Information.

Propargyl LPEI (120 mg, 0.048 mmol) and RhB-N_3 (15.6 mg, 0.029 mmol) were dissolved in 10 mL of DIW. The catalyst cupric sulfate (0.029 mmol) and the reducing agent sodium ascorbate (0.029 mmol) were added to the mixture, which was left under magnetic stirring for 24 h at 50 °C. After 2 days of dialysis against DIW (membrane MWCO: 100-500 Da), the product (LPEI-RhB) was lyophilized and stored as purple powder at -20 °C.

HA activation. HA carboxyl groups were activated through EDC/NHS coupling reaction to enable the crosslinking between the amino groups of LPEI and the polysaccharide chains. In detail, HA (6.75 mg, 0.016 mmol) was dissolved in 1.5 mL of DIW and coupling agents, EDC (15.3 mg, 0.08 mmol) and *N*-hydroxysuccinimide (NHS, 3.76 mg, 0.032 mmol), were

added at a final molar ratio of -COOH : EDC : NHS = 1 : 5 : 2. The mixture was stirred for 3 h at RT and used for the microfluidic synthesis.

NGs microfluidic synthesis. To generate droplets through the HFF microfluidic setup, two immiscible phases are required. A solution of mineral oil with 3 wt% Span 80 was injected as the continuous phase, while the aqueous polymer solution was injected as the dispersed phase (*Figure 3.7b*).

Different MR values (3, 6, and 9) were considered for this study. In detail, a 1.5 mL solution containing 6.75 mg of activated HA was mixed (1 min vortexing) with 1.5 mL of a previously prepared solution of LPEI-RhB and pristine LPEI (1:1 by weight, adjusted to pH 4.5 with 1M HCl to ease solubility of pristine LPEI) at various concentrations containing 13.5, 8, and 4 mg of polycation, respectively.

The final aq. polymer solution and the oil phase were loaded into a 2.5 mL and a 10 mL gas-tight glass syringe (Hamilton Company, Reno, NV), respectively. The syringes were connected to the HFF device through Teflon tubing and actuated by programmable syringe pumps (Nemesys, CETONI GmbH, Korbussen, Germany).

Table 3.1 Complete nomenclature referring to the specific synthesis conditions used for each formulation in terms of flow rate ratio (FRR) between the dispersed and the continuous phase and the initial LPEI/HA molar ratio (MR).

			Factor 2: Q_d/Q_c flow rate ratio (FRR)		
two-factor three-level design			0.1	0.2	0.4
			Coded units		
			-1	*-0.33*	*+1*
Factor 1: LPEI/HA molar ratio (MR)	3	*Coded units* *-1*	$NG_{-1,-1}$	$NG_{-1,-0.33}$	$NG_{-1,+1}$
	6	*0*	$NG_{0,-1}$	$NG_{0,-0.33}$	$NG_{0,+1}$
	9	*+1*	$NG_{+1,-1}$	$NG_{+1,-0.33}$	$NG_{+1,+1}$

Three different FRR levels (namely 0.1, 0.2, and 0.4) were imposed by varying the dispersed phase flow rate (QD) between 1 and 4 μL/min, while keeping the continuous phase flow rate (QC) constant at 10 μL/min.

Hence, MR and FRR defined a two-factor three-level study (FRR = 0.1, 0.2, 0.4; MR = 3, 6, 9). The resulting experimental design is reported in *Table 3.1.*

Droplet formation was monitored over time under a Nikon Eclipse Ti-E fluorescence microscope (4x objective) equipped with a high-sensitivity camera (Neo 5.5, Andor Technology, Belfast, UK). A time-lapse acquisition (1 frame every 10 minutes) was performed during the experiment to ensure the reproducibility and good functioning of the device throughout the process.

The emulsion collected at the outlet of the microfluidic system was broken after 8 h of mild agitation on a tilting plate and the aqueous phase was extracted in a separating funnel by washing with diethyl ether (3 x 10 mL). The NG suspension was dialyzed against DIW (membrane MWCO: 15 kDa) for two days with daily exchange of water. Finally, the samples were lyophilized and stored at -20 °C until use.

Nuclear Magnetic Resonance (NMR). Chemical composition of pristine polymers, intermediates, and final NGs was analyzed by ^{1}H NMR. Analyses were carried out with a Bruker AC spectrometer (400 MHz, Bruker Corp., Billerica, MA) and deuterium oxide (D_2O) as solvent. Chemical shifts were reported as δ values (ppm) relative to the tetramethylsilane internal peak reference.

Dynamic Light Scattering (DLS). NG suspensions in ultrapure water (1 mg/mL) were analyzed through DLS (Zetasizer Nano ZS, Malvern Panalytical, Malvern, UK) to determine the size and polydispersity index (PDI). Before each measurement, specimens were sonicated 10 min to ensure minimal aggregation of the colloidal system. Readings were performed in triplicate.

Drug release. *In vitro* release experiments were performed using doxorubicin (DOX) as a model drug. DOX-loaded nanogels (DOX_NGs) were prepared by dissolving lyophilized samples (1 mg) in 10 μL of 5 mM DOX. The system was centrifuged and left at RT for 30 min to complete drug loading and then diluted to the final NG concentration of 100 μg/mL. 300 μL of the resulting suspension were loaded inside a microdialysis device (membrane

MWCO: 3.5 kDa) and placed into a 96 deep-well plate (Thermo Fisher Scientific) allowing DOX_NGs to exchange against PBS (1.4 mL).

Drug release profile was investigated at 37 °C under gentle shaking (tilting plate at 100 rpm). DOX release was measured fluorometrically at different time points. At each time point, dialysis buffer was replaced with fresh PBS and sequential release was analyzed spectrofluorometrically (λ_{ex} = 488 nm, λ_{em} = 590 nm, Infinite M200 Pro multiplate reader, TECAN, Männedorf, Switzerland) against an experimental standard curve for DOX (Appendix III, *Fig.S1*).

Cell model. The human epithelial ovarian cancer cell line OVCA433 was obtained from the American Type Culture Collection (ATCC, Manassas, VA). OVCA433 cells were cultured in Dulbecco's modified Eagle's medium (DMEM low glucose, GIBCO, Thermo Fisher Scientific), supplemented with 10% fetal bovine serum, 100 U/mL penicillin/streptomycin and 1 mM l-glutamine. Cells were incubated at 37 °C in a humidified atmosphere with 5% CO_2.

Nanogel cytocompatibility. The assessment of NGs' cytocompatibility was conducted on OVCA433 cells employing the Vybrant Cytotoxicity Assay (Thermo Fisher Scientific) [211] and the MTT assay, as previously detailed in Section 3.1. The cells were seeded at a density of 2 x 10^3 cells/well into a 96-well plate for a 24-hour period, followed by incubation with NGs at a concentration of 20 μg/mL. Experiments were performed in triplicate.

Flow cytometric analysis of NG internalization. Cells were seeded at a density of 2.4 × 10^4 cells/well into a 12-well plate for 24 h. Then, cells were incubated with a NG suspension at 20 μg/mL for further 24 h. Cells were then analyzed by flow cytometry (CytoFLEX flow cytometer, Beckman Coulter, Brea, CA). Live cells were gated based on their forward and side scatter parameters; NG signal was recorded in the phycoerythrin (PE-A) channel and quantified as the median intensity value. Experiments were performed in triplicate.

Confocal and super-resolution microscopy. NG internalization was also assessed using confocal and super-resolution microscopy. Cells were seeded at a density of 1.5 × 10^4 cells/well into 8-well glass bottom μ-Slide chambers (Ibidi GmbH, Gräfelfing, Germany) and grown for 24 h before the experiment. Cells were incubated with NGs at a concentration of 20 μg/mL for 24 h, then fixed with 4% buffered paraformaldehyde (PFA) for 15 min at RT and washed with PBS (3 times). For confocal microscopy, cell membranes were stained with CellMask™ Green Plasma Membrane Stain (Thermo Fisher Scientific; 1:1000 dilution

in PBS for 5 min) and nuclei were counterstained with DAPI (Thermo Fisher Scientific; 1:1000 dilution in PBS for 10 min). Specimens were observed under a Nikon A1R+ laser scanning confocal microscope (Nikon Instruments, Tokyo, Japan) with a 20× NA0.7 dry objective. For super-resolution optical microscopy, cells were stained with labelled phalloidin (ActinGreen 488 stain, GeneCopoeia, Rockville, MD; 1:50 in PBS for 45 min), nuclei were counterstained with DAPI, and specimens were viewed under a ZEISS ELYRA 7 microscope (ZEISS Microscopy, Jena, Germany) with a 63× NA1.4 oil immersion objective, using the Lattice SIM^2 post-processing algorithm.

Drug delivery to cancer cells. DOX_NG systems were prepared as described in section 2.2.1 to reach a final DOX concentration of 1 μM, while maintaining the NG concentration at 20 μg/mL. The DOX concentration was selected as a sublethal drug dosage based on a dose-response curve evaluated at 24 hours on the OVCA433 cell line (Appendix III, *Fig.S2*). The DOX_NG suspension was administered to OVCA433 cells seeded at the density of 2 x 10^3 cells/well into a 96-well plate. NGs without DOX and 1 μM free DOX administration were used as internal controls, together with untreated cells (negative control). The effect of DOX-loaded NGs was quantified after 24h via MTT assay, following the protocol reported in section 2.2.1.

To discern the effect of DOX from that of intrinsic NG toxicity on the overall residual cell viability, a Nanoencapsulation Enhancement (NE) parameter was defined as follows:

$$NE\ (\%) = \frac{1}{Abs_{untreated}} \left(\frac{Abs_{NG} - Abs_{DOX\_NG}}{Abs_{untreated} - Abs_{freeDOX}} \right) \times 100 \qquad (22)$$

where Abs_{DOX_NG} is the measured absorbance for cells treated with the DOX_NGs, Abs_{NG} is the absorbance for the corresponding pristine (unloaded) NG group. $Abs_{untr.}$ and $Abs_{freeDOX}$ are the absorbance levels of untreated cells and cells treated with free DOX, respectively.

Empirical model. To build an empirical model, an RSM method, previously applied to different problems [212–216], was adopted. The entire statistical analysis was performed using the programming language R [217] following the statistical strategy described in previous works [212,218–220]. An initial analysis was performed by calculating a correlation matrix in which the value of the Pearson's coefficient (r) was reported, to verify the presence of linear correlations. Then, a model was built by selecting the significantly relevant factors, tested by analysis of variance (ANOVA). The significant level was assigned as follows: p≤0.1 (.),

p≤0.05 (*), p≤0.01 (**), p≤0.001 (***). The complete model is reported in Eq. (23), (with A and B representing MR and FRR, respectively). It should be noticed that not all the terms must be present in the models. In fact, only terms with $p \leq 0.1$ were included while the model was considered significant with a $p \leq 0.05$. The model function (indicated in the equation as F) was chosen to achieve two scopes, the first to normalize the model residues and the second to make the model residues patternless. To evaluate the goodness of fit of the model the coefficient of determination (R^2) was calculated. Models with a perfect fitting have an $R^2 = 1$. To test the predictive value of the model, the predicted residual error sum of squares (PRESS) statistic was applied. The resulting predicted R^2 (R^2_{pred}) represents a good estimator of the out-of-sample performance of the model.

In our case, we also chose to restrict the space of acceptable solutions to those NG formulations characterized by high cytocompatibility. Therefore, we defined a desirability index with binary (0,1) values associated to the cytocompatibility of NGs, which was set to a threshold level of 95% (equation 24).

$$F(Y) = c_0 + c_2 \cdot A + c_1 \cdot B + c_3 \cdot AB + c_4 \cdot A^2 + c_5 \cdot B^2 + c_6 \cdot A^2B + \quad (23)$$

$$c_7 \cdot AB^2 c_9 \cdot A^3 + c_{10} \cdot B^3 + c_{11} \cdot A^2B^2 + c_{12} \cdot A^3B + c_{11} \cdot AB^3 +$$

$$c_{14} \cdot A^4 + c_{15} \cdot B^4 + c_{16} \cdot A^3B^2 + c_{17} \cdot A^2B^3 + c_{18} \cdot A^3B^3$$

$$D(Y) = \begin{cases} 0 & if\ cytocompatibility < l \\ 1 & if\ l < cytocompatibility < 1 \end{cases}; \quad l = 0.90 \quad (24)$$

Statistical analysis. The experimental data were analyzed using Prism ver. 10.2.1 (GraphPad Software, San Diego, CA) and reported as mean ± SD, if not otherwise specified. One-way or two-way analysis of variance (ANOVA) were used as appropriate to assess significance, which was set to the 0.05 level.

3.2.2 Results & Discussions

Results

NG synthesis and characterization. In the present work, a microfluidic synthesis of HA-LPEI NGs based on a HFF droplet-generator device was investigated. *Figure 3.8A* and *3.8B* illustrate the functioning of the HFF microfluidic device as droplet generator when using different FRRs.

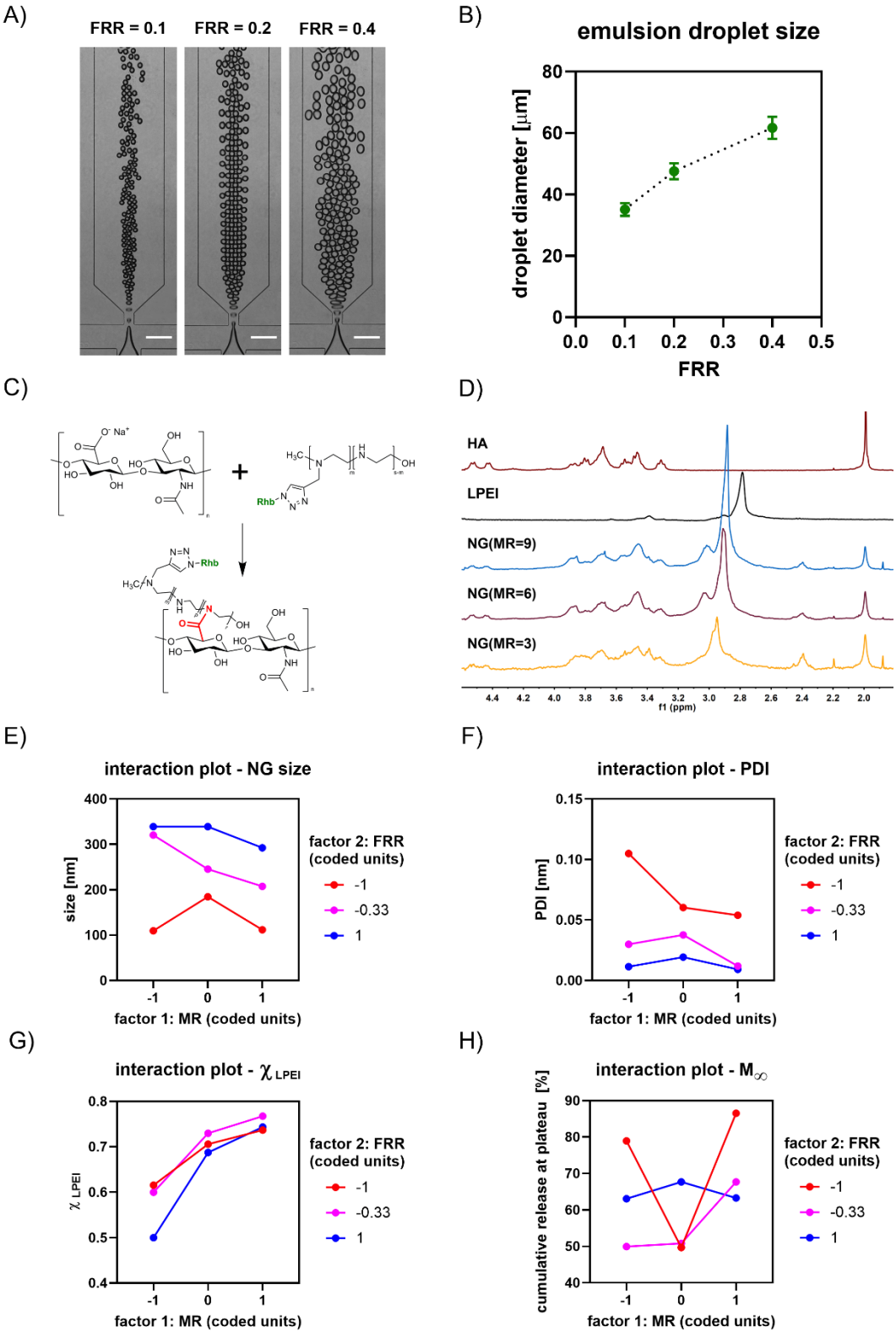

Figure 3.8 A) micrographs showing the functioning of the HFF device at different FRR. Scale bar: 200 μm; B) plot of the averaged droplet diameter (N = 15) as a function of the used FRR; C) schematic of the chemical reaction between HA and LPEI; D) representative ^{1}H-NMR spectra of: sodium hyaluronate (HA); Linear polyethyleneimine (LPEI); and NGs. Reported spectra were chosen as representative of the three different MR levels: MR = 9 ($NG_{+1,-0.33}$), MR = 6 ($NG_{0,+1}$), MR = 3 ($NG_{-1,-0.33}$); E,F,G, H) interaction plots for NG size, PDI, χ_{LPEI},and release plateu, respectively.

The formation of NGs by chemical crosslinking between HA-NHS ester derivates and amine groups in the LPEI backbone (reaction scheme in *Figure 3.8C*) was confirmed by ^{1}H-NMR conducted on each NG formulation and on the starting polymers. A representative spectrum for each of the three MR levels is reported in *Figure 3.8D,* while the spectra of all NG formulations are reported in Appendix III, *Figure S3*. In addition, the resulting LPEI molar fraction (χ_{LPEI}) for each NG formulation was estimated by integrating the NMR signals attributable to the starting HA and LPEI. Results are showed in *Table 3.2*.

Characterization of NG size distribution was performed by DLS analysis (*Table 3.2*). Two-way ANOVA was performed on DLS data to evaluate the effect of the two main variables (MR and FRR) on the resulting morphological parameters. *Figure 3.8E* and *Figure 3.8F* show the interaction plot for NG size and PDI. The effect of FRR was much larger ($F(2,18) = 97.5$, $p < 0.0001$, $\eta^2 = 76.6\%$) than that of MR ($F(2,18) = 9.82$, $p = 0.0013$, $\eta^2 = 7.71\%$). A significant interaction ($F(4,18) = 5.52$, $p = 0.0044$, $\eta^2 = 8.67\%$) was also reported. PDI showed a similar trend, with a significant interaction ($F(4,16)=3.74$, $p = 0.0248$, $\eta^2 = 12.2\%$), and a much larger effect size for FRR ($F(2,16) = 40.8$, $p < 0.0001$, $\eta^2 = 66.5\%$) than for MR ($F(2,16) = 5.16$, $p = 0.0186$, $\eta^2 = 8.4\%$).

Table 3.2 Summary of the results obtained from the physical and chemical characterization of the NGs.

Sample	χ_{LPEI} [-]	Diameter [nm]	PDI [-]
$NG_{-1,-1}$	0.62	109.6 ± 10.5	0.105
$NG_{-1,-0.33}$	0.60	357.8 ± 12.0	0.030
$NG_{-1,+1}$	0.50	339.3 ± 33.3	0.010
$NG_{0,-1}$	0.71	184.5 ± 17.5	0.060
$NG_{0,-0.33}$	0.73	246.4 ± 21.9	0.038
$NG_{0,+1}$	0.69	339.2 ± 32.7	0.019
$NG_{+1,-1}$	0.74	111.7 ± 8.8	0.054
$NG_{+1,-0.33}$	0.77	190.3 ± 12.3	0.012
$NG_{+1,+1}$	0.74	292.5 ± 3.5	0.010

NG composition (in terms of χ_{LPEI}) was also investigated by two-way ANOVA without replications (interaction plot in *Figure 3.8G*). Results showed a large and significant positive main effect of MR on NG composition ($F(2,4)=24.4$, $p = 0.0057$, $\eta^2 = 84.8\%$), while the effect of FRR was not significant ($p = 0.2092$).

Overall, these results demonstrated the ability to exert fine control over the final NGs composition and size in a wide range of molar ratios and diameters using droplet-based microfluidics.

3.2 Drug release

The selection of the appropriate method to evaluate the drug release profile from engineered nanomaterials is a source of debate in the scientific community.[221–224] Despite the reliability of the data obtained by the dialysis method has been questioned in the past, it is by far the most used methodology in the field.[221] In conventional dialysis experiments, two stages may influence the apparent release kinetics from the nanomaterial: (1) the release of the cargo from the nanomaterials into the surrounding solution inside the dialysis bag; and (2) the permeation of the cargo through the dialysis membrane. In most cases, this second step is considered negligible, allowing the actual release kinetics to be revealed by measuring the concentration of the cargo in the receiver compartment.

However, in the present case, the permeation of free DOX through the membrane cannot be neglected, as shown in Appendix III, *Fig. S4A*. This behavior can be attributed to the well-documented interaction between DOX and the dialysis membrane, which has been previously reported in the literature[224–228] and which can lead to an underestimation of the release constant from NGs. For this reason, we chose to consider the amount of drug released at infinite time (M_∞) as the parameter characterizing the release of drug from NG-DOX systems (*Table 3.3*).

Table 3.3 Cumulative release amount at plateau (M_∞) for the NG groups.

Sample	M_∞ (%)
$NG_{-1,-1}$	78.9 ± 2.3
$NG_{-1,-0.33}$	49.9 ± 3.0
$NG_{-1,+1}$	63.1 ± 1.0
$NG_{0,-1}$	49.7 ± 2.3
$NG_{0,-0.33}$	50.8 ± 1.2
$NG_{0,+1}$	67.7 ± 4.0
$NG_{+1,-1}$	87.8 ± 6.7
$NG_{+1,-0.33}$	67.7 ± 3.8
$NG_{+1,+1}$	63.3 ± 3.1

M_∞ levels were also analyzed by two-way ANOVA (interaction plot in *Figure 3.2H*). Results showed a large interaction ($F(4,17) = 12.0$, $p < 0.0001$, $\eta^2 = 37.4\%$), meaning that the effects of each variable depended on the specific level of the other variable, hampering the interpretation of main effects.

3.3 Biocompatibility and cellular internalization

The NG formulations were investigated in terms of cytocompatibility and cellular internalization to preliminary validate them as an effective DDS for the treatment of the ovarian carcinoma. In this scenario, the OVCA433 cell line was selected as a biological model of interest, based on previous publications.[209,210]

First, the cytocompatibility of the NGs was investigated through G6PD and MTT assays after 24h of cell exposure to NGs at a concentration of 20 μg/mL. Notably, none of the NG formulations gave a statistically significant decrease in cell viability when measured with the G6PD assay (Appendix III, *Fig. S5*), which detects the release of glucose 6-phosphate dehydrogenase from damaged/dying cells. However, the determination of cellular metabolic activity through MTT assay revealed a different scenario for NG cytocompatibility, as reported in *Table 3.4*.

Table 3.4. NG cytocompatibility as measured by MTT assay and normalized vs. untreated cells.

Sample	NG cytocompatibility (%) (MTT assay)
$NG_{-1,-1}$	109.3 ± 18.9
$NG_{-1,-0.33}$	99.6 ± 11.1
$NG_{-1,+1}$	102.2 ± 10.2
$NG_{0,-1}$	89.3 ± 16.0
$NG_{0,-0.33}$	105.2 ± 10.6
$NG_{0,+1}$	94.2 ± 4.9
$NG_{+1,-1}$	66.8 ± 11.4
$NG_{+1,-0.33}$	60.5 ± 4.5
$NG_{+1,+1}$	61.8 ± 4.8

Results of two-way ANOVA (interaction plot in *Fig. 3.9A*) showed that MR was the only factor with a strong and extremely significant negative main effect ($F(2,18) = 169$, $p < 0.0001$, $\eta^2 = 72.3\%$) on NG cytocompatibility, despite a significant interaction ($F(6,18) = 4.37$, $p = 0.0068$, $\eta^2 = 5.60\%$).

Table 3.5. Raw and corrected fluorescence levels for each NG group. Corrective factors accounting for the different composition of each NG class were derived from NMR. MFI values were normalized to those of untreated cells.

Sample	Raw fluorescence (MFI)	Normalized corrective factor	Corrected fluorescence (MFI)
$NG_{-1,-1}$	2.29 ± 0.12	1.6	3.61 ± 0.19
$NG_{-1,-0.33}$	3.17 ± 0.07	1.7	5.46 ± 0.13
$NG_{-1,+1}$	1.75 ± 0.02	2.4	4.22 ± 0.05
$NG_{0,-1}$	2.53 ± 0.06	1.2	3.05 ± 0.07
$NG_{0,-0.33}$	2.04 ± 0.09	1.1	2.30 ± 0.10
$NG_{0,+1}$	2.38 ± 0.05	1.3	3.02 ± 0.06
$NG_{+1,-1}$	2.40 ± 0.04	1.1	2.66 ± 0.05
$NG_{+1,-0.33}$	2.28 ± 0.05	1	2.28 ± 0.05
$NG_{+1,+1}$	2.78 ± 0.24	1.1	2.99 ± 0.26

Cellular uptake of NGs was analyzed using a combination of flow cytometry and fluorescence microscopy (confocal and super-resolution) thanks to the intrinsic fluorescence of labelled LPEI (LPEI-RhB). The raw flow cytometry data were adjusted with a correction coefficient accounting for the different χ_{LPEI} values, as measured by NMR (complete discussion has been reported in Appendix III).

Table 3.5 reports the raw fluorescence data, the corrective factors and the corrected fluorescence data which are representative of cell internalization. Two-way ANOVA showed that the main effect of MR ($F(2,18) = 553$, $p < 0.0001$, $\eta^2 = 70.9\%$) overcame that of FRR ($F(2,18) = 14.9$, $p = 0.0002$, $\eta^2 = 1.91\%$) on NG uptake, with the two factors having an extremely significant interaction ($F(4,18) = 102$, $p < 0.0001$, $\eta^2 = 26.1\%$). Despite the large interaction hampers the interpretation of main effects, it can be observed that the specimens with the highest HA content ($NG_{-1,x}$) were characterized by the highest internalization values. A further confirmation of the successful NGs uptake was provided by confocal and super-resolution microscopy (*Figure 3.9C,D*). Red fluorescent NGs showed an intracellular localization (cell membrane stained in green) (*Figure 3.9C*). Super-resolution micrographs (*Figure 3.9D)* gave a clearer insight into the NGs localization inside the cell. Noticeably, the reported figures highlighted the distribution of the NGs around the cell nucleus without the formation of aggregates. These findings suggest that the formulated NGs maintain their structural integrity throughout the cells up to 24 hours after administration.

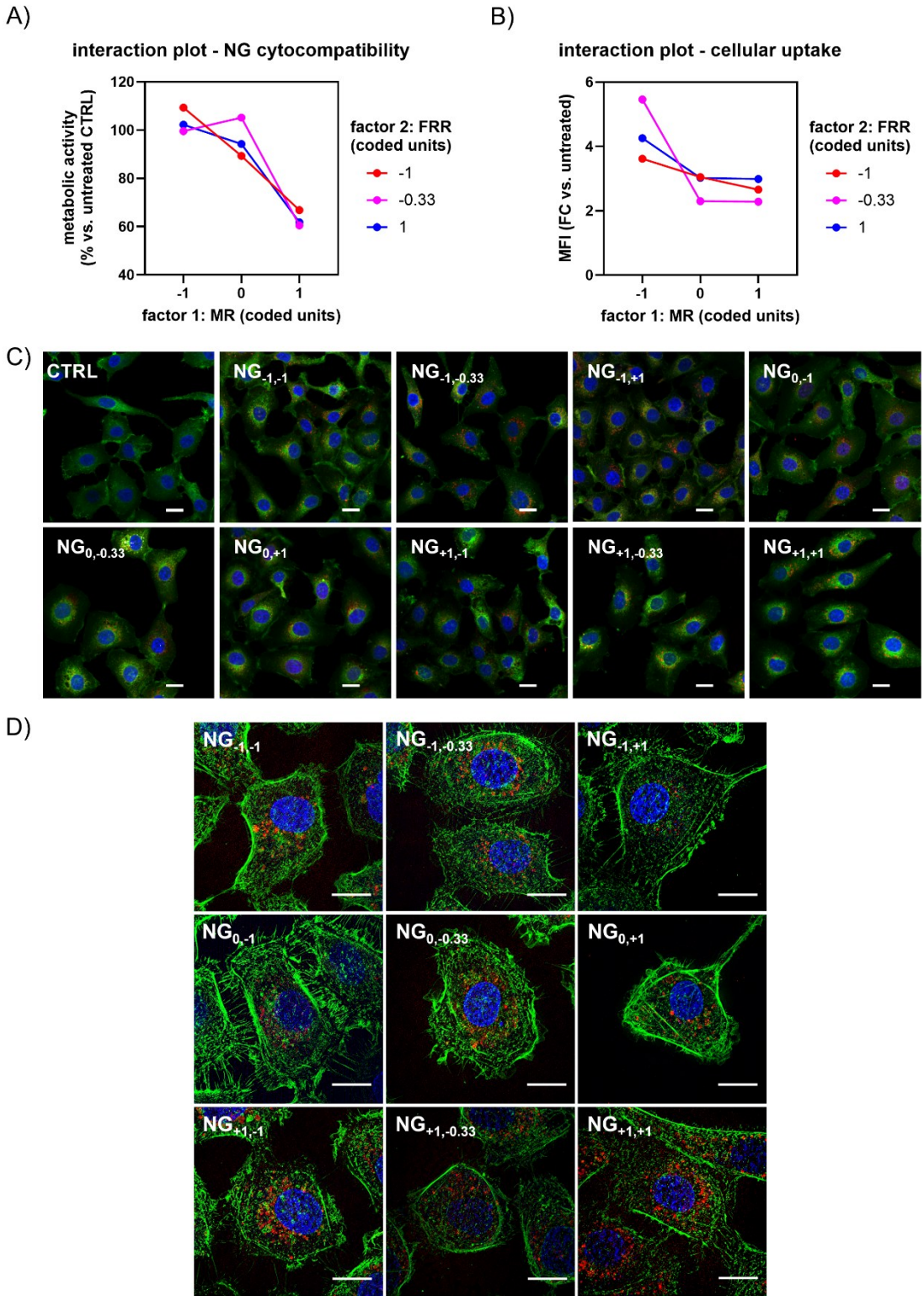

Figure 3.9 A) Interaction plot of NG cytocompatibility, cell metabolic activity measured after 24h of exposure to the NGs via MTT assay; values are reported as percentage vs untreated cells (CTRL); B) Interaction plot of NG uptake. Corrected MFI reported as fold change of the median fluorescence measured by flow cytometry after 24h of exposure to NGs vs. the median fluorescence of the untreated cells; C) Confocal micrographs: cell membrane was stained with CellMask Green Stain, nuclei were counterstained with DAPI. NGs are red-fluorescent. Scale bar 20 µm. D) Super-resolution optical microscopy. Actin cytoskeleton was stained with FITC-phalloidin, nuclei are counterstained with DAPI. NGs are red fluorescent. Scale bar 20 µm.

Drug response. The performance of NGs as drug delivery systems was tested in combination with doxorubicin (DOX) as a model drug and measured *via* MTT assay.

Fig. 3.10A shows the residual cellular metabolic activity after 24 h following administration of DOX_NGs. Data were normalized to untreated controls and statistically tested against cells treated with free DOX.

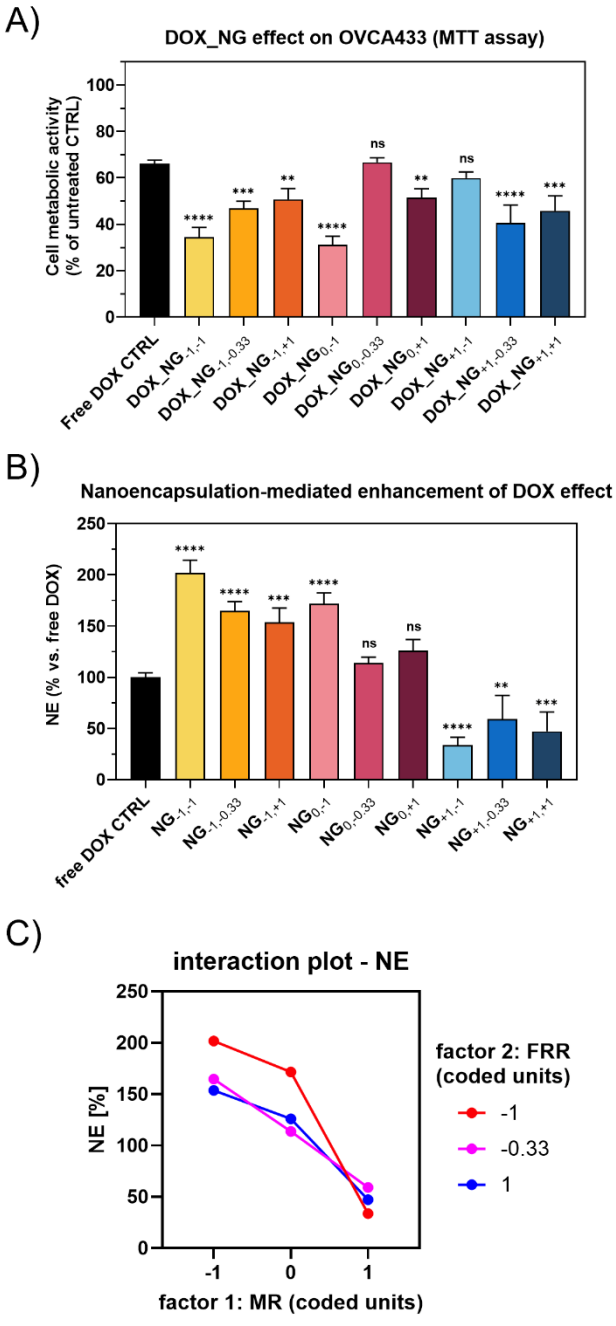

*Figure 3.10 A) Cell metabolic activity measured after 24h exposure to DOX_NGs; values are normalized to untreated cells. B) Nanoencapsulation-mediated enhancement of drug effect (NE) measured after 24h exposure to DOX_NGs; C) Interaction plot of NE. Statistical significance is vs. free DOX CTRL: * p<0.05, ** p<0.01, *** p<0.001, **** p<0.0001.*

It is worth noting that most of the NG samples showed increased toxicity to cells compared to free DOX. However, these results could be misleading, as they did not consider the effect that the NG carriers themselves exert on cell viability, which is not negligible, especially for LPEI-rich compositions. For this reason, a Nanoencapsulation-related Enhancement (NE %) parameter was defined as described in section 3.2.1 (Drug delivery to cancer cells) and results are reported in *Fig. 3.10B*.

Two-way ANOVA on NE data (in *Fig. 3.10C*) revealed a large and significant negative main effect of MR ($F(2,18) = 209$, $p < 0.0001$, $\eta^2 = 84.9\%$), a modest but very significant ($F(2,18) = 10.3$, $p = 0.001$, $\eta^2 = 4.81\%$) main effect of FRR, and a modest but extremely significant interaction ($F(4,18) = 8.97$, $p = 0.0004$, $\eta^2 = 7.28\%$).

Empirical model. The collected experimental data were used to develop an RSM-based empirical model. The first step was to perform an explorative analysis by calculating a correlation matrix (Pearson's) to highlight the presence of first order correlations among variables, including both process parameters and NG properties (*Figure 3.11*). Only variables with $|r| \geq 0.4$ and $p < 0.05$ were considered significantly correlated.
FRR showed a strong direct correlation with NG size and a strong inverse correlation with PDI. Expectedly, also NG size and PDI were inversely correlated.

Not surprisingly, MR exhibited a strong correlation with the resulting χ_{LPEI}. Both MR and χ_{LPEI} showed a strong inverse correlation with NG cytocompatibility, which can be explained by the potential toxicity of the LPEI component.

Moreover, MR and χ_{LPEI} were inversely correlated with the cellular uptake. This can be ascribed to the lower hyaluronan content of LPEI-rich formulations ($\chi_{HA} = 1 - \chi_{LPEI}$) which, in turn, can modulate NG internalization in cells expressing the hyaluronan receptor (CD44).

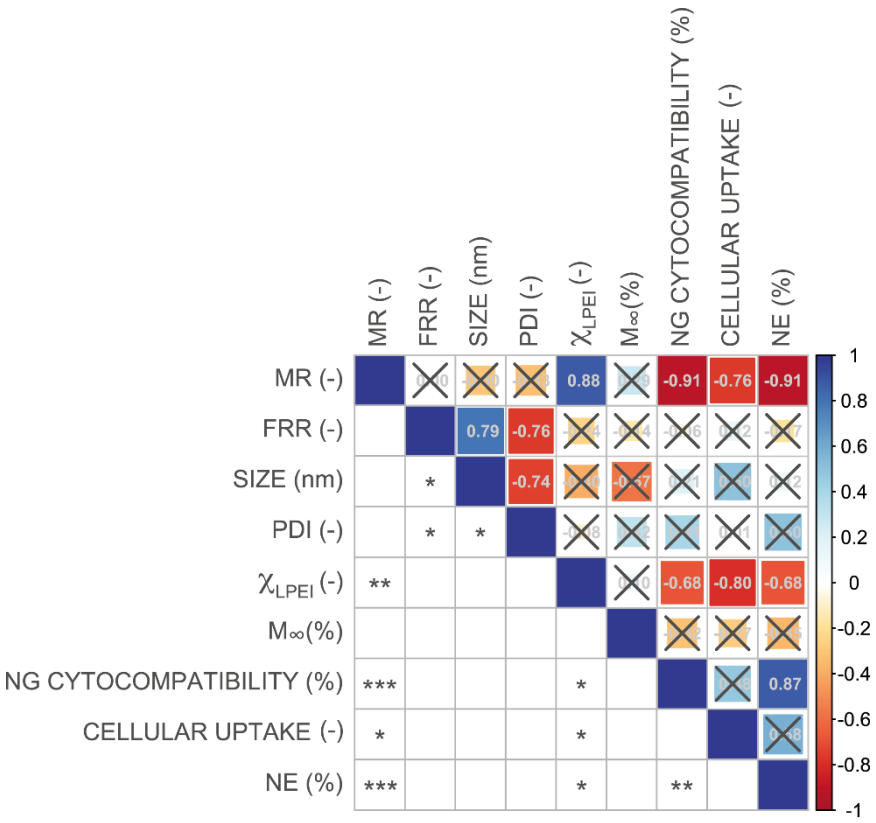

Figure 3.11. Pearson's correlation matrix. The upper triangular portion shows the correlation coefficients, while the lower triangular portion shows the corresponding p-values (p<0.05; ** p<0.01; *** p<0.001).*

The implementation of the RSM led to the definition of the empirical model, represented by the following set of equations (A = MR; B = FRR):

$$\boldsymbol{Size}\ (nm) = -1.14 \cdot 10^{2} + 3.60 \cdot 10^{1} A + 2.22 \cdot 10^{3} B - 3.74 A^{2} - 2.71 \cdot 10^{3} B^{2} - 1.80 \cdot 10^{2} AB^{2} + +1.44 \cdot 10^{1} A^{2}B^{2} \quad (25)$$

$$\boldsymbol{PDI}\ (-) = 2.04 \cdot 10^{-1} - 1.01 \cdot 10^{-2} A - 9.78 \cdot 10^{-1} B + 2.55 \cdot 10^{-2} AB + 1.25 B^{2} \quad (26)$$

$$\boldsymbol{\chi_{LPEI}}\ (-) = 4.96 \cdot 10^{-1} + 4.05 \cdot 10^{-2} A - 2.55 \cdot 10^{-1} B + 2.23 AB \cdot 10^{-1} - 2.21 \cdot 10^{-3} A^{2} - 1.36 B^{2} - 1.30 \cdot 10^{-2} A^{2}B \quad (27)$$

$$\boldsymbol{M_{\infty}}\ (\%) = 1.49 \cdot 10^{-2} + 1.92 \cdot 10^{-4} A + 3.13 \cdot 10^{-2} B - 6.10 \cdot 10^{-4} A^{2}B - 2.74 \cdot 10^{-2} AB^{2} + 3.57 \cdot 10^{-3} A^{2}B^{2} \quad (28)$$

$$\boldsymbol{Cellular\ uptake}\ (-) = 7.25 - 1.33 A + 4.44 B + 8.32 \cdot 10^{-2} A^{2} - 9.56 B^{2} + 3.88 \cdot 10^{-1} AB^{2} + 1.06 \cdot 10^{-2} A^{2}B^{2} \quad (29)$$

$$\boldsymbol{NG\ cytocompatibility}\ (\%) = 8.67 \cdot 10^{1} + 1.04 \cdot 10^{1} A - 1.44 A^{2} - 1.86 \cdot 10^{1} B^{2} + + 8.59 \cdot 10^{-2} A^{2}B + -1.25 \cdot 10^{-1} A^{2}B^{2} \quad (30)$$

$$\boldsymbol{NE}\ (\%) = 4.29 \cdot 10^2 - 6.60 \cdot 10^1\, A - 1.08 \cdot 10^3\, B + 2.08 \cdot 10^2 AB + 4.42\, A^2 - 1.43 \cdot 10^1\, A^2 B \quad (31)$$

The complete set of variance and coefficients tables for Eqs.25-31 are reported in Appendix III (Tables S1-S14), while the surface contour plots are reported in *Fig. 3.12.*

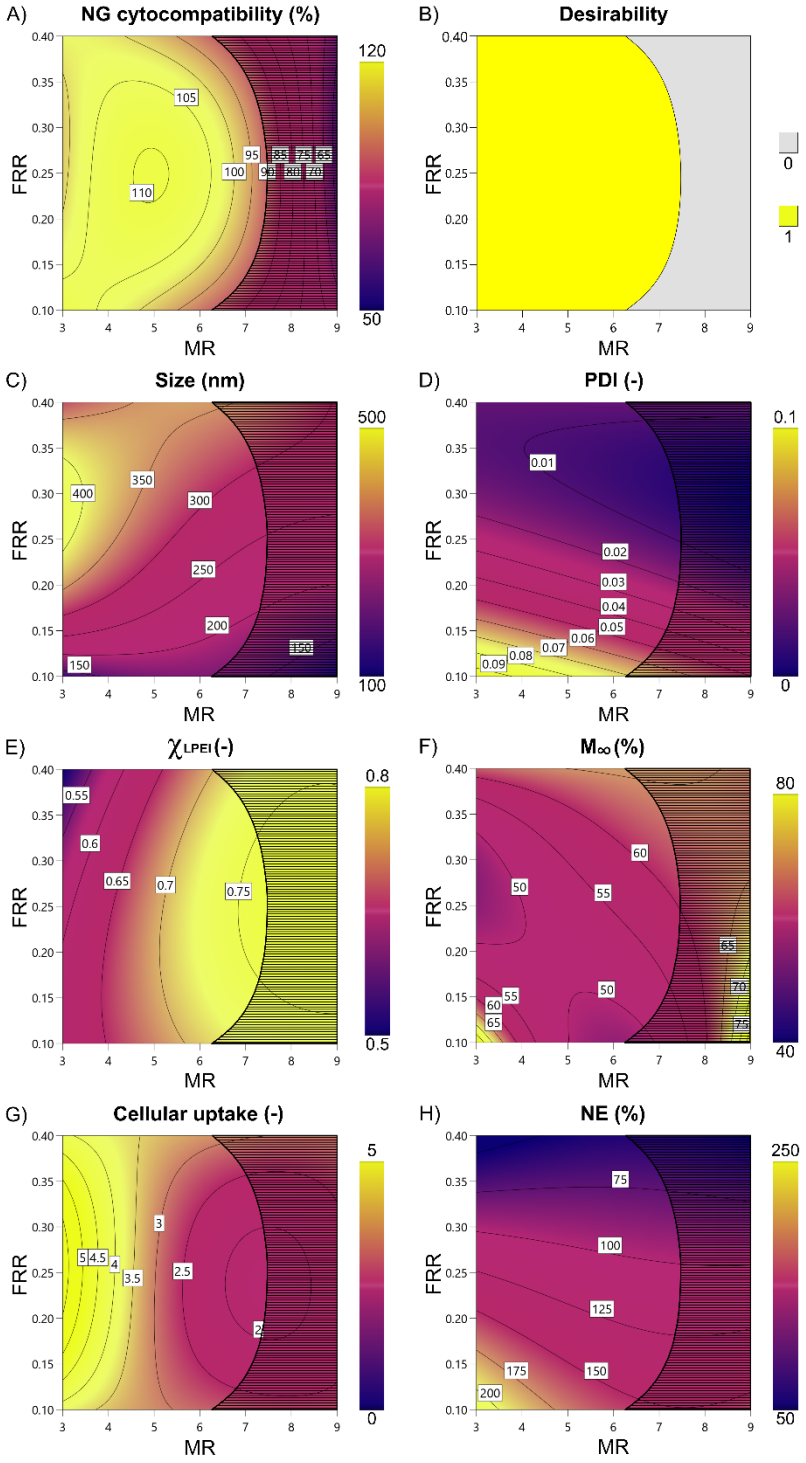

Figure 3.12. Contour plots for: (A) NG cytocompatibility; (B) Desirability map defining the region in which cell viability is greater than 90%; (C) size; (D) PDI; (E) χ_{LPEI}; (F)M_∞; (G) cellular uptake and (H) NE.

With RSM, the dependence of the NG properties on the two process variables was described by polynomials of higher degree, accounting for non-linearities which were concealed at the initial linear correlation test. However, the degree of the polynomials was kept as low as possible while still giving a good fit quality of the experimental data. Moreover, we chose to limit the space of solutions to those formulations not affecting the cellular metabolic activity. To this aim, a desirability function was applied with the constrain of cellular metabolic activity > 90% (*Figure 3.12A, B*) and the corresponding "non-desirable" region has been hatched in each contour plot (*Figure 3.12C-H*).

To qualify the developed empirical models, the Predicted *vs.* Actual plots (Figure 3.13) were analyzed. The coefficient of determination (R^2) gave an indication of the goodness of fit, resulting in good fit quality for all the equations (R^2> 0.8). Noteworthy, an R^2 > 0.9 was reached for NG cytocompatibility (R^2 = 0.953), size (R^2 = 0.95), and cellular uptake (R^2 = 0.975).

Although R^2 is a robust indicator of the goodness of fit, it does not quantify the ability of the model to predict responses for new observations (*i.e.*, which were not used to estimate the model). For this reason, the predicted R^2 (R^2_{pred}) was calculated. The R^2_{pred} can be considered of good quality for all the equations of the empirical model (R^2_{pred}> 0.7).

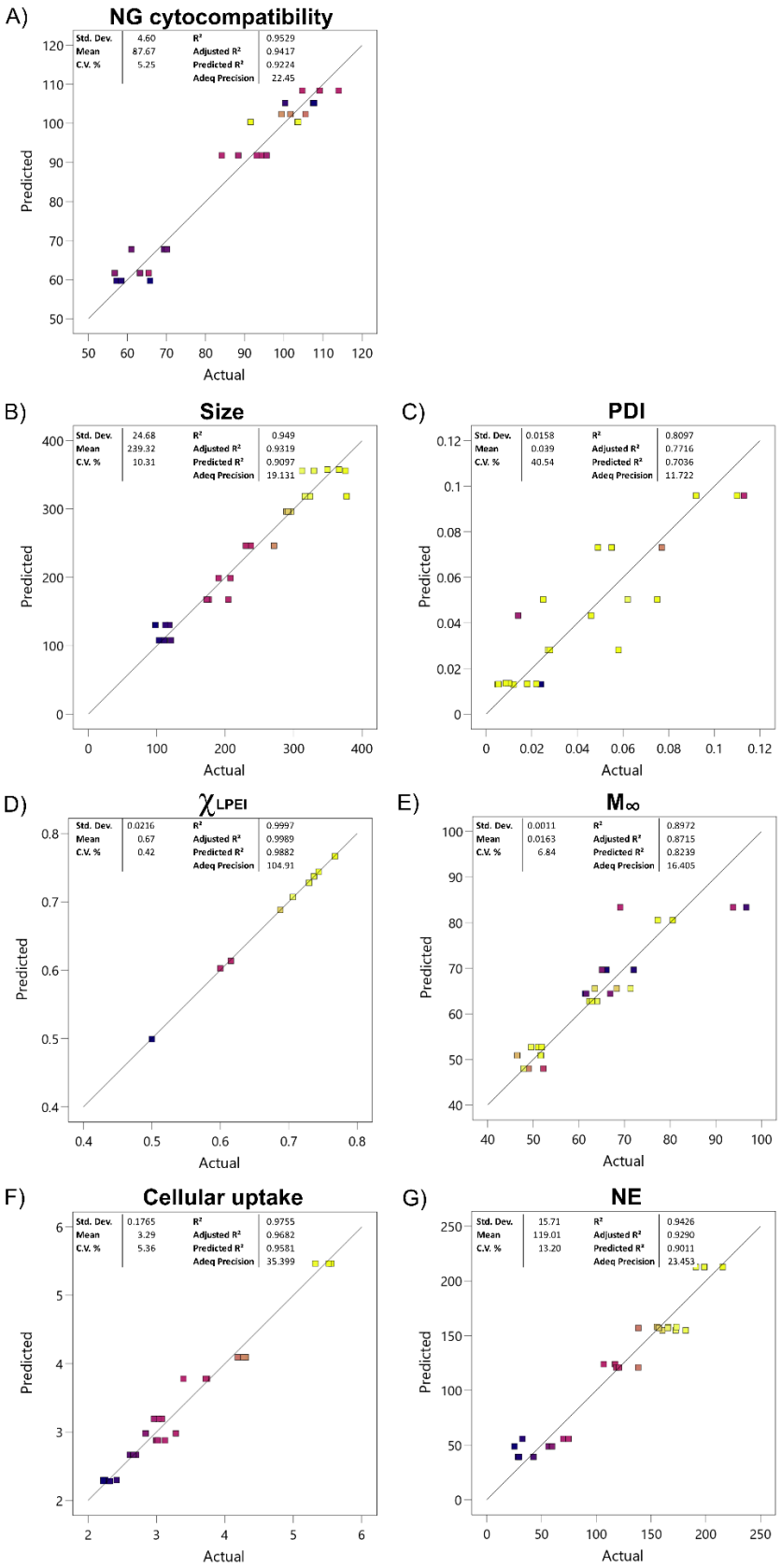

Figure 3.13 Predicted vs. Actual plots. The closer the data points are to the diagonal line, the better the model fits the collected data. The coefficient of determination (R^2) was calculated as a measure of the goodness of fit, while predicted R^2 was calculated as an estimator of out-of-sample forecasts.

Discussion

Recently, the use of microfluidics in the formulation of novel DDSs has gained increasing attention mainly due to the high control over a variety of process parameters, which outperforms the traditional batch syntheses. However, the easy modulation of the fluid-dynamic and compositional parameters offered by microfluidic setups mandates for time-consuming identification of the correct process conditions. Therefore, a DoE approach implementing the RSM was used to reveal the effect of process parameters over a wide range of physicochemical and biological features of the HA-LPEI NGs synthesized *via* droplet-based microfluidics.

Effects of process parameters on NG physicochemical properties. To validate the application of droplet-based microfluidics for the synthesis of polymeric NGs and to deepen the understanding of the effect that process parameters exert over NGs features, the chemical and physical properties of these nanomaterials were investigated in a range of process parameter values.

By comparing the ^{1}H-NMR spectra of the starting polymers with that of the NG samples (*Figure 3.8D*), the presence of signals from both polymers and the chemical shift of the LPEI signal from 2.78 to approximately 2.9 ppm could be observed.[229] Furthermore, the involvement of the activated carboxyl groups of HA resulted in the shift of the signal ascribable to the protons in the sugar ring from 3.8 ppm to 3.38 ppm, thus corroborating the bonding between both polymers for all NG specimens. Moreover, the integration of the signals ascribable to HA and LPEI gave an estimate of the χ_{LPEI} in each specimen, as reported in *Table 3.2*. According to the results of two-way ANOVA on NG composition values, a strong dependence of χ_{LPEI} on the imposed MR was confirmed (84.8% of the total variance, $p<0.0057$), while no significant main effect of FRR was detected. These results are consistent with the strong linear correlation between MR and χ_{LPEI} ($r = 0.88$, $p = 0017$).

Interestingly, as reported in the results section of the NG synthesis and characterization, a major direct influence of FRR on NGs size can be highlighted by the two-way ANOVA (FRR accounts for 76.6% of the total variance, $p < 0.0001$). This might be attributed to the reduction of microdroplet size achieved for low FRR levels, which limit the volume of the reaction chamber where the crosslinking reaction takes place. A reduction in the droplet diameter from ca. 60 to 30 μm was observed when the FRR was decreased from 0.4 to 0.1, resulting in a volume change of approximately 87.5% (*Figure 3.8A, B*). Conversely, MR appeared to exert a minor influence on NG size (8.67% of the total variance, $p = 0.0044$).

However, a slight inverse proportionality can be discerned from the data, which features the pivotal role of LPEI as crosslinker. Indeed, NGs with a lower LPEI content resulted in an overall larger diameter, probably due to a less crosslinked matrix. NG size ranged from 100 to 360 nm (*Table 3.2*), ensuring a size suitable for drug delivery applications for the whole range of process parameters.

All the experimental conditions resulted in monodisperse nanoparticles with PDI values ranging from 0.01 to 0.11 (*Table 3.2*). A strong negative effect of FRR on PDI was evidenced by two-way ANOVA (66.5% of the total variance, $p < 0.0001$) and by the strong inverse correlation between the two variables (r = -0.74, p = 0.017). This behavior could be explained in light of previous literature findings [230] evidencing that the mixing processes occurring within the emulsified dispersed phase is enhanced by an increased droplet velocity. Hence, the narrow size distribution obtained at higher FRR could be ascribed to improved mixing conditions, as reported for other microfluidics-based processes for nanoparticles synthesis [231–235].

Based on the above reported considerations, also NG size and PDI were found to be inversely correlated (r = -0.69, p = 0.023)

Physicochemical properties affect NG bioperformance. In this study, the bioperformance of NGs was evaluated in terms of drug release, NG cytotoxicity, cellular uptake, and performance as a DDS on ovarian cancer cells. Having previously elucidated the relationship between synthesis parameters and NGs physicochemical properties, this section will discuss how these properties influence the *in vitro* bioperformance of these nanomaterials.
A strong and significant inverse correlation (r = -0.76, p = 0.02) between χ_{LPEI} and NG cytocompatibility was evidenced. Indeed, LPEI-rich formulations ($NG_{+1,x}$) resulted in reduced cell viability (71.2%, 60.5% and 61.8%, respectively) compared to the control group. It is recognized that linear and branched PEI are associated with toxicity and non-degradability, limiting their clinical applications [236,237]. Nevertheless, the intrinsic toxicity of LPEI can be mitigated when conjugated with other biopolymers such as HA [25], as inferred from *Table 3.4,* where the NGs with higher HA content demonstrated no significant variation in metabolic activity (MTT assay) compared to untreated cells.

χ_{LPEI} was also reported to dictate the cellular uptake of NGs. Data suggested that NGs with a higher LPEI content were less internalized after 24 hours. This was further demonstrated

by the strong negative correlation between χ_{LPEI} and cellular uptake (r = -0.80, p = 0.01), meaning that NGs with a higher HA fraction resulted in a more facile uptake. This behavior can be explained by considering that the interaction between HA and its receptor (CD44 hyaluronan receptor, highly expressed in ovarian cancer cells) has a fundamental role in driving NG endocytosis, as already demonstrated for NGs with similar composition [210]. Indeed, cell uptake quantification by flow cytometry gave the highest fluorescence levels for HA-rich formulations ($NG_{-1,x}$), with $NG_{-1,-0.33}$ peaking with a 6-fold increase compared to untreated cells.

The NE parameter has been defined as a metric of nanoencapsulation-driven enhancement of drug effect, subtracting the account for the effect of pristine NG material on cell viability. It is worth noting that, for the determination of NE, a superposition principle has been applied, hence under the strong assumption that the net response caused by the two stimuli (pristine NG and released DOX) is the sum of the responses that would have been caused by each stimulus individually. Nonetheless, this parameter allowed us to compare different NG formulations, which are characterized by distinct cytocompatibility levels. χ_{LPEI} was inversely correlated with NE (r = -0.68, p = 0.041), suggesting that HA-rich formulations (low χ_{LPEI}), which are highly biocompatible and easily uptaken by cells, show the largest effect of drug nanoencapsulation strategy, overcoming that of free DOX. Expectedly, given the strong dependence of χ_{LPEI} on MR, the same considerations can be made for the observed direct correlation of NG cytocompatibility, cellular uptake and NE with MR. It is also worth mentioning that, although the use of linear correlations was helpful in identifying the key dependences among different variables, the nature of the studied phenomena goes far beyond linearity. Thus, an interpretation limited to such type of relationship may be misleading and may conceal high-order phenomena, which are instead evidenced by the polynomial equations of the response surface model.

RSM to dictate process parameters selection in microfluidic synthesis of nanomaterials. The RSM-based empirical model built upon the experimental data had a good fit quality, with $R^2 > 0.81$ for all the equations. However, although R^2 is an adequate metric for the goodness of fit, it does not quantify how the model will predict responses for new observations, which were not themselves used to estimate the model. Indeed, a regression model could fit well the existing data, but it could be not as good at making predictions. R^2_{pred} is a statistical tool which helps elucidate the ability of a regression model

to make predictions by removing one data point at a time and each time recalculating the regression each time to test how well the model predicts the missing observation. R^2_{pred} values were generally good for all the equations and not distinctly lower than the corresponding R^2 (below 13.1% decrease), suggesting that the empirical model was not overfitting the experimental data. This finding supports the use of RSM as a predictive tool for the microfluidic droplet-based synthesis of HA-LPEI NGs and, in general, for the continuous flow synthesis of nano-DDSs, allowing operators to match target responses by adapting process parameters.

3.3 Conclusions

Several bulk methods have been described in the literature to synthesize polymeric nanocarriers for controlled drug delivery purposes. However, these procedures are generally characterized by significant constraints, such as limited control over the reaction parameters, difficult optimization of the colloidal properties of the nanosystems, and scarce lot-to-lot reproducibility, which have hampered their potential eligibility as therapies in nanomedicine. In this scenario, microfluidic platforms represent a valid alternative to modulate and control the dimensions and the physico-chemical properties of the nanocarriers toward a more precise and versatile nanomaterial design. In this part, the synthesis of nanogels in a microfluidic chip exploiting the active formation of a W/O microemulsion has been presented. In particular, each generated microdroplet acted as a reaction micro-chamber, where the polymer crosslinking occurred, giving rise to the NG architecture.

Initially, an active tuning of the flow focusing junction was explored thanks to the pneumatic actuator integrated in the chip design. The pneumatic actuation resulted in an on-demand modulation of the microdroplet diameter, which in turn resulted in augmented control over the NG size and monodispersity. The effects of our droplet-based microfluidic process positively impacted the NG drug delivery performances, since modulation of NG size affected the resulting drug release profile, with smaller NGs showing a more sustained DOX release and increased therapeutic effect compared to free drug administration.

Successively, a statistical approach was applied to the continuous flow synthesis of HA-LPEI NGs, which were synthesized by droplet microfluidics exploring a wide range of experimental conditions. The panel of NG formulations were characterized in terms of size, polydispersity, composition, cytocompatibility, drug release, cellular uptake, and performance as a DDS on ovarian cancer cells. The fluid dynamic regime, represented by the Flow Rate Ratio (FRR) parameter, was found to dictate the resulting size and polydispersity index of the NGs, while compositional parameters (LPEI/HA Molar Ratio, MR) dictated the resulting NG composition and influenced relevant biological properties, such as NG cytocompatibility, cellular uptake and nanoencapsulation-driven enhancement of drug effect. Using the Response Surface Methodology, we developed an empirical model describing the effects of process parameters on the resulting NG physicochemical and biological properties. The model showed very good fit quality and robustness to out-of-sample predictions.

Overall, the reported results testify an advancement in NG design, demonstrate the potential of RSM to support and streamline the continuous flow synthesis of nanomaterials, which could support the progress toward an effective clinical translation of the nanoparticle-based technology and meet the needs for ameliorated drug release performances in healthcare scenarios still lacking an efficient treatment.

PART IV
MICROFLUIDIC CELL ENCAPSULATION

4. Microfluidic Cell encapsulation

4.1 A comparative analysis of droplet-based microfluidics for cell encapsulation: focus on T-junction and flow focusing

Alginate is a linear polysaccharide composed of a block copolymer consisting of alternating β-$_D$-mannuronate (M) and α-$_L$-guluronate (G) residues. Its backbone can be arranged as a homopolymeric block of G or M units, or as alternating GM units.[238–240]

Alginate beads are commonly used for drug delivery or cell encapsulation purposes due to their biocompatibility, non-toxicity, biodegradability, and mild gelation conditions. Specifically, the cell-laden microcapsules can serve as a tool for delivering cells for tissue regeneration or as a 3D culturing unit for monitoring and manipulating cells, down to the single-cell level. [240,241]

Alginate microcapsules can be easily obtained *via* ionotropic gelation in the presence of a divalent cation, such as calcium ion (Ca^{2+}).[242,243] Two strategies can be used to induce the gelation process: external gelation[244,245] or internal gelation[246,247]. In the first case, sodium alginate (Na-alginate) is typically dripped into a solution of a water-soluble calcium salt, such as calcium chloride ($CaCl_2$), which induces the formation of calcium alginate (Ca-alginate) beads externally. On the contrary, when internal gelation is applied, a non-soluble salt (*i.e.* calcium carbonate, $CaCO_3$) is mixed with Na-alginate and the release of the calcium ions is triggered, after emulsification, by a change in the pH of the continuous phase.

However, both techniques exhibit several issues related to uncontrolled gelling, leading to low uniformity of the synthesized microgels, or inherent toxicity caused by the gelling conditions.

Droplet-based microfluidic platforms have been extensively studied for producing highly monodisperse microparticles with the desired size, morphology, and composition. A microfluidic process for synthesizing alginate microgels typically involves three steps: (i) Emulsification of the dispersed phase containing the polymer precursor; (ii) Sol-gel transition, which can be performed *ex situ*, where the cross-linking reaction takes place in a dedicated bath, or *in situ*, where the droplets are gelled directly after their generation on-chip; (iii) Transfer of the alginate beads from the oil phase to a water phase after gelation. During this process, the microfluidic setup provides precise control over the applied flow

rates, enabling fine manipulation of the reaction conditions. This allows for unparalleled reproducibility and robustness of the synthesis process.

In this context, two main device geometries are commonly used: the T-junction (TJ) and the flow-focusing junction (FFJ). TJ comprises of two immiscible fluid streams that are orthogonal to each other. The dispersed phase is sheared by the continuous phase, resulting in the generation of droplets.[55] FFJ is characterized by the presence of an orifice at the junction between the central dispersed phase and the two lateral continuous phase channels. The dispersed phase is forced to pass through the orifice, which increases the pressure on the dispersed phase and facilitates droplet formation. [55]

Chang-Hyung Choi and colleagues used a TJ device to encapsulate yeast cells in highly monodisperse alginate microbeads by exploiting chaotic mixing.[248] The authors took advantage of the slow diffusion of the reagents, which hindered their interaction prior to droplet formation, and the chaotic advection inside the droplets to induce the *in situ* sol-gel transition. The viability of the GFP cells was confirmed through fluorescence imaging after the encapsulation process. However, in order to provide a high-throughput system, a novel step-T-junction device was developed.[249] Here, the diameter of the produced alginate-gelatine hydrogel can be easily controlled in the range of 67 - 278 μm, keeping the coefficient of variation (CV) below 5%, even when using an *ex situ* gelling process. Hepatocellular carcinoma (HepG2) cells were successfully cultured till day six maintaining their proper functionalities of secreting urea.

David A. Weitz and his colleagues demonstrated two different applications of FFJ devices in producing alginate microbeads. They initially used a single dispersed phase consisting of a Na-Alginate and calcium-EDTA solution. The sol-gel transition was induced by adding acetic acid to the oil phase to trigger the release of Ca^{2+}. The authors found that encapsulating a single mesenchymal stem cell (MSC) in 25% of the produced beads was possible. They also discovered that a gelation time of less than 2 minutes is crucial to ensure compatibility with the developed technique.[250] To overcome issues related to premature polymerization or poor control over the monodispersity of the emulsion, they developed a triple-flow microdevice to induce hydrogel formation inside droplets before their collection off-chip.[251]

To the best of our knowledge, although several papers have reported the successful implementation of similar methods in the literature, no comprehensive comparison of the performance of TJ and FFJ devices for cell encapsulation has been performed. Therefore, in

the present work, the triple-flow technology was implemented on both TJ and FFJ geometries to investigate the effect of process parameters on the synthesis of Ca-Alginate microcapsules. Next, we demonstrate the feasibility of the cell encapsulation process by measuring cell viability immediately after encapsulation and after seven days of culture.

4.1.1 Materials & Methods

Materials. Sodium alginate with low viscosity and high guluronate content (Pronova® UP VLVG) was purchased from Merck KGaA (Darmstadt, Germany) and used for the synthesis of the microcarriers. SU-8 photoresist, purchased from MicroChem (Newton, Massachusetts), and Sylgard 184 kit containing polydimethylsiloxane (PDMS) and curing agent, obtained from Dow Corning (Midland, Michigan), were used for devices microfabrication. Ovarian cancer cell line SKOV 3 was obtained by American Type Culture Collection (ATCC) (LGC Standards, Teddington, UK). All other chemicals were purchased from Merck KGaA (Darmstadt, Germany) and used as received at the analytical purity grade.

Device fabrication. The microfluidic devices depicted in *Figure 4.1* (namely, FFJ *Figure 4.1A* and TJ *Figure 4.1B*) were fabricated using conventional photolithography and soft lithography techniques. First, a 3" silicon wafer was spin-coated with a layer of SU-8 2075 photoresist (80 µm thick), followed by UV exposure through a photomask to create the desired pattern. The resulting master was silanized overnight in a trimethylchlorosilane (TMCS) vapor saturated chamber to facilitate demolding.

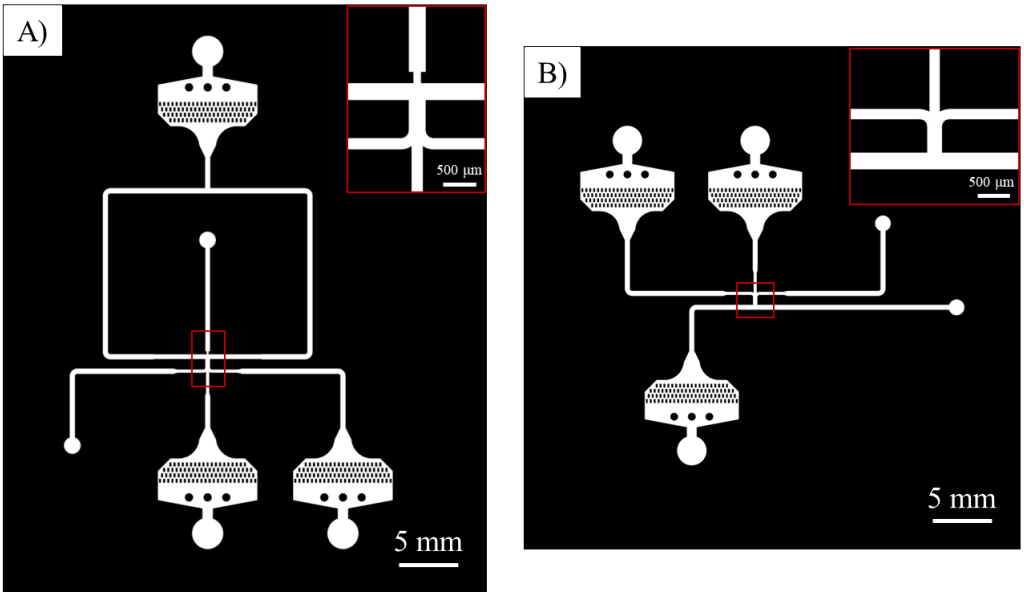

Figure 4.1 Schematic representation of the microfluidic devices: A) Flow Focusing junction; B) T-junction

A PDMS solution (prepolymer:curing agent ratio 10:1 w/w) was then poured onto the silanized silicon master, cured for 2 h at 70°C, and peeled off as the main device assembly component. Microfluidic inlets and outlets were formed using a biopsy puncher. Bonding of PDMS to slides was achieved by oxygen plasma exposure using a femto plasma etcher (Diener electronic, Ebhausen, Germany).

To make the chip surfaces hydrophobic, a stream of TMCS saturated nitrogen was applied for 15 minutes. This was followed by a thermal treatment at 140°C for 10 minutes.

Alginate functionalization (Alg-FITC). The functionalization of alginate with fluorescein isothiocyanate (FITC) groups (Alg-FITC) followed the two-step protocol described by Zhu *et al.*:[252] (i) introduction of amine functionalities into the alginate chain (Alg-NH_2); (ii) attachment of FITC to the amine functionalities.

Briefly, to activate the carboxyl groups of sodium alginate, 120 mg of the latter was mixed with 50 mg of N-(3-dimethylaminopropyl)-N′-ethyl carbodiimide hydrochloride (EDC, MW: 155.245 g/mol) and 30 mg of N-hydroxysuccinimide (NHS, MW: 115.09 g/mol) in acetate buffer (pH 4.7) for 30 min. After complete solubilization, 60 mg of 1,6-diaminohexane (MW: 116.21 g/mol) was added and the mixture stirred at room temperature (RT) for 4 hours. Excess isopropanol (IPA) was added to precipitate the mixture and remove the unreacted diamine by vacuum filtration.

The collected Alg-NH_2 was then reacted with FITC (0.5 mg, MW: 389.382 g/mol) in a sodium bicarbonate solution (pH 8.5) for 4 hours and precipitated in acetone. The final product was obtained by vacuum filtration, resuspended in DIW, and dialyzed against DIW (membrane cut-off: 3.5-5 kDa) for three days with daily water exchange. After dialysis, the Alg-FITC was collected, lyophilized and stored at +4°C until use.

Experimental procedure: microcarriers production. Microcarriers were synthesized by emulsifying an alginate solution in a water-in-oil (W/O) system. When functioning as droplet generators, the fabricated microfluidic devices require the use of two different phases: a continuous oil phase and an aqueous dispersed phase. The former consists of a 3% w/v Span80 solution of mineral oil. Meanwhile, the dispersed aqueous phase consists of three different solutions that meet just before the emulsification junction: (i) a 2% w/w solution of Alg-FITC; (ii) a 75 mM solution of $CaCl_2$; and (iii) pure water. The as obtained solutions were loaded into Hamilton glass syringes and connected to the inlet of the microfluidic devices through Teflon tubing.

Control over the flow rate of each fluidic component was performed using a programmable syringe pump (Nemesys, CETONI GmbH, Korbussen, Germany). In particular, the flow rates of the continuous phase and alginate solution were kept constant at 25 µL/min and 1.5 µL/min, respectively. While the flow rates of pure water and $CaCl_2$ were varied according to the following table (*Table 4.1*).

Table 4.1 List of the synthesis conditions obtained for both devices by varying the flow rates of pure water (H_2O) and $CaCl_2$ in the dispersed phase, and the starting concentration of $CaCl_2$ (75 mM and 150 mM).

Flow Conditions

Concentration ($CaCl_2$): 75 mM				
	$CaCl_2$			
H_2O		*0.5 µL/min*	*1.0 µL/min*	*1.5 µL/min*
	2.5 µL/min	$_{75mM}$_A	$_{75mM}$_B	$_{75mM}$_C
	3.0 µL/min	$_{75mM}$_D	$_{75mM}$_E	$_{75mM}$_F
	4.0 µL/min	$_{75mM}$_G	$_{75mM}$_H	$_{75mM}$_I
Concentration ($CaCl_2$): 150 mM				
	$CaCl_2$			
H_2O		*0.5 µL/min*	*1.0 µL/min*	*1.5 µL/min*
	2.5 µL/min	$_{150mM}$_A	$_{150mM}$_B	$_{150mM}$_C
	3.0 µL/min	$_{150mM}$_D	$_{150mM}$_E	$_{150mM}$_F
	4.0 µL/min	$_{150mM}$_G	$_{150mM}$_H	$_{150mM}$_I

Referring to the flow conditions, the same nomenclature is applied to both TJ and FFJ devices.

Approximately 100 µL of the W/O emulsion was collected in a 1.5 mL Eppendorf tube pre-loaded with 600 µL of a 30 mM $CaCl_2$ solution at the outlet of the microfluidic devices. To promote phase separation and collect the formed microcarriers in the aqueous phase, the system was spun at 1500 rpm for 1 min. After carefully removing the oil supernatant, three

aliquots of 100 µL each were placed in a 96-multiwell plate, and features of interest (such as microbeads equivalent diameter, circularity, and uniformity) were acquired using a confocal microscope.

The same experimental conditions were repeated using a $CaCl_2$ concentration of 150 mM to investigate the effect of the crosslinking concentration on the production of alginate microcarriers.

Cell culture. The human ovarian cancer cell line SKOV3 was cultured at 37°C and 5% CO_2 in low-glucose DMEM supplemented with 10% FBS, 1% L-glutamine, and 1% Penicillin-Streptomycin. Upon confluence, cells were washed three times with PBS and then gently detached by trypsin/EDTA exposure (4 min at 37 °C). After centrifugation, cells were resuspended in low-glucose DMEM and labeled by incubating them with the nuclear dye Hoechst 33342 (1:500 in PBS) at 37 °C for 10 min. After incubation, cells were washed three times with PBS and resuspended in 2% w/w Na-alginate in saline solution (NaCl 0.9% w/w) at the concentration of $2.5 \cdot 10^6$ cell/mL to conduct the microfluidic encapsulation experiments.

Cell encapsulation. Microfluidic cell encapsulation was performed using the experimental condition FFJ_{75mM}_C. 2% w/w Na-alginate in saline solution (NaCl 0.9% w/w) was used to load $2.5 \cdot 10^6$ cell/mL.

Live-dead assay. The process compatibility was evaluated using a cell viability assay for mammalian cells, specifically the Live/Dead Viability/Cytotoxicity assay. The assay was performed at four distinct time points: 0h, 24h, 48h, and 1 week after cell encapsulation. Samples were stained with 4 mM calcein AM (green) and 2 mM ethidium homodimer-1 (red) in the culture medium and observed under confocal microscope. Cell viability values were calculated as the ratio of live cells to the total number of cells counted.

Statistical analysis. The experimental data were analyzed using Prism ver. 10.2.1 (GraphPad Software, San Diego, CA) and reported as mean ± SD, if not otherwise specified. One-way or two-way analysis of variance (ANOVA) were used as appropriate to assess significance, which was set to the 0.05 level.

4.1.2 Results & Discussions

Operation of the devices. As detailed in the Materials and Methods section, droplets were generated using two microfluidic devices, FFJ and TJ, under nine distinct flow conditions

(*Table 4.1*). *Figure 4.1* illustrates the operational principles of both devices, with $CaCl_2$ flow depicted in purple and the sodium alginate solution in green. These images illustrate the importance of the central channel in preventing premature contact between sodium alginate and calcium ions, thereby avoiding device occlusion. Furthermore, *Figure 4.1A–F* illustrates the impact of three water flow conditions — (A) 2.5 µL/min, (B) 3.0 µL/min, and (C) 4 µL/min — on the process. As the volumetric flow rate of water increases, the volume occupied by the water in the junction region also increases, thereby promoting a more stable droplet generation.

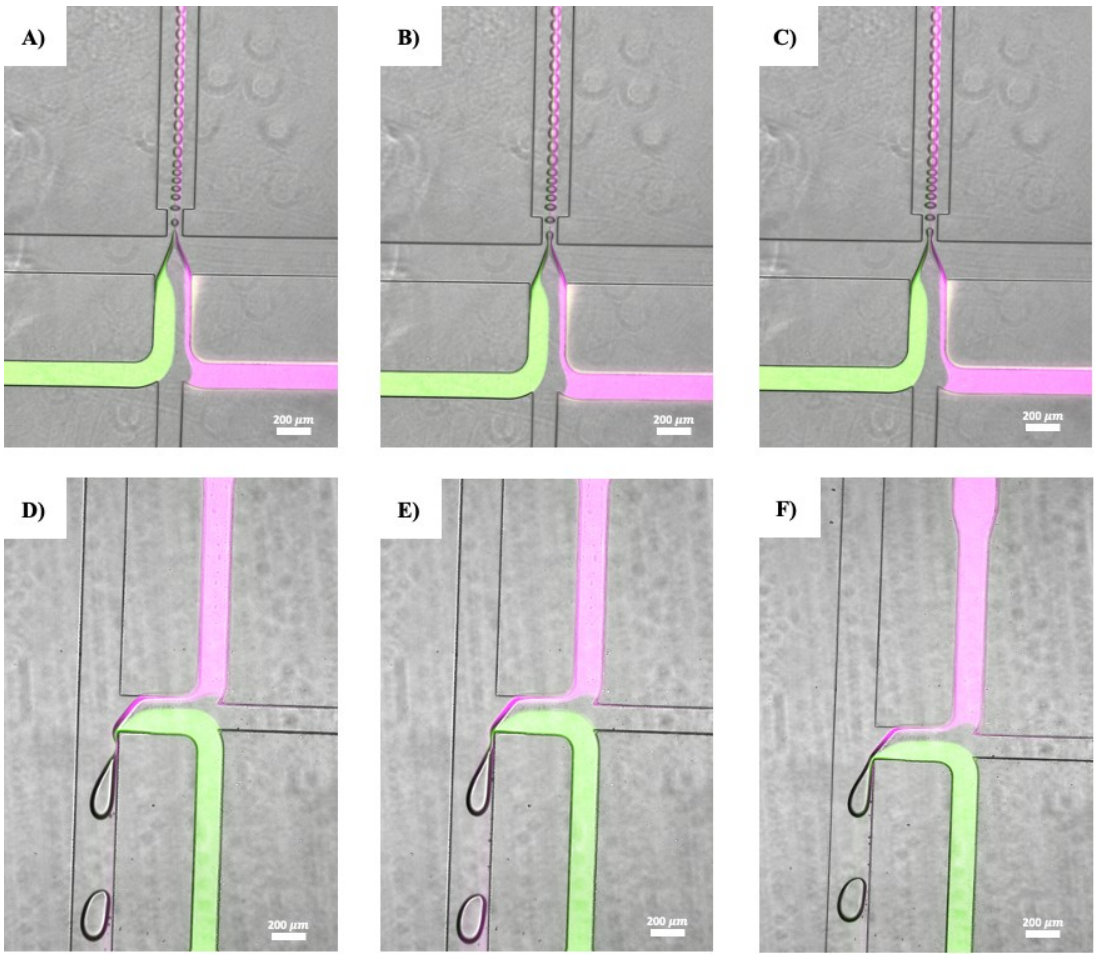

Figure 4.1 Functioning of the FFJ microfluidic system with water flows of: A) 2.5 µL/min; B) 3.0 µL/min; C) 4.0 µL/min, and of the TJ microfluidic system with water flows of D) 2.5 µL/min; E) 3.0 µL/min; F) 4.0 µL/min. Images were captured using Nikon Eclipse Ti2 epifluorescence microscope at a magnification of 4X.

The performances in droplet production yield (as number of droplets per second) of both devices were evaluated with the aid of an epifluorescence microscope equipped with a high-speed camera (Neo 5.5, Andor Technology, Belfast, UK). Due to the differences in frequency of production between the devices, two different frame rates were used: 1699.9 FPS and 357.7 FPS for FFJ and TJ, respectively. Results are reported in *Figure 4.2*.

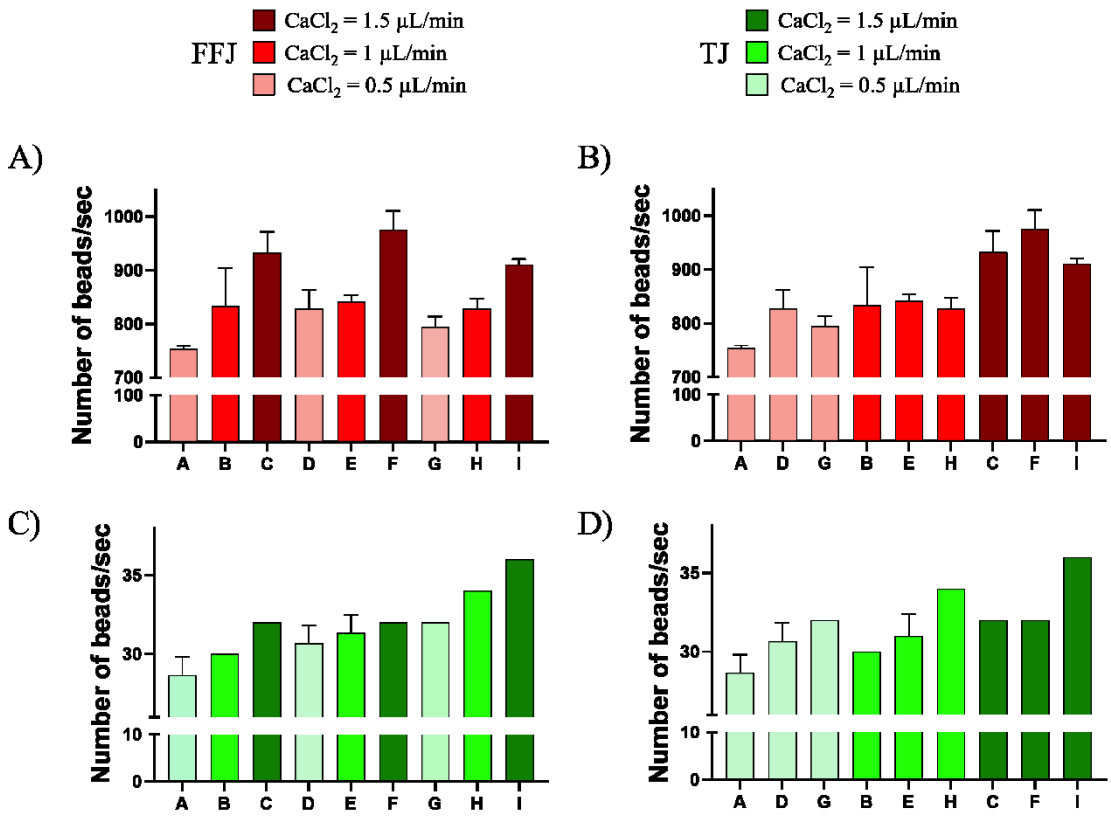

Figure 4.2 Bar charts reporting the frequency values acquired for the individual generation conditions. Number of beads generated per second expressed concerning the increase in: A) dispersed water flow (from 2.5 to 4.0 µL/min), and B) calcium chloride flow (from 0.5 to 1.5 µL/min) for the FFJ device; and C) dispersed water flow (from 2.5 to 4.0 µL/min), and D) calcium chloride flow (from 0.5 to 1.5 µL/min) for the TJ device

In *Figure 4.2* the histograms illustrate the relationship between the variations in dispersed phase flows ($CaCl_2$ – *Figure 4.2A & C*, water – *Figure 4.2B & D*) and the frequency of droplet generation for FFJ and TJ.

Generally, FFJ showed a higher droplets/sec production up to 975 droplets/sec for FFJ_{75mM}_F. Notably, peaks in frequency of production are observed for the conditions FFJ_{75mM}_C (932 droplets/sec), FFJ_{75mM}_F (975 droplets/sec), FFJ_{75mM}_I (911 droplets/sec), where the volumetric flow rate of calcium chloride reaches its maximum at 1.5 µL/min. This underscores how calcium chloride has a greater impact than water in positively influencing the droplet production process in FFJ, a conclusion further supported by the statistical results obtained by the two-way ANOVA analysis reported in *Table 4.2*. Indeed, $CaCl_2$ flow (p-value < 0.0001) showed greater influence on droplet formation rather than water flow (P-value < 0.0496). Moreover, no significant interaction between the variables was detected.

Figure 4.2 also illustrates the changes in droplet frequency resulting from an increase in $CaCl_2$ flow (*Figure 4.2C*) and water flow (*Figure 4.2D*) in the case of TJ. From the data, it can be observed that an increase in both water and calcium chloride flow rates causes a notable rise in the generation frequency, which however is quite lower than that of FFJ. Similarly to FFJ, the TJ device exhibits its highest frequency production at higher $CaCl_2$ concentrations (TJ_{75mM}_C, TJ_{75mM}_F, TJ_{75mM} _I; *Figure 4.2C*). However, the *Figure 4.2C* indicates that water also significantly impacts the production frequency, registering a peak under H_2O = 4.0 µL/min flow conditions (TJ_{75mM}_G, TJ_{75mM}_H, TJ_{75mM}_I). Indeed, two-way ANOVA supported this hypothesis revealing high impact of both variables ($CaCl_2$ flow: p-value < 0.0001; water flow: p-value < 0.0001). Additionally, the statistical analysis highlighted a significant interaction between the variables (interaction: p-value = 0.0329), which however still remains not extremely high. Further analyses on the droplet equivalent diameter are available in the Appendix IV.

Table 4.2 Two-way ANOVA analysis of the frequency of droplets generation for FFJ and TJ devices.

	Source of variation	% of total variation	p-value	p-value summary
FFJ	Interaction	3,956	0.3999	ns
	$CaCl_2$ Flow	82,75	<0.0001	****
	Water Flow	6,818	0.0496	*
TJ	Interaction	4,963	0.0329	*
	$CaCl_2$ Flow	31,51	<0.0001	****
	Water Flow	56,82	<0.0001	****

Alginate microcarriers generation. After carefully examining the operation of each device, the focus is now shifted on analyzing the optimal conditions for generating sodium alginate beads. Here, the experimental results related to three fundamental parameters are explored, namely: equivalent diameter (Eq. Diameter), circularity, and polydispersity index (PDI). These results were obtained by considering each individual generation condition, both using FFJ and TJ microfluidic platforms. In particular, after completing the generation process for each condition, the droplets were collected at the chip outlet into 30 mM $CaCl_2$ centrifugated (1 minute at 1500 rpm) and three aliquots of 100 µL were analyzed *via* confocal microscopy.

FFJ. Results obtained from the acquired images are summarized in *Table 4.3*. Samples generated with higher volumetric flow rates and higher concentration of calcium chloride exhibit greater polydispersity (samples FFJ_{150mM}_C, E, F, and H). Indeed, beads obtained with a higher concentration of calcium chloride (150mM) show general higher PDI values

compared to experiments conducted with $CaCl_2$ (75mM). This can be attributed to the cross-linking kinetic. In a lower concentrated sample, the gelation process is slower allowing the uniform diffusion of the calcium ions throughout the entire volume producing highly monodisperse microgels. On the other side, high Ca^{2+} concentration led to rapid and inhomogeneous gelation with crosslinking times lower than the diffusion time required to the ions to occupy the entire droplet volume. As a consequence, the produced microbeads are polydisperse and show the characteristic tail splash (Appendix IV). However, in the 75 mM syntheses the higher PDI values are recorded under the conditions FFJ_{75mM}_B and FFJ_{75mM}_C, which are characterized by a lower volumetric flow of water. This phenomenon can be explained by the lower quantity of water that results in a higher concentration of calcium ions within the formed microspheres, promoting non-uniform gelation.

Table 4.3 Data obtained for the FFJ device using $CaCl_2$ concentrations of 150 mM and 75 mM.

FFJ	**A**	**B**	**C**	**D**	**E**	**F**	**G**	**H**	**I**
Eq. Diameter$_{150mM}$ [µm]	50.62 ± 5.56	45.12 ± 4.35	49.67 ± 9.58	48.17 ± 3.17	58.31 ± 11.49	63.23 ± 15.37	49.04 ± 3.65	56.52 ± 10.74	71.14 ± 10.22
Circularity$_{150mM}$	0.89 ± 0.05	0.84 ± 0.04	0.86 ± 0.06	0.91 ± 0.03	0.85 ± 0.05	0.83 ± 0.08	0.88 ± 0.07	0.83 ± 0.09	0.81 ± 0.07
PDI	0.11	0.10	0.19	0.07	0.20	0.24	0.07	0.19	0.14
Eq. Diameter$_{75mM}$ [µm]	52.83 ± 2.15	48.64 ±5.32	45.95 ± 5.33	53.62 ± 3.25	47.17 ± 4.09	44.58 ±3.21	58.83 ± 5.13	45.43 ± 4.18	46.87 ±3.37
Circularity$_{75mM}$	0.95 ± 0.02	0.88 ± 0.07	0.89 ± 0.06	0.94 ± 0.04	0.82 ± 0.09	0.90 ± 0.95	0.97 ± 0.01	0.84 ± 0.09	0.80 ± 0.10
PDI	0.04	0.11	0.12	0.06	0.09	0.07	0.09	0.09	0.06

Figure 4.3 illustrates how the equivalent diameter and circularity of microbeads vary based on water and $CaCl_2$ flow rates. Syntheses were conducted at two different $CaCl_2$ concentration: 150 mM (*Figure 4.3A*) and 75 mM (*Figure 4.3B*). When using a $CaCl_2$ concentration of 150 mM, increasing the flow rate of the dispersed phase (both water and $CaCl_2$flows) leads to a significant enlargement of the alginate beads size (*Figure 4.3A I.* and *II.*).

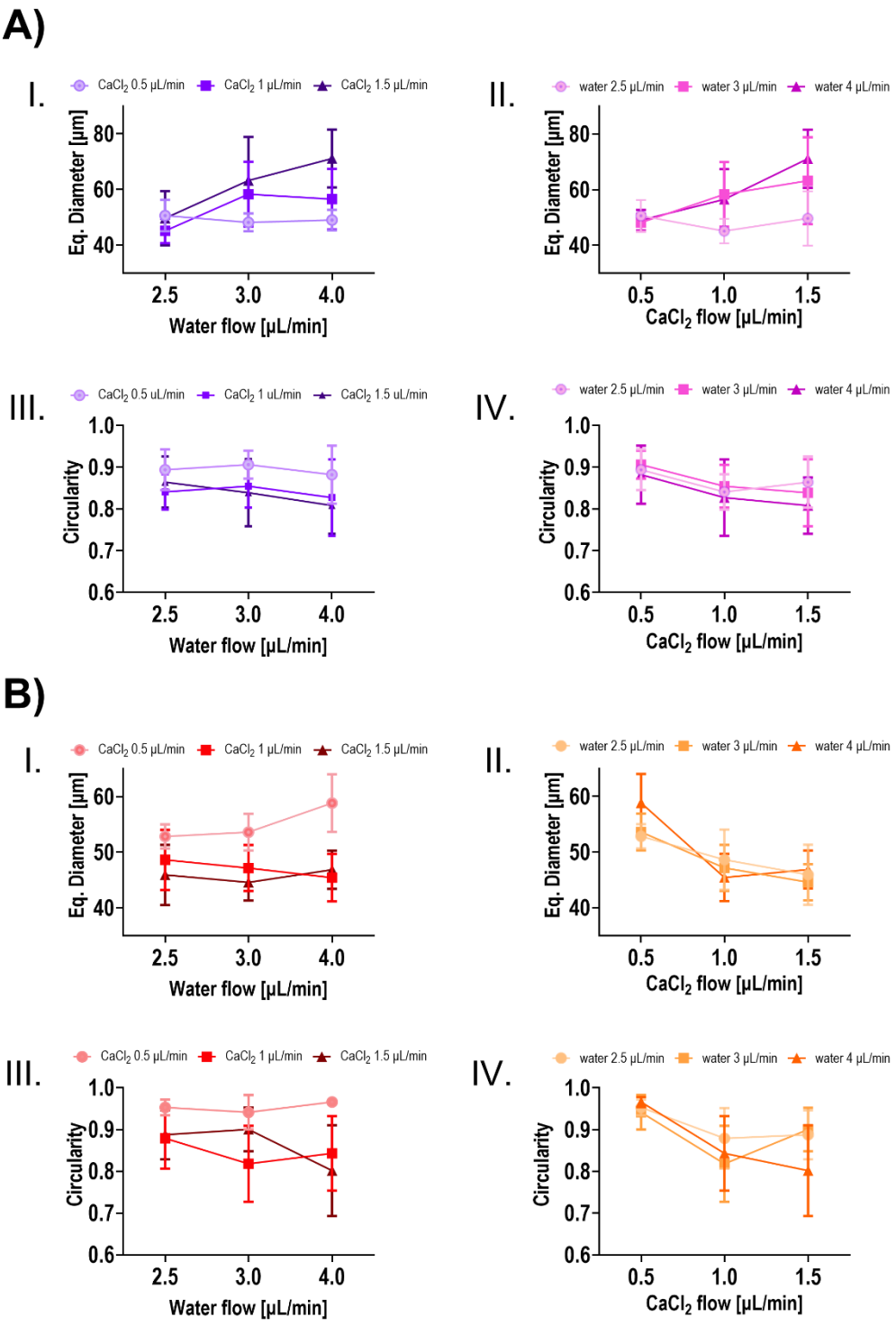

Figure 4.3 FFJ: A) effect of the variation of water and $CaCl_2$ flows on equivalent diameter (I & II) and circularity (III & IV) when using an initial calcium chloride concentration of 150 mM; B) effect of the variation of water and $CaCl_2$ flows on equivalent diameter (I & II) and circularity (III & IV) when using an initial calcium chloride concentration of 75 mM.

Regarding circularity (*Figure 4.3A III.* and *IV.*), lower values of the flow rate of calcium chloride result in higher circularity values, confirming the key role of the $CaCl_2$

concentration in defining the morphological feature of the alginate beads, as previously discussed for the PDI.

In contrast, at 75mM $CaCl_2$, the equivalent diameter of the microbeads remains relatively stable with increasing water flow (*Figure 4.3B I.*). However, a slight decrease in microbeads size can be highlighted in relation with the raises of calcium chloride flow (*Figure 4.3B II.*). It can be assumed that at lower $CaCl_2$ concentrations (*e.g.* $CaCl_{2_{Flux}} \sim 0.5$ µL/min), the lack of Ca^{2+} ions in the reaction mixture results in a low rate of cross-linking of the alginate layer. This leads to larger microcapsules as a consequence of the swelling of the polymer matrix when the crosslinked droplet is transferred from the oil to the water phase.[253] This trend is further supported by *Figure S2* (*Appendix IV*), which confirm that aqueous droplet formed under low calcium chloride and water flow conditions are smaller than the resulting cross-linked alginate beads, which exhibited therefore a swollen size in water.

In line with findings on the equivalent diameter, Similar trends are observed for circularity (*Figure 4.3B III.* and *IV*). Specifically, a marked reduction in the circularity with an increase in the flow rate of both water and calcium chloride is shown. The highest circularity value (0.98) is recorded under the FFJ_{75mM}_G condition, with equally satisfactory values for FFJ_{75mM}_A and FFJ_{75mM}_D, all characterized by a lower concentration of calcium ions.

Table 4.4 FFJ: Two-way ANOVA analysis of the acquired OFF-CHIP beads equivalent diameter and circularity for both 150 mM and 75 mM $CaCl_2$ conditions.

		Source of Variation	% of total variation	p- value	p-value summary
FFJ_{150mM}	Eq. diameter	Interaction	12.22	<0.0001	****
		$CaCl_2$ Flow	17.15	<0.0001	****
		Water Flow	13.61	<0.0001	****
	Circularity	Interaction	1.742	0.2315	ns
		$CaCl_2$ Flow	14.13	<0.0001	****
		Water Flow	3.431	0.0044	**
FFJ_{75mM}	Eq. diameter	Interaction	6.856	0.0009	***
		$CaCl_2$ Flow	0.3750	0.5897	ns
		Water Flow	0.2835	0.6707	ns
	Circularity	Interaction	13.05	<0.0001	****
		$CaCl_2$ Flow	26.87	<0.0001	****
		Water Flow	5.154	<0.0001	****

All the collected data were further analyzed through two-way ANOVA test and results are shown in *Table 4.4*. The statistical analysis corroborates the aforementioned findings and elucidates the pivotal role of the interaction between the analyzed variables.

TJ. Droplet formation in TJ devices is primarily influenced by the continuous phase flow. Because only variations in the dispersed phase flows are explored, it is reasonable to posit that the analyzed samples will exhibit a low polydispersity index (PDI) and constant bead sizes, in accordance with the observations made in the previous section regarding the operation of the devices.

Data reported in *Table 4.5* highlights minimal variation in polydispersity within the analyzed groups. However, different concentrations of calcium chloride led to the formation of more uniform microspheres with well-distributed sizes.

Table 4.5 List of the data obtained for the TJ device using $CaCl_2$ concentrations of 150 mM and 75 mM.

TJ	A	B	C	D	E	F	G	H	I
Eq. Diameter$_{150mM}$ [μm]	131.48 ± 20.36	140.21 ± 9.31	136.38 ± 7.56	137.67 ± 13.54	129.24 ± 11.73	140.01 ± 8.68	138.96 ± 14.81	137.05 ± 7.81	135.73 ± 11.03
Circularity$_{150mM}$	0.86 ± 0.07	0.86 ± 0.04	0.60 ± 0.18	0.88 ± 0.07	0.87 ± 0.06	0.71 ± 0.13	0.86 ± 0.07	0.83 ± 0.05	0.77 ± 0.08
PDI	0.16	0.07	0.06	0.10	0.09	0.06	0.11	0.06	0.08
Eq. Diameter$_{75mM}$ [μm]	145.12 ± 15.24	146.72 ± 13.83	148.65 ± 10.53	148.16 ± 25.64	143.92 ± 22.56	140.80 ± 11.31	152.69 ± 24.27	133.38 ± 19.82	140.80 ± 12.35
Circularity$_{75mM}$	0.92 ± 0.08	0.84 ± 0.13	0.78 ± 0.17	0.90 ± 0.09	0.89 ± 0.09	0.83 ± 0.11	0.92 ± 0.06	0.89 ± 0.09	0.81 ± 0.11
PDI	0.11	0.09	0.07	0.17	0.16	0.08	0.16	0.15	0.11

The presence of a higher concentration of divalent ions (150 mM) within the gel network enhances the cross-linking reaction, ensuring effective microsphere gelation. However, this effect diminishes when the calcium chloride concentration is reduced to 75 mM and the dispersed phase flow rate is lowered. Under these conditions, the T-junction microfluidic device generates larger droplets (~150 μm), which may hinder complete gelation due to insufficient crosslinker concentration. This setup increases the risk of droplet coalescence within the exit channel. To mitigate this, the collection solution containing 30 mM calcium chloride supports the completion of the cross-linking reaction in batch mode. Nonetheless,

this can lead to non-uniform gelation and particle size variability, resulting in a heterogeneous sample characterized by significant polydispersity. Furthermore, a nearly constant trend emerges in the equivalent diameter, both with variations in the volumetric flow of water and the cross-linking agent (*Figure 4.4A I. & II.; 4.4B I. & II.*), confirming the prevalent role of continuous flow rate in defining the dimensions of the generated microgels.

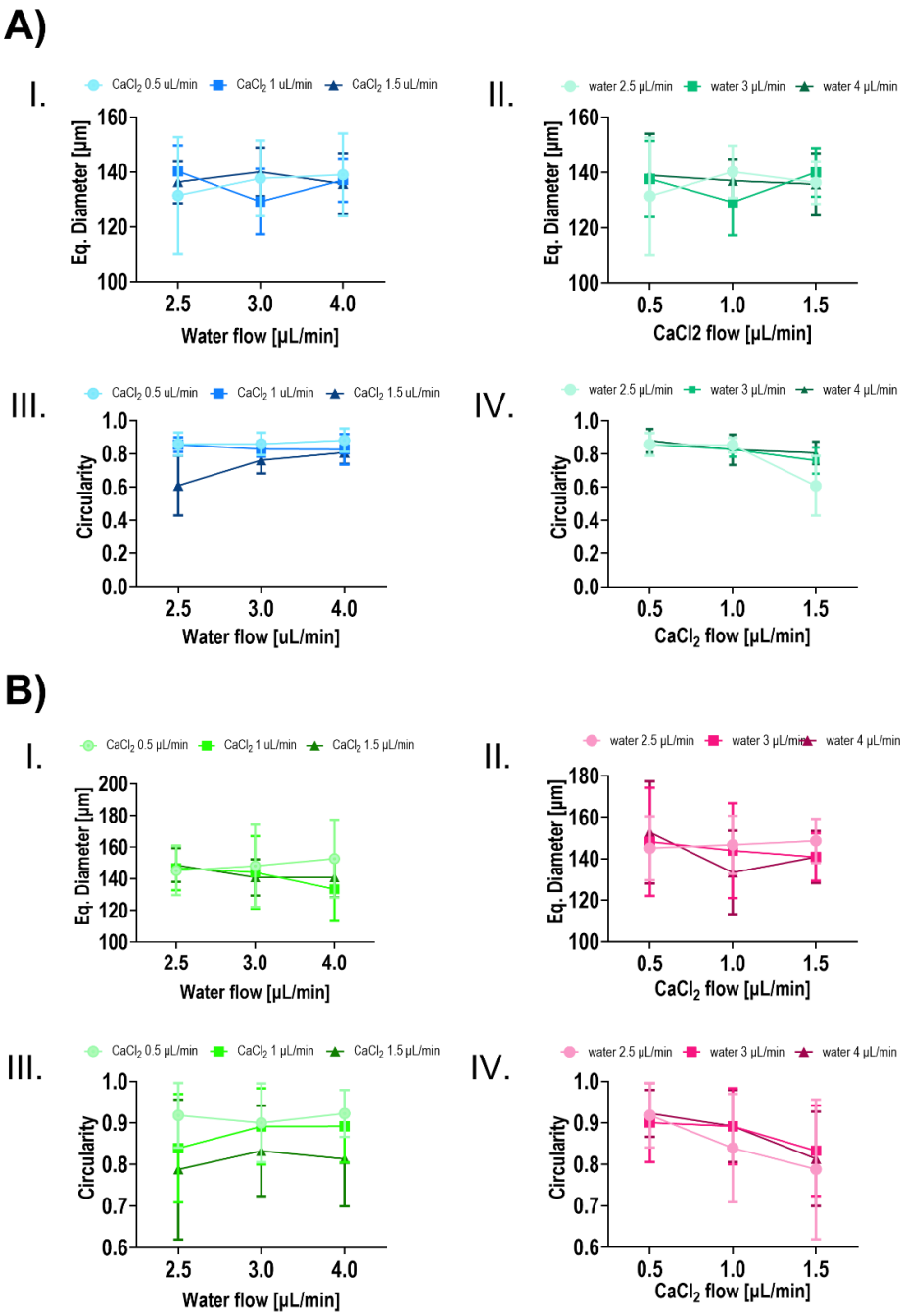

Figure 4.4 TJ: A) effect of the variation of water flow and $CaCl_2$ on equivalent diameter (I. & II.) and circularity (III. & IV) when using an initial calcium chloride concentration of 150 mM; B) effect of the variation of water flow and $CaCl_2$ on equivalent diameter (I. & II.) and circularity (III. & IV) when using an initial calcium chloride concentration of 75 mM.

When discussing the circularity of the produced alginate beads, different observation can be made on the basis of the calcium chloride initial concentration. Synthesizing the microbeads with higher $CaCl_2$ content (150 mM) produced minimal variation in their circular shape when water flow or $CaCl_2$ are changed (*Figure 4.4A III. & IV.*). On the other side, when generating alginate microbeads using low concentrated $CaCl_2$ (75 mM), water flow appeared to have minimal influence (*Figure 4.4B III.*), while the trend due to the variations in cross-linking agent flow rate (*Figure 4.4B IV.*) showed a marked reduction in circularity values linked to the increasing calcium chloride content.

The results of the statistical analyses on the alginate microbeads generated with the TJ device is provided in *Table 4.5*. As expected, the dispersed phase variables had relatively low, or none influence on the equivalent diameter of the microbeads. However, the interaction between water and calcium flows is of considerable importance in the 150 mM case, even if no substantial size change was observed from the graph. Consequently, the performed analysis of variance suggests that, although fluid interaction plays a crucial role, it may have a destructive effect in determining the equivalent diameter.

Table 4.5 TJ: Two-way ANOVA analysis of the acquired OFF-CHIP beads equivalent diameter and circularity for both 150 mM and 75 mM $CaCl_2$ conditions

		Source of Variation	% of total variation	p-value	p-value summary
TJ_{150mM}	Eq. diameter	Interaction	6.856	0.0009	***
		$CaCl_2$ Flow	0.3750	0.5897	ns
		Water Flow	0.2835	0.6707	ns
	Circularity	Interaction	13.05	<0.0001	****
		$CaCl_2$ Flow	26.87	<0.0001	****
		Water Flow	5.154	<0.0001	****
TJ_{75mM}	Eq. diameter	Interaction	4.287	0.0180	*
		$CaCl_2$ Flow	2.650	0.0247	*
		Water Flow	0.9644	0.2568	ns
	Circularity	Interaction	1.396	0.3652	ns
		$CaCl_2$ Flow	13.33	<0.0001	****
		Water Flow	1.210	0.1549	ns

More intriguing results came from the analyses of the circularity. In the case of 150 mM calcium chloride water and calcium flows were found to be highly influential (p-value < 0.0001), so as the interaction between these flows. Similar to the equivalent diameter, this interaction may be a destructive interaction, as can be deduced from *Figures 4.4A III. & IV.*, which demonstrate an almost constant trend as the flows of water and calcium chloride change. To note, under low concentrations of calcium chloride (75mM), only the volumetric

flow rate of the cross-linking agent plays a significant role in defining the microsphere morphology. This phenomenon can be ascribed to a overall lower calcium concentration in the latter case, which causes a slow gelation process. In contrast, the higher $CaCl_2$ level established during the 150 mM synthesis provide fast gelation processes. Therefore, the variation in water flow can influence the mixing efficiency and calcium diffusion within the un-crosslinked droplet revealing its importance.

FFJ vs. TJ. The FFJ device demonstrated superior sensitivity to flow parameters, enabling the production of uniform beads with high circularity and narrow size distribution. This property is particularly advantageous for generating precisely sized, spherical beads suitable for cell encapsulation, as evidenced in *Figure 4.5A*, which highlights the high sphericity achieved post-generation.

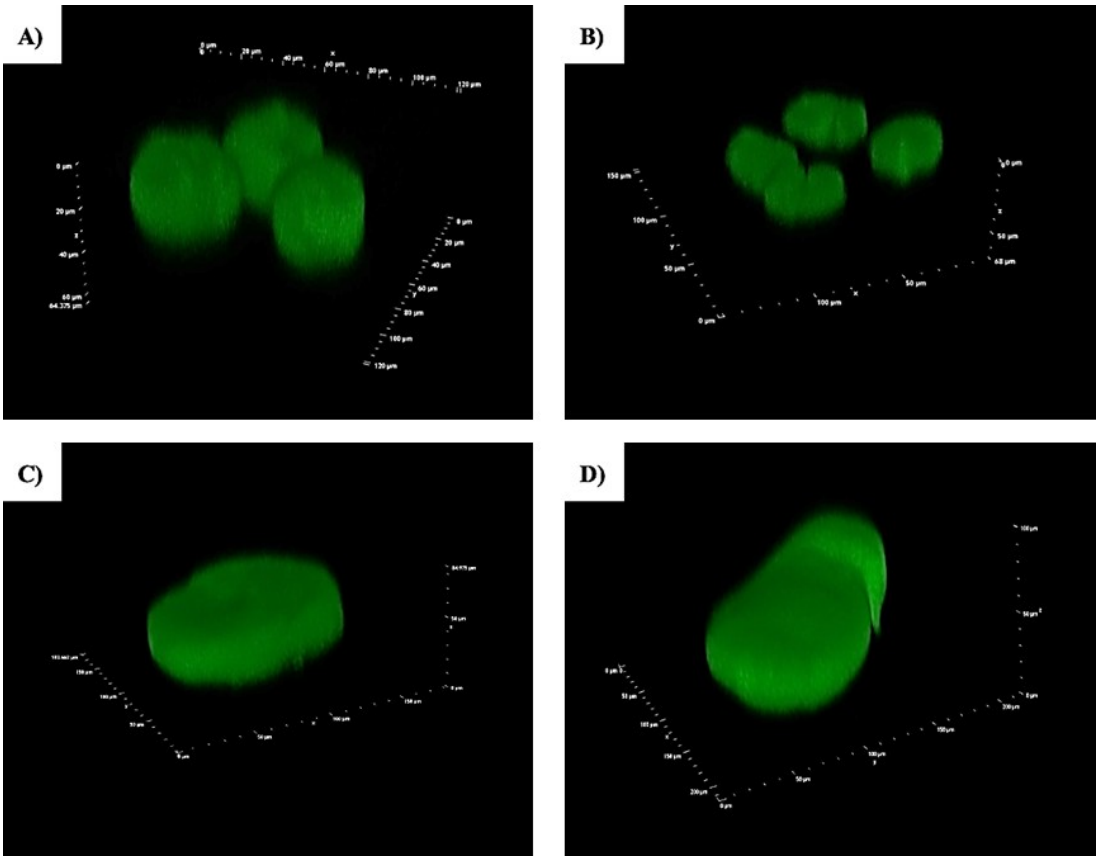

Figure 4.5 Confocal microscopy z-stacks of the alginate microspheres generated by using the FFJ device with flow conditions (A) FFJ_{75mM}_A; (B) FFJ_{75mM}_C; and TJ with flow conditions (C) TJ_{75mM}_A; (D) TJ_{75mM}_C.

In contrast, the TJ device showed less precision in bead production, resulting in a broader dimensional distribution and variable bead shapes, including globular or "sheet-like" forms, as illustrated in *Figure 4.5 C & D*. At higher concentrations, resulting from higher $CaCl_2$

flow rate, the TJ device also exhibited a spray tail (*Figure 4.5D*), whereas the FFJ consistently produced semi-spherical beads (*Figure 4.5B*).

Overall, while both devices effectively produced sodium alginate beads, the FFJ exhibited superior control over flow parameters, achieving greater uniformity and sphericity, in particular at 75 mM $CaCl_2$. Additionally, the FFJ device maintained a tighter dimensional distribution compared to the TJ device, making it more suitable for applications requiring precise bead morphology, such as cell encapsulation.

Cell encapsulation and preliminary evaluation of process biocompatibility. The comparative analysis and optimization of operational parameters revealed the considerable advantages of the FFJ microfluidic device in microsphere production. The device offers several key benefits, including a high generation frequency, the capacity to produce highly monodisperse microspheres, and elevated circularity values, which make it particularly well-suited for cell encapsulation.

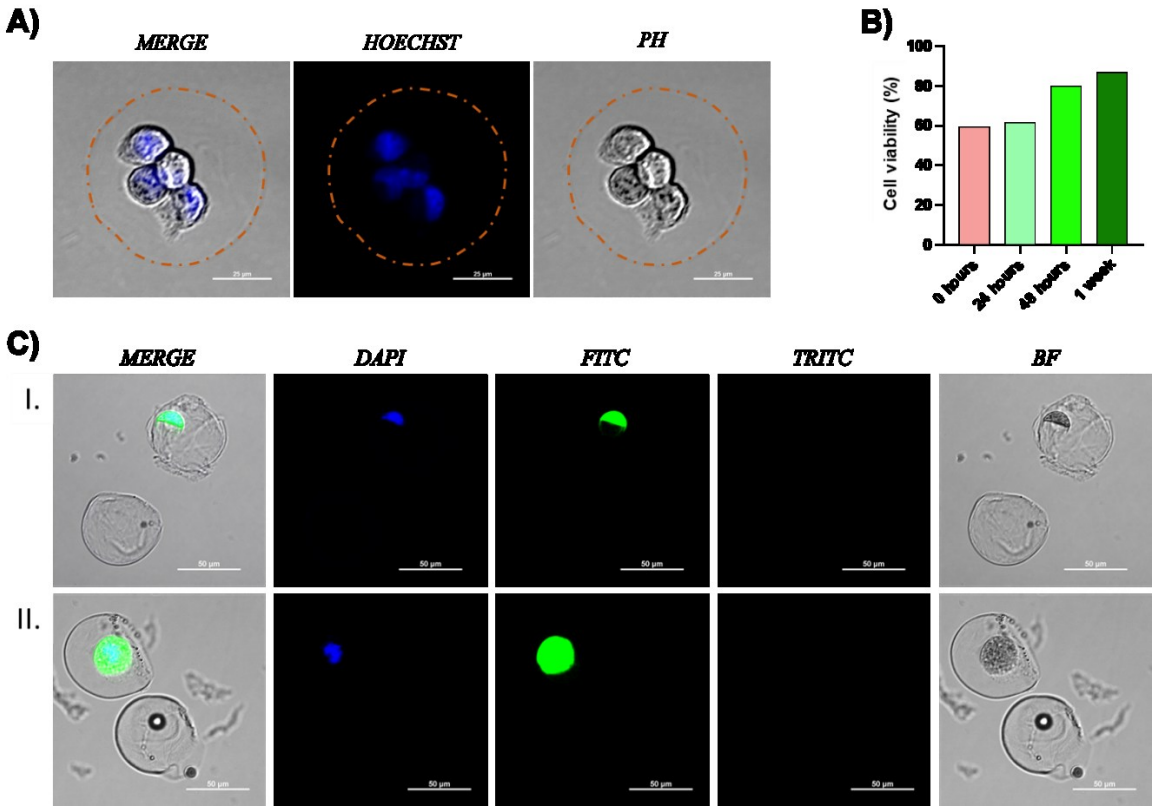

Figure 4.6 A) representative micrographs of the successful encapsulation of SKOV3 cells into alginate microbeads. Blue signals represent the nuclear dye HOECHST and colocalize the nuclei of the encapsulated cells. B) Preliminary evaluation of cell viability at different timepoints: T0, 24h, 48h, 7 days performed through live/dead assay. C) representative micrograph of viable encapsulated cells after 24h in culture.

Based on these findings, the FFJ device was evaluated for its performance in encapsulating the SKOV3 cell line under optimized generation conditions (FFJ_{75mM}_A), which achieved the lowest PDI and the highest circularity.

Following the selected synthesis, droplets were collected at the outlet of the microfluidic device and separated through centrifugation. The collected volume was placed in a multi-well plate and separated beads were analyzed under confocal microscopy. As illustrated in *Figure 4.6A*, the successful encapsulation of cells can be observed, and the precise localization of these cells within the alginate bead is revealed through the co-localization of the Hoechst blue signal with the cell nuclei.

Subsequently, cell viability was assessed through a fluorescence assay employing the live/dead viability/cytotoxicity assay methodology. This method allows for the distinction between live and dead cells through the simultaneous staining of green fluorescent calcein, which highlights intracellular activity, and red fluorescent ethidium homodimer-1, which indicates loss of plasma membrane integrity. The cell viability ratios, which indicate the percentage of live cells to total cells, are depicted in *Figure 4.6B*. The preliminary results (obtained from a single experiment) demonstrated an initial loss in cell viability (60% of viable cells at T0), followed by a progressive recovery of optimal cell viability after one week of cell culture without exchange of media. *Figure 4.6C* reports representative images of viable encapsulated cells after 24 hours. The data indicate a favorable trend over time, suggesting the potential for culturing encapsulated cells for extended periods, up to a week at least.

4.2 Conclusions

This study undertook a comprehensive investigation of the performance of two distinct microfluidic devices, designated as FFJ and TJ, in the generation of alginate microbeads. By examining the impact of water and calcium chloride flows on pivotal parameters such as droplet frequency, polydispersity, size, and circularity, the research yielded invaluable insights into the operational dynamics of these systems. Two-way ANOVA demonstrated that calcium chloride flow plays a predominant role in determining critical outcomes such as circularity and equivalent diameter, regardless of device geometry.

The findings highlighted the superior performance of the FFJ device, which demonstrated higher droplet generation frequencies, lower PDI, and beads with smaller sizes and enhanced circularity. These attributes render the FFJ device especially advantageous for applications that require precise control of the microbeads generation, such as single-cell encapsulation. Preliminary validation experiments further demonstrated the FFJ's capability to encapsulate SKOV3 cells in alginate microbeads, with biocompatibility confirmed over a seven-day period. This highlights the robustness and practicality of the entire process.

In addition to demonstrating the feasibility of the FFJ for single-cell encapsulation, this work also elucidates the intricate interplay between device geometry and process parameters in shaping alginate microgels through ionic gelation. These findings not only establish a strong foundation for the application of microfluidic systems in biomedical research but also pave the way for future innovations in cell encapsulation technologies for advanced biological assays and therapeutic developments.

PART V
CONCLUSIONS

5. Conclusions

The present work reports novel strategies and validations in the synthesis, and application of nanomaterials and microfluidic technologies for drug delivery and single-cell encapsulation scenarios. Innovative solutions, integrating novel techniques and the use of statistical modeling, were provided to address the limitations of conventional methodologies, such as poor batch-to-batch reproducibility, limited scalability, and constrained material design.

In particular, a new Mixed Emulsion/Evaporation Technique (MEET) was developed to synthesize HA-LPEI NGs. The objective was to overcome the constraints of hydrophobic/hydrophilic polymer coupling in traditional emulsion/evaporation synthesis. The resulting hydrophilic NGs were tested for their stability, controlled drug release, and selective targeting via CD44 receptor interactions in ovarian cancer cells. Successively, NGs were surface functionalized with folate functionalities to target alpha-FR-overexpressing cancer cells. Indeed, comparative cellular uptake studies were performed in tumoral and non-tumoral cellular models highlighting the selective uptake of the synthesized nanomaterials. These findings underline the potential of these NG systems in achieving precise and efficient drug delivery with minimal off-target effects.

Additionally, a deep investigation on the design and application of advanced microfluidic devices in the synthesis of polymeric nanocarriers was performed. Indeed, a novel droplet-based microfluidic chip endowed with pneumatic micro-actuation of the flow-focusing geometry facilitated on-demand control of HA-LPEI NG size and monodispersity. Results highlighted the direct influence of the NGs physical properties on drug release profiles and, as a consequence, on the enhanced therapeutic outcomes. Moreover, robust predictive models were developed using a Response Surface Methodology (RSM). The aim of this statistical framework was to optimize NG properties based on synthesis parameters (Flow Rate Ration, FRR, & Molar Ratio, MR), streamlining the design and production processes for drug delivery systems.

In parallel, the performances of two microfluidic device geometries, flow-focusing junction (FFJ) and T-junction (TJ), in the generation of alginate microbeads for single-cell encapsulation were investigated. In general, FFJ device outperformed the TJ device providing higher droplet generation frequencies, lower polydispersity, and enhanced microbeads circularity. Altogether, these results led to the choice of FFJ device for the encapsulation of Serous Cystadenocarcinoma Ovary-3 (SKOV3) cells with confirmed process

biocompatibility, up to 7 days post-encapsulation. This comprehensive analysis of device geometry and process parameters offers a pathway for future advancements in cellular encapsulation and biomedical research.

Collectively, this work not only proposes novel methodologies for NGs synthesis and microfluidic cell encapsulation and functionalized nanomaterials but also provides new insights aiming at the clinical translation of these technologies. The integration of empirical modeling, functionalized materials, and innovative device designs positions this research as a step forward in nanomedicine and biomedical engineering. These contributions not only address existing limitations in the literature but also set the stage for future advancements in targeted therapies, personalized medicine, and single-cell analysis technologies.

Bibliography.

(1) Joudeh, N.; Linke, D. Nanoparticle Classification, Physicochemical Properties, Characterization, and Applications: A Comprehensive Review for Biologists. *J. Nanobiotechnology* **2022**, *20* (1), 262. https://doi.org/10.1186/s12951-022-01477-8.

(2) Roduner, E. Size Matters: Why Nanomaterials Are Different. *Chem. Soc. Rev.* **2006**, *35* (7), 583–592. https://doi.org/10.1039/B502142C.

(3) Eker, F.; Duman, H.; Akdaşçi, E.; Bolat, E.; Sarıtaş, S.; Karav, S.; Witkowska, A. M. A Comprehensive Review of Nanoparticles: From Classification to Application and Toxicity. *Molecules* **2024**, *29* (15), 3482. https://doi.org/10.3390/molecules29153482.

(4) Jiao, M.; Zhang, P.; Meng, J.; Li, Y.; Liu, C.; Luo, X.; Gao, M. Recent Advancements in Biocompatible Inorganic Nanoparticles towards Biomedical Applications. *Biomater. Sci.* **2018**, *6* (4), 726–745. https://doi.org/10.1039/C7BM01020F.

(5) Tan, M. C.; Chow, G. M.; Ren, L.; Zhang, Q. Inorganic Nanoparticles for Biomedical Applications. In *NanoScience in Biomedicine*; Shi, D., Ed.; Springer: Berlin, Heidelberg, 2009; pp 272–289. https://doi.org/10.1007/978-3-540-49661-8_11.

(6) Giner-Casares, J. J.; Henriksen-Lacey, M.; Coronado-Puchau, M.; Liz-Marzán, L. M. Inorganic Nanoparticles for Biomedicine: Where Materials Scientists Meet Medical Research. *Mater. Today* **2016**, *19* (1), 19–28. https://doi.org/10.1016/j.mattod.2015.07.004.

(7) Khan, I.; Saeed, K.; Khan, I. Nanoparticles: Properties, Applications and Toxicities. *Arab. J. Chem.* **2019**, *12* (7), 908–931. https://doi.org/10.1016/j.arabjc.2017.05.011.

(8) Eatemadi, A.; Daraee, H.; Karimkhanloo, H.; Kouhi, M.; Zarghami, N.; Akbarzadeh, A.; Abasi, M.; Hanifehpour, Y.; Joo, S. W. Carbon Nanotubes: Properties, Synthesis, Purification, and Medical Applications. *Nanoscale Res. Lett.* **2014**, *9* (1), 393. https://doi.org/10.1186/1556-276X-9-393.

(9) Liu, R.; Luo, C.; Pang, Z.; Zhang, J.; Ruan, S.; Wu, M.; Wang, L.; Sun, T.; Li, N.; Han, L.; Shi, J.; Huang, Y.; Guo, W.; Peng, S.; Zhou, W.; Gao, H. Advances of Nanoparticles as Drug Delivery Systems for Disease Diagnosis and Treatment. *Chin. Chem. Lett.* **2023**, *34* (2), 107518. https://doi.org/10.1016/j.cclet.2022.05.032.

(10) Ezike, T. C.; Okpala, U. S.; Onoja, U. L.; Nwike, C. P.; Ezeako, E. C.; Okpara, O. J.; Okoroafor, C. C.; Eze, S. C.; Kalu, O. L.; Odoh, E. C.; Nwadike, U. G.; Ogbodo, J. O.; Umeh, B. U.; Ossai, E. C.; Nwanguma, B. C. Advances in Drug Delivery Systems, Challenges and Future Directions. *Heliyon* **2023**, *9* (6), e17488. https://doi.org/10.1016/j.heliyon.2023.e17488.

(11) Joudeh, N.; Linke, D. Nanoparticle Classification, Physicochemical Properties, Characterization, and Applications: A Comprehensive Review for Biologists. *J. Nanobiotechnology* **2022**, *20* (1), 262. https://doi.org/10.1186/s12951-022-01477-8.

(12) Singh, D.; Singh, S.; Sahu, J.; Srivastava, S.; Singh, M. R. Ceramic Nanoparticles: Recompense, Cellular Uptake and Toxicity Concerns. *Artif. Cells Nanomedicine Biotechnol.* **2016**, *44* (1), 401–409. https://doi.org/10.3109/21691401.2014.955106.

(13) C. Thomas, S.; Harshita; Kumar Mishra, P.; Talegaonkar, S. Ceramic Nanoparticles: Fabrication Methods and Applications in Drug Delivery. *Curr. Pharm. Des.* **2015**, *21* (42), 6165–6188.

(14) Kazemzadeh, H.; Mozafari, M. Fullerene-Based Delivery Systems. *Drug Discov. Today* **2019**, *24* (3), 898–905. https://doi.org/10.1016/j.drudis.2019.01.013.

(15) Jarai, B. M.; Kolewe, E. L.; Stillman, Z. S.; Raman, N.; Fromen, C. A. Polymeric Nanoparticles. In *Nanoparticles for Biomedical Applications*; Elsevier, 2020; pp 303–324. https://doi.org/10.1016/B978-0-12-816662-8.00018-7.

(16) Patra, J. K.; Das, G.; Fraceto, L. F.; Campos, E. V. R.; Rodriguez-Torres, M. D. P.; Acosta-Torres, L. S.; Diaz-Torres, L. A.; Grillo, R.; Swamy, M. K.; Sharma, S.; Habtemariam, S.; Shin, H.-S. Nano Based Drug Delivery Systems: Recent Developments and Future Prospects. *J. Nanobiotechnology* **2018**, *16* (1), 71. https://doi.org/10.1186/s12951-018-0392-8.

(17) Horn, D.; Rieger, J. Organic Nanoparticles in the Aqueous Phase—Theory, Experiment, and Use. *Angew. Chem. Int. Ed.* **2001**, *40* (23), 4330–4361. https://doi.org/10.1002/1521-3773(20011203)40:23<4330::AID-ANIE4330>3.0.CO;2-W.

(18) Lombardo, D.; Kiselev, M. A.; Caccamo, M. T. Smart Nanoparticles for Drug Delivery Application: Development of Versatile Nanocarrier Platforms in Biotechnology and Nanomedicine. *J. Nanomater.* **2019**, *2019* (1), 3702518. https://doi.org/10.1155/2019/3702518.

(19) Alavi, M.; Karimi, N.; Safaei, M. Application of Various Types of Liposomes in Drug Delivery Systems. *Adv. Pharm. Bull.* **2017**, *7* (1), 3–9. https://doi.org/10.15171/apb.2017.002.

(20) Lee, Y.; Thompson, D. h. Stimuli-Responsive Liposomes for Drug Delivery. *WIREs Nanomedicine Nanobiotechnology* **2017**, *9* (5), e1450. https://doi.org/10.1002/wnan.1450.

(21) Vega-Vásquez, P.; Mosier, N. S.; Irudayaraj, J. Nanoscale Drug Delivery Systems: From Medicine to Agriculture. *Front. Bioeng. Biotechnol.* **2020**, *8*, 79. https://doi.org/10.3389/fbioe.2020.00079.

(22) Banik, B. L.; Fattahi, P.; Brown, J. L. Polymeric Nanoparticles: The Future of Nanomedicine. *WIREs Nanomedicine Nanobiotechnology* **2016**, *8* (2), 271–299. https://doi.org/10.1002/wnan.1364.

(23) Mittal, P.; Saharan, A.; Verma, R.; Altalbawy, F. M. A.; Alfaidi, M. A.; Batiha, G. E.-S.; Akter, W.; Gautam, R. K.; Uddin, Md. S.; Rahman, Md. S. Dendrimers: A New Race of Pharmaceutical Nanocarriers. *BioMed Res. Int.* **2021**, *2021* (1), 8844030. https://doi.org/10.1155/2021/8844030.

(24) Chis, A. A.; Dobrea, C.; Morgovan, C.; Arseniu, A. M.; Rus, L. L.; Butuca, A.; Juncan, A. M.; Totan, M.; Vonica-Tincu, A. L.; Cormos, G.; Muntean, A. C.; Muresan, M. L.; Gligor, F. G.; Frum, A. Applications and Limitations of Dendrimers in Biomedicine. *Molecules* **2020**, *25* (17), 3982. https://doi.org/10.3390/molecules25173982.

(25) Fortuni, B.; Inose, T.; Ricci, M.; Fujita, Y.; Van Zundert, I.; Masuhara, A.; Fron, E.; Mizuno, H.; Latterini, L.; Rocha, S.; Uji-i, H. Polymeric Engineering of Nanoparticles for Highly Efficient Multifunctional Drug Delivery Systems. *Sci. Rep.* **2019**, *9* (1), 2666. https://doi.org/10.1038/s41598-019-39107-3.

(26) Sung, Y. K.; Kim, S. W. Recent Advances in Polymeric Drug Delivery Systems. *Biomater. Res.* **2020**, *24* (1), 12. https://doi.org/10.1186/s40824-020-00190-7.

(27) Zhang, X.; Zhang, P. Polymersomes in Nanomedicine - A Review. *Curr. Nanosci.* **2017**, *13* (2), 124–129.

(28) Thambi, T.; Lee, D. S. 15 - Stimuli-Responsive Polymersomes for Cancer Therapy. In *Stimuli Responsive Polymeric Nanocarriers for Drug Delivery Applications*; Makhlouf, A. S. H., Abu-Thabit, N. Y., Eds.; Woodhead Publishing Series in Biomaterials; Woodhead Publishing, 2019; pp 413–438. https://doi.org/10.1016/B978-0-08-101995-5.00016-7.

(29) Leong, J.; Teo, J. Y.; Aakalu, V. K.; Yang, Y. Y.; Kong, H. Engineering Polymersomes for Diagnostics and Therapy. *Adv. Healthc. Mater.* **2018**, *7* (8), 1701276. https://doi.org/10.1002/adhm.201701276.

(30) Ghosh, B.; Biswas, S. Polymeric Micelles in Cancer Therapy: State of the Art. *J. Controlled Release* **2021**, *332*, 127–147. https://doi.org/10.1016/j.jconrel.2021.02.016.

(31) *Progress in Polymeric Micelles for Drug Delivery Applications*. https://www.mdpi.com/1999-4923/14/8/1636 (accessed 2024-11-23).

(32) Grimaudo, M. A.; Concheiro, A.; Alvarez-Lorenzo, C. Nanogels for Regenerative Medicine. *J. Controlled Release* **2019**, *313*, 148–160. https://doi.org/10.1016/j.jconrel.2019.09.015.

(33) Zhang, H.; Zhai, Y.; Wang, J.; Zhai, G. New Progress and Prospects: The Application of Nanogel in Drug Delivery. *Mater. Sci. Eng. C* **2016**, *60*, 560–568. https://doi.org/10.1016/j.msec.2015.11.041.

(34) Duan, Q.-Y.; Zhu, Y.-X.; Jia, H.-R.; Wang, S.-H.; Wu, F.-G. Nanogels: Synthesis, Properties, and Recent Biomedical Applications. *Prog. Mater. Sci.* **2023**, *139*, 101167. https://doi.org/10.1016/j.pmatsci.2023.101167.

(35) *How Softness Matters in Soft Nanogels and Nanogel Assemblies | Chemical Reviews*. https://pubs.acs.org/doi/abs/10.1021/acs.chemrev.2c00035 (accessed 2024-11-23).

(36) Hajebi, S.; Rabiee, N.; Bagherzadeh, M.; Ahmadi, S.; Rabiee, M.; Roghani-Mamaqani, H.; Tahriri, M.; Tayebi, L.; Hamblin, M. R. Stimulus-Responsive Polymeric Nanogels as Smart Drug Delivery Systems. *Acta Biomater.* **2019**, *92*, 1–18. https://doi.org/10.1016/j.actbio.2019.05.018.

(37) Crucho, C. I. C.; Barros, M. T. Polymeric Nanoparticles: A Study on the Preparation Variables and Characterization Methods. *Mater. Sci. Eng. C* **2017**, *80*, 771–784. https://doi.org/10.1016/j.msec.2017.06.004.

(38) Allouche, J. Synthesis of Organic and Bioorganic Nanoparticles: An Overview of the Preparation Methods. In *Nanomaterials: A Danger or a Promise? A Chemical and Biological Perspective*; Brayner, R., Fiévet, F., Coradin, T., Eds.; Springer: London, 2013; pp 27–74. https://doi.org/10.1007/978-1-4471-4213-3_2.

(39) Rao, J. P.; Geckeler, K. E. Polymer Nanoparticles: Preparation Techniques and Size-Control Parameters. *Prog. Polym. Sci.* **2011**, *36* (7), 887–913. https://doi.org/10.1016/j.progpolymsci.2011.01.001.

(40) *Interfacial turbulence: Hydrodynamic instability and the marangoni effect - Sternling - 1959 - AIChE Journal - Wiley Online Library*. https://aiche.onlinelibrary.wiley.com/doi/abs/10.1002/aic.690050421 (accessed 2025-03-03).

(41) Battat, S.; Weitz, D. A.; Whitesides, G. M. An Outlook on Microfluidics: The Promise and the Challenge. *Lab. Chip* **2022**, *22* (3), 530–536. https://doi.org/10.1039/D1LC00731A.

(42) Xie, M.; Zhan, Z.; Li, Y.; Zhao, J.; Zhang, C.; Wang, Z.; Wang, Z. Functional Microfluidics: Theory, Microfabrication, and Applications. *Int. J. Extreme Manuf.* **2024**, *6* (3), 032005. https://doi.org/10.1088/2631-7990/ad2c5f.

(43) Sackmann, E. K.; Fulton, A. L.; Beebe, D. J. The Present and Future Role of Microfluidics in Biomedical Research. *Nature* **2014**, *507* (7491), 181–189. https://doi.org/10.1038/nature13118.

(44) Zhong, Q.; Ding, H.; Gao, B.; He, Z.; Gu, Z. Advances of Microfluidics in Biomedical Engineering. *Adv. Mater. Technol.* **2019**, *4* (6), 1800663. https://doi.org/10.1002/admt.201800663.

(45) Xiang, N.; Ni, Z. Microfluidics for Biomedical Applications. *Biosensors* **2023**, *13* (2), 161. https://doi.org/10.3390/bios13020161.

(46) Squires, T. M.; Quake, S. R. Microfluidics: Fluid Physics at the Nanoliter Scale. *Rev. Mod. Phys.* **2005**, *77* (3), 977–1026. https://doi.org/10.1103/RevModPhys.77.977.

(47) Lee, C.-Y.; Wang, W.-T.; Liu, C.-C.; Fu, L.-M. Passive Mixers in Microfluidic Systems: A Review. *Chem. Eng. J.* **2016**, *288*, 146–160. https://doi.org/10.1016/j.cej.2015.10.122.

(48) Wu, J.; Yadavali, S.; Lee, D.; Issadore, D. A. Scaling up the Throughput of Microfluidic Droplet-Based Materials Synthesis: A Review of Recent Progress and Outlook. *Appl. Phys. Rev.* **2021**, *8* (3), 031304. https://doi.org/10.1063/5.0049897.

(49) Beebe, D. J.; Mensing, G. A.; Walker, G. M. Physics and Applications of Microfluidics in Biology. *Annu. Rev. Biomed. Eng.* **2002**, *4* (1), 261–286. https://doi.org/10.1146/annurev.bioeng.4.112601.125916.

(50) Zhu, P.; Wang, L. Passive and Active Droplet Generation with Microfluidics: A Review. *Lab. Chip* **2017**, *17* (1), 34–75. https://doi.org/10.1039/C6LC01018K.

(51) Whitesides, G. M. The Origins and the Future of Microfluidics. *Nature* **2006**, *442* (7101), 368–373. https://doi.org/10.1038/nature05058.

(52) Geng, Y.; Ling, S.; Huang, J.; Xu, J. Multiphase Microfluidics: Fundamentals, Fabrication, and Functions. *Small* **2020**, *16* (6), 1906357. https://doi.org/10.1002/smll.201906357.

(53) Leman, M.; Abouakil, F.; Griffiths, A. D.; Tabeling, P. Droplet-Based Microfluidics at the Femtolitre Scale. *Lab. Chip* **2015**, *15* (3), 753–765. https://doi.org/10.1039/C4LC01122H.

(54) Amirifar, L.; Besanjideh, M.; Nasiri, R.; Shamloo, A.; Nasrollahi, F.; De Barros, N. R.; Davoodi, E.; Erdem, A.; Mahmoodi, M.; Hosseini, V.; Montazerian, H.; Jahangiry, J.; Darabi, M. A.; Haghniaz, R.; Dokmeci, M. R.; Annabi, N.; Ahadian, S.; Khademhosseini, A. Droplet-Based Microfluidics in Biomedical Applications. *Biofabrication* **2022**, *14* (2), 022001. https://doi.org/10.1088/1758-5090/ac39a9.

(55) Moragues, T.; Arguijo, D.; Beneyton, T.; Modavi, C.; Simutis, K.; Abate, A. R.; Baret, J.-C.; deMello, A. J.; Densmore, D.; Griffiths, A. D. Droplet-Based Microfluidics. *Nat. Rev. Methods Primer* **2023**, *3* (1), 32.

(56) Chen, Z.; Kheiri, S.; Young, E. W. K.; Kumacheva, E. Trends in Droplet Microfluidics: From Droplet Generation to Biomedical Applications. *Langmuir* **2022**, *38* (20), 6233–6248. https://doi.org/10.1021/acs.langmuir.2c00491.

(57) Ming Zhang, J.; A. Aguirre-Pablo, A.; Qiang Li, E.; Buttner, U.; T. Thoroddsen, S. Droplet Generation in Cross-Flow for Cost-Effective 3D-Printed "Plug-and-Play" Microfluidic Devices. *RSC Adv.* **2016**, *6* (84), 81120–81129. https://doi.org/10.1039/C6RA11724D.

(58) Zhang, J.; Xu, W.; Xu, F.; Lu, W.; Hu, L.; Zhou, J.; Zhang, C.; Jiang, Z. Microfluidic Droplet Formation in Co-Flow Devices Fabricated by Micro 3D Printing. *J. Food Eng.* **2021**, *290*, 110212. https://doi.org/10.1016/j.jfoodeng.2020.110212.

(59) Lashkaripour, A.; Rodriguez, C.; Ortiz, L.; Densmore, D. Performance Tuning of Microfluidic Flow-Focusing Droplet Generators. *Lab. Chip* **2019**, *19* (6), 1041–1053. https://doi.org/10.1039/C8LC01253A.

(60) Li, Z.; Leshansky, A. M.; Pismen, L. M.; Tabeling, P. Step-Emulsification in a Microfluidic Device. *Lab. Chip* **2015**, *15* (4), 1023–1031. https://doi.org/10.1039/C4LC01289E.

(61) Nan, L.; Zhang, H.; Weitz, D. A.; Shum, H. C. Development and Future of Droplet Microfluidics. *Lab. Chip* **2024**, *24* (5), 1135–1153. https://doi.org/10.1039/D3LC00729D.

(62) van Loo, S.; Stoukatch, S.; Kraft, M.; Gilet, T. Droplet Formation by Squeezing in a Microfluidic Cross-Junction. *Microfluid. Nanofluidics* **2016**, *20* (10), 146. https://doi.org/10.1007/s10404-016-1807-1.

(63) Fu, T.; Wu, Y.; Ma, Y.; Li, H. Z. Droplet Formation and Breakup Dynamics in Microfluidic Flow-Focusing Devices: From Dripping to Jetting. *Chem. Eng. Sci.* **2012**, *84*, 207–217. https://doi.org/10.1016/j.ces.2012.08.039.

(64) Montanero, J. M.; Gañán-Calvo, A. M. Dripping, Jetting and Tip Streaming. *Rep. Prog. Phys.* **2020**, *83* (9), 097001. https://doi.org/10.1088/1361-6633/aba482.

(65) Zhu, P.; Kong, T.; Kang, Z.; Tian, X.; Wang, L. Tip-Multi-Breaking in Capillary Microfluidic Devices. *Sci. Rep.* **2015**, *5* (1), 11102. https://doi.org/10.1038/srep11102.

(66) Sharma, S.; Parveen, R.; Chatterji, B. P. Toxicology of Nanoparticles in Drug Delivery. *Curr. Pathobiol. Rep.* **2021**, *9* (4), 133–144. https://doi.org/10.1007/s40139-021-00227-z.

(67) El-Say, K. M.; El-Sawy, H. S. Polymeric Nanoparticles: Promising Platform for Drug Delivery. *Int. J. Pharm.* **2017**, *528* (1–2), 675–691. https://doi.org/10.1016/j.ijpharm.2017.06.052.

(68) Odegard, G. M.; Clancy, T. C.; Gates, T. S. Modeling of the Mechanical Properties of Nanoparticle/Polymer Composites *. In *Characterization of Nanocomposites*; Jenny Stanford Publishing, 2017.

(69) Pulingam, T.; Foroozandeh, P.; Chuah, J.-A.; Sudesh, K. Exploring Various Techniques for the Chemical and Biological Synthesis of Polymeric Nanoparticles. *Nanomaterials* **2022**, *12* (3), 576. https://doi.org/10.3390/nano12030576.

(70) Yao, F.; Zhu, P.; Chen, J.; Li, S.; Sun, B.; Li, Y.; Zou, M.; Qi, X.; Liang, P.; Chen, Q. Synthesis of Nanoparticles via Microfluidic Devices and Integrated Applications. *Microchim. Acta* **2023**, *190* (7), 256. https://doi.org/10.1007/s00604-023-05838-4.

(71) Zhang, Q.; Kuang, G.; Wang, L.; Fan, L.; Zhao, Y. Tailoring Drug Delivery Systems by Microfluidics for Tumor Therapy. *Mater. Today* **2024**, *73*, 151–178. https://doi.org/10.1016/j.mattod.2024.01.004.

(72) Ma, J.; Lee, S. M.-Y.; Yi, C.; Li, C.-W. Controllable Synthesis of Functional Nanoparticles by Microfluidic Platforms for Biomedical Applications – a Review. *Lab. Chip* **2017**, *17* (2), 209–226. https://doi.org/10.1039/C6LC01049K.

(73) Khizar, S.; Zine, N.; Errachid, A.; Jaffrezic-Renault, N.; Elaissari, A. Microfluidic-Based Nanoparticle Synthesis and Their Potential Applications. *ELECTROPHORESIS* **2022**, *43* (7–8), 819–838. https://doi.org/10.1002/elps.202100242.

(74) Karnik, R.; Gu, F.; Basto, P.; Cannizzaro, C.; Dean, L.; Kyei-Manu, W.; Langer, R.; Farokhzad, O. C. Microfluidic Platform for Controlled Synthesis of Polymeric Nanoparticles. *Nano Lett.* **2008**, *8* (9), 2906–2912. https://doi.org/10.1021/nl801736q.

(75) Hamdallah, S. I.; Zoqlam, R.; Erfle, P.; Blyth, M.; Alkilany, A. M.; Dietzel, A.; Qi, S. Microfluidics for Pharmaceutical Nanoparticle Fabrication: The Truth and the Myth. *Int. J. Pharm.* **2020**, *584*, 119408. https://doi.org/10.1016/j.ijpharm.2020.119408.

(76) Galan, E. A.; Zhao, H.; Wang, X.; Dai, Q.; Huck, W. T. S.; Ma, S. Intelligent Microfluidics: The Convergence of Machine Learning and Microfluidics in Materials Science and Biomedicine. *Matter* **2020**, *3* (6), 1893–1922. https://doi.org/10.1016/j.matt.2020.08.034.

(77) Heshmatnezhad, F.; Nazar, A. R. S. Synthesis of Polycaprolactone Nanoparticles through Flow-Focusing Microfluidic-Assisted Nanoprecipitation. *Chem. Eng. Technol.* **2020**, *43* (10), 2073–2082. https://doi.org/10.1002/ceat.202000222.

(78) Fabozzi, A.; Della Sala, F.; Di Gennaro, M.; Borzacchiello, A. Synthesis of Hyaluronic Acid Core–Shell Nanoparticles *via* Simple Microfluidic-Assisted Nanoprecipitation Method for Active Tumor Targeting. *New J. Chem.* **2022**, *46* (41), 19763–19772. https://doi.org/10.1039/D2NJ03279A.

(79) Bovone, G.; Guzzi, E. A.; Tibbitt, M. W. Flow-Based Reactor Design for the Continuous Production of Polymeric Nanoparticles. *AIChE J.* **2019**, *65* (12), e16840. https://doi.org/10.1002/aic.16840.

(80) Baby, T.; Liu, Y.; Yang, G.; Chen, D.; Zhao, C.-X. Microfluidic Synthesis of Curcumin Loaded Polymer Nanoparticles with Tunable Drug Loading and pH-Triggered Release. *J. Colloid Interface Sci.* **2021**, *594*, 474–484. https://doi.org/10.1016/j.jcis.2021.03.035.

(81) Shestopalov, I.; Tice, J. D.; Ismagilov, R. F. Multi-Step Synthesis of Nanoparticles Performed on Millisecond Time Scale in a Microfluidic Droplet-Based System. *Lab. Chip* **2004**, *4* (4), 316. https://doi.org/10.1039/b403378g.

(82) Abalde-Cela, S.; Taladriz-Blanco, P.; De Oliveira, M. G.; Abell, C. Droplet Microfluidics for the Highly Controlled Synthesis of Branched Gold Nanoparticles. *Sci. Rep.* **2018**, *8* (1), 2440. https://doi.org/10.1038/s41598-018-20754-x.

(83) Wacker, J. B.; Lignos, I.; Parashar, V. K.; Gijs, M. A. M. Controlled Synthesis of Fluorescent Silica Nanoparticles inside Microfluidic Droplets. *Lab. Chip* **2012**, *12* (17), 3111. https://doi.org/10.1039/c2lc40300e.

(84) Kašpar, O.; Koyuncu, A. H.; Pittermannová, A.; Ulbrich, P.; Tokárová, V. Governing Factors for Preparation of Silver Nanoparticles Using Droplet-Based Microfluidic Device. *Biomed. Microdevices* **2019**, *21* (4), 88. https://doi.org/10.1007/s10544-019-0435-4.

(85) Baruah, A.; Singh, A.; Sheoran, V.; Prakash, B.; Ganguli, A. K. Droplet-Microfluidics for the Controlled Synthesis and Efficient Photocatalysis of TiO2 Nanoparticles. *Mater. Res. Express* **2018**, *5* (7), 075019. https://doi.org/10.1088/2053-1591/aaafed.

(86) Rezvantalab, S.; Keshavarz Moraveji, M. Microfluidic Assisted Synthesis of PLGA Drug Delivery Systems. *RSC Adv.* **2019**, *9* (4), 2055–2072. https://doi.org/10.1039/C8RA08972H.

(87) Hung, L.-H.; Teh, S.-Y.; Jester, J.; Lee, A. P. PLGA Micro/Nanosphere Synthesis by Droplet Microfluidic Solvent Evaporation and Extraction Approaches. *Lab. Chip* **2010**, *10* (14), 1820. https://doi.org/10.1039/c002866e.

(88) Effati, E.; Pourabbas, B.; Zakerhamidi, M. S. Continuous Microfluidic Fabrication of Polypyrrole Nanoparticles. *RSC Adv.* **2019**, *9* (30), 16977–16988. https://doi.org/10.1039/C9RA00946A.

(89) Bains, A.; Wulff, J. E.; Moffitt, M. G. Microfluidic Synthesis of Dye-Loaded Polycaprolactone-Block-Poly(Ethylene Oxide) Nanoparticles: Insights into Flow-Directed Loading and in Vitro Release for Drug Delivery. *J. Colloid Interface Sci.* **2016**, *475*, 136–148. https://doi.org/10.1016/j.jcis.2016.04.010.

(90) Xu, Z.; Lu, C.; Riordon, J.; Sinton, D.; Moffitt, M. G. Microfluidic Manufacturing of Polymeric Nanoparticles: Comparing Flow Control of Multiscale Structure in Single-Phase Staggered Herringbone and Two-Phase Reactors. *Langmuir* **2016**, *32* (48), 12781–12789. https://doi.org/10.1021/acs.langmuir.6b03243.

(91) Ling, S. D.; Geng, Y.; Chen, A.; Du, Y.; Xu, J. Enhanced Single-Cell Encapsulation in Microfluidic Devices: From Droplet Generation to Single-Cell Analysis. *Biomicrofluidics* **2020**, *14* (6), 061508. https://doi.org/10.1063/5.0018785.

(92) Schmid, A.; Kortmann, H.; Dittrich, P. S.; Blank, L. M. Chemical and Biological Single Cell Analysis. *Curr. Opin. Biotechnol.* **2010**, *21* (1), 12–20. https://doi.org/10.1016/j.copbio.2010.01.007.

(93) Stuart, T.; Satija, R. Integrative Single-Cell Analysis. *Nat. Rev. Genet.* **2019**, *20* (5), 257–272. https://doi.org/10.1038/s41576-019-0093-7.

(94) Mohajeri, M.; Eskandari, M.; Ghazali, Z. S.; Ghazali, H. S. Cell Encapsulation in Alginate-Based Microgels Using Droplet Microfluidics; a Review on Gelation Methods and Applications. *Biomed. Phys. Eng. Express* **2022**, *8* (2), 022001. https://doi.org/10.1088/2057-1976/ac4e2d.

(95) Kang, A.; Park, J.; Ju, J.; Jeong, G. S.; Lee, S.-H. Cell Encapsulation via Microtechnologies. *Biomaterials* **2014**, *35* (9), 2651–2663. https://doi.org/10.1016/j.biomaterials.2013.12.073.

(96) Yu, L.; Chen, M. C. W.; Cheung, K. C. Droplet-Based Microfluidic System for Multicellular Tumor Spheroid Formation and Anticancer Drug Testing. *Lab. Chip* **2010**, *10* (18), 2424–2432. https://doi.org/10.1039/C004590J.

(97) Martinez, C. J.; Kim, J. W.; Ye, C.; Ortiz, I.; Rowat, A. C.; Marquez, M.; Weitz, D. A Microfluidic Approach to Encapsulate Living Cells in Uniform Alginate Hydrogel Microparticles. *Macromol. Biosci.* **2012**, *12* (7), 946–951. https://doi.org/10.1002/mabi.201100351.

(98) Ahmed, H.; Ahsan Khan, E.; Torger Stokke, B. Microfluidic Dual Picoinjection Based Encapsulation of Hemoglobin in Alginate Microcapsules Reinforced by a Poly(l -Lysine)- g -Poly(Ethylene Glycol). *Soft Matter* **2023**, *19* (1), 69–79. https://doi.org/10.1039/D2SM01045C.

(99) Wang, Y.; Li, P.; Truong-Dinh Tran, T.; Zhang, J.; Kong, L. Manufacturing Techniques and Surface Engineering of Polymer Based Nanoparticles for Targeted Drug Delivery to Cancer. *Nanomaterials* **2016**, *6* (2), 26. https://doi.org/10.3390/nano6020026.

(100) Vinogradov, S. V.; Zeman, A. D.; Batrakova, E. V.; Kabanov, A. V. Polyplex Nanogel Formulations for Drug Delivery of Cytotoxic Nucleoside Analogs. *J. Controlled Release* **2005**, *107* (1), 143–157. https://doi.org/10.1016/j.jconrel.2005.06.002.

(101) Papa, S.; Veneruso, V.; Mauri, E.; Cremonesi, G.; Mingaj, X.; Mariani, A.; De Paola, M.; Rossetti, A.; Sacchetti, A.; Rossi, F.; Forloni, G.; Veglianese, P. Functionalized Nanogel for Treating Activated Astrocytes in Spinal Cord Injury. *J. Controlled Release* **2021**, *330*, 218–228. https://doi.org/10.1016/j.jconrel.2020.12.006.

(102) Vinogradov, S. V.; Kohli, E.; Zeman, A. D. Comparison of Nanogel Drug Carriers and Their Formulations with Nucleoside 5′-Triphosphates. *Pharm. Res.* **2006**, *23* (5), 920–930. https://doi.org/10.1007/s11095-006-9788-5.

(103) Reddy HV, R.; Bhattacharyya, S. *In Vitro* Evaluation of Mucoadhesive *in Situ* Nanogel of Celecoxib for Buccal Delivery. *Ann. Pharm. Fr.* **2021**, *79* (4), 418–430. https://doi.org/10.1016/j.pharma.2021.01.006.

(104) Reeves, A.; Vinogradov, S. V.; Morrissey, P.; Chernin, M.; Ahmed, M. M. Curcumin-Encapsulating Nanogels as an Effective Anticancer Formulation for Intracellular Uptake. *Mol. Cell. Pharmacol.* **2015**, *7* (3), 25–40. https://doi.org/10.4255/mcpharmacol.15.04.

(105) Tripodo, G.; Trapani, A.; Torre, M. L.; Giammona, G.; Trapani, G.; Mandracchia, D. Hyaluronic Acid and Its Derivatives in Drug Delivery and Imaging: Recent Advances and Challenges. *Eur. J. Pharm. Biopharm.* **2015**, *97*, 400–416. https://doi.org/10.1016/j.ejpb.2015.03.032.

(106) Vasvani, S.; Kulkarni, P.; Rawtani, D. Hyaluronic Acid: A Review on Its Biology, Aspects of Drug Delivery, Route of Administrations and a Special Emphasis on Its Approved Marketed Products and Recent Clinical Studies. *Int. J. Biol. Macromol.* **2020**, *151*, 1012–1029. https://doi.org/10.1016/j.ijbiomac.2019.11.066.

(107) Luo, Z.; Dai, Y.; Gao, H. Development and Application of Hyaluronic Acid in Tumor Targeting Drug Delivery. *Acta Pharm. Sin. B* **2019**, *9* (6), 1099–1112. https://doi.org/10.1016/j.apsb.2019.06.004.

(108) Karbownik, M. S.; Nowak, J. Z. Hyaluronan: Towards Novel Anti-Cancer Therapeutics. *Pharmacol. Rep.* **2013**, *65* (5), 1056–1074. https://doi.org/10.1016/S1734-1140(13)71465-8.

(109) Cheng, X.; Shi, S.; Wu, Y.; Zhu, L.; Xu, J.; Hu, T.; Wei, B.; Tang, R. Cisplatin-Cross-Linked and Oxygen-Resupply Hyaluronic Acid-Based Nanocarriers for Chemo-Photodynamic Therapy. *ACS Appl. Nano Mater.* **2021**, *4* (10), 10194–10208. https://doi.org/10.1021/acsanm.1c01662.

(110) Zou, Y.; Li, D.; Shen, M.; Shi, X. Polyethylenimine-Based Nanogels for Biomedical Applications. *Macromol. Biosci.* **2019**, *19* (11), 1900272. https://doi.org/10.1002/mabi.201900272.

(111) Bus, T.; Traeger, A.; Schubert, U. S. The Great Escape: How Cationic Polyplexes Overcome the Endosomal Barrier. *J. Mater. Chem. B* **2018**, *6* (43), 6904–6918. https://doi.org/10.1039/C8TB00967H.

(112) Zakeri, A.; Kouhbanani, M. A. J.; Beheshtkhoo, N.; Beigi, V.; Mousavi, S. M.; Hashemi, S. A. R.; Karimi Zade, A.; Amani, A. M.; Savardashtaki, A.; Mirzaei, E.; Jahandideh, S.; Movahedpour, A. Polyethylenimine-Based Nanocarriers in Co-Delivery of Drug and Gene: A Developing Horizon. *Nano Rev. Exp.* **2018**, *9* (1), 1488497. https://doi.org/10.1080/20022727.2018.1488497.

(113) Yu, K.; Zhao, J.; Yu, C.; Sun, F.; Liu, Y.; Zhang, Y.; Lee, R. J.; Teng, L.; Li, Y. Role of Four Different Kinds of Polyethylenimines (PEIs) in Preparation of Polymeric Lipid Nanoparticles and Their Anticancer Activity Study. *J. Cancer* **2016**, *7* (7), 872–882. https://doi.org/10.7150/jca.13855.

(114) Zhu, Y.; Wang, Y.; Sun, Y.; Shen, J.; Xu, J.; Chai, Y.; Yang, Y. In Situ Self Imine-Crosslinked Nanocomplexes Loaded with Small Noncoding RNA for Efficient Osteoarthritis Attenuation. *Chem. Eng. J.* **2021**, *420*, 127631. https://doi.org/10.1016/j.cej.2020.127631.

(115) Sahiner, N.; Sagbas, S.; Sahiner, M.; Ayyala, R. S. Polyethyleneimine Modified Poly(Hyaluronic Acid) Particles with Controllable Antimicrobial and Anticancer Effects. *Carbohydr. Polym.* **2017**, *159*, 29–38. https://doi.org/10.1016/j.carbpol.2016.12.024.

(116) Yeh, P.-H.; Sun, J.-S.; Wu, H.-C.; Hwang, L.-H.; Wang, T.-W. Stimuli-Responsive HA-PEI Nanoparticles Encapsulating Endostatin Plasmid for Stem Cell Gene Therapy. *RSC Adv.* **2013**, *3* (31), 12922–12932. https://doi.org/10.1039/C3RA40880A.

(117) Chen, C.; Zhou, B.; Zhu, X.; Shen, M.; Shi, X. Branched Polyethyleneimine Modified with Hyaluronic Acid via a PEG Spacer for Targeted Anticancer Drug Delivery. *RSC Adv.* **2016**, *6* (11), 9232–9239. https://doi.org/10.1039/C5RA23022E.

(118) Wang, S.; Zhang, J.; Wang, Y.; Chen, M. Hyaluronic Acid-Coated PEI-PLGA Nanoparticles Mediated Co-Delivery of Doxorubicin and miR-542-3p for Triple Negative Breast Cancer Therapy. *Nanomedicine Nanotechnol. Biol. Med.* **2016**, *12* (2), 411–420. https://doi.org/10.1016/j.nano.2015.09.014.

(119) Xu, Y.; Liu, D.; Hu, J.; Ding, P.; Chen, M. Hyaluronic Acid-Coated pH Sensitive Poly (β-Amino Ester) Nanoparticles for Co-Delivery of Embelin and TRAIL Plasmid for Triple Negative Breast Cancer Treatment. *Int. J. Pharm.* **2020**, *573*, 118637. https://doi.org/10.1016/j.ijpharm.2019.118637.

(120) Zheng, X.; Zhang, F.; Zhao, Y.; Zhang, J.; Dawulieti, J.; Pan, Y.; Cui, L.; Sun, M.; Shao, D.; Li, M.; He, K.; Zhang, M.; Li, J.; Chen, L. Self-Assembled Dual Fluorescence Nanoparticles

for CD44-Targeted Delivery of Anti-miR-27a in Liver Cancer Theranostics. *Theranostics* **2018**, *8* (14), 3808–3823. https://doi.org/10.7150/thno.25255.

(121) Park, J. S.; Yi, S. W.; Kim, H. J.; Park, K.-H. Receptor-Mediated Gene Delivery into Human Mesenchymal Stem Cells Using Hyaluronic Acid-Shielded Polyethylenimine/pDNA Nanogels. *Carbohydr. Polym.* **2016**, *136*, 791–802. https://doi.org/10.1016/j.carbpol.2015.09.053.

(122) Ganesh, S.; Iyer, A. K.; Morrissey, D. V.; Amiji, M. M. Hyaluronic Acid Based Self-Assembling Nanosystems for CD44 Target Mediated siRNA Delivery to Solid Tumors. *Biomaterials* **2013**, *34* (13), 3489–3502. https://doi.org/10.1016/j.biomaterials.2013.01.077.

(123) Park, K.; Lee, M.-Y.; Kim, K. S.; Hahn, S. K. Target Specific Tumor Treatment by VEGF siRNA Complexed with Reducible Polyethyleneimine–Hyaluronic Acid Conjugate. *Biomaterials* **2010**, *31* (19), 5258–5265. https://doi.org/10.1016/j.biomaterials.2010.03.018.

(124) *Hyaluronic Acid-Coated Nanomedicine for Targeted Cancer Therapy*. https://www.mdpi.com/1999-4923/11/7/301 (accessed 2024-11-24).

(125) Fortuni, B.; Inose, T.; Ricci, M.; Fujita, Y.; Van Zundert, I.; Masuhara, A.; Fron, E.; Mizuno, H.; Latterini, L.; Rocha, S.; Uji-i, H. Polymeric Engineering of Nanoparticles for Highly Efficient Multifunctional Drug Delivery Systems. *Sci. Rep.* **2019**, *9* (1), 2666. https://doi.org/10.1038/s41598-019-39107-3.

(126) Mauri, E.; Veglianese, P.; Papa, S.; Mariani, A.; Paola, M. D.; Rigamonti, R.; F. Chincarini, G. M.; Vismara, I.; Rimondo, S.; Sacchetti, A.; Rossi, F. Double Conjugated Nanogels for Selective Intracellular Drug Delivery. *RSC Adv.* **2017**, *7* (48), 30345–30356. https://doi.org/10.1039/C7RA04584K.

(127) Elbert, D. L. Liquid–Liquid Two-Phase Systems for the Production of Porous Hydrogels and Hydrogel Microspheres for Biomedical Applications: A Tutorial Review. *Acta Biomater.* **2011**, *7* (1), 31–56. https://doi.org/10.1016/j.actbio.2010.07.028.

(128) Sheth, T.; Seshadri, S.; Prileszky, T.; Helgeson, M. E. Multiple Nanoemulsions. *Nat. Rev. Mater.* **2020**, *5* (3), 214–228. https://doi.org/10.1038/s41578-019-0161-9.

(129) Hack, M. A.; Vondeling, P.; Cornelissen, M.; Lohse, D.; Snoeijer, J. H.; Diddens, C.; Segers, T. Asymmetric Coalescence of Two Droplets with Different Surface Tensions Is Caused by Capillary Waves. *Phys. Rev. Fluids* **2021**, *6* (10), 104002. https://doi.org/10.1103/PhysRevFluids.6.104002.

(130) Vismara, I.; Papa, S.; Veneruso, V.; Mauri, E.; Mariani, A.; De Paola, M.; Affatato, R.; Rossetti, A.; Sponchioni, M.; Moscatelli, D.; Sacchetti, A.; Rossi, F.; Forloni, G.; Veglianese, P. Selective Modulation of A1 Astrocytes by Drug-Loaded Nano-Structured Gel in Spinal Cord Injury. *ACS Nano* **2020**, *14* (1), 360–371. https://doi.org/10.1021/acsnano.9b05579.

(131) Mauri, E.; Gori, M.; Giannitelli, S. M.; Zancla, A.; Mozetic, P.; Abbruzzese, F.; Merendino, N.; Gigli, G.; Rossi, F.; Trombetta, M.; Rainer, A. Nano-Encapsulation of Hydroxytyrosol into

Formulated Nanogels Improves Therapeutic Effects against Hepatic Steatosis: An *in Vitro* Study. *Mater. Sci. Eng. C* **2021**, *124*, 112080. https://doi.org/10.1016/j.msec.2021.112080.

(132) Son, G. M.; Kim, H. Y.; Ryu, J. H.; Chu, C. W.; Kang, D. H.; Park, S. B.; Jeong, Y.-I. Self-Assembled Polymeric Micelles Based on Hyaluronic Acid-g-Poly(d,l-Lactide-Co-Glycolide) Copolymer for Tumor Targeting. *Int. J. Mol. Sci.* **2014**, *15* (9), 16057–16068. https://doi.org/10.3390/ijms150916057.

(133) Zhou, B.; Zheng, L.; Peng, C.; Li, D.; Li, J.; Wen, S.; Shen, M.; Zhang, G.; Shi, X. Synthesis and Characterization of PEGylated Polyethylenimine-Entrapped Gold Nanoparticles for Blood Pool and Tumor CT Imaging. *ACS Appl. Mater. Interfaces* **2014**, *6* (19), 17190–17199. https://doi.org/10.1021/am505006z.

(134) Quiñones, J. P.; Brüggemann, O.; Covas, C. P.; Ossipov, D. A. Self-Assembled Hyaluronic Acid Nanoparticles for Controlled Release of Agrochemicals and Diosgenin. *Carbohydr. Polym.* **2017**, *173*, 157–169. https://doi.org/10.1016/j.carbpol.2017.05.048.

(135) Muzzarelli, C.; Stanic, V.; Gobbi, L.; Tosi, G.; Muzzarelli, R. A. A. Spray-Drying of Solutions Containing Chitosan Together with Polyuronans and Characterisation of the Microspheres. *Carbohydr. Polym.* **2004**, *57* (1), 73–82. https://doi.org/10.1016/j.carbpol.2004.04.002.

(136) Shah, C. B.; Barnett, S. M. Swelling Behavior of Hyaluronic Acid Gels. *J. Appl. Polym. Sci.* **1992**, *45* (2), 293–298. https://doi.org/10.1002/app.1992.070450211.

(137) Dong, Q.; Guo, X.; Li, L.; Yu, C.; Nie, L.; Tian, W.; Zhang, H.; Huang, S.; Zang, H. Understanding Hyaluronic Acid Induced Variation of Water Structure by Near-Infrared Spectroscopy. *Sci. Rep.* **2020**, *10* (1), 1387. https://doi.org/10.1038/s41598-020-58417-5.

(138) Collins, M. N.; Birkinshaw, C. Investigation of the Swelling Behavior of Crosslinked Hyaluronic Acid Films and Hydrogels Produced Using Homogeneous Reactions. *J. Appl. Polym. Sci.* **2008**, *109* (2), 923–931. https://doi.org/10.1002/app.27631.

(139) Neu, M.; Fischer, D.; Kissel, T. Recent Advances in Rational Gene Transfer Vector Design Based on Poly(Ethylene Imine) and Its Derivatives. *J. Gene Med.* **2005**, *7* (8), 992–1009. https://doi.org/10.1002/jgm.773.

(140) Mauri, E.; Chincarini, G. M. F.; Rigamonti, R.; Magagnin, L.; Sacchetti, A.; Rossi, F. Modulation of Electrostatic Interactions to Improve Controlled Drug Delivery from Nanogels. *Mater. Sci. Eng. C* **2017**, *72*, 308–315. https://doi.org/10.1016/j.msec.2016.11.081.

(141) Welti, D.; Rees, D. A.; Welsh, E. J. Solution Conformation of Glycosaminoglycans: Assignment of the 300-MHz 1H-Magnetic Resonance Spectra of Chondroitin 4-Sulphate, Chondroitin 6-Sulphate and Hyaluronate, and Investigation of an Alkali-Induced Conformation Change. *Eur. J. Biochem.* **1979**, *94* (2), 505–514. https://doi.org/10.1111/j.1432-1033.1979.tb12919.x.

(142) Ghosh, S.; Kobal, I.; Zanette, D.; Reed, W. F. *Conformational contraction and hydrolysis of hyaluronate in sodium hydroxide solutions*. ACS Publications. https://doi.org/10.1021/ma00069a042.

(143) Gribbon, P.; Heng, B. C.; Hardingham, T. E. The Molecular Basis of the Solution Properties of Hyaluronan Investigated by Confocal Fluorescence Recovery After Photobleaching. *Biophys. J.* **1999**, *77* (4), 2210–2216. https://doi.org/10.1016/S0006-3495(99)77061-X.

(144) Ren, J.; Crivoi, A.; Duan, F. Disk-Ring Deposition in Drying a Sessile Nanofluid Droplet with Enhanced Marangoni Effect and Particle Surface Adsorption. *Langmuir* **2020**, *36* (49), 15064–15074. https://doi.org/10.1021/acs.langmuir.0c02607.

(145) Su, R.; Park, S. H.; Li, Z.; McAlpine, M. C. 13 - 3D Printed Electronic Materials and Devices. In *Robotic Systems and Autonomous Platforms*; Walsh, S. M., Strano, M. S., Eds.; Woodhead Publishing in Materials; Woodhead Publishing, 2019; pp 309–334. https://doi.org/10.1016/B978-0-08-102260-3.00013-5.

(146) Ding, J.; Liang, T.; Zhou, Y.; He, Z.; Min, Q.; Jiang, L.; Zhu, J. Hyaluronidase-Triggered Anticancer Drug and siRNA Delivery from Cascaded Targeting Nanoparticles for Drug-Resistant Breast Cancer Therapy. *Nano Res.* **2017**, *10* (2), 690–703. https://doi.org/10.1007/s12274-016-1328-y.

(147) Yeo, Y.; Bellas, E.; Highley, C. B.; Langer, R.; Kohane, D. S. Peritoneal Adhesion Prevention with an *in Situ* Cross-Linkable Hyaluronan Gel Containing Tissue-Type Plasminogen Activator in a Rabbit Repeated-Injury Model. *Biomaterials* **2007**, *28* (25), 3704–3713. https://doi.org/10.1016/j.biomaterials.2007.04.033.

(148) *A Hyaluronidase-Responsive Nanoparticle-Based Drug Delivery System for Targeting Colon Cancer Cells | Cancer Research | American Association for Cancer Research*. https://aacrjournals.org/cancerres/article/76/24/7208/614602/A-Hyaluronidase-Responsive-Nanoparticle-Based-Drug (accessed 2024-11-24).

(149) Wei, P.; Gangapurwala, G.; Pretzel, D.; Leiske, M. N.; Wang, L.; Hoeppener, S.; Schubert, S.; Brendel, J. C.; Schubert, U. S. Smart pH-Sensitive Nanogels for Controlled Release in an Acidic Environment. *Biomacromolecules* **2019**, *20* (1), 130–140. https://doi.org/10.1021/acs.biomac.8b01228.

(150) Schmitz, D.; Pich, A. Responsive Microgels with Supramolecular Crosslinks: Synthesis and Triggered Degradation in Aqueous Medium. *Polym. Chem.* **2016**, *7* (36), 5687–5697. https://doi.org/10.1039/C6PY01039C.

(151) Bajaj, G.; Kim, M. R.; Mohammed, S. I.; Yeo, Y. Hyaluronic Acid-Based Hydrogel for Regional Delivery of Paclitaxel to Intraperitoneal Tumors. *J. Controlled Release* **2012**, *158* (3), 386–392. https://doi.org/10.1016/j.jconrel.2011.12.001.

(152) Hoelscher, F.; Machado, T. O.; de Oliveira, D.; Hermes de Araújo, P. H.; Sayer, C. Enzymatically Catalyzed Degradation of Poly (Thioether-Ester) Nanoparticles. *Polym. Degrad. Stab.* **2018**, *156*, 211–217. https://doi.org/10.1016/j.polymdegradstab.2018.09.007.

(153) Hong, Y.; Che, S.; Hui, B.; Yang, Y.; Wang, X.; Zhang, X.; Qiang, Y.; Ma, H. Lung Cancer Therapy Using Doxorubicin and Curcumin Combination: Targeted Prodrug Based, pH Sensitive Nanomedicine. *Biomed. Pharmacother.* **2019**, *112*, 108614. https://doi.org/10.1016/j.biopha.2019.108614.

(154) Zheng, G.; Zheng, M.; Yang, B.; Fu, H.; Li, Y. Improving Breast Cancer Therapy Using Doxorubicin Loaded Solid Lipid Nanoparticles: Synthesis of a Novel Arginine-Glycine-Aspartic Tripeptide Conjugated, pH Sensitive Lipid and Evaluation of the Nanomedicine *in Vitro* and *in Vivo*. *Biomed. Pharmacother.* **2019**, *116*, 109006. https://doi.org/10.1016/j.biopha.2019.109006.

(155) Capanema, N. S. V.; Carvalho, I. C.; Mansur, A. A. P.; Carvalho, S. M.; Lage, A. P.; Mansur, H. S. Hybrid Hydrogel Composed of Carboxymethylcellulose–Silver Nanoparticles–Doxorubicin for Anticancer and Antibacterial Therapies against Melanoma Skin Cancer Cells. *ACS Appl. Nano Mater.* **2019**, *2* (11), 7393–7408. https://doi.org/10.1021/acsanm.9b01924.

(156) Chung, D. Y.; Kang, D. H.; Kim, J. W.; Ha, J. S.; Kim, D. K.; Cho, K. S. Comparison of Oncologic Outcomes of Dose-Dense Methotrexate, Vinblastine, Doxorubicin, and Cisplatin (ddMVAC) with Gemcitabine and Cisplatin (GC) as Neoadjuvant Chemotherapy for Muscle-Invasive Bladder Cancer: Systematic Review and Meta-Analysis. *Cancers* **2021**, *13* (11), 2770. https://doi.org/10.3390/cancers13112770.

(157) *Ratio-Dependent Synergism of a Doxorubicin and Olaparib Combination in 2D and Spheroid Models of Ovarian Cancer | Molecular Pharmaceutics*. https://pubs.acs.org/doi/abs/10.1021/acs.molpharmaceut.7b00843 (accessed 2024-11-24).

(158) Paul, P. K. C. Aromatic Ring–Aliphatic Ring Stacking in Organic Crystal Structures. *Cryst. Eng.* **2002**, *5* (1), 3–8. https://doi.org/10.1016/S1463-0184(01)00030-2.

(159) Ninković, D. B.; Vojislavljević-Vasilev, D. Z.; Medaković, V. B.; Hall, M. B.; Brothers, E. N.; Zarić, S. D. Aliphatic–Aromatic Stacking Interactions in Cyclohexane–Benzene Are Stronger than Aromatic–Aromatic Interaction in the Benzene Dimer. *Phys. Chem. Chem. Phys.* **2016**, *18* (37), 25791–25795. https://doi.org/10.1039/C6CP03734H.

(160) *On the Nature of σ–σ, σ–π, and π–π Stacking in Extended Systems | ACS Omega*. https://pubs.acs.org/doi/full/10.1021/acsomega.8b01339 (accessed 2024-11-24).

(161) Ma, J. C.; Dougherty, D. A. The Cation−π Interaction. *Chem. Rev.* **1997**, *97* (5), 1303–1324. https://doi.org/10.1021/cr9603744.

(162) Mauri, E.; Cappella, F.; Masi, M.; Rossi, F. PEGylation Influences Drug Delivery from Nanogels. *J. Drug Deliv. Sci. Technol.* **2018**, *46*, 87–92. https://doi.org/10.1016/j.jddst.2018.05.003.

(163) Huang, X.; Brazel, C. S. On the Importance and Mechanisms of Burst Release in Matrix-Controlled Drug Delivery Systems. *J. Controlled Release* **2001**, *73* (2), 121–136. https://doi.org/10.1016/S0168-3659(01)00248-6.

(164) Senbanjo, L. T.; Chellaiah, M. A. CD44: A Multifunctional Cell Surface Adhesion Receptor Is a Regulator of Progression and Metastasis of Cancer Cells. *Front. Cell Dev. Biol.* **2017**, *5*. https://doi.org/10.3389/fcell.2017.00018.

(165) Price, Z. K.; Lokman, N. A.; Ricciardelli, C. Differing Roles of Hyaluronan Molecular Weight on Cancer Cell Behavior and Chemotherapy Resistance. *Cancers* **2018**, *10* (12), 482. https://doi.org/10.3390/cancers10120482.

(166) Rios de la Rosa, J. M.; Pingrajai, P.; Pelliccia, M.; Spadea, A.; Lallana, E.; Gennari, A.; Stratford, I. J.; Rocchia, W.; Tirella, A.; Tirelli, N. Binding and Internalization in Receptor-Targeted Carriers: The Complex Role of CD44 in the Uptake of Hyaluronic Acid-Based Nanoparticles (siRNA Delivery). *Adv. Healthc. Mater.* **2019**, *8* (24), 1901182. https://doi.org/10.1002/adhm.201901182.

(167) Tirella, A.; Kloc-Muniak, K.; Good, L.; Ridden, J.; Ashford, M.; Puri, S.; Tirelli, N. CD44 Targeted Delivery of siRNA by Using HA-Decorated Nanotechnologies for KRAS Silencing in Cancer Treatment. *Int. J. Pharm.* **2019**, *561*, 114–123. https://doi.org/10.1016/j.ijpharm.2019.02.032.

(168) *Withaferin A Synergizes the Therapeutic Effect of Doxorubicin through ROS-Mediated Autophagy in Ovarian Cancer | PLOS ONE*. https://journals.plos.org/plosone/article?id=10.1371/journal.pone.0042265 (accessed 2024-11-24).

(169) Tang, Y.; McGoron, A. J. Combined Effects of Laser-ICG Photothermotherapy and Doxorubicin Chemotherapy on Ovarian Cancer Cells. *J. Photochem. Photobiol. B* **2009**, *97* (3), 138–144. https://doi.org/10.1016/j.jphotobiol.2009.09.001.

(170) Norouzi-Barough, L.; Sarookhani, M.; Salehi, R.; Sharifi, M.; Moghbelinejad, S. CRISPR/Cas9, a New Approach to Successful Knockdown of ABCB1/P-Glycoprotein and Reversal of Chemosensitivity in Human Epithelial Ovarian Cancer Cell Line. *Iran. J. Basic Med. Sci.* **2018**, *21* (2), 181–187. https://doi.org/10.22038/IJBMS.2017.25145.6230.

(171) Sutradhar, K. B.; Amin, Md. L. Nanotechnology in Cancer Drug Delivery and Selective Targeting. *Int. Sch. Res. Not.* **2014**, *2014* (1), 939378. https://doi.org/10.1155/2014/939378.

(172) Manzari, M. T.; Shamay, Y.; Kiguchi, H.; Rosen, N.; Scaltriti, M.; Heller, D. A. Targeted Drug Delivery Strategies for Precision Medicines. *Nat. Rev. Mater.* **2021**, *6* (4), 351–370. https://doi.org/10.1038/s41578-020-00269-6.

(173) Attama, A. A.; Nnamani, P. O.; Onokala, O. B.; Ugwu, A. A.; Onugwu, A. L. Nanogels as Target Drug Delivery Systems in Cancer Therapy: A Review of the Last Decade. *Front. Pharmacol.* **2022**, *13*. https://doi.org/10.3389/fphar.2022.874510.

(174) Omote, S.; Takata, K.; Tanaka, T.; Miyata-Takata, T.; Ayada, Y.; Noujima-Harada, M.; Omote, R.; Tabata, T.; Sato, Y.; Toyokawa, T.; Kato, H.; Yagi, T.; Okada, H.; Yoshino, T. Overexpression of Folate Receptor Alpha Is an Independent Prognostic Factor for Outcomes of Pancreatic Cancer Patients. *Med. Mol. Morphol.* **2018**, *51* (4), 237–243. https://doi.org/10.1007/s00795-018-0197-8.

(175) Cheung, A.; Bax, H. J.; Josephs, D. H.; Ilieva, K. M.; Pellizzari, G.; Opzoomer, J.; Bloomfield, J.; Fittall, M.; Grigoriadis, A.; Figini, M.; Canevari, S.; Spicer, J. F.; Tutt, A. N.; Karagiannis, S. N. Targeting Folate Receptor Alpha for Cancer Treatment. *Oncotarget* **2016**, *7* (32), 52553–52574. https://doi.org/10.18632/oncotarget.9651.

(176) Gonzalez, T.; Muminovic, M.; Nano, O.; Vulfovich, M. Folate Receptor Alpha—A Novel Approach to Cancer Therapy. *Int. J. Mol. Sci.* **2024**, *25* (2), 1046. https://doi.org/10.3390/ijms25021046.

(177) Hamidi, M.; Azadi, A.; Rafiei, P. Hydrogel Nanoparticles in Drug Delivery. *Adv. Drug Deliv. Rev.* **2008**, *60* (15), 1638–1649. https://doi.org/10.1016/j.addr.2008.08.002.

(178) Standardization, I. Biological Evaluation of Medical Devices., 2009.

(179) Günther, A.; Jensen, K. F. Multiphase Microfluidics: From Flow Characteristics to Chemical and Materials Synthesis. *Lab. Chip* **2006**, *6* (12), 1487–1503. https://doi.org/10.1039/B609851G.

(180) Bandulasena, M. V.; Vladisavljević, G. T.; Benyahia, B. Droplet-Based Microfluidic Method for Robust Preparation of Gold Nanoparticles in Axisymmetric Flow Focusing Device. *Chem. Eng. Sci.* **2019**, *195*, 657–664. https://doi.org/10.1016/j.ces.2018.10.010.

(181) Choi, J. W.; Kim, Y. J.; Lee, J. M.; Choi, J.-H.; Choi, J.-W.; Chung, B. G. Droplet-Based Synthesis of Homogeneous Gold Nanoparticles for Enhancing HRP-Based ELISA Signals. *BioChip J.* **2020**, *14* (3), 298–307. https://doi.org/10.1007/s13206-020-4307-z.

(182) Jung, S.-H.; Bulut, S.; Busca Guerzoni, L. P. B.; Günther, D.; Braun, S.; De Laporte, L.; Pich, A. Fabrication of pH-Degradable Supramacromolecular Microgels with Tunable Size and Shape via Droplet-Based Microfluidics. *J. Colloid Interface Sci.* **2022**, *617*, 409–421. https://doi.org/10.1016/j.jcis.2022.02.065.

(183) Gregoritza, M.; Abstiens, K.; Graf, M.; Goepferich, A. M. Fabrication of Antibody-Loaded Microgels Using Microfluidics and Thiol-Ene Photoclick Chemistry. *Eur. J. Pharm. Biopharm.* **2018**, *127*, 194–203. https://doi.org/10.1016/j.ejpb.2018.02.024.

(184) Zhi Chong, Z.; Hwa Tan, S.; M. Gañán-Calvo, A.; Beng Tor, S.; Hiang Loh, N.; Nguyen, N.-T. Active Droplet Generation in Microfluidics. *Lab. Chip* **2016**, *16* (1), 35–58. https://doi.org/10.1039/C5LC01012H.

(185) Lee, C.-Y.; Lin, Y.-H.; Lee, G.-B. A Droplet-Based Microfluidic System Capable of Droplet Formation and Manipulation. *Microfluid. Nanofluidics* **2009**, *6* (5), 599–610. https://doi.org/10.1007/s10404-008-0340-2.

(186) *Hyaluronic Acid-Based Nanomaterials for Cancer Therapy*. https://www.mdpi.com/2073-4360/10/10/1133 (accessed 2024-11-24).

(187) Shrimal, P.; Jadeja, G.; Patel, S. A Review on Novel Methodologies for Drug Nanoparticle Preparation: Microfluidic Approach. *Chem. Eng. Res. Des.* **2020**, *153*, 728–756. https://doi.org/10.1016/j.cherd.2019.11.031.

(188) Abate, A. R.; Romanowsky, M. B.; Agresti, J. J.; Weitz, D. A. Valve-Based Flow Focusing for Drop Formation. *Appl. Phys. Lett.* **2009**, *94* (2), 023503. https://doi.org/10.1063/1.3067862.

(189) Costantini, M.; Jaroszewicz, J.; Kozoń, Ł.; Szlązak, K.; Święszkowski, W.; Garstecki, P.; Stubenrauch, C.; Barbetta, A.; Guzowski, J. 3D-Printing of Functionally Graded Porous Materials Using On-Demand Reconfigurable Microfluidics. *Angew. Chem. Int. Ed.* **2019**, *58* (23), 7620–7625. https://doi.org/10.1002/anie.201900530.

(190) Stolzenburg, P.; Lorenz, T.; Dietzel, A.; Garnweitner, G. Microfluidic Synthesis of Metal Oxide Nanoparticles via the Nonaqueous Method. *Chem. Eng. Sci.* **2018**, *191*, 500–510. https://doi.org/10.1016/j.ces.2018.07.007.

(191) Xu, L.; Peng, J.; Yan, M.; Zhang, D.; Shen, A. Q. Droplet Synthesis of Silver Nanoparticles by a Microfluidic Device. *Chem. Eng. Process. Process Intensif.* **2016**, *102*, 186–193. https://doi.org/10.1016/j.cep.2016.01.017.

(192) Zhang, L.; Chen, Q.; Ma, Y.; Sun, J. Microfluidic Methods for Fabrication and Engineering of Nanoparticle Drug Delivery Systems. *ACS Appl. Bio Mater.* **2020**, *3* (1), 107–120. https://doi.org/10.1021/acsabm.9b00853.

(193) Capretto, L.; Carugo, D.; Mazzitelli, S.; Nastruzzi, C.; Zhang, X. Microfluidic and Lab-on-a-Chip Preparation Routes for Organic Nanoparticles and Vesicular Systems for Nanomedicine Applications. *Adv. Drug Deliv. Rev.* **2013**, *65* (11), 1496–1532. https://doi.org/10.1016/j.addr.2013.08.002.

(194) Wang, L.; Wang, J. Self-Assembly of Colloids Based on Microfluidics. *Nanoscale* **2019**, *11* (36), 16708–16722. https://doi.org/10.1039/C9NR06817A.

(195) Hung, L.-H.; Teh, S.-Y.; Jester, J.; Lee, A. P. PLGA Micro/Nanosphere Synthesis by Droplet Microfluidic Solvent Evaporation and Extraction Approaches. *Lab. Chip* **2010**, *10* (14), 1820–1825. https://doi.org/10.1039/C002866E.

(196) Mahdavi, Z.; Rezvani, H.; Moraveji, M. K. Core–Shell Nanoparticles Used in Drug Delivery-Microfluidics: A Review. *RSC Adv.* **2020**, *10* (31), 18280–18295. https://doi.org/10.1039/D0RA01032D.

(197) Roces, C. B.; Christensen, D.; Perrie, Y. Translating the Fabrication of Protein-Loaded Poly(Lactic-Co-Glycolic Acid) Nanoparticles from Bench to Scale-Independent Production Using Microfluidics. *Drug Deliv. Transl. Res.* **2020**, *10* (3), 582–593. https://doi.org/10.1007/s13346-019-00699-y.

(198) Maguire, C. M.; Rösslein, M.; Wick, P.; Prina-Mello, A. Characterisation of Particles in Solution – a Perspective on Light Scattering and Comparative Technologies. *Sci. Technol. Adv. Mater.* **2018**, *19* (1), 732–745. https://doi.org/10.1080/14686996.2018.1517587.

(199) Zhang, C.; Akcora, P. Evaporation Controlled Particle Patterns in a Polymer Droplet. *RSC Adv.* **2017**, *7* (30), 18321–18326. https://doi.org/10.1039/C7RA01687E.

(200) Horigome, K.; Ueki, T.; Suzuki, D. Direct Visualization of Swollen Microgels by Scanning Electron Microscopy Using Ionic Liquids. *Polym. J.* **2016**, *48* (3), 273–279. https://doi.org/10.1038/pj.2015.103.

(201) Garcia-Salinas, M. J.; Donald, A. M. Use of Environmental Scanning Electron Microscopy to Image Poly(*N*-Isopropylacrylamide) Microgel Particles. *J. Colloid Interface Sci.* **2010**, *342* (2), 629–635. https://doi.org/10.1016/j.jcis.2009.10.064.

(202) Cabaleiro-Lago, E. M.; Rodríguez-Otero, J. On the Nature of σ–σ, σ–π, and π–π Stacking in Extended Systems. *ACS Omega* **2018**, *3* (8), 9348–9359. https://doi.org/10.1021/acsomega.8b01339.

(203) Limiti, E.; Mozetic, P.; Giannitelli, S. M.; Pinelli, F.; Han, X.; Del Rio, D.; Abbruzzese, F.; Basoli, F.; Rosanò, L.; Scialla, S.; Trombetta, M.; Gigli, G.; Zhang, Z. J.; Mauri, E.; Rainer, A. Hyaluronic Acid–Polyethyleneimine Nanogels for Controlled Drug Delivery in Cancer Treatment. *ACS Appl. Nano Mater.* **2022**, *5* (4), 5544–5557. https://doi.org/10.1021/acsanm.2c00524.

(204) Kannan, G.; Kambhampati, S. P.; Kudchadkar, S. R. Effect of Anesthetics on Microglial Activation and Nanoparticle Uptake: Implications for Drug Delivery in Traumatic Brain Injury. *J. Controlled Release* **2017**, *263*, 192–199. https://doi.org/10.1016/j.jconrel.2017.03.032.

(205) N. Politis, S.; Colombo, P.; Colombo, G.; M. Rekkas, D. Design of Experiments (DoE) in Pharmaceutical Development. *Drug Dev. Ind. Pharm.* **2017**, *43* (6), 889–901. https://doi.org/10.1080/03639045.2017.1291672.

(206) Khuri, A. I.; Mukhopadhyay, S. Response Surface Methodology. *WIREs Comput. Stat.* **2010**, *2* (2), 128–149. https://doi.org/10.1002/wics.73.

(207) Terada, T.; Kulkarni, J. A.; Huynh, A.; Chen, S.; Van Der Meel, R.; Tam, Y. Y. C.; Cullis, P. R. Characterization of Lipid Nanoparticles Containing Ionizable Cationic Lipids Using Design-of-Experiments Approach. *Langmuir* **2021**, *37* (3), 1120–1128. https://doi.org/10.1021/acs.langmuir.0c03039.

(208) Whiteley, Z.; Ho, H. M. K.; Gan, Y. X.; Panariello, L.; Gkogkos, G.; Gavriilidis, A.; Craig, D. Q. M. Microfluidic Synthesis of Protein-Loaded Nanogels in a Coaxial Flow Reactor Using a Design of Experiments Approach. *Nanoscale Adv.* **2021**, *3* (7), 2039–2055. https://doi.org/10.1039/D0NA01051K.

(209) Giannitelli, S. M.; Limiti, E.; Mozetic, P.; Pinelli, F.; Han, X.; Abbruzzese, F.; Basoli, F.; Del Rio, D.; Scialla, S.; Rossi, F.; Trombetta, M.; Rosanò, L.; Gigli, G.; Zhang, Z. J.; Mauri, E.;

Rainer, A. Droplet-Based Microfluidic Synthesis of Nanogels for Controlled Drug Delivery: Tailoring Nanomaterial Properties *via* Pneumatically Actuated Flow-Focusing Junction. *Nanoscale* **2022**, *14* (31), 11415–11428. https://doi.org/10.1039/D2NR00827K.

(210) Limiti, E.; Mozetic, P.; Giannitelli, S. M.; Pinelli, F.; Han, X.; Del Rio, D.; Abbruzzese, F.; Basoli, F.; Rosanò, L.; Scialla, S.; Trombetta, M.; Gigli, G.; Zhang, Z. J.; Mauri, E.; Rainer, A. Hyaluronic Acid–Polyethyleneimine Nanogels for Controlled Drug Delivery in Cancer Treatment. *ACS Appl. Nano Mater.* **2022**, *5* (4), 5544–5557. https://doi.org/10.1021/acsanm.2c00524.

(211) Gori, M.; Giannitelli, S. M.; Torre, M.; Mozetic, P.; Abbruzzese, F.; Trombetta, M.; Traversa, E.; Moroni, L.; Rainer, A. Biofabrication of Hepatic Constructs by 3D Bioprinting of aCell-Laden Thermogel: An Effective Tool to AssessDrug-Induced Hepatotoxic Response. *Adv Healthcare Materials* **2020**, *9* (21). https://doi.org/10.1002/adhm.202001163.

(212) Bucciarelli, A.; Chiera, S.; Quaranta, A.; Yadavalli, V. K.; Motta, A.; Maniglio, D. A Thermal-Reflow-Based Low-Temperature, High-Pressure Sintering of Lyophilized Silk Fibroin for the Fast Fabrication of Biosubstrates. *Adv. Funct. Mater.* **2019**, *29* (42), 1901134. https://doi.org/10.1002/adfm.201901134.

(213) Gaiardo, A.; Novel, D.; Scattolo, E.; Crivellari, M.; Picciotto, A.; Ficorella, F.; Iacob, E.; Bucciarelli, A.; Petti, L.; Lugli, P.; Bagolini, A. Optimization of a Low-Power Chemoresistive Gas Sensor: Predictive Thermal Modelling and Mechanical Failure Analysis. *Sensors* **2021**, *21* (3), 783. https://doi.org/10.3390/s21030783.

(214) Lam, J. K. W.; Xu, Y.; Worsley, A.; Wong, I. C. K. Oral Transmucosal Drug Delivery for Pediatric Use. *Adv. Drug Deliv. Rev.* **2014**, *73*, 50–62. https://doi.org/10.1016/j.addr.2013.08.011.

(215) Bucciarelli, A.; Adami, A.; Chandaiahgari, C. R.; Lorenzelli, L. Multivariable Optimization of Inkjet Printing Process of Ag Nanoparticle Ink on Kapton. In *2020 IEEE International Conference on Flexible and Printable Sensors and Systems (FLEPS)*; IEEE: Manchester, United Kingdom, 2020; pp 1–4. https://doi.org/10.1109/FLEPS49123.2020.9239474.

(216) Bossi, A. M.; Bucciarelli, A.; Maniglio, D. Molecularly Imprinted Silk Fibroin Nanoparticles. *ACS Appl. Mater. Interfaces* **2021**, *13* (27), 31431–31439. https://doi.org/10.1021/acsami.1c05405.

(217) Team, R. C. R: A Language and Environment for Statistical Computing. *Vienna Austria* **2019**.

(218) Bucciarelli, A.; Reddy Chandraiahgari, C.; Adami, A.; Mulloni, V.; Lorenzelli, L. Precise Dot Inkjet Printing Thought Multifactorial Statistical Optimization of the Piezoelectric Actuator Waveform. *Flex. Print. Electron.* **2020**, *5* (4), 045002. https://doi.org/10.1088/2058-8585/abbb7e.

(219) Bucciarelli, A.; Muthukumar, T.; Kim, J. S.; Kim, W. K.; Quaranta, A.; Maniglio, D.; Khang, G.; Motta, A. Preparation and Statistical Characterization of Tunable Porous Sponge Scaffolds

Using UV Cross-Linking of Methacrylate-Modified Silk Fibroin. *ACS Biomater. Sci. Eng.* **2019**, *5* (12), 6374–6388. https://doi.org/10.1021/acsbiomaterials.9b00814.

(220) Bucciarelli, A.; Adami, A.; Chandaiahgari, C. R.; Lorenzelli, L. Multivariable Optimization of Inkjet Printing Process of Ag Nanoparticle Ink on Kapton. In *2020 IEEE International Conference on Flexible and Printable Sensors and Systems (FLEPS)*; IEEE, 2020; pp 1–4. https://doi.org/10.1109/FLEPS49123.2020.9239474.

(221) Zambito, Y.; Pedreschi, E.; Di Colo, G. Is Dialysis a Reliable Method for Studying Drug Release from Nanoparticulate Systems?—A Case Study. *Int. J. Pharm.* **2012**, *434* (1–2), 28–34. https://doi.org/10.1016/j.ijpharm.2012.05.020.

(222) Paswan, S. K.; Saini, T. R. Comparative Evaluation of In Vitro Drug Release Methods Employed for Nanoparticle Drug Release Studies. *Dissolution Technol.* **2021**, *28* (4), 30–38. https://doi.org/10.14227/DT280421P30.

(223) Wallace, S. J.; Li, J.; Nation, R. L.; Boyd, B. J. Drug Release from Nanomedicines: Selection of Appropriate Encapsulation and Release Methodology. *Drug Deliv. Transl. Res.* **2012**, *2* (4), 284–292. https://doi.org/10.1007/s13346-012-0064-4.

(224) Yu, M.; Yuan, W.; Li, D.; Schwendeman, A.; Schwendeman, S. P. Predicting Drug Release Kinetics from Nanocarriers inside Dialysis Bags. *J. Controlled Release* **2019**, *315*, 23–30. https://doi.org/10.1016/j.jconrel.2019.09.016.

(225) Curry, D.; Scheller, H.; Lu, M.; Mkandawire, M.; Servos, M. R.; Cui, S.; Zhang, X.; Oakes, K. D. Prevention of Doxorubicin Sorptive Losses in Drug Delivery Studies Using Polyethylene Glycol. *RSC Adv.* **2015**, *5* (33), 25693–25698. https://doi.org/10.1039/C5RA01799H.

(226) Missirlis, D.; Kawamura, R.; Tirelli, N.; Hubbell, J. A. Doxorubicin Encapsulation and Diffusional Release from Stable, Polymeric, Hydrogel Nanoparticles. *Eur. J. Pharm. Sci.* **2006**, *29* (2), 120–129. https://doi.org/10.1016/j.ejps.2006.06.003.

(227) Manocha, B.; Margaritis, A. Controlled Release of Doxorubicin from Doxorubicin/ γ -Polyglutamic Acid Ionic Complex. *J. Nanomater.* **2010**, *2010*, 1–9. https://doi.org/10.1155/2010/780171.

(228) Wu, D. C.; Ofner, C. M. Adsorption and Degradation of Doxorubicin from Aqueous Solution in Polypropylene Containers. *AAPS PharmSciTech* **2013**, *14* (1), 74–77. https://doi.org/10.1208/s12249-012-9885-1.

(229) Jiang, G.; Park, K.; Kim, J.; Kim, K. S.; Oh, E. J.; Kang, H.; Han, S.; Oh, Y.; Park, T. G.; Kwang Hahn, S. Hyaluronic Acid–Polyethyleneimine Conjugate for Target Specific Intracellular Delivery of siRNA. *Biopolymers* **2008**, *89* (7), 635–642. https://doi.org/10.1002/bip.20978.

(230) Zhao, S.; Riaud, A.; Luo, G.; Jin, Y.; Cheng, Y. Simulation of Liquid Mixing inside Micro-Droplets by a Lattice Boltzmann Method. *Chem. Eng. Sci.* **2015**, *131*, 118–128. https://doi.org/10.1016/j.ces.2015.03.066.

(231) Arruebo, M.; Uson, L.; Miana, M.; Ortiz De Solorzano, I.; Sebastian, V.; Larrea, A. Continuous Synthesis of Drug-Loaded Nanoparticles Using Microchannel Emulsification and Numerical Modeling: Effect of Passive Mixing. *Int. J. Nanomedicine* **2016**, *Volume 11*, 3397–3416. https://doi.org/10.2147/IJN.S108812.

(232) Sarrazin, F.; Loubière, K.; Prat, L.; Gourdon, C.; Bonometti, T.; Magnaudet, J. Experimental and Numerical Study of Droplets Hydrodynamics in Microchannels. *AIChE J.* **2006**, *52* (12), 4061–4070. https://doi.org/10.1002/aic.11033.

(233) Tiribocchi, A.; Montessori, A.; Lauricella, M.; Bonaccorso, F.; Succi, S.; Aime, S.; Milani, M.; Weitz, D. A. The Vortex-Driven Dynamics of Droplets within Droplets. *Nat. Commun.* **2021**, *12* (1), 82. https://doi.org/10.1038/s41467-020-20364-0.

(234) Song, H.; Bringer, M. R.; Tice, J. D.; Gerdts, C. J.; Ismagilov, R. F. Experimental Test of Scaling of Mixing by Chaotic Advection in Droplets Moving through Microfluidic Channels. *Appl. Phys. Lett.* **2003**, *83* (22), 4664–4666. https://doi.org/10.1063/1.1630378.

(235) Kašpar, O.; Koyuncu, A. H.; Hubatová-Vacková, A.; Balouch, M.; Tokárová, V. Influence of Channel Height on Mixing Efficiency and Synthesis of Iron Oxide Nanoparticles Using Droplet-Based Microfluidics. *RSC Adv.* **2020**, *10* (26), 15179–15189. https://doi.org/10.1039/D0RA02470H.

(236) Parhamifar, L.; Larsen, A. K.; Hunter, A. C.; Andresen, T. L.; Moghimi, S. M. Polycation Cytotoxicity: A Delicate Matter for Nucleic Acid Therapy—Focus on Polyethylenimine. *Soft Matter* **2010**, *6* (17), 4001. https://doi.org/10.1039/c000190b.

(237) Pandey, A. P.; Sawant, K. K. Polyethylenimine: A Versatile, Multifunctional Non-Viral Vector for Nucleic Acid Delivery. *Mater. Sci. Eng. C* **2016**, *68*, 904–918. https://doi.org/10.1016/j.msec.2016.07.066.

(238) Sahoo, D. R.; Biswal, T. Alginate and Its Application to Tissue Engineering. *SN Appl. Sci.* **2021**, *3* (1), 30. https://doi.org/10.1007/s42452-020-04096-w.

(239) Ahmad Raus, R.; Wan Nawawi, W. M. F.; Nasaruddin, R. R. Alginate and Alginate Composites for Biomedical Applications. *Asian J. Pharm. Sci.* **2021**, *16* (3), 280–306. https://doi.org/10.1016/j.ajps.2020.10.001.

(240) Kang, S.-M.; Lee, J.-H.; Huh, Y. S.; Takayama, S. Alginate Microencapsulation for Three-Dimensional In Vitro Cell Culture. *ACS Biomater. Sci. Eng.* **2021**, *7* (7), 2864–2879. https://doi.org/10.1021/acsbiomaterials.0c00457.

(241) Eleftheriadou, D.; Evans, R. E.; Atkinson, E.; Abdalla, A.; Gavins, F. K. H.; Boyd, A. S.; Williams, G. R.; Knowles, J. C.; Roberton, V. H.; Phillips, J. B. An Alginate-Based Encapsulation System for Delivery of Therapeutic Cells to the CNS. *RSC Adv.* **2022**, *12* (7), 4005–4015. https://doi.org/10.1039/D1RA08563H.

(242) Bajpai, S. K.; Sharma, S. Investigation of Swelling/Degradation Behaviour of Alginate Beads Crosslinked with Ca2+ and Ba2+ Ions. *React. Funct. Polym.* **2004**, *59* (2), 129–140. https://doi.org/10.1016/j.reactfunctpolym.2004.01.002.

(243) Kuo, C. K.; Ma, P. X. Ionically Crosslinked Alginate Hydrogels as Sca!Olds for Tissue Engineering: Part 1. Structure, Gelation Rate and Mechanical Properties. **2001**.

(244) Hu, M.; Zheng, G.; Zhao, D.; Yu, W. Characterization of the Structure and Diffusion Behavior of Calcium Alginate Gel Beads. *J. Appl. Polym. Sci.* **2020**, *137* (31), 48923. https://doi.org/10.1002/app.48923.

(245) Jeong, C.; Kim, S.; Lee, C.; Cho, S.; Kim, S.-B. Changes in the Physical Properties of Calcium Alginate Gel Beads under a Wide Range of Gelation Temperature Conditions. *Foods* **2020**, *9* (2), 180. https://doi.org/10.3390/foods9020180.

(246) Reis, C. P.; Neufeld, R. J.; Vilela, S.; Ribeiro, A. J.; Veiga, F. Review and Current Status of Emulsion/Dispersion Technology Using an Internal Gelation Process for the Design of Alginate Particles. *J. Microencapsul.* **2006**, *23* (3), 245–257. https://doi.org/10.1080/02652040500286086.

(247) Jeoh, T.; Wong, D. E.; Strobel, S. A.; Hudnall, K.; Pereira, N. R.; Williams, K. A.; Arbaugh, B. M.; Cunniffe, J. C.; Scher, H. B. How Alginate Properties Influence in Situ Internal Gelation in Crosslinked Alginate Microcapsules (CLAMs) Formed by Spray Drying. *PLOS ONE* **2021**, *16* (2), e0247171. https://doi.org/10.1371/journal.pone.0247171.

(248) Choi, C.-H.; Jung, J.-H.; Rhee, Y. W.; Kim, D.-P.; Shim, S.-E.; Lee, C.-S. Generation of Monodisperse Alginate Microbeads and in Situ Encapsulation of Cell in Microfluidic Device. *Biomed. Microdevices* **2007**, *9* (6), 855–862. https://doi.org/10.1007/s10544-007-9098-7.

(249) Ling, S. D.; Liu, Z.; Ma, W.; Chen, Z.; Du, Y.; Xu, J. A Novel Step-T-Junction Microchannel for the Cell Encapsulation in Monodisperse Alginate-Gelatin Microspheres of Varying Mechanical Properties at High Throughput. *Biosensors* **2022**, *12* (8), 659. https://doi.org/10.3390/bios12080659.

(250) Utech, S.; Prodanovic, R.; Mao, A. S.; Ostafe, R.; Mooney, D. J.; Weitz, D. A. Microfluidic Generation of Monodisperse, Structurally Homogeneous Alginate Microgels for Cell Encapsulation and 3D Cell Culture. *Adv. Healthc. Mater.* **2015**, *4* (11), 1628–1633. https://doi.org/10.1002/adhm.201500021.

(251) Mazutis, L.; Vasiliauskas, R.; Weitz, D. A. Microfluidic Production of Alginate Hydrogel Particles for Antibody Encapsulation and Release. *Macromol. Biosci.* **2015**, *15* (12), 1641–1646. https://doi.org/10.1002/mabi.201500226.

(252) Zhu, H.; Srivastava, R.; McShane, M. J. Spontaneous Loading of Positively Charged Macromolecules into Alginate-Templated Polyelectrolyte Multilayer Microcapsules. *Biomacromolecules* **2005**, *6* (4), 2221–2228. https://doi.org/10.1021/bm0501656.

(253) Nguyen, D. K.; Son, Y. M.; Lee, N.-E. Hydrogel Encapsulation of Cells in Core–Shell Microcapsules for Cell Delivery. *Adv. Healthc. Mater.* **2015**, *4* (10), 1537–1544. https://doi.org/10.1002/adhm.201500133.

Appendix I.

Doxorubicin calibration curves at pH 4.5, 7.4 (PBS) and 8.5

According to the NG-mediated releases of DOX performed in PBS, acidic and basic buffers, a 34 mM stock solution of DOX was prepared in the corresponding solutions. The calibration solutions with concentration of 17 µM, 8.5 µM, 4.25 µM, 2.125 µM, 1.063 µM, 0.531 µM, 0.266 µM, 0.133 µM and 0.066 µM were prepared by serial dilutions of the stock solution in PBS, acidic and alkaline medium, respectively. UV-vis measurements were recorded on a TECAN M200 spectrophotometer. Calibration curve was obtained by plotting fluorescence values at 590 nm *vs.* drug concentration and using a sigmoidal-based fitting of the experimental data as the best fitting (Figure S1).

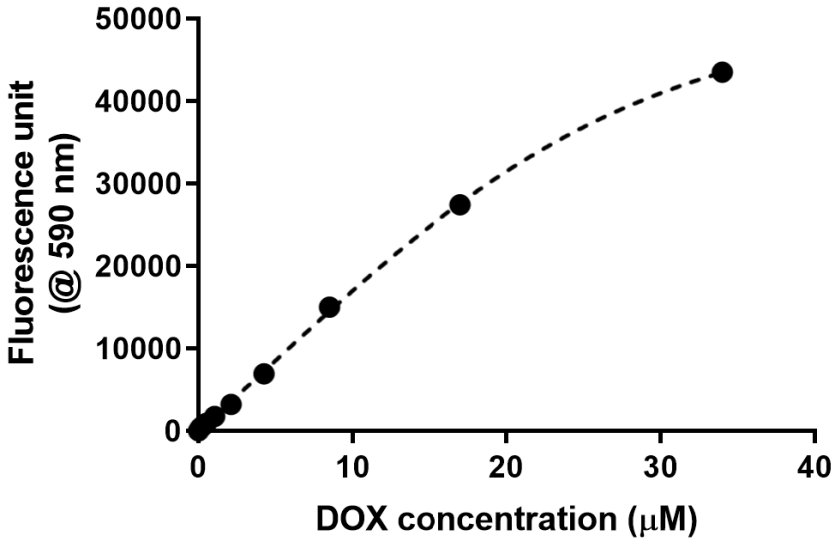

Figure S1 DOX calibration curve.

DLS analysis of drug-loaded NGs

NG size was evaluated through DLS analysis following the nanoencapsulation of DOX, as reported in Figure S2. The drug loading resulted in a slight variation of NG size, compared to the hydrodynamic diameters of empty NGs, due to the steric hindrance of DOX and the consequent interactions with HA through aliphatic-aromatic stacking, which we hypothesize that could promote a small NG shrinking in the first hours. However, considering the typical swelling behavior of the nanocarriers, the difference in size can be considered non-significant in terms of NG internalization in cells. Moreover, drug-loaded NGs showed a good stability over time, exhibiting a trend similar to neat NGs.

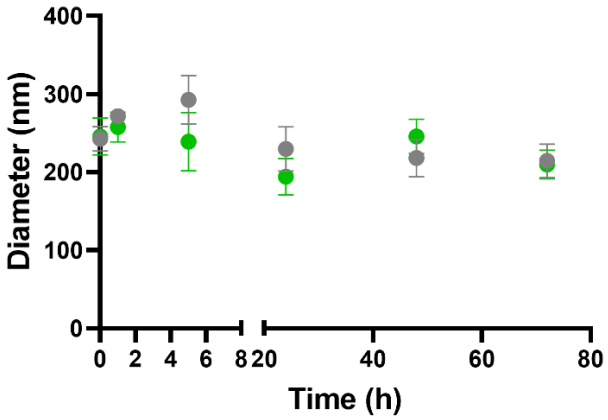

Figure S2 DLS measurements of the hydrodynamic diameter of DOX-loaded NGs (green) and empty NGs (grey) in PBS.

Drug release in HAase solutions

DOX loading in NGs was performed following the protocol discussed in the manuscript. The resulting drug-loaded nanosystems were allowed to exchange against HAase solutions 10 U/mL and 150 U/mL (0.6 mL), at 37 °C. For both enzymatic conditions, at defined time points, 100 µL aliquots were withdrawn and spotted into 96-well plates for fluorescence spectrophotometric analysis. At each withdrawal, elution buffer was changed with fresh enzymatic solution, to preserve the HAase activity over time. Cumulative percentage of released DOX was estimated by fluorescence spectroscopy (λ_{ex} = 488 nm and λ_{em} = 590 nm), according to the respective drug calibration curve in HAase solution 10 U/mL or 150 U/mL. Figure S3a shows the obtained drug release profiles.

The faster release against HAase solution 150 U/mL was in accordance with the more sustained enzymatic degradation of NGs, which resulted in a higher cumulative release percentage over time *vs*. specimen treated with HAase solution 10 U/mL. Moreover, plotting the drug release against time to the power of 0.43 (i.e., $t^{1/2.3}$), linear trends were clearly recognizable in both investigated conditions, suggesting that DOX release was mediated by Fickian diffusion regime. In particular, as discussed in the manuscript, a double diffusion regime with different slopes could be detected: the first trend (*i*) could be representative of the DOX localized at the interface NGs/enzymatic solution, which was rapidly released due to the NG surface degradation; whereas the second regime (*ii*) could correspond to the release of DOX entrapped in the inner nanocarrier supported by the progressive and sustained HAase-mediated degradation of the NG architecture.

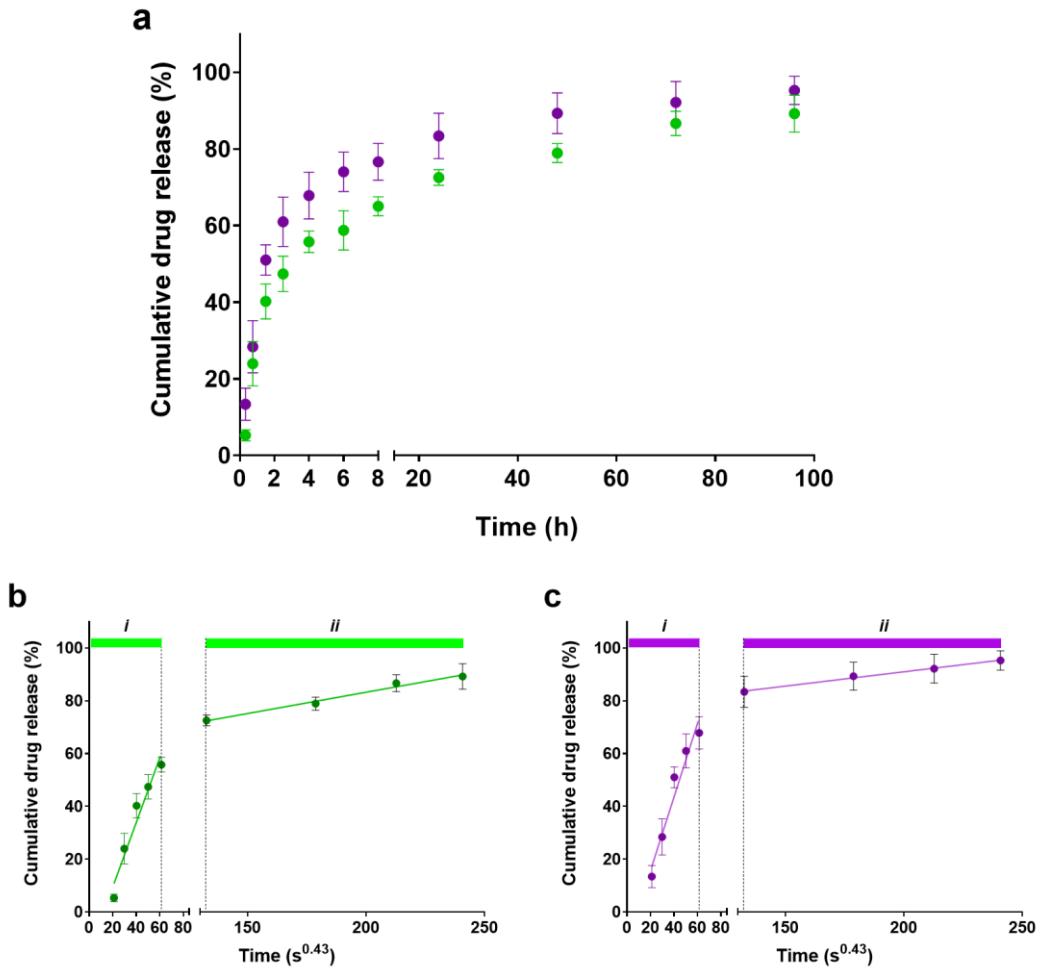

Figure S3(a) DOX release profile by NGs in HAase solutions 10 U/mL (green) and 150 U/mL (violet). (b,c) The slope of the drug release against time expressed as t1/2.3 is representative of the Fickian diffusion coefficient of the drug in NGs, in the two conditions of enzymatic degradation. Cumulative drug release is represented as a percentage of the total drug payload (mean value ± SD is plotted).

Western blotting (WB)

For WB analysis, total cells were detached by scraping, collected by centrifugation, and lysed in RIPA buffer [50 mM Tris·HCl (pH 7.5), 150 mm NaCl, 1% Nonidet P-40, 0.5% sodium deoxycholate (NaDoc), 0.1% SDS] and proteases and phosphatase inhibitors (Roche). Protein concentrations were determined using the DC Protein assay (Bio-Rad Laboratories). Cell lysates were resolved on MiniPROTEAN TGX gels and transferred to nitrocellulose membranes (Bio-Rad Laboratories), followed by WB using the primary antibodies. Primary antibody was Recombinant Anti-CD44 mouse antibody [EPR1013Y] (ab51037) and was revealed using horseradish peroxidase-conjugated goat anti-rabbit or anti-mouse Abs (Bio-Rad Laboratories). Proteins were visualized by chemiluminescence (Clarity Western ECL Substrates, Bio-Rad Laboratories). Quantification analyses were

performed by Image J (https://imagej.nih.gov/ij/), Java based freeware, and reflects the relative amounts of each protein band relative to the lane's loading control (GAPDH). We compared the CD44 protein expression of different tumor lines(OVCA433, SKMEL, BXPC3), highlighting that OVCA433 showed an enhanced CD44 level, justifying its selection for HA-based NGs uptake studies (Figure S4).

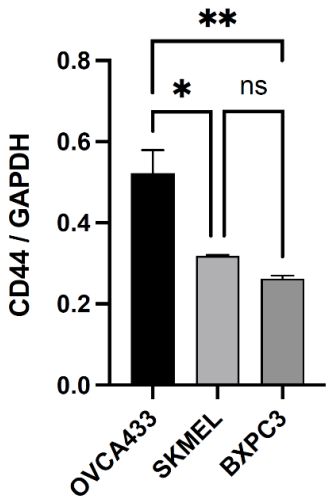

*Figure S4 WB for comparative CD44 protein expression among different tumor lines: OVCA433, SKMEL and BXPC3. OVCA433 show an enhanced CD44 level as highlighted. Results are expressed as the mean ± SD and statistical analysis was performed using one-way ANOVA. * $p < 0.05$; ** $p < 0.01$; ns = not significant.*

3D rendering of NGs internalization

Figure S5 shows a representative 3D rendering of the confocal Z-stack micrographs of NGs internalization in OVCA433 cells after 24 h incubation.

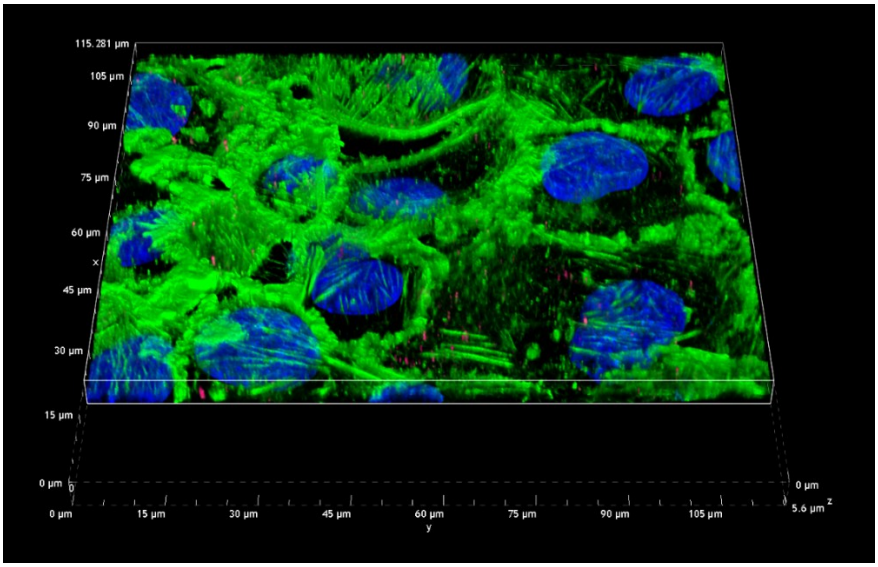

Figure S5 Representative 3D rendering of the NGs (in red) internalization in OVCA433. Cell membranes were labeled with FITC-labeled phalloidin stain (green) and nuclei were counterstained with DAPI (blue). The images were collected with a 60× NA1.4 oil immersion objective.

Dose-response curve of DOX

Figure S6 shows the dose-response curve of DOX evaluated at 24 h on OVCA433 cultured in adhesion using the MTT assay. The value of 4.4 μM was identified as the IC_{50} level. The sublethal concentration of 0.2 μM used in our work is showed by the red dashed line.

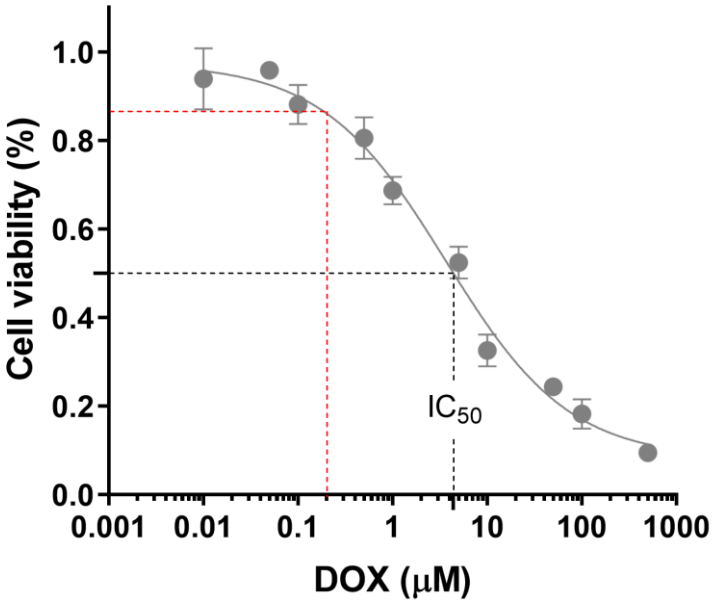

Figure S6 Dose-response curve of DOX. IC50 level (black dashed line) and the used sublethal DOX concentration of 0.2 μM (red dashed line) are highlighted.

Appendix II.

Doxorubicin calibration curve

A 34 μM stock solution of DOX was prepared in PBS. The calibration solutions with concentration of 17 μM, 8.5 μM, 4.25 μM, 2.125 μM, 1.063 μM, 0.531 μM, 0.266 μM, 0.133 μM and 0.066 μM were prepared by serial dilutions of the stock solution in PBS. Fluorescence measurements (λ_{ex} = 488 nm; λ_{em} = 590 nm) were recorded on a TECAN M200 spectrophotometer. Calibration curve was obtained by plotting fluorescence levels *vs.* drug concentration and using a sigmoidal-based fitting of the experimental data (Figure S1).

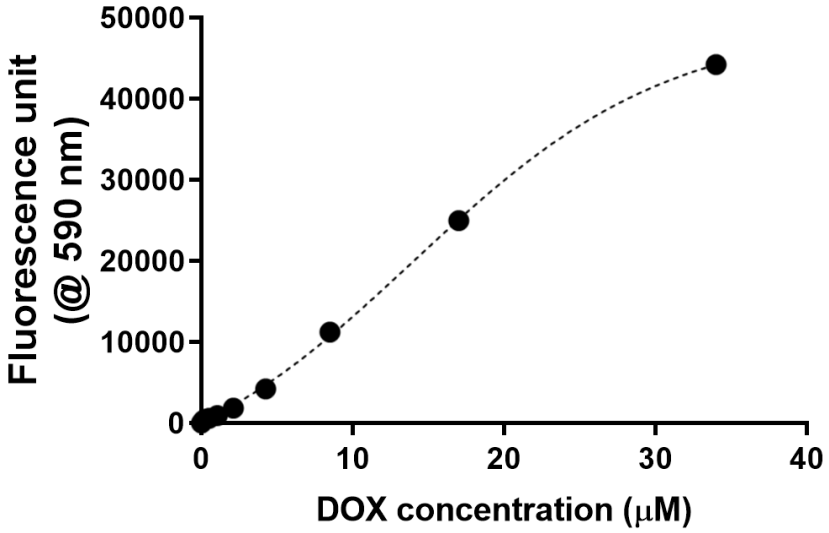

Figure S1 DOX calibration curve.

3D rendering of the tunable hydrodynamic flow focusing geometry

Figure S2 shows a representative 3D volume reconstruction of the hydrodynamic flow-focusing (HFF) geometry at different actuation levels (in the range 0 – 2 bar), as obtained by confocal microscopy. The microfluidic channels were flooded with an aq. FITC solution and confocal micrographs were collected using a Nikon A1R+ laser scanning confocal microscope (Nikon Instruments, Tokyo, Japan) with a 20× NA 1.0 air objective.

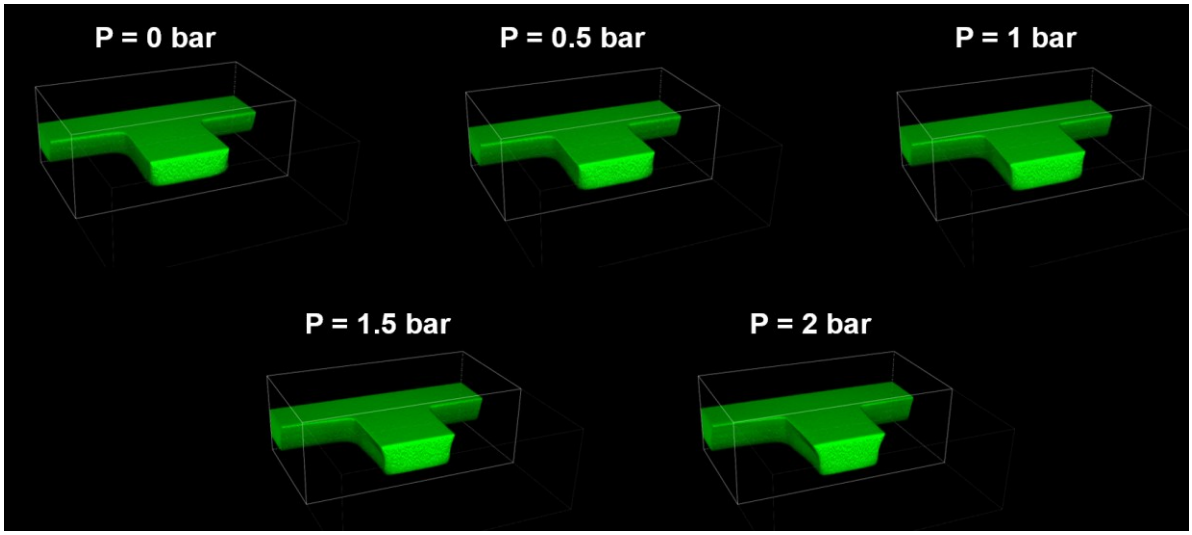

Figure S2 3D volume reconstruction of the HFF junction at different pressure actuation levels.Chemical crosslinking between HA and LPEI in microdroplets

To demonstrate that the formation of covalent bonds between HA and LPEI took place in each microdroplet and that the microfluidic pathway was necessary to form NGs, an aqueous solution of activated HA and LPEI was prepared in the same manner of the dispersed phase used in chip and left at room temperature up to 24 h. In this way, we reproposed the same reaction conditions for HA and LPEI, except for the microfluidic flow and droplet generation steps.

The polymeric solution was dialyzed (membrane MWCO = 6-8 kDa) against distilled water, for 3 days, with daily water change, in order to remove potential by-products. Finally, the resulting solution was freeze-dried and analyzed by ^{1}H-NMR.

Figure S3 shows the ^{1}H-NMR spectra of the *status* of HA-LPEI solution after 24 h, compared to the spectrum of obtained NGs (NG_0, as a representative specimen). In all spectra of the bulk polymeric solution, the signals corresponding to the covalent crosslinking were missing. In particular, the characteristic shift (3.39 ppm) of LPEI peaks were not detectable. This result confirmed that the covalent linkage between the two polymers was conceivably

favored by the diffusion mixing, the convective transport and the flow field inside the forming microdroplets[1-3], and, as a result, the NGs were produced.

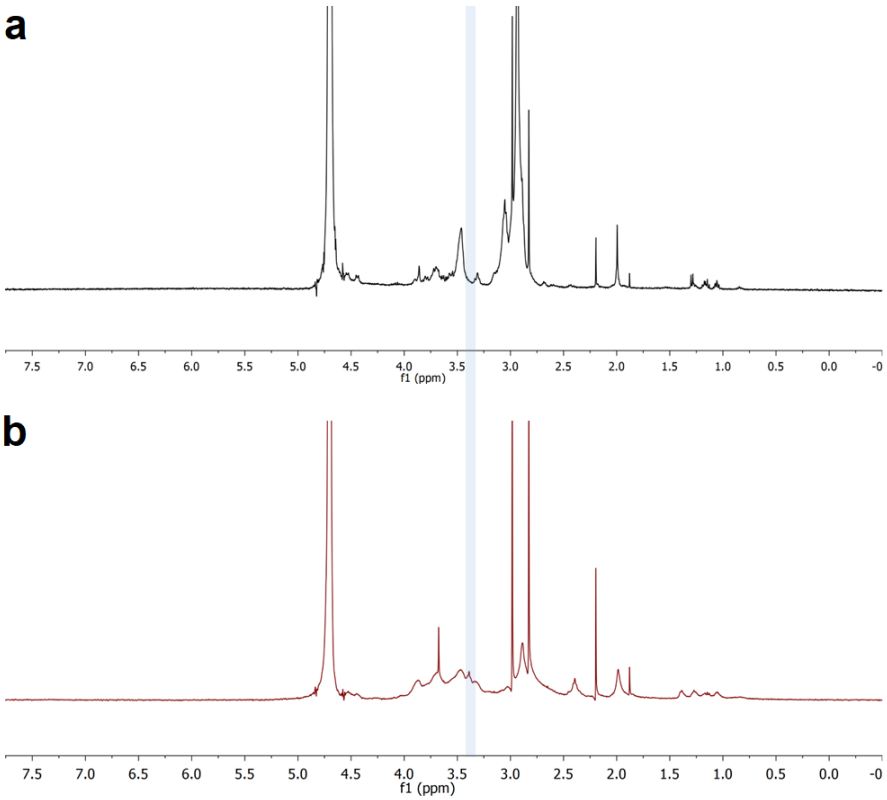

Figure S3(a) ^{1}H-NMR spectrum of the HA-LPEI solution equal to the dispersed phase used in droplet-based microfluidics, left at room temperature for 24 h without implementation in microfluidic steps and dialyzed. Compared to NGs spectrum (b, NG_0), the signals of chemical crosslinking HA-LPEI are missing (as highlighted in the blue area).

DLS comparison between conventional W/O emulsion and microfluidic NG syntheses

NGs obtained via our microfluidic strategy (i.e., NG_0 and NG_2) were characterized by DLS and contrasted with NGs produced *via* a standard W/O emulsion batch process (NG_W/O): the main differences in size and PDI related to the two synthetic routes are reported in Figure S4. In detail, NG_W/O were synthetized using the same polymer solution of the droplet-based microfluidic approach, following these steps: LPEI-Cy5 (6.8 mg, 2.7 μmol) and pristine LPEI (6.8 mg, 2.7 μmol) were dissolved in acid solution (1.5 mL, pH = 4.5); then it was added dropwise to the solution of activated HA (1.5 mL) and vortexed for 1 min. The resulting system represented the aqueous phase. The organic phase was 3% w/v Span 80 in mineral oil (5 mL). Finally, the polymer solution (1 mL) was added dropwise to the organic phase, under stirring, and the obtained W/O emulsion was stirred 8 h. NGs were collected as a powder after extraction with diethyl ether, dialysis against DIW and freeze-drying, as discussed in the microfluidic synthesis of NG_0 and NG_2.

As showed in Table S1, NG_W/O was characterized by higher values of mean hydrodynamic diameter (D) and polydispersity index (PDI) than NGs obtained through microfluidics: this confirmed the high potential of the microfluidic platform to control the NG synthesis and produce nanomaterials having extremely similar size.

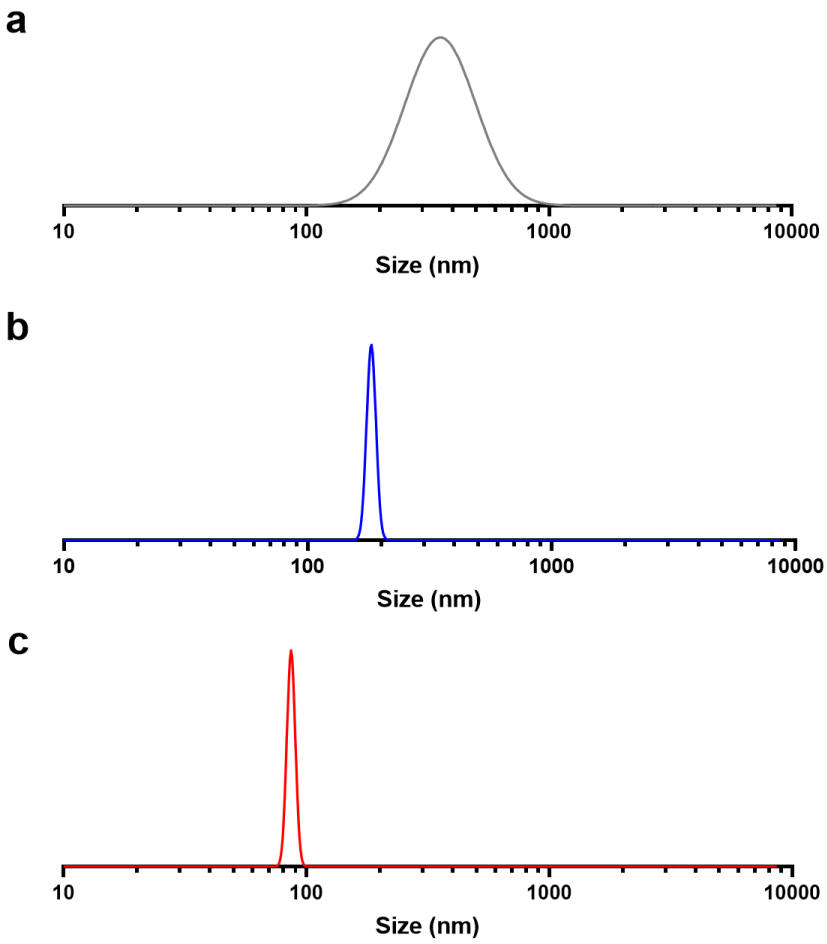

Figure S4 DLS graphs of NG_W/O (a, black), NG_0 (b, blue) and NG_2 (c, red).

Table S1 DLS analysis of NGs specimens.

	D (nm)	**PDI (-)**
NG_W/O	342.1	0.193
NG_0	188.3	0.023
NG_2	92.4	0.015

Furthermore, DLS analysis indicated that NG_0 and NG_2 did not show significant coalescence and aggregation in PBS, preserving their size as reported in Figure S5.

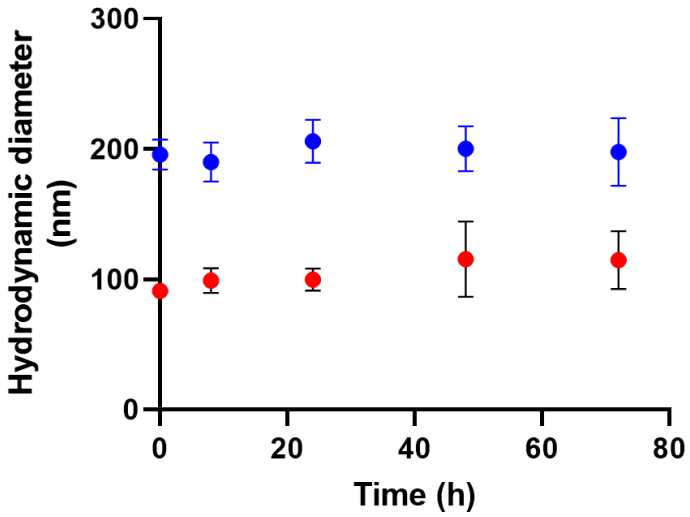

Figure S5 Stability of NG_0 (blue) and NG_2 (red) specimens in PBS. The experiments were performed in triplicate.

Drug release by NGs produced through conventional W/O emulsion (NG_W/O)

NG_W/O were tested as reference drug delivery system for our NG_0 and NG_2 specimens, to highlight the different performances between the traditional NG synthesis and our innovative microfluidic production. Drug loading and release study were performed as discussed in the main text. Briefly, 30 µL of a 100 µM DOX solution were added to the lyophilized NG_W/O (3 mg) and left to RT for 15 min to complete the drug adsorption within the nanonetwork; the encapsulation efficiency was estimated following dialysis against PBS (30 min). The resulting DOX-loaded NGs were diluted to a final concentration of 10 mg/mL and 100 µL of the suspension were allowed to exchange against PBS, withdrawing aliquots at defined time points to determine the eluted drug concentration by fluorescence spectroscopy (λ_{ex} = 488 nm, λ_{em} = 590 nm). NG_W/O were characterized by *ca.* 70% drug loading and exhibited an almost completed drug release in the first 6 h (Figure S6), which results faster than DOX/NG_0 and DOX/NG_2 specimens (*ca.* 74.5% and 63% after 6 h, respectively). This different trend could be ascribed to two aspects: *i)* the larger size of NG_W/O compared to the counterparts and *ii)* the diverse LPEI-HA composition. In particular, drug release is reliably affected by the aliphatic-aromatic stacking occurring between DOX and HA. NG_W/O were characterized by LPEI:HA 2.5:1 molar ratio, which indicated lower amount of glycosaminoglycan in the nanoscaffolds than NG_0 and NG_2 specimens; consequently, the overall drug-polymer interactions within the nanomeshes

decreased. This condition was magnified by the higher dimensions of NG_W/O, which further reduced the stacking effect due to the increase in the mean free path of the drug molecules towards HA component, leading to a faster DOX release compared to the microfluidic-derived NGs. Moreover, plotting the drug release against time to the power of 0.43 (i.e., $t^{1/2.3}$), a linear trend was clearly recognizable, suggesting that DOX release was mediated by Fickian diffusion regime, as in NG_0 and NG_2.

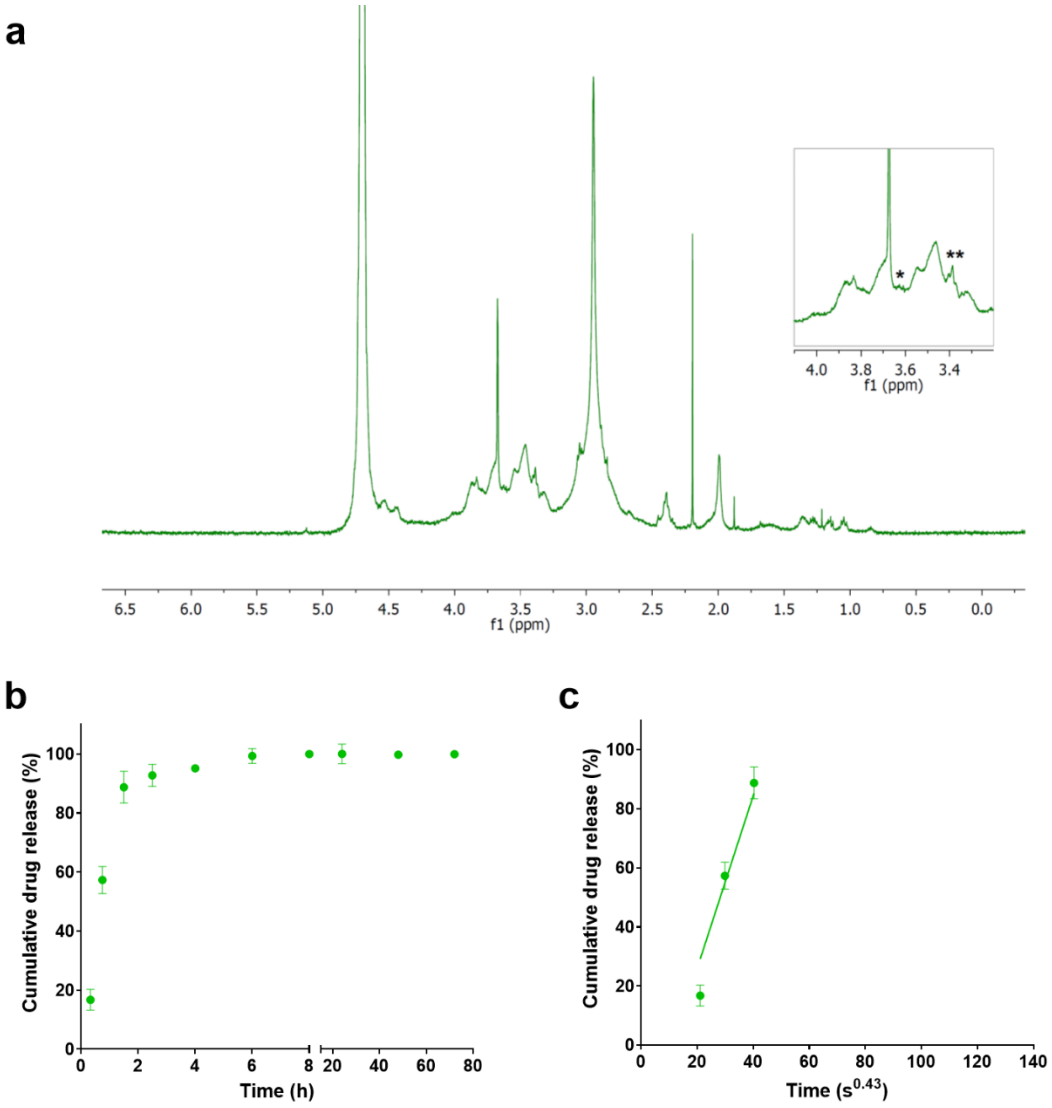

Figure S6 (a) ^{1}H-NMR spectrum of NG_W/O: the characteristic signals of HA-LPEI crosslinking (and **) are highlighted. (b) DOX release profile by NG_W/O. (c) The slope of the drug release against time expressed as t1/2.3 is representative of the Fickian diffusion coefficient of the drug in NGs. Cumulative drug release is represented as a percentage of the total drug payload (mean value ± SD is plotted).*

Overall, these results confirmed that NG_0 and NG_2 were more efficient nanocarriers than NG_W/O, and eligible as controlled drug delivery systems for therapeutic applications.

Cytotoxicity and metabolic effects of NG_W/O-mediated DOX release

Cytotoxicity of NG_W/O and the potential therapeutic effect of NG_W/O-mediated release of DOX were evaluated using G6PD and MTT assays, respectively. The specimens were administered to OVCA433 following the procedures described in the manuscript. As shown in Figure S7, NG_W/O did not exhibited cytotoxicity (cell viability close to 99%) and provided an improved therapeutic effect compared to DOX administration in free form after 24 h ($p<0.1$ *vs.* DOX and $p<0.01$ *vs.* CTRL). However, the reduced cell viability was less meaningful than the DOX/NG_0 and DOX/NG_2 (82 % for DOX/NG_W/O *vs*. 18 % for DOX/NG_0 and 5 % for DOX/NG_2, after 1 week), indicating that the NGs synthetized by droplet-based microfluidics were more promising drug-loaded nanocarriers in terms of lowering and mitigating the metabolic activity, compared to the respective NGs obtained by conventional W/O emulsion.

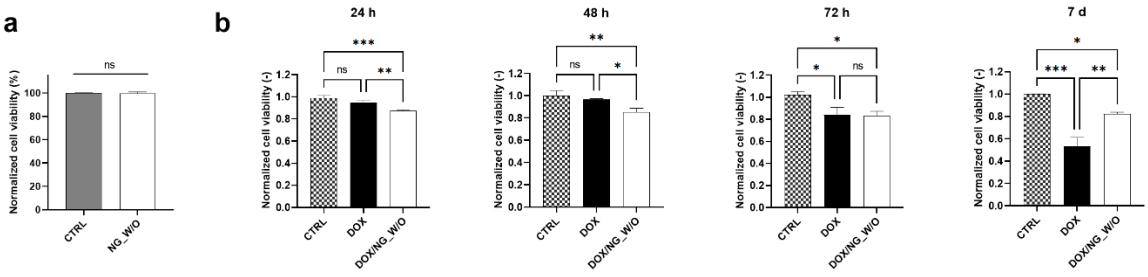

*Figure S7(a) Cytocompatibility of pristine NG_W/O by G6PD assay. Viability levels have been normalized to CTRL group and expressed as mean ± SD. (b) Comparison of DOX-induced cytotoxicity in OVCA433 at 24 h, 48 h, 72 h and 7 days, after the administration of free-drug (DOX) and drug-loaded NGs (DOX/NG_W/O). Groups refer to a 30 min incubation with the treatment. The therapeutic effect is expressed in terms of cell viability levels normalized against their internal controls, measured through the MTT assay. Results are the mean ± SD. Statistical analysis was performed using one-way ANOVA. * $p < 0.05$, ** $p < 0.01$, **** $p < 0.001$, **** $p < 0.0001$, ns = not significant.*

References

1. R. Seemann, M. Brinkmann, T. Pfohl and S. Herminghaus, *Rep Prog Phys*, 2011, **75**, 016601.
2. O. Carrier, F. G. Ergin, H.-Z. Li, B. B. Watz and D. Funfschilling, *J Micromech Microeng*, 2015, **25**, 084014.
3. J. D. Tice, H. Song, A. D. Lyon and R. F. Ismagilov, *Langmuir*, 2003, **19**, 9127-9133.

Appendix III.

DOX standard calibration curve

A calibration solution of DOX in PBS was prepared by a two-fold dilution (down to 0.02 μM) starting from a DOX concentration of 5 μM. Fluorescence measurements (λex = 488 nm; λem = 590 nm) were recorded on a TECAN M200 spectrophotometer. A standard calibration curve was obtained by plotting fluorescence levels against drug concentration. The linear fitting of the experimental data demonstrated an excellent fit, with an R2 value of 0.999.

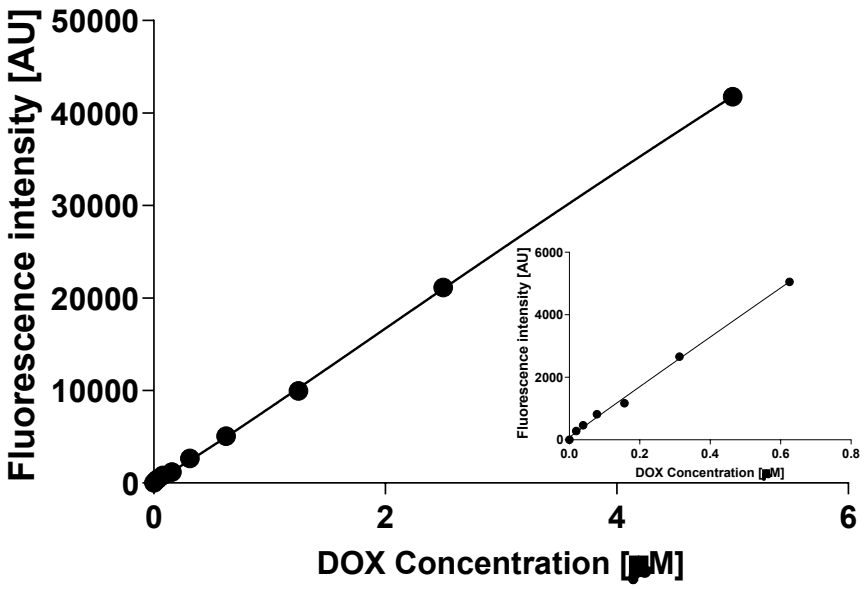

Figure S1 DOX standard calibration curve.

Dose-Response curve of DOX

Figure S2 showed the dose-response curve of DOX evaluated at 24 h on OVCA433 cultured in adhesion using the MTT assay. The value of 4.98 µM was identified as the IC_{50} level. The sublethal concentration of 1 µM used in our work is showed by the black dashed line.

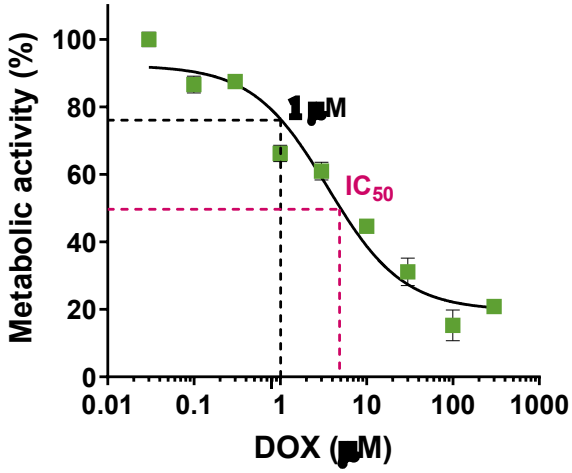

Figure S2 DOX Dose-Response curve. IC_{50} level (purple dashed line) and the used sublethal DOX concentration of 1 µM (black dashed line) are highlighted.

^{1}H-NMR spectra

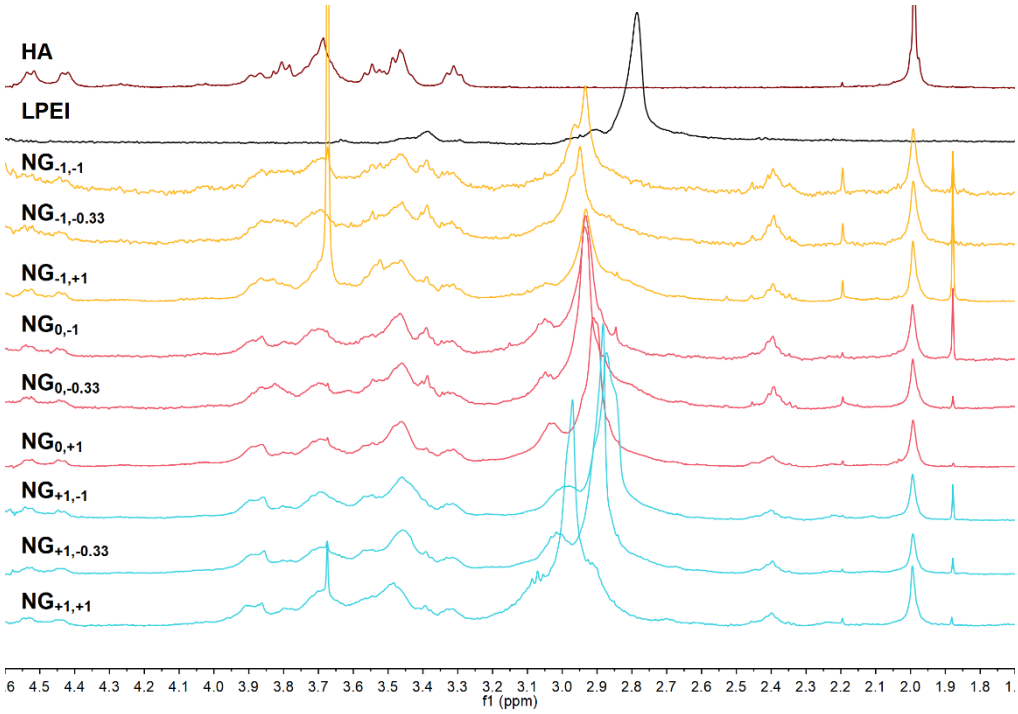

Figure S3 ^{1}H-NMR spectra of each tested synthesis condition. Yellow, red and blue spectra are referred to the NGs synthesized with $MR_{LPEI/HA}$ of 3, 6 and 9, respectively.

Drug release

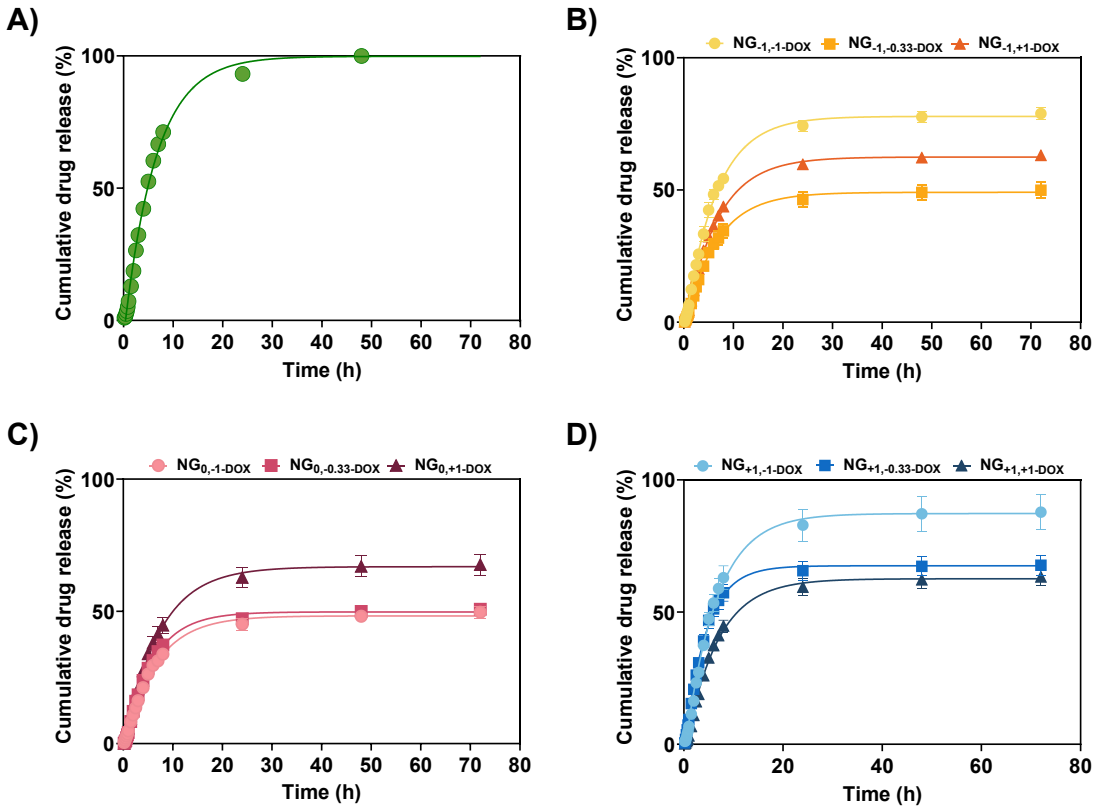

Figure S4 A) Free DOX cumulative release (%). B-D) Drug release curves for NGs synthesized with MR level of 3 (B), 6 (C) and 9 (D).

From *FigureS4 A* it is possible to appreciate the slow diffusion of DOX through the dialysis bag. The complete release (100%) was achieved only after 48 hours, indicating that the drug-membrane interactions cannot be considered negligible. This same profile can be observed in the release experiments of the DOX-NGs. However, even if the release kinetics were affected by the experimental setup used, the different plateau levels account for a different behavior between the specimens that can be observed.

G6PD assay

NGs cytotoxicity was evaluated through G6PD assay. NGs were administered to the OVCA433 cell line following the protocol described in the manuscript. None of the tested formulations showed altered cell viability after 24h, as reported in *Figure S5*.

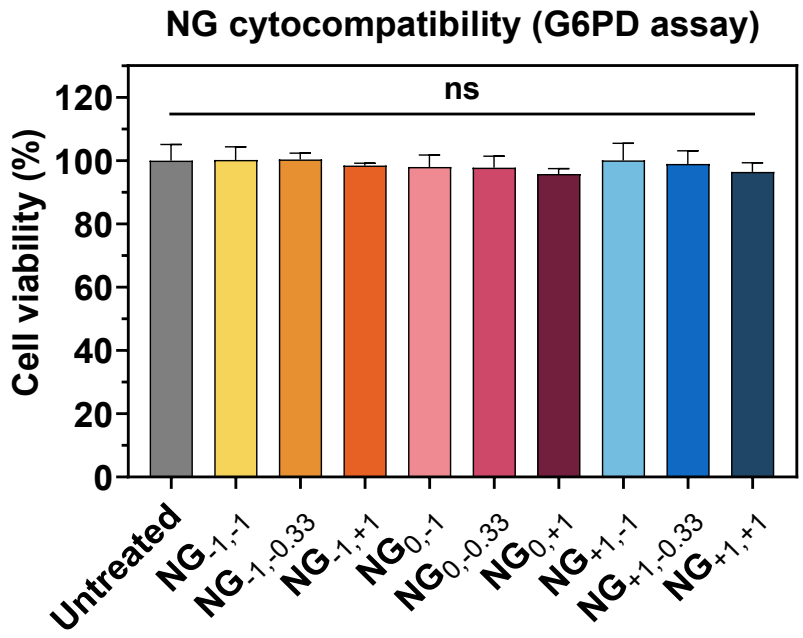

Figure S5 NG cytocompatibility assessed via G6PD assay.

MTT assay

NGs influence on metabolic activity was evaluated through MTT assay. NGs were administered to the OVCA433 cell line following the protocol described in the manuscript.

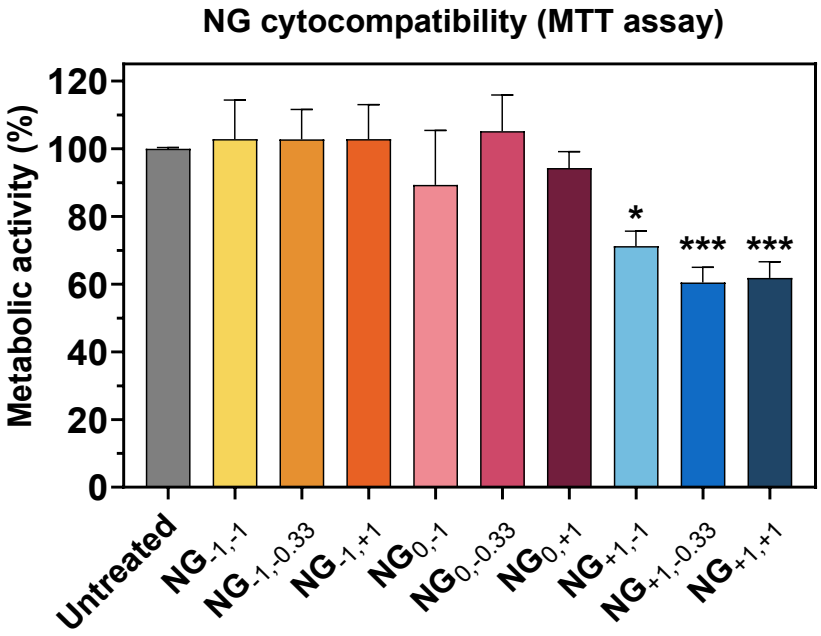

Figure S6 NG cytocompatibility assessed via MTT assay.

Confocal microscopy

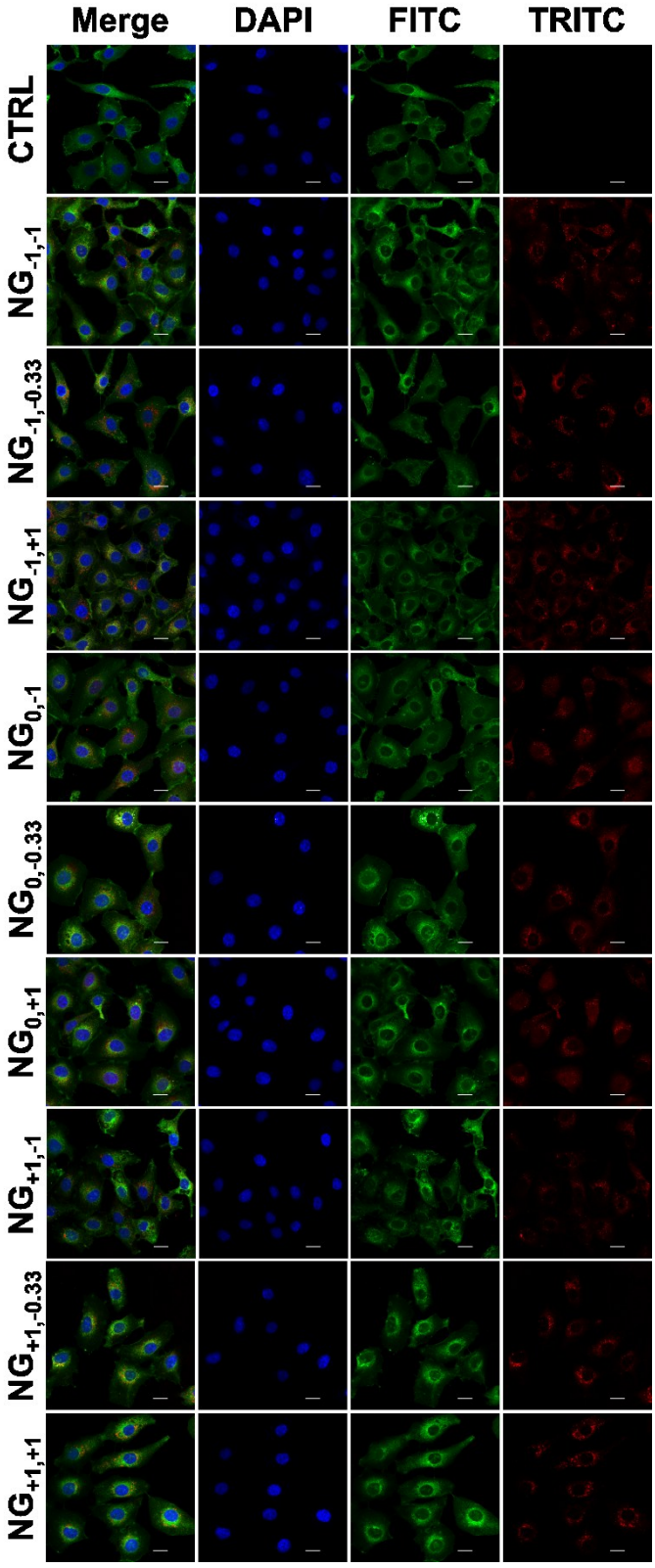

Figure S7 representative fluorescence confocal micrographs. Nuclei are stained with DAPI, cellular membrane with FITC, and red signals are ascribable to the successful NGs internalization. Scale bar 20 μm.

Calculation of corrective factors for flow cytometry

As a first step, the molar ratio $\frac{n_{LPEI}}{n_{HA}}$ has been calculated integrating the respective signals of LPEI and HA in each NG spectrum: from 3.417-3.376 ppm and 3.142-2.587 ppm for LPEI, and 4.59-3.419 ppm and 3.336-3.262 ppm for HA.

Successively, we calculated the LPEI/HA weight ratio $\frac{m_{LPEI}}{m_{HA}}$ by taking into consideration their respective molecular weight (MW):

$$\frac{m_{LPEI}}{m_{HA}} = \frac{n_{LPEI} \cdot MW_{LPEI}}{n_{HA} \cdot MW_{HA}}$$

As the fluorescent dye is linked to LPEI, the corrective factor (CF) must take into account the different amount of LPEI present in each NGs. Thus, we define the LPEI weight fraction as follows:

$$\frac{m_{LPEI}}{m_{NG}} = \frac{m_{LPEI}}{m_{LPEI+}\, m_{HA}} = \frac{m_{LPEI}/m_{HA}}{m_{LPEI}/m_{HA} + 1}$$

Given the weight fraction of LPEI in each NG formulation, the corresponding corrective factor was defined as:

$$CF_i = \left(\frac{m_{LPEI}}{m_{NG}}\right)_i^{-1}$$

CFs were further normalized to the lowest value:

$$\overline{CF_i} = \frac{CF_i}{min\{CF\}}$$

Empirical model

Table S1. Variance table for NG cytocompatibility (%)

Source	Sum of Squares	df	Mean Square	F-value	p-value	
Model	9005.80	5	1801.16	85.03	< 0.0001	significant
A-Mr	7438.59	1	7438.59	351.15	< 0.0001	
A^2	1262.35	1	1262.35	59.59	< 0.0001	
B^2	359.23	1	359.23	16.96	0.0005	
A^2B	110.35	1	110.35	5.21	0.0330	
A^2B^2	497.34	1	497.34	23.48	< 0.0001	
Residual	444.85	21	21.18			
Lack of Fit	45.11	3	15.04	0.6771	0.5773	not significant
Pure Error	399.74	18	22.21			
Cor Total	9450.65	26				

Table S2. Coefficients table for NG cytocompatibility (%)

Factor	Coefficient Estimate	df	Standard Error	95% CI Low	95% CI High	VIF
Intercept	106.87	1	3.00	100.64	113.11	
A-Mr	-20.33	1	1.08	-22.58	-18.07	1.0000
A^2	-28.61	1	3.71	-36.32	-20.90	3.89
B^2	-15.08	1	3.66	-22.69	-7.46	3.00
A^2B	-3.03	1	1.33	-5.80	-0.2693	1.04
A^2B^2	21.86	1	4.51	12.48	31.24	5.89

Table S3. Variance table for NG size (nm)

Source	Sum of Squares	df	Mean Square	F-value	p-value	
Model	2.038E+05	6	33963.27	55.77	< 0.0001	significant
A-Mr	24319.02	1	24319.02	39.93	< 0.0001	
B-Qd/Qc	1.596E+05	1	1.596E+05	262.13	< 0.0001	
A^2	2385.93	1	2385.93	3.92	0.0633	
B^2	500.00	1	500.00	0.8210	0.3769	
AB^2	13952.70	1	13952.70	22.91	0.0001	
A^2B^2	7791.92	1	7791.92	12.79	0.0022	
Residual	10962.49	18	609.03			
Lack of Fit	4340.74	2	2170.37	5.24	0.0177	significant
Pure Error	6621.75	16	413.86			
Cor Total	2.147E+05	24				

Table S4. Coefficients table for NG cytocompatibility (%)

Factor	Coefficient Estimate	df	Standard Error	95% CI Low	95% CI High	VIF
Intercept	279.75	1	16.23	245.66	313.84	
A-Mr	-87.90	1	13.91	-117.12	-58.68	5.08
B-Qd/Qc	94.18	1	5.82	81.96	106.40	1.03
A^2	42.08	1	21.26	-2.59	86.75	4.28
B^2	-17.90	1	19.75	-59.40	23.60	2.55
AB^2	76.72	1	16.03	43.05	110.40	5.08
A^2B^2	-90.65	1	25.34	-143.90	-37.41	6.17

Table S5. Variance table for NG PDI (-)

Source	Sum of Squares	df	Mean Square	F-value	p-value	
Model	0.0213	4	0.0053	21.27	< 0.0001	significant
A-Mr	0.0020	1	0.0020	8.08	0.0101	
B-Qd/Qc	0.0161	1	0.0161	64.38	< 0.0001	
AB	0.0016	1	0.0016	6.52	0.0189	
B^2	0.0031	1	0.0031	12.26	0.0022	
Residual	0.0050	20	0.0002			
Lack of Fit	0.0016	4	0.0004	1.85	0.1692	not significant
Pure Error	0.0034	16	0.0002			
Cor Total	0.0263	24				

Table S6. Coefficients table for NG PDI (-)

Factor	Coefficient Estimate	df	Standard Error	95% CI Low	95% CI High	VIF
Intercept	0.0150	1	0.0069	0.0007	0.0294	
A-Mr	-0.0113	1	0.0040	-0.0196	-0.0030	1.01
B-Qd/Qc	-0.0299	1	0.0037	-0.0377	-0.0221	1.03
AB	0.0115	1	0.0045	0.0021	0.0209	1.01
B^2	0.0282	1	0.0080	0.0114	0.0449	1.03

Table S7. Variance table for χ_{LPEI} (-)

Source	Sum of Squares	df	Mean Square	F-value	p-value	
Model	0.0610	6	0.0102	1215.11	0.0008	significant
A-Mr	0.0500	1	0.0500	5981.97	0.0002	
B-Qd/Qc	0.0002	1	0.0002	22.10	0.0424	
AB	0.0038	1	0.0038	454.04	0.0022	
A^2	0.0047	1	0.0047	566.76	0.0018	
B^2	0.0014	1	0.0014	169.84	0.0058	
A^2B	0.0004	1	0.0004	50.72	0.0192	
Residual	0.0000	2	8.360E-06			

Cor Total	0.0610	8

Table S8. Coefficients table for χ_{LPEI} (-)

Factor	Coefficient Estimate	df	Standard Error	95% CI Low	95% CI High	VIF
Intercept	0.7281	1	0.0024	0.7179	0.7383	
A-Mr	0.0921	1	0.0012	0.0870	0.0972	1.02
B-Qd/Qc	-0.0095	1	0.0020	-0.0182	-0.0008	3.04
AB	0.0303	1	0.0014	0.0241	0.0364	1.02
A^2	-0.0491	1	0.0021	-0.0580	-0.0402	1.02
B^2	-0.0305	1	0.0023	-0.0406	-0.0204	1.04
A^2B	-0.0175	1	0.0025	-0.0281	-0.0069	3.02

Table S9. Variance table for M∞ (%)

Source	Sum of Squares	df	Mean Square	F-value	p-value	
Model	0.0002	5	0.0000	34.91	< 0.0001	significant
A-Mr	0.0000	1	0.0000	32.70	< 0.0001	
B-Qd/Qc	0.0000	1	0.0000	38.82	< 0.0001	
A^2B	0.0001	1	0.0001	67.27	< 0.0001	
AB^2	0.0000	1	0.0000	18.31	0.0004	
A^2B^2	0.0001	1	0.0001	74.63	< 0.0001	
Residual	0.0000	20	1.247E-06			
Lack of Fit	4.998E-06	3	1.666E-06	1.42	0.2716	not significant
Pure Error	0.0000	17	1.173E-06			
Cor Total	0.0002	25				

Table S10. Coefficients table for M∞ (%)

	Coefficient Estimate	df	Standard Error	95% CI Low	95% CI High	VIF
Intercept	0.0181	1	0.0003	0.0175	0.0188	
A-Mr	-0.0029	1	0.0005	-0.0040	-0.0019	3.60
B-Qd/Qc	-0.0028	1	0.0004	-0.0037	-0.0019	2.85
A^2B	0.0045	1	0.0006	0.0034	0.0057	2.85
AB^2	0.0027	1	0.0006	0.0014	0.0041	3.62
A^2B^2	-0.0041	1	0.0005	-0.0050	-0.0031	1.04

Table S11. Variance table for cellular uptake (a.u.)

Source	Sum of Squares	df	Mean Square	F-value	p-value	
Model	24.83	6	4.14	132.80	< 0.0001	significant
A-Mr	13.94	1	13.94	447.41	< 0.0001	
B-Qd/Qc	0.4438	1	0.4438	14.24	0.0012	
A^2	4.70	1	4.70	150.84	< 0.0001	

B^2	0.9276	1	0.9276	29.77	< 0.0001	
AB^2	4.28	1	4.28	137.35	< 0.0001	
A^2B^2	2.02	1	2.02	64.87	< 0.0001	
Residual	0.6232	20	0.0312			
Lack of Fit	0.3298	2	0.1649	10.11	0.0011	significant
Pure Error	0.2935	18	0.0163			
Cor Total	25.45	26				

Table S12. Coefficients table for cellular uptake (%)

Factor	Coefficient Estimate	df	Standard Error	95% CI Low	95% CI High	VIF
Intercept	2.26	1	0.1161	2.02	2.51	
A-Mr	-1.72	1	0.0813	-1.89	-1.55	3.82
B-Qd/Qc	0.1570	1	0.0416	0.0702	0.2438	1.04
A^2	1.73	1	0.1409	1.44	2.02	3.82
B^2	0.7709	1	0.1413	0.4761	1.07	3.04
AB^2	1.16	1	0.0993	0.9566	1.37	3.82
A^2B^2	-1.39	1	0.1720	-1.74	-1.03	5.82

Table S13. Variance table for NE (%)

Source	Sum of Squares	df	Mean Square	F-value	p-value	
Model	85217.56	5	17043.51	69.03	< 0.0001	significant
A-Mr	2355.43	1	2355.43	9.54	0.0056	
B-Qd/Qc	16280.01	1	16280.01	65.93	< 0.0001	
AB	3340.47	1	3340.47	13.53	0.0014	
A^2	337.93	1	337.93	1.37	0.2552	
A^2B	1549.78	1	1549.78	6.28	0.0205	
Residual	5185.18	21	246.91			
Cor Total	90402.74	26				

Table S14. Coefficients table for NE (%)

Factor	Coefficient Estimate	df	Standard Error	95% CI Low	95% CI High	VIF
Intercept	106.85	1	5.28	95.86	117.84	
A-Mr	-11.54	1	3.74	-19.31	-3.77	1.02
B-Qd/Qc	-51.15	1	6.30	-64.25	-38.05	3.00
AB	16.38	1	4.45	7.12	25.65	1.02
A^2	7.57	1	6.47	-5.89	21.03	1.02
A^2B	-19.33	1	7.72	-35.37	-3.28	3.02

Appendix IV

Evaluation of the pre-gelling droplet diameter dependencies to the dispersed phase flow variation

FFJ and TJ functioning are reported in *Figure S1*. In particular, the images highlight the droplet generation cycle for both devices in dripping regime: after the pinch-off of a droplet, the dispersed phase rapidly retract and then starts to expand again. When the shear stress applied by the continuous phase exceeds the surface tension, the dispersed thread collapse and a new droplet is formed.

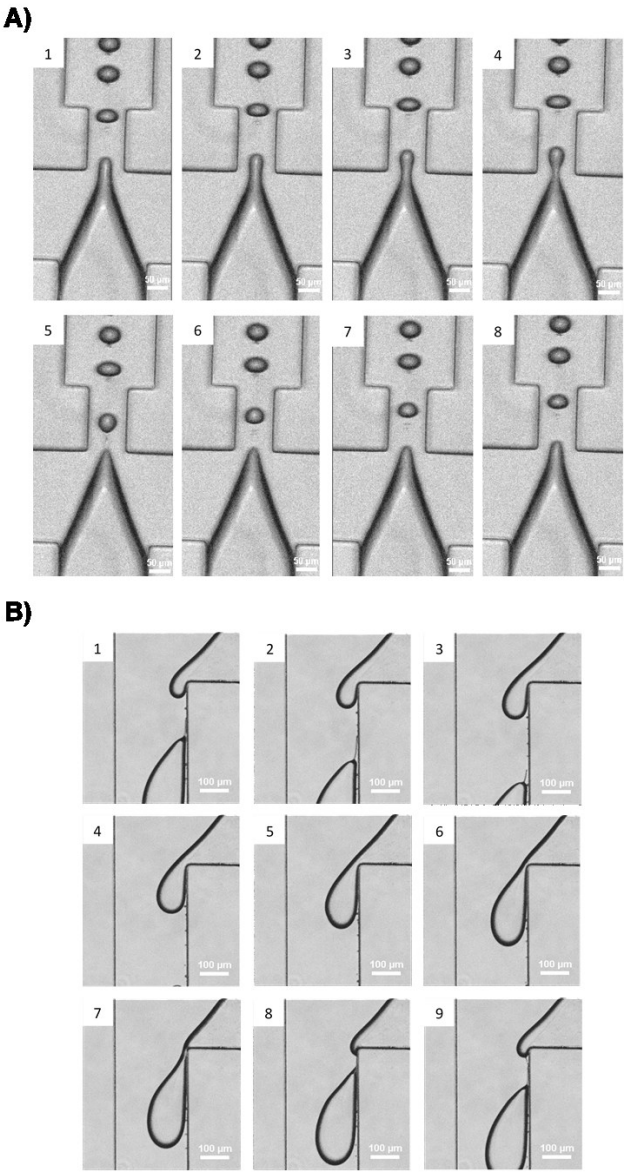

Figure S1 Droplet generation cycle in dripping regime for A) FFJ and B) TJ.

Figure S2 illustrates the correlation between the variation in the dispersed phase and the equivalent diameter of the microspheres generated at the junction of both devices. *Figure S1 A I.* and *B I.* refer to the increase in the dispersed phase of water for FFJ and TJ, respectively, while *Figure S1 A II. and B II.* concern that of calcium chloride.

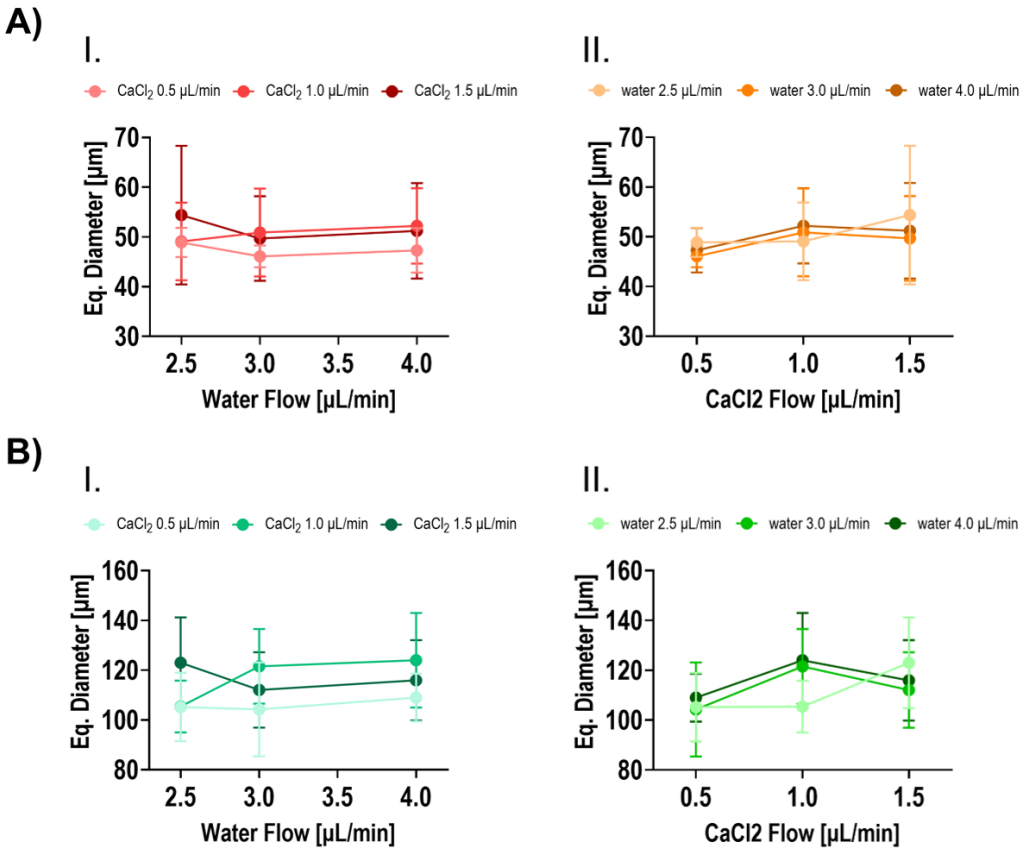

Figure S2 Graphs displaying the measured equivalent diameter values for A) FFJ and B) TJ concerning the increase in I.) water flow [µL/min] and II.) in calcium chloride flow [µL/min].

The results obtained from both the FFJ and TJ systems demonstrate a consistent pattern with regard to the influence of flow rates on droplet size. In both systems, variations in the water phase flow rate have been observed to have a minimal impact on the equivalent droplet diameter, indicating that the water phase plays a relatively minor role in regulating droplet size. In contrast, an increase in droplet diameter is observed with higher flow rates for calcium chloride in both systems, though this effect is more pronounced in the TJ system.

The two-way ANOVA statistical analysis (*Table S1*) corroborates these findings, confirming that the flow of calcium chloride exerts a more pronounced influence on droplet size compared to water flow.

Table S1 Two-way ANOVA analysis of the acquired ON-CHIP droplet equivalent diameter for the Flow Focusing junction (FFJ) and T junction (TJ) devices.

	Source of Variation	% of total variation	P value	P value summary
FFJ	Interaction	2.416	0.5072	ns
	$CaCl_2$ Flow	5.170	0.0313	*
	Water Flow	0.9615	0.5174	ns
TJ	Interaction	9.657	0.0508	ns
	$CaCl_2$ Flow	9.590	0.0097	**
	Water Flow	1.694	0.4237	ns

Effect of Ca^{++} concentration on the microbeads gelation process

From the study conducted, two different types of cross-linking kinetics were observed for the microfluidic platforms, strictly determined by the variation in calcium chloride concentration: external and internal. *Figure S3* reported representative images of the alginate microbeads obtained in FFJ device when different cross-linking kinetics occurs. Same processes are also reported for TJ device.

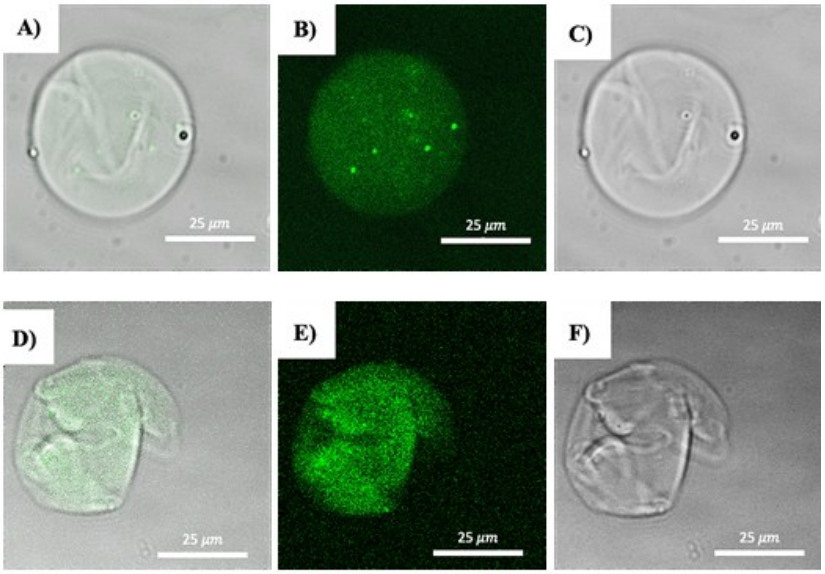

Figure S3 Comparison between the beads generated through internal gelation (A-C) and those produced via external gelation (D-F); A) Merged images acquired in confocal microscopy (magnification 20X) for the FFJ_{75mM}_G flow condition; B) Fluorescence image (FITC) of the bead; C) Bright-field image; D) Merged images obtained in confocal microscopy for the FFJ_{75mM}_A flow condition; E) Fluorescence image (FITC) of the bead; F) Bright-field image.

Slow gelation: Reducing the concentration of calcium chloride results in more uniform and regular microspheres (see *Figure S3 A, B* and *C* for flow condition FFJ75mM_G). This phenomenon occurs for high cross-linking times, which allow the uniform distribution of the calcium cations across the whole droplet volume through the convective flows in the early stages of the gelation process.

Fast gelation: At elevated concentrations of calcium chloride, an increase in the number of polydisperse microspheres can be observed, which are characterized by a tail splash (*Figure S3 D, E* and *F* for flow condition FFJ75mM_A). This phenomenon is associated with excessively short cross-linking times. In other words, employing large quantities of calcium chloride alongside a reduced water flow enables instant interaction between sodium alginate and $CaCl_2$, promoting an external-initiated cross-linking reaction that subsequently penetrates the core of the droplet through convective movements during the gelling process.

Scientific Dissemination

List of Publications

1. Limiti E.; Mozetic P.; Giannitelli S.M.; Pinelli F.; Han X.; Del Rio D.; Abbruzzese F.; Basoli F.; Rosanò L.; Scialla S.; Trombetta M.; Gigli G.; Zhang Z.J.; Mauri E.; Rainer A. "**Hyaluronic Acid-Polyethyleneimine Nanogels for Controlled Drug Delivery in Cancer Treatment**", ACS Applied Nano Materials, 2022, 5, 5544-5557. DOI: 10.1021/acsanm.2c00524.
2. Giannitelli S.M. †; Limiti E. †; Mozetic P.; Pinelli F.; Han X.; Abbruzzese F.; Basoli F.; Del Rio D.; Scialla S.; Rossi F.; Trombetta M.: Rosanò L.; Gigli G.; Zhang Z. J.; Mauri E.; Rainer A. "**Droplet-based microfluidic synthesis of nanogels for controlled drug delivery: tailoring nanomaterial properties via pneumatically actuated flow-focusing junction**", Nanoscale, 2022, 14, 11415. DOI: 10.1039/d2nr00827k.
3. Brandi C. †; De Ninno A. †; Ruggiero F.; Limiti E.; Abbruzzese F.; Trombetta M.; Rainer A.; Bisegna P.; Caselli F. "**On the compatibility of single-cell microcarriers (nanovials) with microfluidic impedance cytometry**", Lab on a Chip, 2024, 2883-2892. DOI: 10.1039/D4LC00002A.
4. Han X.; Scialla S.; Limiti E.; Davis E. T.; Trombetta M.; Rainer A.; Jones S. W.; Mauri E.; Zhang Z. J. "**Nanoscopic gel particle for intra-articular injection formulation**", Biomaterial Advances, 2024, DOI: 10.1016/j.bioadv.2024.213956.
5. Lacroce E.; Nunziata G.; Cianniello F.; Limiti E.; Rainer A.; Vangosa F. B.; Sacchetti A.; Sponchioni M.; Rossi F. "**Amphiphilic pH-responsive core-shell nanoparticles can increase the performances of cellulose-based drug delivery systems**", International Journal of Biological Macromolecules, 2024, 137659, DOI: 10.1016/j.ijbiomac.2024.137659.
6. Limiti E.†; D'Alessandro E.†; Bucciarelli A.; Raniolo S.; Mozetic P.; De Luca E.; Lemma E. D.; Basoli F.; Gigli G.; Mauri E.; Rossi F.; Trombetta M.; Giannitelli S. M.; Rainer A. "**Optimization of the Droplet-based Microfluidic Synthesis of Nanogels for Drug Delivery**", Small – *Submitted*.
7. Facchino M.; Pietrelli L.; Menegoni P.; Capocelli M.; Limiti E.; Trombetta M.; Basoli F.; De Falco M. "**Shifting towards sustainable coagulants for the removal of microplastics**", ChemPlusChem – *Submitted*.

8. Della Posta S.; Gallo V.; Limiti E.; Trombetta M.; Gherardi M.; Gentili A.; De Gara L.; Fanali C. "**DES modified silica gel as dispersing material for miniaturized matrix solid phase dispersion applied to triazoles determination**", Advances in Sample Preparation – *Submitted*.

† Authors equal contribution

Conference Presentations

Oral presentation

1. International conference "Polymer Network Group (PNG) 2022", Rome, 12-16 June 2022 – *Oral presentation* – Title: **Droplet-based microfluidic synthesis of tunable nanogels for controlled drug delivery in ovarian cancer treatment.**
2. Workshop "International Conference on Material Science and Nanotechnology" (ICMN2022), Rome, 3-5 October 2022 – *Invited speaker, oral presentation* – Title: **Hyaluronan-based nanogels for controlled delivery of doxorubicin in ovarian cancer treatment.**
3. XIII Congresso Nazionale AICIng - II Congresso Nazionale Divisione CT Società Chimica Italiana Milan, 25-28 June 2023 – *Oral presentation* – Title: **Tailoring the physicochemical properties of nanogels via a pneumatically driven microfluidic device.**
4. International conference "Humboldt Colloquium", Rome, 21-23 September 2023 – *Oral presentation* – Title: **Droplet-based microfluidics for nanotechnology and biomedical applications.**

Poster presentation

1. National workshop of the Italian chapter of the Controlled Release Society (CRS Italian Chapter), Genova, 7-9 October - *Poster presentation* – Title: **Continuous flow synthesis of PEI/hyaluronan nanogels via droplet-based microfluidics.**
2. International conference "Nanoscience & Nanotechnology 2024", Frascati, 3-6 June 2024 – *Poster presentation* – Title: **Microfluidic droplet-based synthesis of nanogel for drug delivery in ovarian cancer: a design of experiment study**.
3. International conference "Micro-Total Analysis System (μTAS 2024)", Montréal, 13-18 October 2024 – *Poster Presentation* – Title: **Microfluidic droplet-based synthesis of nanogel for drug delivery in ovarian cancer: a design of experiment study**.

table of acronyms

ISO	International Organization for Standardization
AFM	Atomic force microscopy
Alg-FITC	FITC-modified alginate
ANOVA	Analysis of variance
APS	ammonium persulfate
Bo	Bond number
Ca	Capillary number
CD44	Cluster of differentiation 44
CJM	coaxial jet mixer
CMC	critical micelle concentration
CTRL	Control
CuAAC	copper(I)-catalyzed alkyne− azide cycloaddition
CV	coefficient of variation
Cy5	cyanine 5
D2O	deuterium oxide
DCM	dichloromethane
DIW	deionized water
DLS	dynamic light scattering
DMEM	Dulbecco's Modified Eagle's Medium
DMF	dimethylformamide
DMSO	dimethylsulfoxide
DoE	Design of Experiment
DOX	doxorubicin
EDC	N-(3-dimethylaminopropyl)-N′-ethyl carbodiimide hydrochloride
EE %	encapsulation efficiency
FA	folic acid
FBS	fetal bovine serum
FFJ	flow-focusing junction
FITC	fluorescein isothiocyanate
FRR	flow rate ratio
FT-IR	Fourier transform infrared spectroscopy
G6PD	glucose 6-phosphate dehydrogenase
GFP	Green fluorescent protein
HA	hyaluronic acid
HAase	hyaluronidase
Hb	hemoglobin
HCl	hydrochloric acid

HDF	Human Dermal Fibroblasts
HeLa	Human Epithelial Cervical Carcinoma
HepG2	Hepatocellular carcinoma
HFF	hydrodynamic flow-focusing
IPA	isopropanol
LPEI	Linear polyethyleneimine
MEET	Mixed Emulsion/Evaporation Technique
MFI	median fluorescence intensity
MR	Molar ratio
MSC	mesenchymal stem cell
MWCO	molecular weight cut-off
Na_{ASC}	sodium ascorbate
NE	Nanoencapsulation Enhancement
NG	nanogel
NHS	N-hydroxy succinimide
NMR	nuclear magnetic resonance
NP	Nanoparticle
OVCA433	human epithelial ovarian cancer cell line
PBAE	Poly beta(amino ester)
PBS	phosphate-buffered saline
PCL	polycaprolactone
PDI	polydispersity index
PDMS	polydimethylsiloxane
Pe	Péclet number
PEG	Polyethylen glycol
PEI	polyethyleneimine
PEO	poly(ethylene oxide)
PFA	paraformaldehyde
PLA	polylactic acid
PLGA	poly(lactic-co-glycolic) acid
PPy	polypyrrole
PVA	polyvinyl alcohol
QC	continuous phase flow rate
QD	dispersed phase flow rate
qPCR	Quantitative polymerase chain reaction
R^2	coefficient of determination
RBC	red blood cell
Re	Reynold number
RNA-seq	RNA sequencing
RSM	Response Surface Method

RT	room temperature
SD	standard deviation
SEM	scanning electron microscopy
SHM	staggered herringbone micromixers
SLNP	solid-lipid NP
TEM	transmission electron microscopy
TFR	total flow rate
THF	tetrahydrofuran
TJ	T-junction
TMCS	trimethylchlorosilane
TMS	Tetramethylsilane
UV	Ultraviolet
W/O	water-in-oil
We	Weber number
αFR	alpha isoform of the Folate Receptor